論文 / 著書情報
Article / Book Information

題目(和文)	乱流中のコヒーレント微細構造に基づく噴霧燃焼に関する研究
Title(English)	Investigation of spray combustion mechanism based on coherent fine scale structure in turbulence
著者(和文)	佐藤允
Author(English)	Makoto Sato
出典(和文)	学位:博士(工学), 学位授与機関:東京工業大学, 報告番号:甲第8700号, 授与年月日:2012年3月26日, 学位の種別:課程博士, 審査員:宮内 敏雄
Citation(English)	Degree:Doctor (Engineering), Conferring organization: Tokyo Institute of Technology, Report number:甲第8700号, Conferred date:2012/3/26, Degree Type:Course doctor, Examiner:
学位種別(和文)	博士論文
Type(English)	Doctoral Thesis

Doctoral Dissertation

Investigation of Spray Combustion Mechanism Based on Coherent Fine Scale Structure in Turbulence

Supervisors

Professor : Toshio Miyauchi

Associate Professor : Mamoru Tanahashi

Department of Mechanical and Aerospace Engineering
Graduate School of Science and Engineering
Tokyo Institute of Technology

Makoto Sato

Contents

Chapter 1

Introduction

1.1 Development of Science and Technology

1.1.1 Ancient Greek and Middle Ages in Europe

Since the dawn of history, science and technology have been developed by wisdom and techniques of human beings. A lot of philosophers in ancient Greek tried to find the root of the universe in order to figure out the principle which subjects the universe. Thales thought ”Water” is a first principle and everything comes from water. Heraclitus of Ephesus regarded ”Fire” as the basic element, and he thought all things move and nothing remains still. Pythagoras believed ”Number” as an alche.

Aristotle, who was the greatest philosopher in ancient Greek and is known as the father of all study, proposed four basic elements in the world, ”Fire”, ”Water”, ”Air” and ”Earth”. This thought was derived from Empedocles’s four-element-hypothesis. However, for Aristotle, these four elements were the matters which assume the four fundamental qualities, ”hot”, ”cold”, ”dry” and ”wet”, which cannot be reduced any more. In this mean, Aristotle thought that the qualities are the principal elements composing nature.

On the other hand, Leukippos and Dēmokritos thought the universe is composed of atom which cannot be divided any more. This atomic hypothesis is similar to the modern atomic theory in part. Although Epicurus further developed

the hypothesis, it ended for the denial by people of the Academia.

Aristotle studied about nature in the actual world, differently from his teacher, Plato. He wrote many books in various fields such as art, ethics, physics, astronomy, aerology, zoology, botany and so on. His thoughts and studies have significantly influenced the progress of science, and the diminish of it unexpectedly as follows.

As a consequence of the anabasis of Alexander the Great, who was a student of Aristotle, Hellenistic was born over the east coast of the Mediterranean Sea and the oriental region. Subsequently, the Roman Empire flourished in Europe over 300 years, and Christianity became the established religion of the Roman Empire. After the Roman age, Christianity had a strong power in medieval Europe. Augustine established theology, which studies about Christianity. He gave a strong authority to it, and he thought unknown phenomena should be understood as unknown. In addition, he considered it good attitude to be unconcerned about the principle of nature, because interrogation beyond the Bible was contrary to the Christian beliefs. At the late middle ages, Islam came to contact with Christendom of Europe. From Islam, Greek culture which had been missed in Europe after Roman era was reimported. Especially, books of Aristotle received a lot of attention from European in these days. Albertus Magnus and Thomas Aquinas integrated their theology with Aristotelian physics, and then they accomplished Scholasticism. Scholasticism completely dominated the academism in Europe during the middle ages, so it contributed to the progress but mainly diminish of science. In this way, the influence of Aristotle was authorized by Scholasticism of Christianity, and this authority reminded strong for a long time. Aristotelian physics dominated perspectives of natural science of European over 1,000 years. This is not only because of cozy relations with Christianity, but also of the great and comprehensive Aristotelian ethics and metaphysical philosophy.

1.1.2 The Renaissance and Dawn of Modern Natural Science

These situations for scientific study began to change in the Renaissance at last. In the Renaissance, a lot of knowledge was introduced into European through Christian Crusade, and many European intellectuals were interested in the knowledge. Additionally, the thoughts that it had been regarded as heresy in a society of medieval Christianity such as Hermeticism, and a possibility of utilizing forces of nature by understanding the law of it without relying on wired had began to be discussed openly in the Renaissance.

Furthermore, it is enormously noticeable that some intellectuals who recognized the advantage of knowledge developed by craftspeople and magicians appeared. In this age, almost intellectuals usually regarded handwork as unimportant and only studied about interpretation of ancient books. Before the days of the Renaissance, of course, there were both demonstrative knowledge and technical knowledge in many civilizations, however, they had kept away from each other. It was only the European civilization at this time to achieve an integration of these two knowledge.

Modern natural science started in this movement. Its essence was physical and mathematical understanding of natural phenomena which had been represented in occult element before. Here, one big problem occurred. Modern natural science was inconsistent with Aristotelian physics, which had influenced all studies for more than 1,000 years because of authority given by middle age Scholasticism. As mentioned above, Aristotelian physics is not suitable for quantification, because the qualities are the principal element in it. On the other hand, the object of modern natural science is to find out the mathematical law of natural phenomena based upon an accurate measurement and a precise observation. The experiment of Galilei is a good representation of it. Galilei established a method of modern science which consists of hypothesis, argument and experiment. He conducted the precise experiments with the use of sophisticated experimental instrument, and

found out the concept of acceleration. His manners for experiment have affected the development of science and technology.

In the field of astronomy, revolution of the perspective of the universe started in suggestion of the heliocentric theory by Copernicus against the geocentric theory believed from ancient Greek. The perspective on the universe based on the heliocentric theory finally came to Newton by the hands of Kepler, Galilei and Hook. Newton found out a gravity described in mathematical function through the detailed observation data by Kepler, and he clarified a dynamics of the solar system based on a gravity. This means motion of a planet in the universe and an object in the world follows the same physical law. Here, the new perspective on the universe was eventually born alternative to the system of planetary motion from ancient Greek. The clarification of the laws which dominates the world became a main driving force of the development of modern natural science.

In addition, it is also noted that the new technology which was invented and developed from twelve century, such as compass, black gunpowder, cast iron, paper, typography, lens and so on, significantly influenced on the formation of these natural science. Then, further development was achieved in the field of industrial technology in accordance with an advance of natural science as follows. Science and technology became complementary with each other from this time.

1.1.3 Industrial Revolution and Thermodynamics

Industrial Revolution in England at eighteenth century dramatically changed the life of people by drastic improvement of productivity, and has significantly influenced a global situation after age. Realization of Industrial Revolution was triggered by an invention and improvement of a steam engine. The origin of a steam engine was Huygens invention of the model of piston driving by gunpowder. Denis Papin replaced the working material of the engine from gunpowder, which was difficult to control, to steam of water. The steam engine, literal meaning of the word, was made, however, it was only laboratory scale and far from

practical use. Thomas Newcomen improved the idea and made the Newcomen engine in early eighteenth century, which was the first steam engine as product.

After fifty years, James Watt attended to the Newcomen engine. The improvement by Watt was different from other improvements which was ad hoc, depending on experience and guess. He did improvement the steam engine with throughout theoretical considering, so Watt engine brought out the essential feature of the thermal engine and can be verified in principle discussion. It is said that about 75% of fuel was reduced by improvement of Watt. Here, practical realization and improvement of a steam engine had the strong impact to the European society by showing an application of ”fire” to power, because they had known only the water, wind, animal and human as a source of power. Fire had been used for air heating and cooking at most.

In addition, a steam engine made a huge contribute to the development of ”thermology”. There were some main theories in thermology discipline in this time, such as caloric theory. From the study of efficiency of a steam engine, Sadi Carnot gave the answer about the problem whether there was principal limitation to a generation of a power from heat, or not. Carnot showed that it needs difference of temperature to generate a power, and a maximum efficiency is determined by only temperature. On the other hand, Myer and Joule insisted the heat-work equivalence and the conservation of them in entire system. The insistence seemed to be inconsistent with the Carnot's theory that it needs the particular condition to generate a power from heat. Through the Carnot's theory and Meyer and Joule insists, Clasius and Thomson established the ”thermodynamics”. It was based on the conservation of energy and entropy enhancement, which means irreversible process exists in nature. From a steam engine, thermodynamics was established and the concept of energy was spread over the world. Then, based on the thermodynamics, many industrial machines have been produced.

1.2 Energy and Environmental Problems

1.2.1 Consumption of Fossil Fuels and CO_2 Emission

After the Industrial Revolution, the human desire for improvement of life has been no limitation, and science and technology have continued to be developed in response to it. Various industries made it possible to supply a large number of products and service, and social structures of the world have been changed. As a result, high civilized societies have been constructed in many regions, nowadays. However, fossil fuels, which had been stockpiled for long time, have been rapidly consumed by human beings from the Industrial Revolution to the present. The problem for exhaustion of fossil fuels by further consumption is deeply serious because of the limitation of its availability. Figure 1.1 shows the development and prediction of energy consumption for fossil fuels in the world [1]. The total consumption is predicted to be doubled in 2030 compared with that in 1990.

Additionally, increase of use of fossil fuels has large influence on the global environment, for example, air pollution has gone from bad to worse year after year all over the world. Among many environmental problems, global warming is considered to be most serious. The main cause of global warming is thought as the increase of the Green house gas. In particular, suppression of emission of CO_2, which is main matter in Green house gas, has been desired globally. Figure 1.2 shows the development of CO_2 emission from consumption of fossil fuels [2]. CO_2 emission has rapidly increased year by year. The Kyoto Protocol, whose object is the prevention of global warming, was concluded at the COP 3, on December 11th, 1997. Under the Kyoto Protocol, Japan has pledged to reduce its 1990 emissions by 6 $\%$ by 2012.

The large part of CO_2 emission is from many combustors such as automobile engines and gas turbine engine. In particular, rate of contribution from automobile to entire CO_2 emission in Japan is about 20 $\%$. From these points, the development of high efficiency and low environment load combustors has large contribute to solve the energy and environmental problems.

1.2.2 Fire and Combustor

The combustor generates a power by using fire. Before the dawn of history, fire was forceful tool and mystery for human beings. There have been the rites and worship of fire from primitive age to nowadays. In about sixth century B.C., Zoroastrianism, which worships a fire as an arcanum, had been founded by Zoroastar, and it became the established religion in the Persia. In ancient Greek, Heraclitus regarded a fire as a basic element. The story about ”Prometheus’s fire” in Greek myths has been well known as good suggestion of the risk for using fire by human beings. In Japan, many Fire Festivals, which enshrine God by making a fire, have been held for a long time.

Investigations of a fire in natural science were activated from the Renaissance. In the end of seventeenth century, the phlogiston theory was proposed by some scientists. This theory insisted that burning of matter was caused by the phlogiston, and combustible materials had a lot of the phlogiston. Then, the clarification of the phenomenon of oxidization ended the phlogiston theory at eighteenth century. From this sense, the modern study of combustion started. Then, the use of a fire in industry has explosively expanded all over the world, being coupled with the Industrial Revolution.

At the present days, it has becomes more important to make combustors efficient, such as internal-combustion engine and industrial burner reactor, so the improvement of conversion efficiency from heat energy by combustion to mechanical work has been needed. In addition, because the problems of toxic emissions from combustors are very serious, it needs to clarify the detailed mechanism of toxic emissions. For achieve these, the establish of low emission and high efficiency combustion control technology based on accurate understanding of combustion phenomena is essential.

In many industrial combustors, spray combustion has been applied, such as gas turbine engine, diesel and direct injection engines, because of its controllability and applicability to various flame configurations. However, the phenomena in

spray combustion are very complex, since it consists of several processes such as atomization, dispersion of fuel droplet, their evaporation, vapor mixing, ignition, and they proceed simultaneously with interaction between each other. Therefore, it is necessary to clarify the phenomena in spray combustion in detail to make combustors more efficient. The recent researches about each process are shown in later chapters.

In particular, since the influence of flow field in a combustor on these processes is very significant, to clarify the relationship between them is important. However, flow field in a combustor is commonly turbulent, so the clarification is quite difficult for complexity of the flow structure. From this reason, understanding of turbulent phenomena is needed.

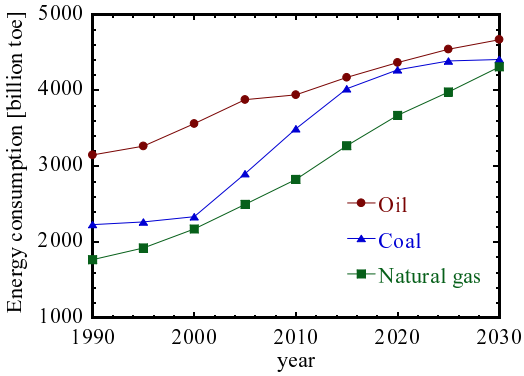

Figure 1.1: Time development and prediction of fossil fuels consumption in the world.

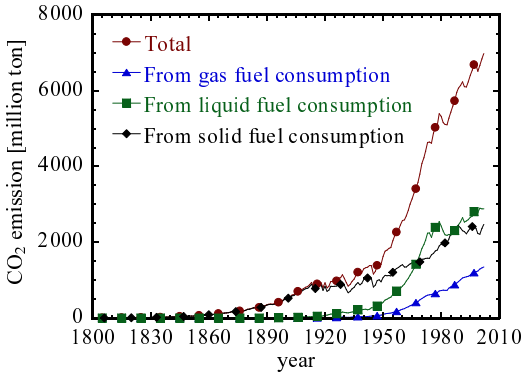

Figure 1.2: Time development of CO_2 emission from consumption of fossil fuels.

1.3 Turbulence

1.3.1 Study on Turbulence

Turbulence, which is essentially complicated phenomenon, is observed in almost all flows in both the natural environments and many practical engineering processes. The basic understanding of turbulence phenomenon or its physics is very important for controls and prediction of many industrial applications. Thus, turbulence has been unceasingly investigated for several decades to understand its essential physics and to develop turbulence models.

The studies on equations of viscous fluid motion started by Navier in nineteenth century, and Stokes had finally accomplished it. In the late of nineteenth century, Reynolds conducted the visualization experiments on circular tube flow, and he clarified that disturbed flows are observed over the critical point with increase of flow rate. From some parameters of the flow and tube conditions, Reynolds derived non-dimensional number, Reynolds number, and he found out that disturbed flow, turbulence, is observed at high Reynolds number. In addition, he showed the dynamical effect of disturbance in turbulence as turbulent stress. This stress has been used by many theories and experiments in turbulence research.

As mentioned above, technologies have been developed after Industrial Revolution. In particular, the developments of a motor vehicle and an aircraft were significant, so the studies on turbulence were activated in accordance with these. Many researchers, Prandtl, Karman, Pohlhausen and so on, suggested a lot of theories of fluid mechanics, and these theories derived some turbulence models. In the fields of turbulence theory, isotropic turbulence theory by Taylor, local isotropic turbulence theory and prediction of inertial sub-range by Kolmogorov were suggested around the same time.

From the 1960', computational technology has rapidly progressed, and computational simulation of turbulence and turbulent heat transfer has started. In these simulations, direct numerical simulation (DNS) is an important tool in turbulence

research because DNS can provide exact three-dimensional velocity field which is available to investigate three-dimensional structures of turbulence in detail. In DNS, the governing equations are solved numerically on a fine calculation grid without any turbulence models. Recently, DNSs of high-Reynolds turbulent flows have been conducted using vector/parallel super computers with a high-speed operating system and huge memory.

1.3.2 Coherent Fine Scale Structure in Turbulence

Theoretical description of intermittent character in small-scale motions has been studied one of the most important subjects in turbulence research. Theorists have made efforts to establish theories of fine scale structure in turbulence by assuming various types of vortices as fine scale structure [4][5][6][7][8]. Most of them are based on an assumption that many tube-like vortices are embedded in turbulence randomly. Each vortex is considered to be an analytical solution of Navier-Stokes equations; for example a Burger's vortex.

Recent DNS studies of turbulent flows have clarified that turbulence is composed of many fine scale tube-like vortices [9][10][11][12][13][15][16]. Tanahashi et al. [10][11][12][13][14] have shown that the diameter and the maximum azimuthal velocity of these fine scale vortices can be scaled by the Kolmogorov length (η) and the Kolmogorov velocity (u_k), respectively. The most expected diameter is about 8 times η and the most expected maximum azimuthal velocity is about 1.2 times u_k except for the fine scale vortices near the wall [13]. Here, it should be noted that variance of the diameter and the maximum azimuthal velocity are relatively large. The maximum azimuthal velocity of intense fine scale vortices whose diameter are about 8η reaches about $3 \sim 4$ times r. m. s. of velocity fluctuation (u_{rms}). These intense vortices are closely related with the intermittency of turbulent energy dissipation rate. On the other hand, there are vortex structure which has large diameter, and their maximum azimuthal velocity approaches u_{rms} with the increase of diameter.

These fine scale vortices have been found in various turbulent flow fields; homogeneous isotropic turbulence [10][11], turbulent mixing layers [12][16], turbulent channel flows [13][15], turbulent Taylor-Couette flow [17] and so on, shown in Fig. 1.3. Since these fine scale tube-like vortices show similar characteristics and weak Reynolds number dependence, these vortices are called as a ”coherent fine scale eddy”, and regarded as a universal structure of turbulence.

Furthermore, Tanahashi et al.[11], who investigated three-dimensional structure of the coherent fine scale eddy, have suggested that the axis of the coherent fine scale eddy has several nodes which are identified as the minima of the second invariant of the velocity gradient tensor on the axis as shown in Fig. 1.4.

Even for complicated turbulent flows in a engineering combustor, the coherent fine scale eddies exist and may play important roles on the droplet dispersion, evaporation and mixing because they show strong swirling motion around them. Therefore, it is considered that spray combustion can be more efficient by adopting the droplet whose time scale is suitable for dispersion, evaporation, vapor mixing and ignition, based on the time scale of the coherent fine scale eddy in turbulence of combustor.

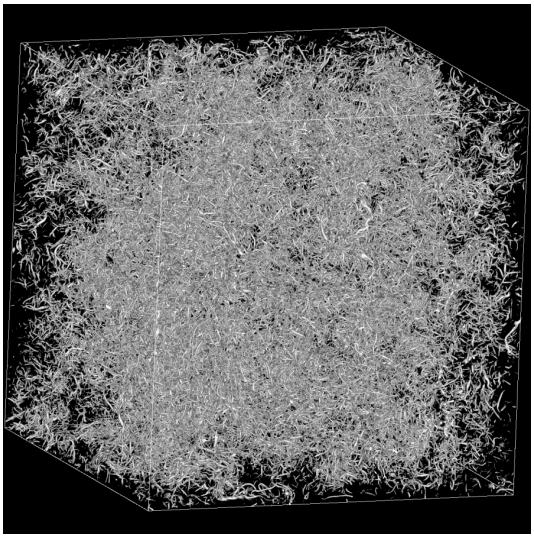

Homogeneous isotropic turbulence

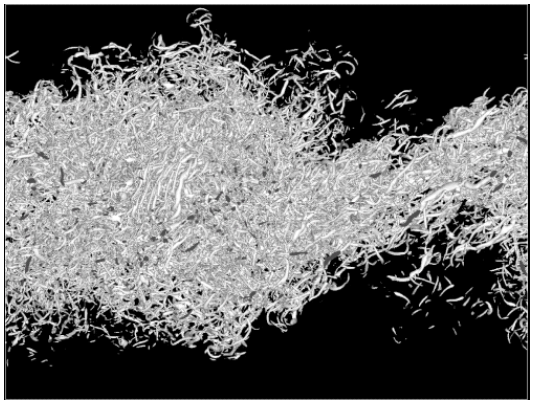

Mixing layer

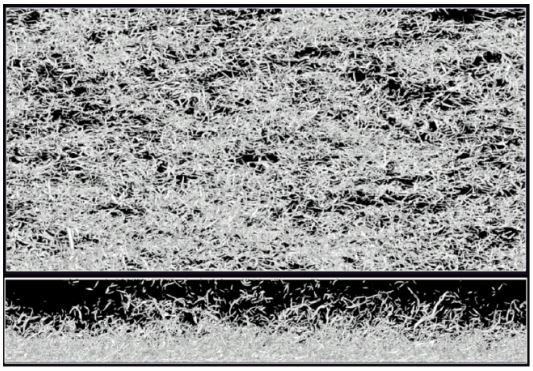

Channel flow

Figure 1.3: Isosurfaces of the second invariant of the velocity gradient tensor for various flow fields.

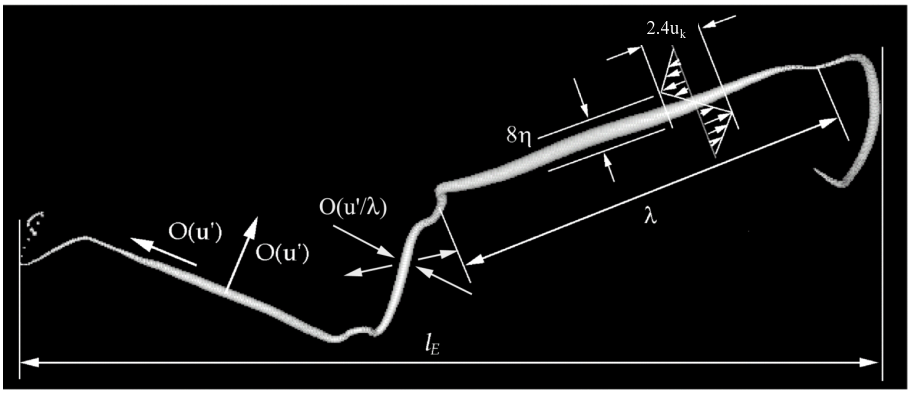

Figure 1.4: The axis of a typical coherent fine scale eddy in homogeneous isotropic turbulence.

1.4 Future Perspective

On 11 March 2011, many precious lives were lost in the Great East Japan Earthquake. In addition, the serious accident at the Fukushima No.1 nuclear power plant has given a strong impact on not just Japan but all over the world. Then, it makes the prediction and the policy for energy supply overturned, completely.

From the theory of relativity derived by Einstein in 1905, the concept of energy, which had been based on the thermodynamics, was further extended. It is noted that ”nuclear power” was created only through the physical theory. It is different from the natural powers such as, water, wind and fire, which began with experience and practical use. Nuclear bomb was purely derived from the brains of the physicians. Nuclear power plant is a byproduct of it. Here, the technology which was perfectly leaded by the science theory was born in this way, so the use of nuclear power is one of the goals of science and technology, developed from the dawn of the history.

However, the nuclear power plant of Fukushima No.1 made by the essence of the developed technologies was broken by natural threats, and many people were forced out of the place they lived. In addition, even more people have been scared of the radioactive materials.

The discussion about energy problems has been accelerated, and a great deal of attention has focused on a natural energy, in particular, renewable energy. In ancient Greek, Alistotle proposed four basic elements in the world, ”Fire”, ”Water”, ”Air” and ”Earth”. At the present, we have to make a better use of the natural material and phenomena, ”Fire”, ”Water”, ”Air”, to keep the ”Earth” be clean for future generation. For achieving that, it is necessary not only to develop the science and technology further and further, but also to advance the wisdom and techniques of human beings.

1.5 Objectives

The main objective of the present study is to clarify the relationships between the coherent fine scale structure regarded as a universal structure in turbulence and each process in spray combustion by direct numerical simulations. The objectives in each chapters are as follows.

In chapter 2, to clarify the relationship between particle dispersion and the coherent fine scale eddies, DNSs of homogeneous isotropic turbulence with particles which have different Stokes number are conducted for three Reynolds number cases.

In chapter 3, to clarify the relationships between droplet dispersion, vapor mixing and the coherent fine scale eddies, DNSs of homogeneous isotropic turbulence with evaporating n-heptane droplets which have different initial Stokes number are conducted for two Reynolds number cases.

In chapter 4, to clarify the effects of turbulence on the ignition and flame propagation process, DNSs of ignition and propagation of n-heptane/air premixed flame in two-dimensional homogeneous isotropic turbulence are conducted, including reduced kinetic reaction of n-heptane/air mixture with temperature dependence of the transport and thermal properties.

In chapter 5, to clarify the relationship between the ignition in spray combustion and the coherent fine scale eddies, DNS of homogeneous isotropic turbulence with evaporating n-heptane droplets under high temperature condition are conducted, including reduced kinetic reaction of n-heptane/air mixture with temperature dependence of the transport and thermal properties.

Chapter 2

Particle Dispersion in Fine Scales of Homogeneous Isotropic Turbulence

2.1 Preface

Turbulent flows laden with particles can be observed in many engineering applications and natural phenomena. The controls of turbulence and enhancement of heat transfer by particle injections are very important to improve efficiency of applications. Therefore, for effective controls, it is required to clarify the relationship between turbulence structures and particle dispersion.

A number of studies on dispersion of particle in turbulence have been conducted by numerical and experimental approaches. Squires and Eaton [18][19] have shown that particles whose time scale are about Kolmogorov time scale concentrate in low vorticity and high strain rate regions in homogeneous isotropic turbulence by DNS. This dispersion phenomenon is called as ”preferential concentration”, and same phenomenon has been observed in various turbulent fields studied by numerical [20][21][22][23][24] and experimental [25][26] approaches.

In the recent studies [27][28][32], the length scale of particle clusters and their dependence on the particle Stokes number has been investigated. Aliseda et al. [27] have studied the behavior of particles in decaying homogeneous isotropic turbulence experimentally, and shown that the length scale where the particle concentration is most correlated is the order of 10 times Kolmogorov length scale by

adapting the methods proposed by Fessler et al. [25] and Wang and Maxey [20].

However, they have not mentioned what kind of turbulence structures creates these small scale clusters. Yoshimoto and Goto [28] have shown that distribution of particles whose time scale are within the inertial scale of turbulence has a self-similar multi-scale nature from their DNS results. They suggested that not only small scale vortices but also large scale ones affect the clustering of particles. These characteristics have also been shown by Bec et al. [32]. In these studies, the definition of vortex structure is vague, and vortex structures which determine the particle clustering have not been clarified.

The objective of this chapter is to clarify the relationship between particle dispersion and coherent fine scale eddies by conducting DNS of homogeneous isotropic turbulence with particles which have different Stokes number.

2.2 Numerical Method

Multiphase flow, which is composed of continuous phase and dispersed phase such as particles and droplets, has been modeled in some mathematical presentations. The continuum model is that both continuous phase and dispersed phase are treated as an Eulerian frame. The Eulerian-Lagrangian model is that continuous phase is calculated as an Eulerian frame, and dispersed phase are tracked in a Lagrangian approach as mass point.

In the Eulerian-Lagrangian model, the equation and concept are relatively simple, so this model is more appropriate for numerical simulation. The disadvantage of this model is that computational cost becomes so large with increase of number of particle. In this study, fluid flow is treated in an Eulerian frame, and particles are tracked in a Lagrangian frame.

2.2.1 Governing Equations

The governing equations of flow field are following continuity equation and incompressible Navier-Stokes equations;

$$\frac{\partial u_i}{\partial x_i} = 0 \,, \tag{2.1}$$

$$\frac{\partial u_i}{\partial t} + u_j \frac{\partial u_i}{\partial x_j} = -\frac{\partial p}{\partial x_j}\,\delta_{ij} + \frac{1}{Re}\frac{\partial^2 u_i}{\partial x_i^2}\,, \tag{2.2}$$

where p and δ_{ij} are a pressure and the Kronecker delta. Re is the Reynolds number based on $L/2\pi$ and initial u_{rms}. L is a length of a computational box.

2.2.2 Equations of Particle Motion

In this study, volume of particle is assumed to be zero and the particle is tracked in a Lagrangian approach as mass point, because the scale of particle is far smaller than Kolmogorov scale of turbulence. The Basset-Boussinesq-Ossen equation is equation of motion of hard-sphere particle in flow field as follows [33];

$$\begin{aligned}\left(\frac{4}{3}\pi r_p^3 \rho_p\right) =& 6\pi r_p \mu (u_f[x_p(t),t] - u_p(t)) \\ &+ \left(\frac{4}{3}\pi r_p^3 \rho_f\right)\frac{Du_f}{Dt}|_{x_p(t)} \\ &+ \frac{1}{2}\left(\frac{4}{3}\pi r_p^3 \rho_f\right)\left(\frac{du_p}{dt} - \frac{Du_f}{Dt}|_{x_p(t)}\right) \\ &+ 6r^2(\pi\rho_f)^{1/2}\int_{t_0}^{t}\frac{\frac{d}{d\tau}(u_f[x_p(\tau),\tau] - u_p(\tau))}{(t-\tau)^{1/2}}d\tau \\ &+ \left(\frac{4}{3}\pi r_p^3\right)(\rho_p - \rho_f)g,\end{aligned} \tag{2.3}$$

where subscripts p and f represent particle and fluid, respectively. r and μ are a radius of droplet and a fluid viscosity. The terms of right-hand side of this equation represent drag force of flow based on Stokes's law, the force by pressure gradient and viscous stress of flow, inertia force of additional mass, viscous force by unsteady relative acceleration (Basset history) and buoyancy force. It is noted that

some other forces are ignored in the process of derivation of this equation for the complexity of particle motion in turbulence. In general, drag and buoyancy force of flow is dominant as compared with other terms. In addition, if the density of dispersed phase is much larger than that of flow field, only drag force is dominant. In the case of motion of particle in static fluid or at the moment of particle relative motion to flow field, Basset history and inertia force of additional mass become important. These effects can be ignored by enough computational time.

In this chapter, the equations of particle motions are given by follows based on these assumptions;

$$\frac{du_p}{dt} = \frac{1}{\tau_p}(u_f[x_p(t), t] - u_p(t)) \ , \tag{2.4}$$

$$\frac{dx_p}{dt} = u_p \ . \tag{2.5}$$

Here, τ_p is the particle response time defined by follows;

$$\tau_p = \frac{\rho_p}{\rho_f}\frac{{D_p}^2}{18\nu}, \tag{2.6}$$

where D_p and ν are a diameter of particle and the kinematic viscosity of fluid. The motions of particles are analyzed for several particle response times using instantaneous velocity field of fluid obtained by DNS, where fluid velocity at particle position is estimated by a fourth-order Lagrange interpolation.

2.2.3 Numerical Procedure and Numerical Conditions

To solve the governing equations, the spectral methods are used in all directions. The spatial derivatives are evaluated by Fourier spectral methods because boundary conditions are assumed to be periodic. The spectral methods deal with periodic functions specified by the values at a set of uniformly spaced points with the aid of a discrete Fourier series as follows;

$$\begin{aligned}&\hat{u}(k_x, k_y, k_z, t)\\ &= \frac{1}{N_x N_y N_z}\sum_{j=0}^{N_x-1}\sum_{k=0}^{N_y-1}\sum_{l=0}^{N_z-1} u(x_j, y_k, z_l, t)\exp(-ik_x x_j - ik_y y_k - ik_z z_l),\end{aligned} \tag{2.7}$$

and Fourier coefficient $\hat{u}(k_x, k_y, k_z, t)$ is transformed back to physical space by

$$\begin{aligned} & u(x_j, y_k, z_l, t) \\ &= \sum_{k_x=-N_x/2}^{N_x/2-1} \sum_{k_y=-N_y/2}^{N_y/2-1} \sum_{k_z=-N_z/2}^{N_z/2-1} \hat{u}(k_x, k_y, k_z, t) \exp(ik_x x_j + ik_y y_k + ik_z z_l). \end{aligned} \tag{2.8}$$

The aliasing errors, which are involved in the nonlinear terms, are fully removed by the 3/2 rule. Time advancement is conducted by a low storage third-order Runge-Kutta scheme as follows.

$$\begin{aligned} \Delta u_k &= \left(\frac{\partial u_k}{\partial t} \right) \times \frac{1}{3} \Delta t \\ u_{k'} &= u_k + \Delta u_k \\ \Delta u_{k'} &= \left\{ \frac{5}{9} \Delta u_k + \left(\frac{\partial u_{k'}}{\partial t} \right) \right\} \times \frac{15}{16} \Delta t \\ u_{k''} &= u_{k'} + \Delta u_{k'} \\ \Delta u_{k''} &= \left\{ \frac{153}{128} \Delta u_{k'} + \left(\frac{\partial u_{k''}}{\partial t} \right) \right\} \times \frac{8}{15} \Delta t \\ u_{k+1} &= u_{k''} + \Delta u_{k''} \end{aligned} \tag{2.9}$$

A second-order Adams-Bashforth scheme is used for time advancement of equations of particle motions as follows;

$$u_k^{n+1} = u_k^n + \Delta t \left(\frac{3}{2} S_k^n - \frac{1}{2} S_k^{n-1} \right). \tag{2.10}$$

For the first time step, a first-order Euler scheme is used.

$$u_k^{n+1} = u_k^n + \Delta t S_k^n \tag{2.11}$$

In this study, decaying homogeneous isotropic turbulence is used for the flow field. Homogeneous isotropic turbulence is generally used in fundamental study of turbulence, because there is no influence of boundary condition, and an analysis is comparatively easier than other flow fields.

Fully-developed homogeneous isotropic turbulence which was obtained from preliminary DNS is used for the initial velocity field. DNS are conducted for $Re_\lambda = 60.1$ with $128 \times 128 \times 128$ grid points, $Re_\lambda = 97.1$ with $256 \times 256 \times 256$ grid

points and $Re_\lambda = 175.4$ with $512 \times 512 \times 512$ grid points. Here, Re_λ represents the Reynolds number based on the Taylor micro scale. The statistics of each initial flow field are shown in Table 2.1. The computational domain is selected to be $(2\pi)^3$. The number of particles is 1 million, and their initial positions are assumed to be random. Their initial velocities are supposed to be equal to the fluid velocity at their positions. Figure 2.1 shows isosurface of the second invariant of velocity gradient tensor and particles.

The Stokes numbers of the particles, which is defined as follows, are shown in Tables 2.2, 2.3 and 2.4 for each Reynolds number case.

$$St_f = \frac{\tau_p}{\tau_f} \tag{2.12}$$

In Tables 2.2, 2.3 and 2.4, St_η, St_λ, St_l and St_c denote the Stokes numbers based on Kolmogorov time scale (τ_η), Taylor time scale (τ_λ), integral time scale (τ_l) and time scale of the coherent fine scale eddy (τ_c) which is calculated from their most expected diameter 8η and most expected maximum azimuthal velocity $1.2u_k$.

In this chapter, it is assumed that particles do not affect the fluid flow, and the interactions between particles are neglected. Elghobashi [34] has classified the interaction between particle and fluid or particles based on the response time and volume fraction of particle. In the present simulation, since particles are assumed to be solid particles or droplets and fluid is gas, the ratio of density is nearly 1000. From this assumption, one-way coupling or two-way coupling can be assumed for the numerical condition listed in Table 2.2, 2.3 and 2.4 except for PL1 case. Here, to estimate the effect of particles on fluid motion, additional DNS which considers the interaction between particle and fluid were conducted for the same turbulence and the same Stokes numbers of PL1-PL6. The obtained results showed that vortex structures are almost same with those of one-way coupling except for PL1 case. In PL1 case, vortex structure was changed by the particle compared with one-way coupling case. However, whether effect of particles on fluid is considered or not, particle distribution in the case is nearly uniform in space because of the large inertia, and the result shown in following sections is not changed.

Table 2.1: Statistics of the initial flow filed.

Re_λ	l	λ	η	u_{rms}
60.1	0.997	0.299	0.0196	0.664
97.1	0.918	0.173	0.00907	0.731
175.4	0.918	0.114	0.000434	0.797

Table 2.2: Numerical conditions for $Re_\lambda = 60.1$.

Case	τ_p	St_η	St_λ	St_l	St_c
PL1	1.20	10.2	2.65	0.811	1.53
PL2	0.359	3.07	0.794	0.243	0.460
PL3	0.245	2.09	0.542	0.166	0.314
PL4	0.124	1.06	0.274	0.0838	0.158
PL5	0.0587	0.501	0.130	0.0398	0.0751
PL6	0.01329	0.0114	0.00294	0.000901	0.00170

Table 2.3: Numerical conditions for $Re_\lambda = 97.1$.

Case	τ_p	St_η	St_λ	St_l	St_c
PM1	0.683	10.8	2.89	0.545	1.62
PM2	0.191	3.04	0.812	0.153	0.456
PM3	0.130	2.05	0.547	0.103	0.307
PM4	0.0636	1.01	0.269	0.0507	0.151
PM5	0.0331	0.523	0.140	0.0264	0.0785
PM6	0.000636	0.0105	0.00269	0.000507	0.00151

Table 2.4: Numerical conditions for $Re_\lambda = 175.4$.

Case	τ_p	St_η	St_λ	St_l	St_c
PH1	0.372	10.2	2.61	0.323	1.53
PH2	0.112	3.06	0.786	0.0972	0.459
PH3	0.0759	2.08	0.533	0.0660	0.311
PH4	0.0387	1.06	0.272	0.0337	0.159
PH5	0.0184	0.504	0.130	0.0160	0.0757
PH6	0.000387	0.0106	0.00272	0.000337	0.00159

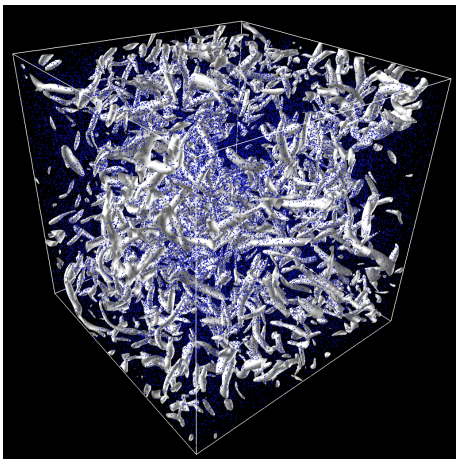

(a) $Re_\lambda = 60.1$

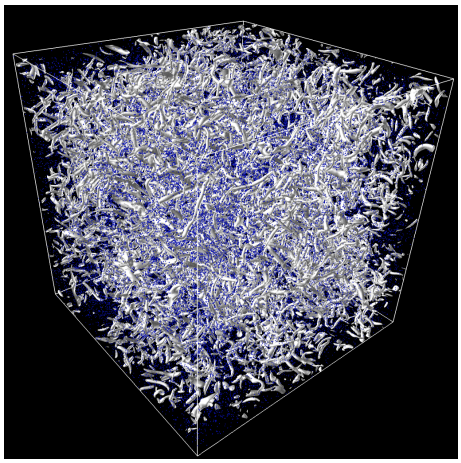

(b) $Re_\lambda = 97.1$

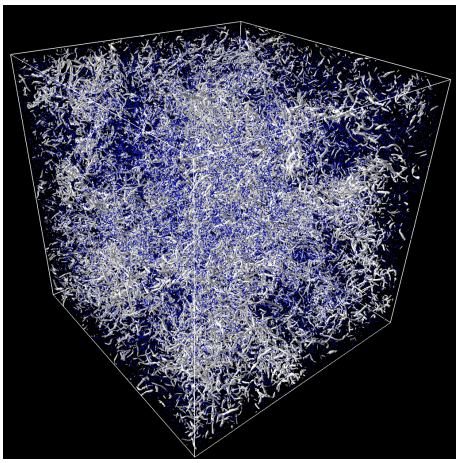

(c) $Re_\lambda = 175.4$

Figure 2.1: Isosurface of the second invariant of the velocity gradient tensor and particles.

2.3 Particle Dispersion in Fine Scale Turbulence

2.3.1 Particle Distributions and Turbulent Structure

Figure 2.2 shows the developments of r. m. s. of the velocity difference between particle and fluid at the particle position. Here, t^+ means the time normalized by the initial eddy turnover time which is defined by initial u_{rms} and integral length. As the initial velocities of particles were set equal to fluid velocities at the particles positions, velocity difference increases with time in the initial period except for small Stokes number cases. After showing the peak, the velocity difference decreases slowly. In this period, particle motions include no effect of the initial condition. In this chapter, the results at the final period of each DNS are used for the analysis of particle motions in homogeneous isotropic turbulence.

There are several methods for identification of vortical structures in turbulent flows. Extraction of high vorticity or enstrophy regions is the simplest method to visualize the vortical structures. In previous works related to fine scale structures in homogeneous isotropic turbulence, high vorticity regions have been used to identify the intermittent fine scale structure of turbulence [9][42][43][44][45][46] [47] [48]. However, the high vorticity regions may represent tube-like and sheet-like structures in a shear flow simultaneously. The tube-like structures are the core regions which indicate a swirling motion, whereas sheet-like structures are not vortex cores because these regions include the strong strain rate as well as the strong rotation rate. In the case of a strong mean shear like the flows near the wall or center of free shear flows, employment of high vorticity or enstrophy regions fails to represent coherent eddies.

To solve the problem of the definitions mentioned above, the invariants of the velocity gradient tensor have been used by many researchers [41][49][50][51]. Chong et al. [50] have classified the local flow pattern in the turbulent flows by using the characteristic equation for the eigenvalues of the velocity gradient tensor.

The velocity gradient tensor is given by

$$A_{ij} = \frac{\partial u_i}{\partial x_j}. \tag{2.13}$$

The characteristic equation for the eigenvalues λ of Eq. (2.13) is given by

$$\lambda^3 + P\lambda^2 + Q\lambda + R = 0, \tag{2.14}$$

where P, Q and R indicate the first, second and third invariant of the velocity gradient tensor, respectively. They are represented as follows;

$$P = -(A_{11} + A_{22} + A_{33}), \tag{2.15}$$

$$\begin{aligned} Q &= \begin{vmatrix} A_{11} & A_{12} \\ A_{21} & A_{22} \end{vmatrix} + \begin{vmatrix} A_{11} & A_{13} \\ A_{31} & A_{33} \end{vmatrix} + \begin{vmatrix} A_{22} & A_{23} \\ A_{32} & A_{33} \end{vmatrix} \\ &= \frac{1}{2}(P^2 - trace[A^2]) = \frac{1}{2}(W_{ij}W_{ij} - S_{ij}S_{ij}), \end{aligned} \tag{2.16}$$

$$\begin{aligned} R &= \begin{vmatrix} A_{11} & A_{12} & A_{13} \\ A_{21} & A_{22} & A_{23} \\ A_{31} & A_{32} & A_{33} \end{vmatrix}, \\ &= \frac{1}{3}(-P^3 + 3PQ - trace[A^3]) = \frac{1}{3}(-3W_{ij}W_{jk}S_{ki} - S_{ij}S_{jk}S_{ki}). \end{aligned} \tag{2.17}$$

Here, S_{ij} and W_{ij} are the symmetric and antisymmetric parts of the velocity gradient tensor A_{ij}, which are given by

$$S_{ij} = \frac{1}{2}\left(\frac{\partial u_i}{\partial x_j} + \frac{\partial u_j}{\partial x_i}\right), \tag{2.18}$$

and

$$W_{ij} = \frac{1}{2}\left(\frac{\partial u_i}{\partial x_j} - \frac{\partial u_j}{\partial x_i}\right). \tag{2.19}$$

The second invariant of the velocity gradient tensor represents a local balance between shear strain rate and vorticity magnitude. The vortical structures (coherent vortices) can be identified as the positive Q regions of the velocity gradient tensor.

Figures 2.3-2.5 show the distributions of particles and the second invariant of the velocity gradient tensor on a typical cross-section for each Reynolds number case. Figures 2.6-2.8 show the velocity vectors of particles and fluid with the second invariant on the same plane in Fig. 2.3-2.5.

In these figures, red area means positive second invariant, blue area means negative one. For the cases of $St_\eta \approx 0.01$ and $St_\eta \approx 10$ of $Re_\lambda = 60.1$, particle dispersions are nearly uniform in space. The particles with $St_\eta \approx 0.01$ can follow the fluid motion and behave like a fluid element as shown in Fig. 2.6(c). On the other hand, particles with $St_\eta \approx 10$ cannot follow the fluid motion and they are moving independent to the fluid flow due to their strong inertia as shown in Fig. 2.6(a). These characteristics result in nearly homogeneous distribution in space for both cases. In other Reynolds number cases, the tendency of particle distribution is almost same of $Re_\lambda = 60.1$ case. However, note that particle distribution shows large-scale fluctuation in space for $St_\eta \approx 10$ of large Reynolds number cases, which might be caused by a large-scale turbulence structure [22][35]. For the case of $St_\eta \approx 1.0$, particle dispersion shows non-uniform distribution in space. They tend to present around high second invariant regions, and the rotating motions of particles around these regions are observed clearly in Figs. 2.6(b) - 2.8(b).

2.3.2 Statistical Characteristics of Particle Distribution

Figure 2.9 shows probability density functions (PDFs) of the second invariant of the velocity gradient tensor at the particle position for each Reynolds number case. For comparison, PDF of the second invariant of the whole flow field is plotted by a solid line. The second invariant is normalized by Kolmogorov length and Kolmogorov velocity. Here after, all of variables with an asterisk denote this normalization. For large and small Stokes number cases, probabilities of the second invariant at the particle positions nearly coincide with those of the whole flow field. This result suggests that the spatial distribution of particles has no correlation with the second invariant. However, for the cases of particular Stokes number, probabilities of particles in high second invariant region decrease and those in negative second invariant region increase. This tendency is significant for the case of $St_\eta = 0.5 \sim 1.0$. As mentioned above, it has been reported that particles with Kolmogorov time scale tend to concentrate in low vorticity

and high strain rate region [18][19]. As the second invariant is defined by $Q = (W_{ij}W_{ij} - S_{ij}S_{ij})/2$, negative second invariant regions do not always correspond to low vorticity and high strain rate region.

Figures 2.10 and 2.11 show PDFs of ${W_{ij}}^*{W_{ij}}^*$ and ${S_{ij}}^*{S_{ij}}^*$ at the particle position for each Reynolds number case. The probabilities of particles with particular Stokes number are low in the high vorticity region, whereas probabilities for all investigated Stokes number show nearly same profile for all range of the strain rate. These results imply that the balance of vorticity and strain rate is important to determine the preferential distribution of particle in turbulence.

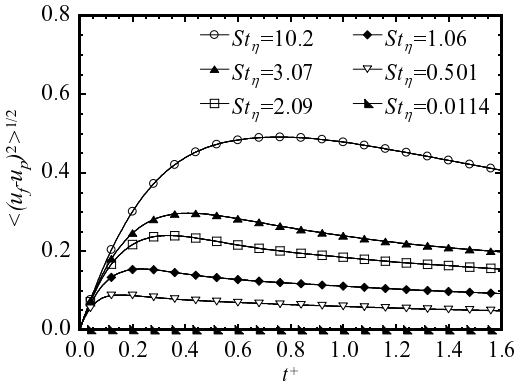

(a) $Re_\lambda = 60.1$

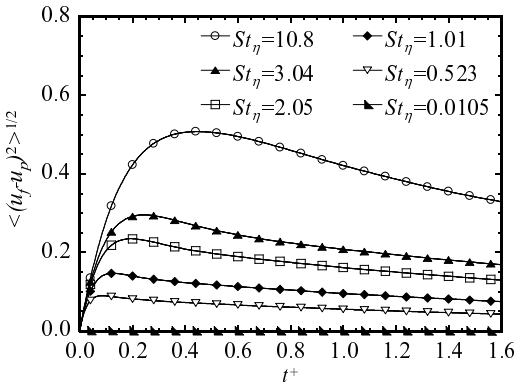

(b) $Re_\lambda = 97.1$

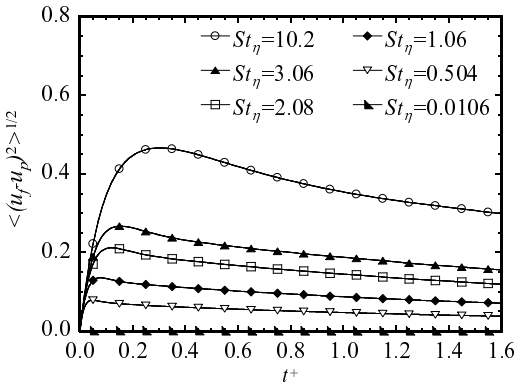

(c) $Re_\lambda = 175.4$

Figure 2.2: Developments of the velocity difference between the particle and fluid.

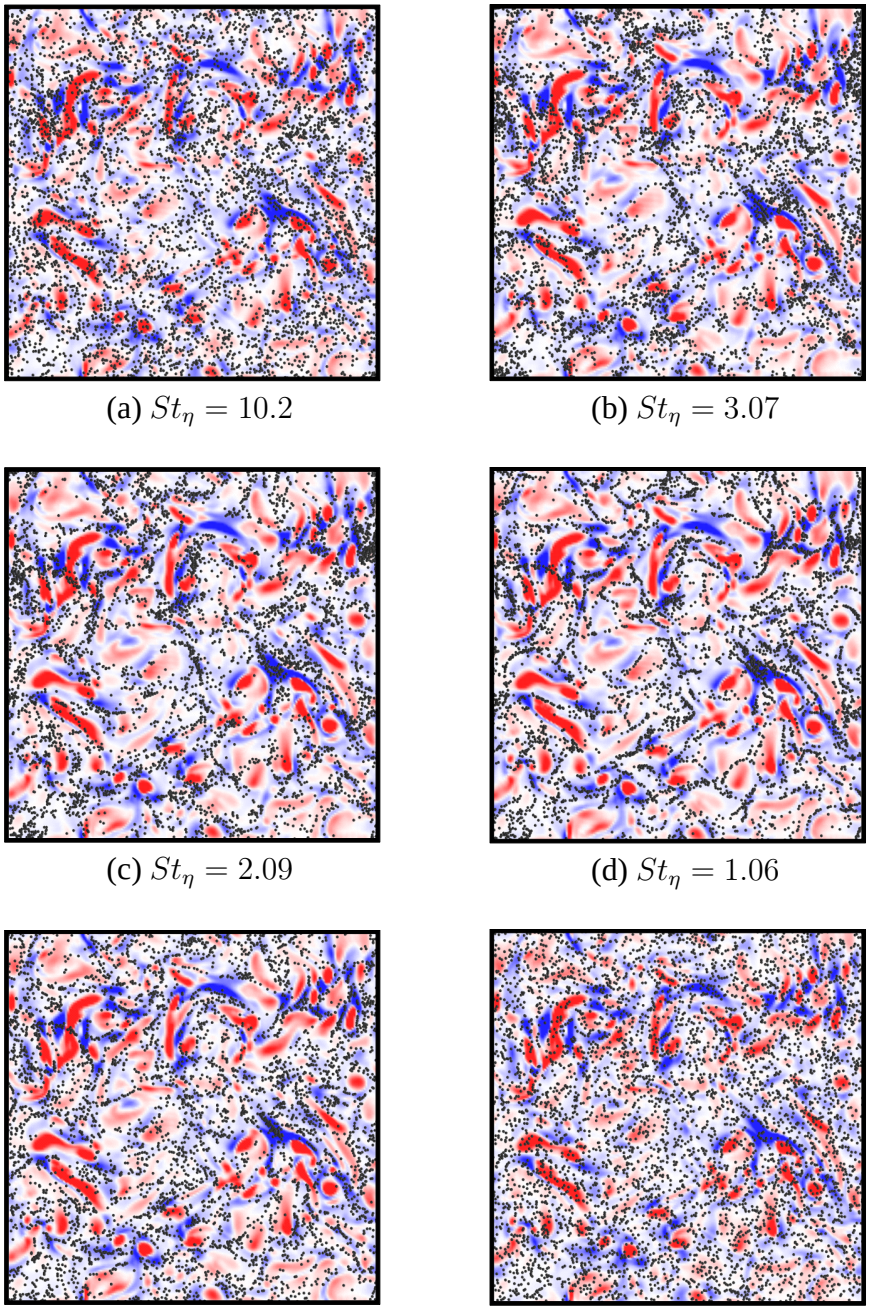

(a) $St_\eta = 10.2$ (b) $St_\eta = 3.07$

(c) $St_\eta = 2.09$ (d) $St_\eta = 1.06$

(e) $St_\eta = 0.501$ (f) $St_\eta = 0.0114$

Figure 2.3: Distributions of particles and the second invariant of the velocity gradient tensor on a typical cross-section for $Re_\lambda = 60.1$.

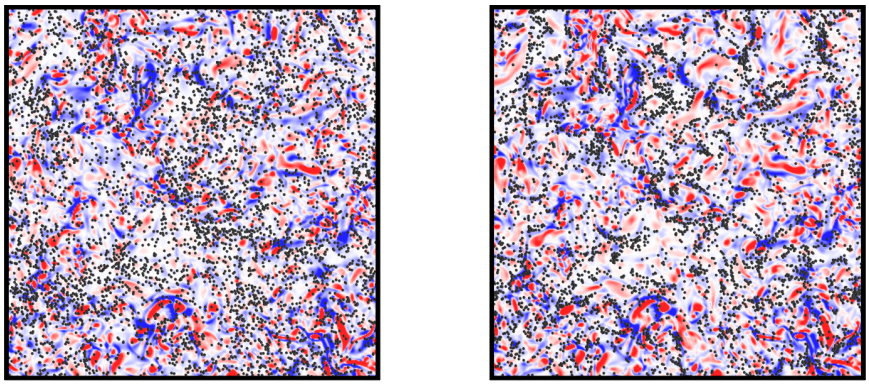

(a) $St_\eta = 10.8$ (b) $St_\eta = 3.04$

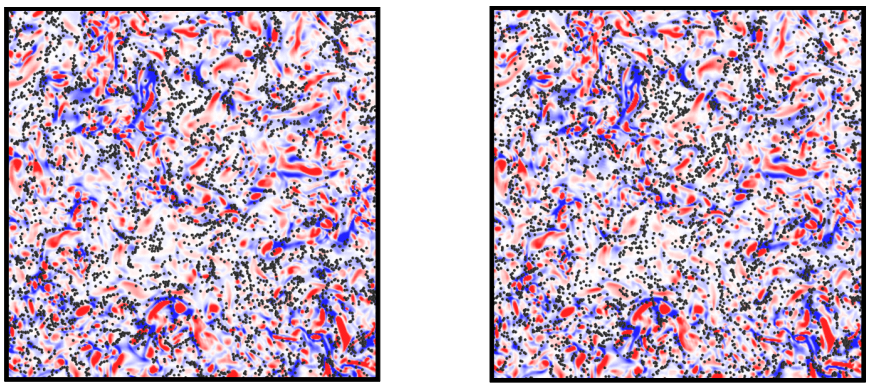

(c) $St_\eta = 2.05$ (d) $St_\eta = 1.01$

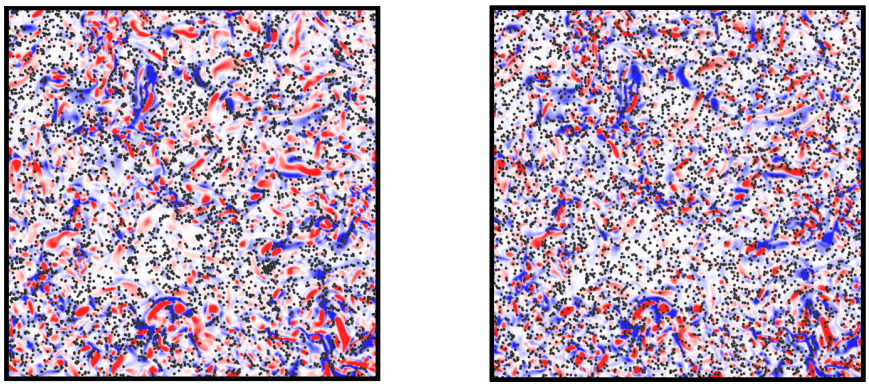

(e) $St_\eta = 0.523$ (f) $St_\eta = 0.0105$

Figure 2.4: Distributions of particles and the second invariant of the velocity gradient tensor on a typical cross-section for $Re_\lambda = 97.1$.

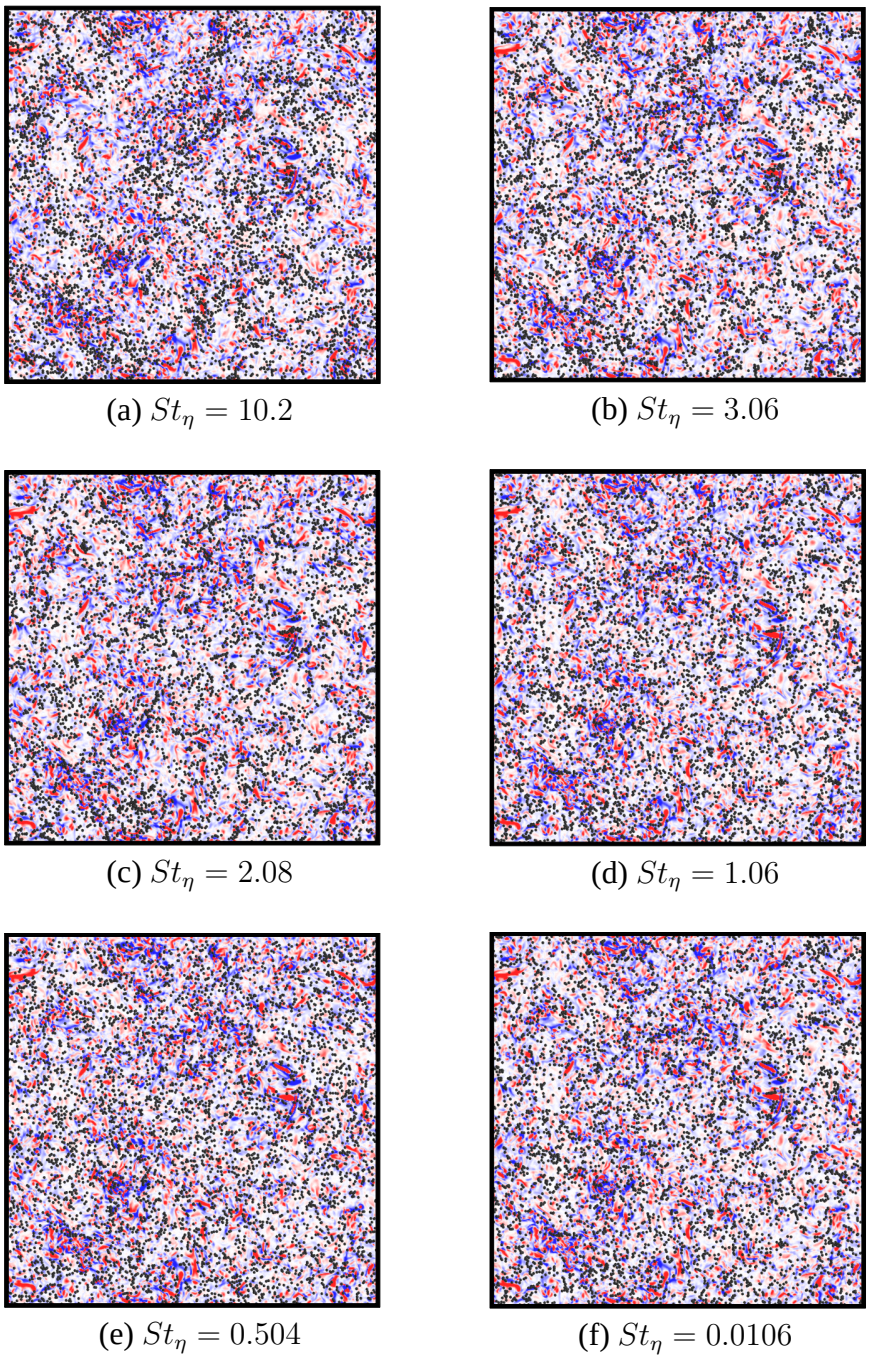

(a) $St_\eta = 10.2$ (b) $St_\eta = 3.06$

(c) $St_\eta = 2.08$ (d) $St_\eta = 1.06$

(e) $St_\eta = 0.504$ (f) $St_\eta = 0.0106$

Figure 2.5: Distributions of particles and the second invariant of the velocity gradient tensor on a typical cross-section for $Re_\lambda = 175.4$.

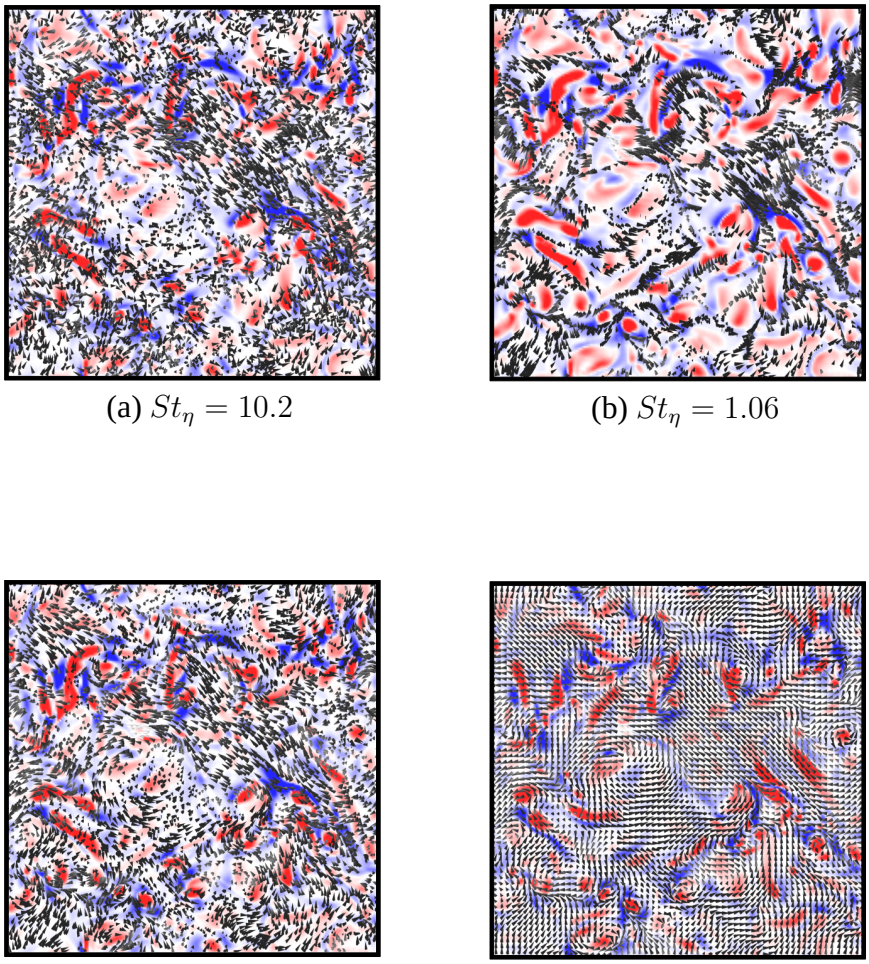

(a) $St_\eta = 10.2$ (b) $St_\eta = 1.06$

(c) $St_\eta = 0.0114$ (d) Fluid

Figure 2.6: Particle velocity vectors (a)(b)(c) and fluid velocity vectors (d) with the second invariant of the velocity gradient tensor on a typical cross-section for $Re_\lambda = 60.1$.

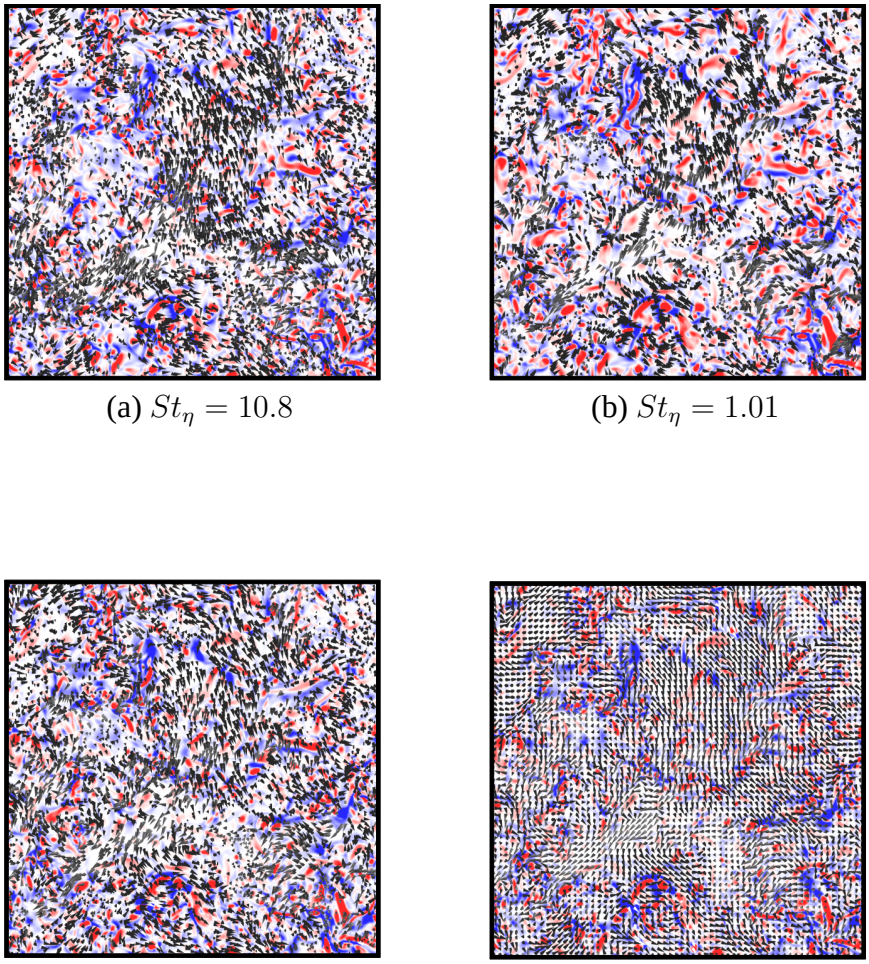

(a) $St_\eta = 10.8$ (b) $St_\eta = 1.01$

(c) $St_\eta = 0.0105$ (d) Fluid

Figure 2.7: Particle velocity vectors (a)(b)(c) and fluid velocity vectors (d) with the second invariant of the velocity gradient tensor on a typical cross-section for $Re_\lambda = 97.1$.

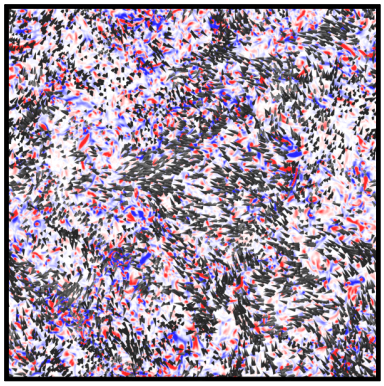

(a) $St_\eta = 10.2$

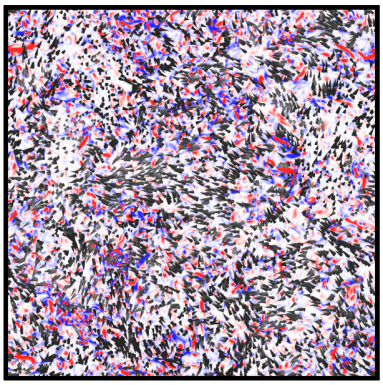

(b) $St_\eta = 1.06$

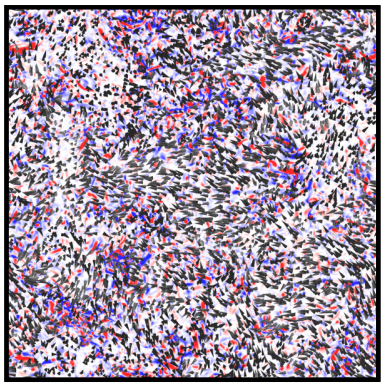

(c) $St_\eta = 0.0106$

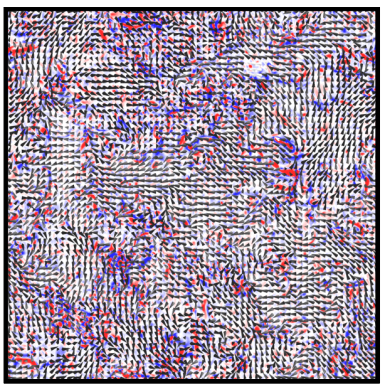

(d) Fluid

Figure 2.8: Particle velocity vectors (a)(b)(c) and fluid velocity vectors (d) with the second invariant of the velocity gradient tensor on a typical cross-section for $Re_\lambda = 175.4$.

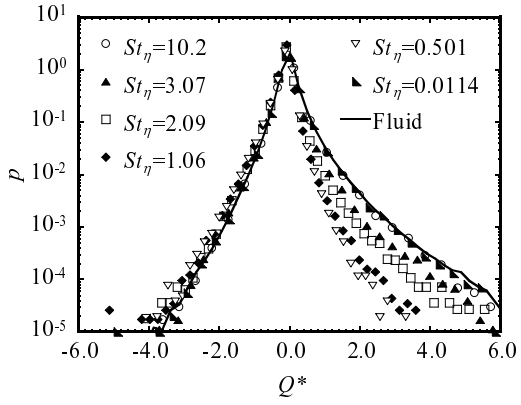

(a) $Re_\lambda = 60.1$

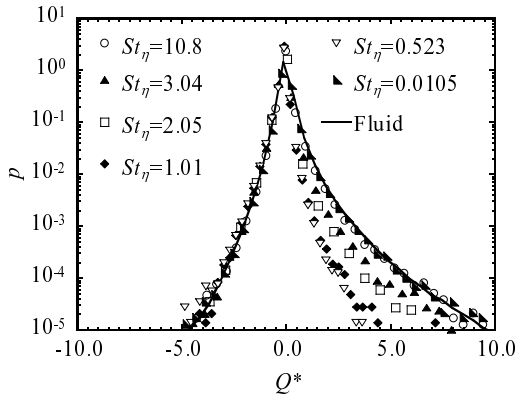

(b) $Re_\lambda = 97.1$

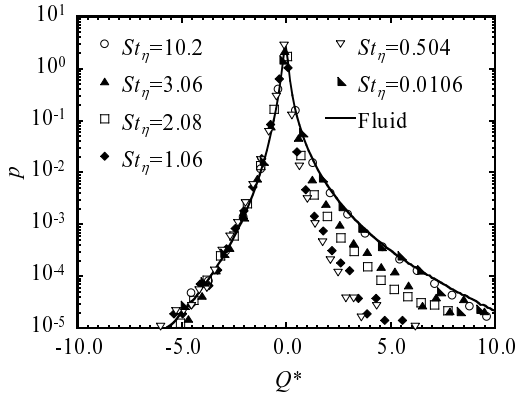

(c) $Re_\lambda = 175.4$

Figure 2.9: Probability density functions of the second invariant of the velocity gradient tensor at the particle position. Solid lines represent flow field.

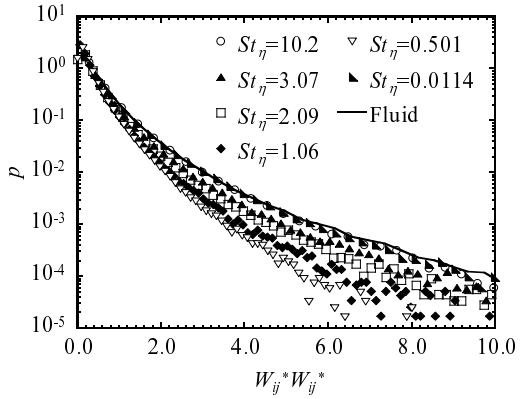

(a) $Re_\lambda = 60.1$

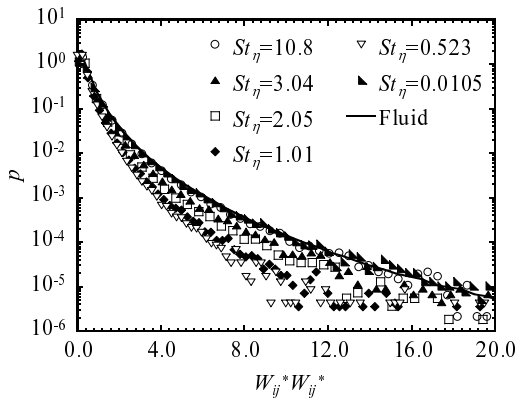

(b) $Re_\lambda = 97.1$

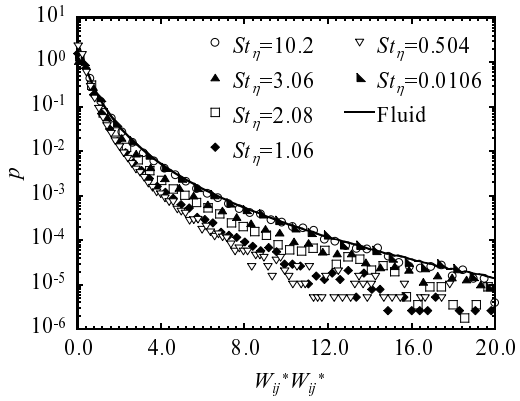

(c) $Re_\lambda = 175.4$

Figure 2.10: Probability density functions of $W_{ij}{}^*W_{ij}{}^*$ at the particle position. Solid lines represent flow field.

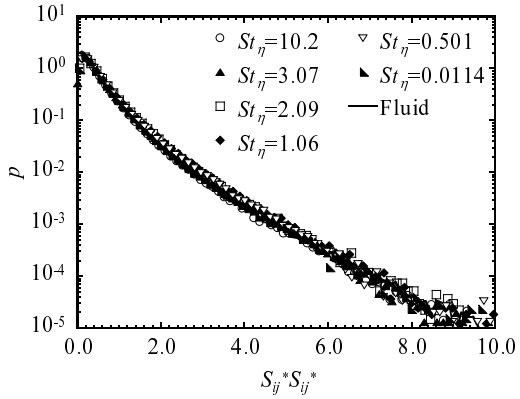

(a) $Re_\lambda = 60.1$

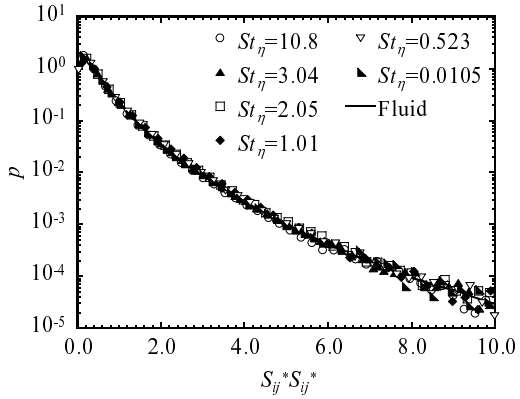

(b) $Re_\lambda = 97.1$

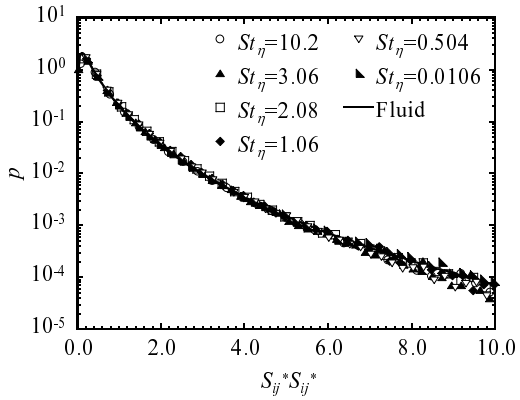

(c) $Re_\lambda = 175.4$

Figure 2.11: Probability density functions of ${S_{ij}}^*{S_{ij}}^*$ at the particle position. Solid lines represent flow field.

2.4 Number Density of Particle around the Coherent Fine Scale Eddies

2.4.1 Identification Scheme of the Coherent Fine Scale Eddy

In this study, axes of the coherent fine scale eddy is extracted from DNS data by using the method that has been developed in our previous studies [10][11][12][13][16] to investigate effects of the coherent fine scale eddies on particle dispersion quantitatively.

The identification scheme consists of the following steps:

(a) Evaluation of *Q* at each collocation point from the results of DNS.

(b) Probability of existence of positive local maximum of *Q* near the collocation points is evaluated at each collocation point from *Q* distribution. Because the case that a local maximum of *Q* coincides with a collocation point is very rare, it is necessary to define probability on collocation points.

(c) Collocation points with non-zero probability are selected to survey actual maxima of *Q*. Locations of maximal *Q* are determined within the accuracy of 10^{-6} by applying a three dimensional 4th-order Lagrange interpolation to DNS data.

(d) A cylindrical coordinate system (r, θ, z) is considered by setting the maximal point as the origin. The coordinate system is assumed to have advection velocity at the origin. The z direction is selected to be parallel to the vorticity vector at the maximal point. The velocity vectors are projected on this coordinate and azimuthal velocity u_θ is calculated.

(e) Point that has small variance in azimuthal velocity compared with surroundings is determined. If the azimuthal velocities at $r = 1/5$ computational grid width show same sign for all θ, that point is identified as the center of the swirling motion.

(f) Statistical properties are calculated around the points.

From (a)-(f) steps, the center of swirling motion ($\boldsymbol{x_s}$) is identified on the cross-section with *Q* maxima on the axis of the eddy. From $\boldsymbol{x_s}$, axes of each coherent fine scale eddy are searched by using a following auto-tracing algorism which has developed by Tanahashi et al. [11][13] (Fig. 2.12).

(g) From $\boldsymbol{x_s}$, the investigated point is moved in the axial direction with short distance $\boldsymbol{ds}$. $\boldsymbol{ds}$ is parallel to the vorticity vector at $\boldsymbol{x_s}$. A new cylindrical coordinate system (r', θ', z') is considered by setting the new point as the origin. On the (r', θ') plane with $z' = 0$, the point with maximum *Q* is determined, and the steps (c)-(e) are applied.

(h) Central axis is determined by repeating the step (g). In this procedure, $|\boldsymbol{ds}|$ is set equal to 1/5 computational grid width. If angle (ϕ_n) between $\boldsymbol{x_{n-1}}$ and $\boldsymbol{x_n}$ is greater than 30 degree, the step (g) is applied again with $|\boldsymbol{ds'}|=|\boldsymbol{ds}|\cos(\phi_n)$.

(i) After the calculation of statistical properties, above steps are repeated until second invariant on the axis becomes negative or swirling motion cannot be detected.

(j) The steps (g)-(i) are conducted in the opposite direction of vorticity vector at $\boldsymbol{x_s}$.

(k) The steps (g)-(j) are applied for the next starting point.

Figure 2.13 shows distribution of the axis of the coherent fine scale eddy for $Re_\lambda = 60.1$. The visualized diameters and colors of axes are drawn to be proportional to the square root of the second invariant on the axis. Larger diameter and red color correspond to stronger swirling motion. The relations between the fine scale eddies and particle dispersion are investigated using these results. Figure 2.14 shows the schematic of calculation method of number density of particle

around the coherent fine scale eddies. First, the axes of fine scale eddies are extracted from DNS results as shown in Fig. 2.13. As for each axis of fine scale eddy, the number of particles near the plane perpendicular to the axis is counted. Then, the number density of particle is calculated at each radial position. Note that the fine scale eddies whose diameter are smaller than 20η are analyzed. These eddies are more than 90% of all fine scale eddies.

Figure 2.15 shows number densities of particle around the coherent fine scale eddies for each Reynolds number case. Here, radial distance (r) and number densities (N) are normalized by radius of fine scale eddy (r_c) and mean number density in all domain (N_0), respectively. For large Stokes number cases, number densities are independent of distance from the center of fine scale eddies and nearly coincide with the mean number density, because particles with large Stokes number cannot follow the fluid motion and their spatial distributions are nearly uniform as shown in Figs. 2.3(a) - 2.5(a). In the same way, for small Stokes number cases, number densities nearly coincide with the mean number density, since particles with small Stokes number move like a fluid element as shown in Figs. 2.3(f) - 2.5(f). However, for particular Stokes number cases, number densities are low near the center of fine scale eddies, and increase with distance from the center and reach the maxima at about $r = 1.0r_c \sim 2.0r_c$. At the center of fine scale eddies, the number densities show the minimum value for $St_\eta = 0.5 \sim 1.0$.

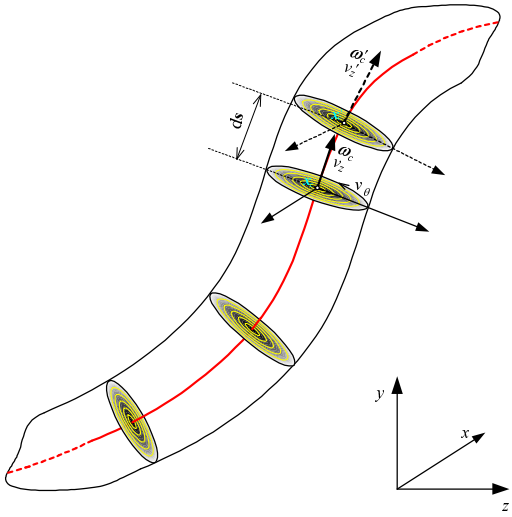

Figure 2.12: Schematic of identification scheme of the axis of the coherent fine scale eddy.

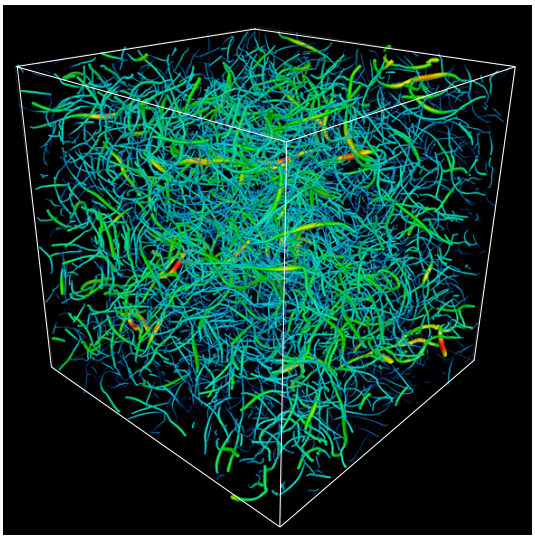

Figure 2.13: Distribution of the axis of the coherent fine scale eddy for $Re_\lambda = 60.1$.

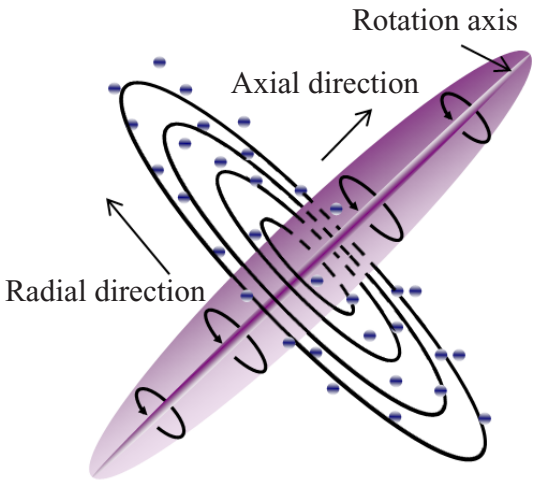

Figure 2.14: Schematic of calculation method of number density around fine scale eddy.

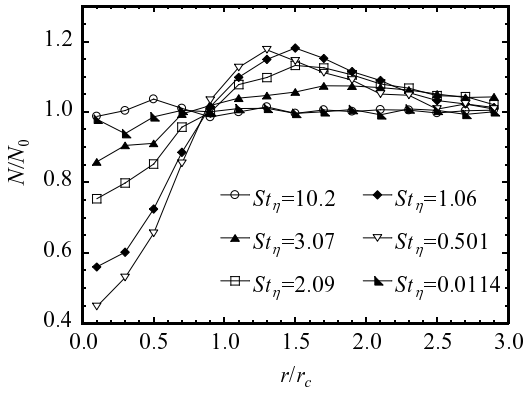

(a) $Re_\lambda = 60.1$

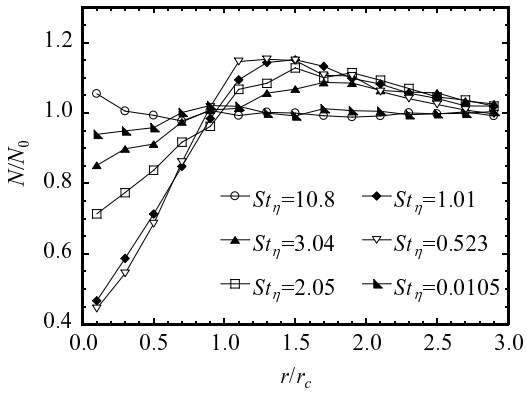

(b) $Re_\lambda = 97.1$

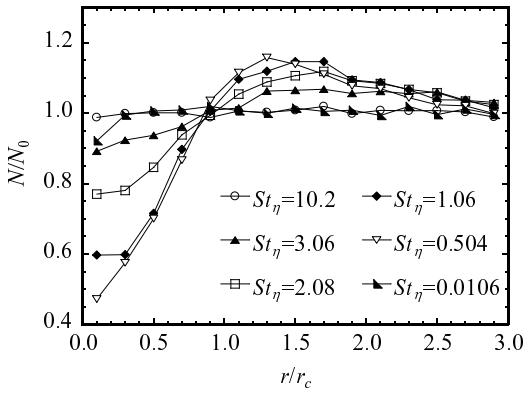

(c) $Re_\lambda = 175.4$

Figure 2.15: Number densities of particle around the coherent fine scale eddies.

2.4.2 Influential Stokes Number

These relations between the coherent fine scale eddy and particle dispersion can be estimated theoretically. Marcu et al. [36] have investigated particle motion in Burgers' vortex. They showed that a particle with a Stokes number which is larger than the critical Stokes number circulates around the vortex, and this radius is a function of both Stokes number of particle and stretching parameter of Burgers' vortex. In our previous research [37], the influential Stokes number has been introduced by assuming a Burgers' vortex for fine scale eddy of turbulence, since it has been shown that mean azimuthal velocity of the coherent fine scale eddy can be approximated by that of Burgers' vortex [10] (Fig. 2.16). The Burgers' vortex is defined in a (r, θ, z) coordinate as follows;

$$v_r = -\frac{\alpha}{2} r, \tag{2.20}$$

$$v_\theta = \frac{\Gamma}{2\pi r}\left[1 - \exp\left(-\frac{\alpha r^2}{4\nu}\right)\right], \tag{2.21}$$

$$v_z = \alpha z, \tag{2.22}$$

where v_r, v_θ and v_z are radial, azimuthal and axial velocity of fluid. α and Γ are the stretching parameter and the circulation. Figure 2.17 shows distributions of velocity vectors of particles and drag force acting on particles around a typical axis of the coherent fine scale eddy. The particles show distinct orbital motions around the coherent fine scale eddy. These orbital motions are sustained by the drag force as shown in Fig. 2.17. From these results, it can be assumed that particles circulate around the coherent fine scale eddy. Therefore, the equation of particle motion becomes as follows;

$$\frac{4}{3}\pi\left(\frac{D_p}{2}\right)^3 \rho_p \frac{{u_\theta}^2}{r} = -6\pi\mu\left(\frac{D_p}{2}\right)(v_r - u_r), \tag{2.23}$$

where u_θ and u_r are azimuthal velocity and radial velocity of the particle. In this study, it is assumed that the particle circulate at the radius (r_c) with the maximum

azimuthal velocity. From Eq. (2.21), r_c becomes

$$r_c = \sqrt{\frac{4\nu s_m}{\alpha}}, \tag{2.24}$$

where s_m satisfies

$$2s_m + 1 = \exp(s_m). \tag{2.25}$$

As the most expected diameter of the coherent fine scale eddies is 8η, α can be calculated as follow;

$$\alpha = \frac{\nu s_m}{4\eta^2}. \tag{2.26}$$

By supposing the most expected maximum azimuthal velocity to $1.2u_k$ in addition, the response time of particle which circulates around the coherent fine scale eddy is derived as follow;

$$\tau_{pi} = \frac{\rho_p}{\rho_f}\frac{{D_p}^2}{18\nu} = -\frac{v_r}{{u_\theta}^2}r = \frac{\alpha}{{v_\theta}^2}\frac{r^2}{2} \approx \frac{\nu s_m}{4\eta^2}\frac{{r_c}^2}{2{v_\theta}^2} = \frac{2}{1.2^2}\frac{\eta}{u_k}s_m. \tag{2.27}$$

From the definition, the influential Stokes number based on Kolmogorov scale can be calculated;

$$St_{\eta i} = \left(\frac{2}{1.2^2}\frac{\eta}{u_k}s_m\right) \Big/ \left(\frac{\eta}{u_k}\right) = 1.7450433\cdots. \tag{2.28}$$

From this theoretical expectation and Fig. 2.15, it is considered that particles with the Stokes number which is close to the influential Stokes number are localized around the coherent fine scale eddies.

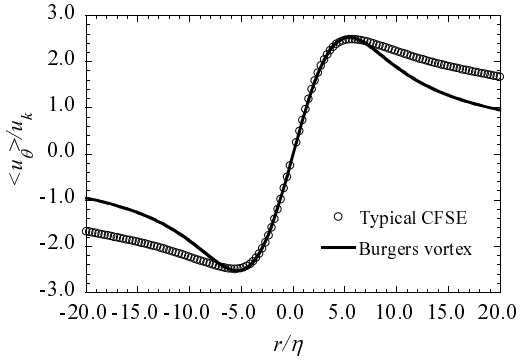

Figure 2.16: Mean azimuthal velocity profile of a typical fine scale eddy.

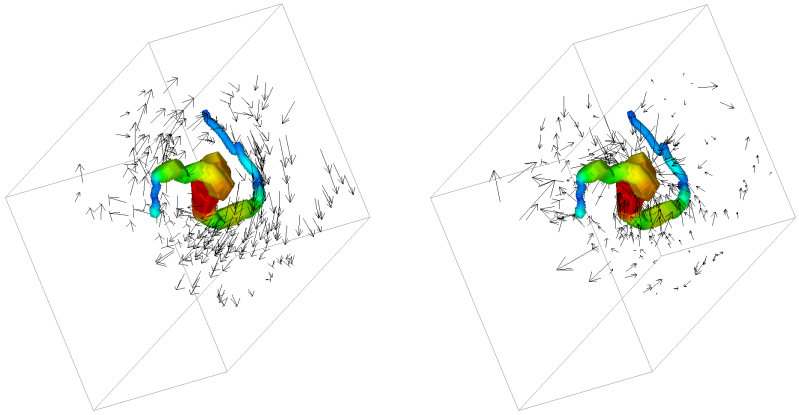

Figure 2.17: The velocity vectors of particles (left) and the drag forces on particles (right) around a typical coherent fine scale eddy.

2.4.3 Phase-averaging Analysis

To investigate relationship between particle dispersion and coherent fine scale eddies in more detail, a phase-averaging analysis on the plane perpendicular to the axis of the coherent fine scale eddy is conducted.

Figure 2.18 shows contour plots of the azimuthal velocity of a typical coherent fine scale eddy. The radius of display region in Fig. 2.18 is $2.5r_c$. The dotted and solid lines show the positive and negative velocity, respectively. Here, velocity vectors in a counterclockwise direction have positive values. Note that the contour plots in Fig. 2.18 is defined as the relative velocity with respective to the center of the coherent fine scale eddy. If the convective velocity is added to the value of the contour, it shows different trend, because the coherent fine scale eddy itself moves with large velocity in turbulence. Figure 2.18 shows that shape of contour plots of the azimuthal velocity are ellipse near the center of fine scale structure, and this elliptic feature suggests the azimuthal velocity has a distinct character around the center of the coherent fine scale eddy. Figure 2.19 shows the azimuthal velocity at $r = r_c$. Some large fluctuations of the azimuthal velocity of fine scale structure are observed. Figure 2.20 shows energy spectra of azimuthal velocity of a typical coherent fine scale eddy at $r = r_c$. In this figure, k_θ denotes the wave number in the azimuthal direction. The Fourier transformation of the azimuthal velocity is given by

$$v_\theta(r, \theta) = \sum_{k_\theta} \tilde{v}_\theta(r, k_\theta) \exp(-ik_\theta\theta) \tag{2.29}$$

where $\tilde{v}_\theta$ is the Fourier coefficient of the azimuthal velocity for k_θ. From Fig. 2.20, the azimuthal velocity of the typical coherent fine scale eddy is dominated by $k_\theta = 2$ mode near the center, and energy at high wave number is very low compared with that of low wave number. These energy spectra of azimuthal velocity are calculated for each coherent fine scale eddy, and dominant mode of azimuthal velocity at fine scale structure is determined.

Figures 2.21 shows mean energy spectra of the azimuthal velocity for $Re_\lambda = 60.1$ and $Re_\lambda = 97.1$. Here, energy spectra is normalized with the mean azimuthal

velocity at each point. In this study, the energy spectra of the azimuthal velocity of the coherent fine scale eddies with $D < 20\eta$ have been investigated. These figures show that the azimuthal velocity is dominated by $k_\theta = 2$ mode near the center of the coherent fine scale eddy, which is independent of the Reynolds number. The energy in each k_θ mode tends to increase with the increase of r, which is prominently observed in $k_\theta = 1$ mode. On the other hand, the rate of increase in the energy at $k_\theta = 2$ mode is very low compared with those in other modes. Therefore, the phase-averaging analysis is conducted based on $k_\theta = 2$ mode of the azimuthal velocity at $r = 0.25r_c$ for each fine scale eddy, as below (Fig. 2.22):

(a) Extracting of $k_\theta = 2$ mode of azimuthal velocity at $r = 0.25r_c$ for each fine scale eddy.

(b) Calculating phase difference, τ, from sinewave of $k_\theta = 2$ mode.

(c) Rotating physical quantity around center on the plane perpendicular to the axis of the coherent fine scale eddy to be $\tau = 0$.

(d) The step(c) is conducted for all coherent fine scale eddies except for $D > 20\eta$, and averaging these results.

Figure 2.23 shows phase-averaged distributions of the second invariant of the velocity gradient tensor, energy dissipation rate, radial velocity, azimuthal velocity and velocity vectors on the plane perpendicular to the axis of the coherent fine scale eddy. The radius of the visualized region is 2.5 times r_c. The second invariant shows positive value in the central area of fine scale structure, which represents that solid body rotation is strong in the central area. The shape of distribution is not circular but obviously elliptic where major and minor axis can be defined. The energy dissipation rate has two large positive peaks on the major axis, and velocity on the minor axis is larger than that on the major axis. Here, the energy dissipation rate denotes difference from the mean value in turbulence. These results show that the coherent fine scale eddy has specific elliptic feature on the plane perpendicular to the axis [38][39]. Moffatt et al. [40] have analyzed a stretched vortex under

asymmetric strain field as a fine scale structure of turbulence. To discuss the characteristics of the stretched vortex, they have introduced the strain rate ratio which is defined by the minimum and intermediate eigenvalues of the strain rate tensor under the hypothesis that the maximum strain rate aligns with the rotating axis of the vortex. In our previous researches [12][13][16], however, it has been clarified that the intermediate strain rate aligns with the direction of rotating axis, and the minimum and maximum strain rate is acting on the plane perpendicular to the axis for the most of the coherent fine scale eddies in turbulence.

Figures 2.24 and 2.25 show phase-averaged distributions of number density of particle for $Re_\lambda = 60.1$ and $Re_\lambda = 97.1$. In these figures, number density is normalized by mean number density in all domains. For large and small Stokes number cases, the distributions are nearly uniform. In other cases, number density shows a minimum value at the center of the coherent fine scale structure. The number density increases with distance from the center and show the maxima on the major axis. This tendency is significant for the case of $St_\eta = 0.5 \sim 1.0$ and consistent with the result shown in Fig. 2.15. Comparisons of these number density distributions with the results shown in Fig. 2.23 indicate that the number densities are low in the regions with strong solid body rotation, and high in the regions with high energy dissipation rate. The high density region is located at about 1.5 to 2.0 times of r_c on the major axis.

As mentioned above, it has been clarified that most of the coherent fine scale eddies are strongly compressed and stretched in the two directions perpendicular to the rotating axis [12][13][16]. Therefore, each fine scale eddy has elliptic feature as shown in Fig. 2.23. In these eddies, since azimuthal velocity on the minor axis is larger than that on the major axis, the residence time of particle on the major axis becomes longer than that on the minor axis. Therefore, the number of particles on the major axis increase compared with that on the minor axis. Goto and Vassilicos [23] and Chen et al. [24] have shown that particles concentrate zero-acceleration points in two-dimensional turbulence. Although the present results in three-dimensional turbulence shown in Figs. 2.24 and 2.25 may coincide

with Goto and Vassilicos [23] and Chen et al. [24], the coherent fine scale structure in real three dimensional turbulence has strong three-dimensionality [11]. As discussed in above, strong three-dimensional strain field is acting on the coherent fine scale eddy. The strain rate ratio at the center of the eddy is $-5 : 1 : 4$ [12][13][16]. Even for the high energy dissipation rate region around the coherent fine scale eddy, strain field is three-dimensional and cannot be treated as a simple stagnation point which can easily defined in two-dimensional turbulence. Soria et al. [41] have investigated local flow patterns in three-dimensional turbulence based on the invariants of the velocity gradient tensor. They have shown that strain rate ratio of high energy dissipation rate tend to be $-4 : 1 : 3$, and the flow patterns of these regions are classified into unstable-node-saddle-saddle. As shown by Soria et al. [41], the strain field of $-4 : 1 : 3$ can be decomposed to two-dimensional shear. In this sense, the particle is clustered near the pseudo-stagnation points around the coherent fine scale eddy. The length scale of particle cluster around fine scale eddy is about $8 \sim 16$ times η by considering the most expected diameter of the coherent fine scale eddy. This scale agrees with the results of Aliseda et al. [27]. The present results show that particle clusters in fine scales are formed by the coherent fine scale eddies.

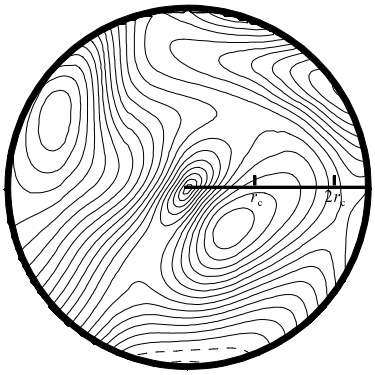

Figure 2.18: Contour plots of the azimuthal velocity of a typical coherent fine scale eddy.

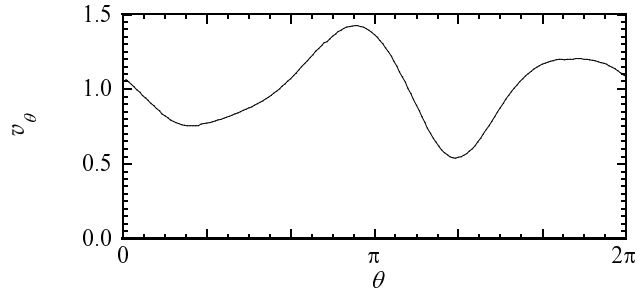

Figure 2.19: Azimuthal velocity of a typical coherent fine scale eddy.

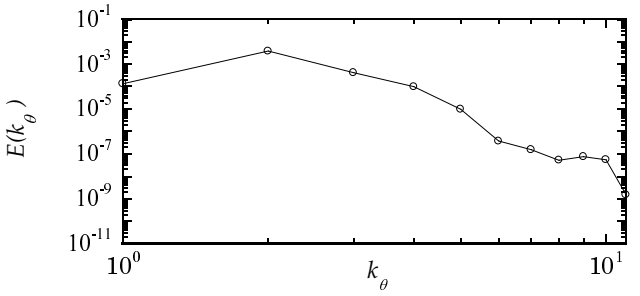

Figure 2.20: Energy spectrum of the azimuthal velocity of a typical coherent fine scale eddy.

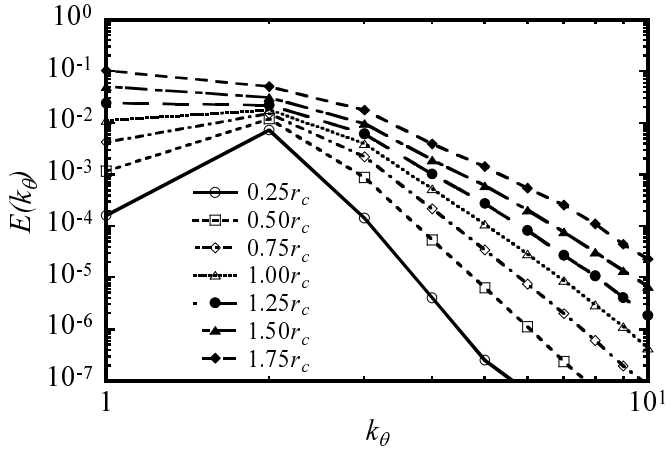

(a) $Re_\lambda = 60.1$

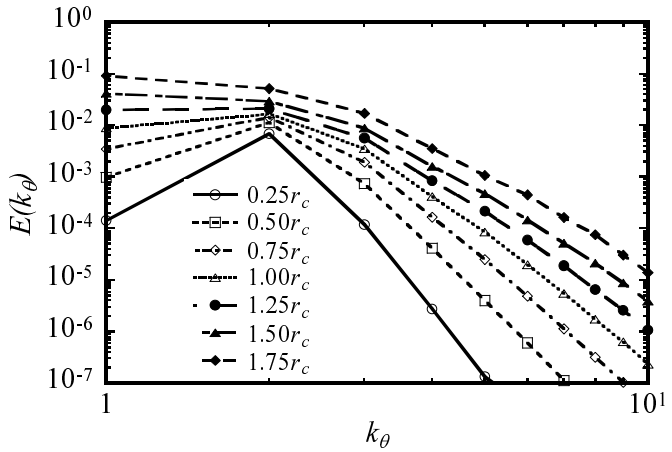

(b) $Re_\lambda = 97.1$

Figure 2.21: Mean energy spectra of the azimuthal velocity of the coherent fine scale eddy.

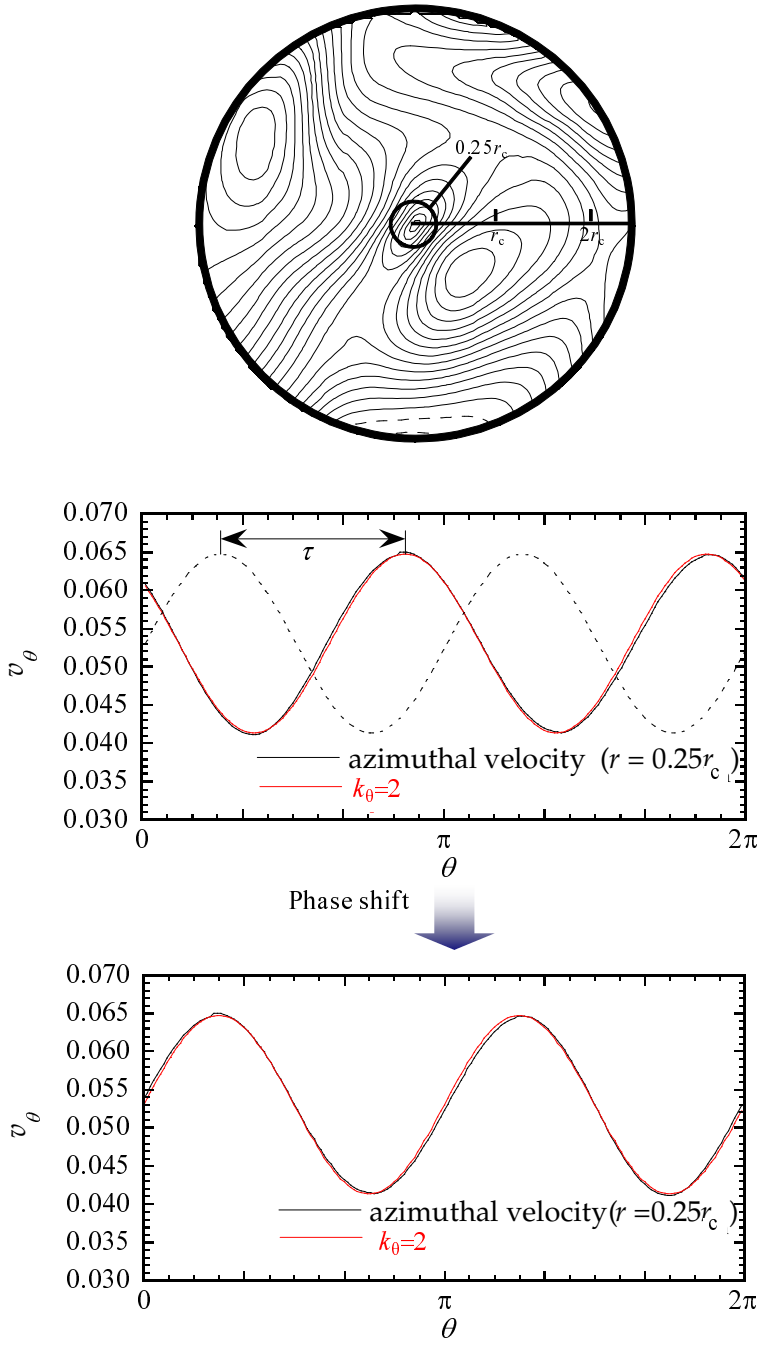

Figure 2.22: Operation of phase-average.

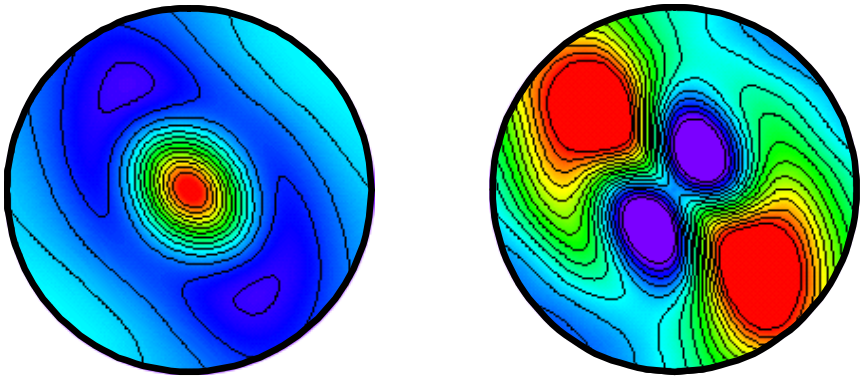

(a) Second invariant

(b) Energy dissipation rate

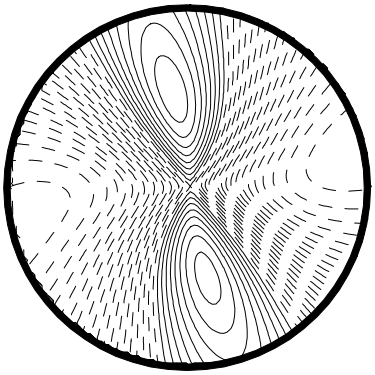

(c) Radial velocity

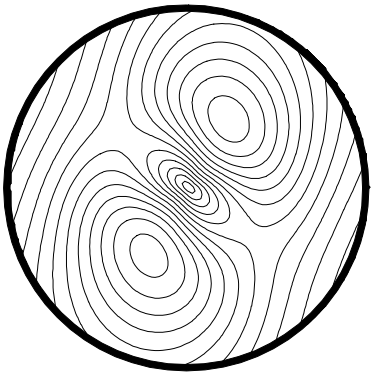

(d) Azimuthal velocity

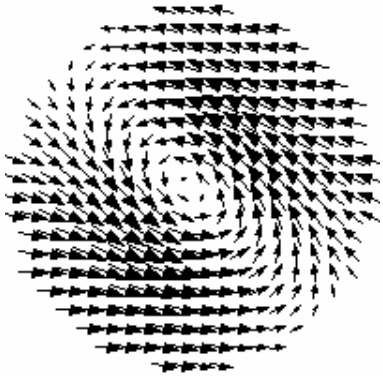

(e) Velocity vectors

Figure 2.23: Phase-averaged distributions on the plane perpendicular to the axis of the coherent fine scale eddy for $Re_\lambda = 60.1$.

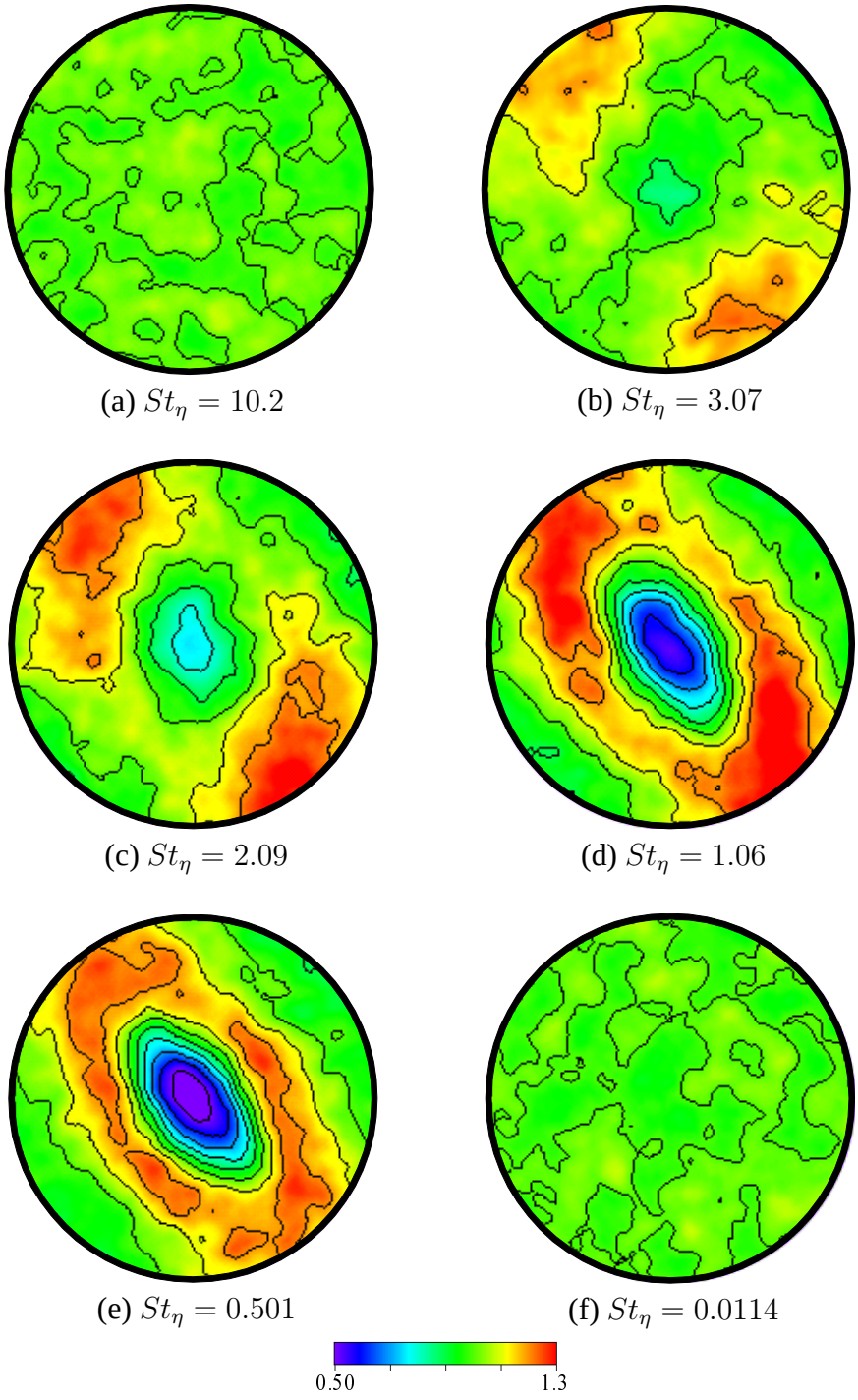

(a) $St_\eta = 10.2$ (b) $St_\eta = 3.07$

(c) $St_\eta = 2.09$ (d) $St_\eta = 1.06$

(e) $St_\eta = 0.501$ (f) $St_\eta = 0.0114$

Figure 2.24: Phase-averaged distributions of number density of particle on the plane perpendicular to the axis of the coherent fine scale eddy for $Re_\lambda = 60.1$.

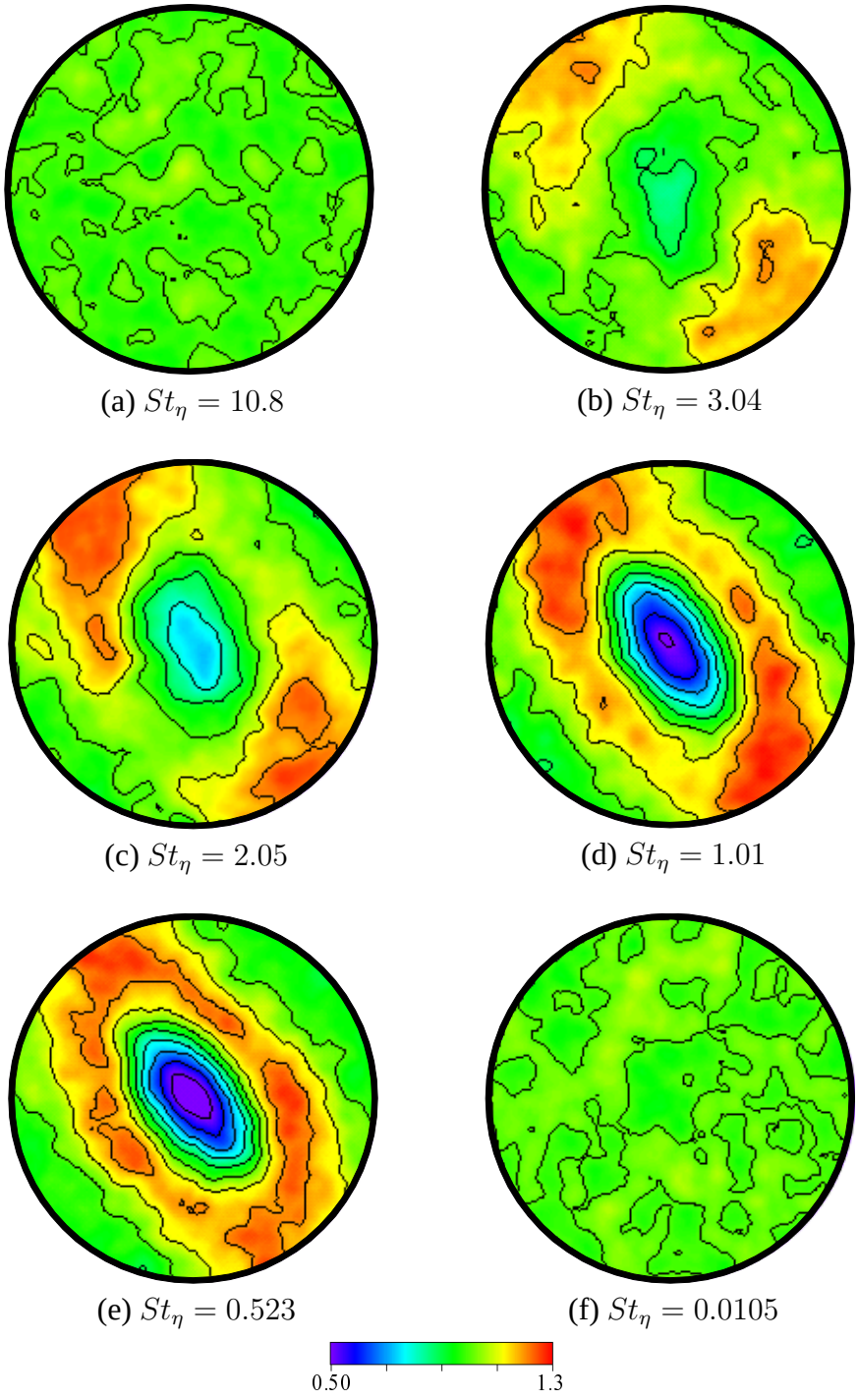

(a) $St_\eta = 10.8$ (b) $St_\eta = 3.04$

(c) $St_\eta = 2.05$ (d) $St_\eta = 1.01$

(e) $St_\eta = 0.523$ (f) $St_\eta = 0.0105$

Figure 2.25: Phase-averaged distributions of number density of particle on the plane perpendicular to the axis of the coherent fine scale eddy for $Re_\lambda = 97.1$.

2.4.4 Nonuniformity of Particle Distribution

In previous studies, several methods of evaluating the nonuniformity of particle distribution have been suggested [19][20][52][53]. In this study, the PDF variance [19][20] and the correlation dimension [52] are used to quantify the degree of nonuniformity of the particle distribution.

Figure 2.26 shows D_{PDF} calculated by the PDF variance for each Stokes number case. Here, all D_{PDF} are normalized by maximum D_{PDF} at each Reynolds number for easy understanding. D_{PDF} shows peak at $St_\eta \approx 1.0$ and becomes lower for larger or smaller Stokes number cases. This tendency is independent of the Reynolds number. In Fig. 2.27, the correlation dimensions are plotted as a function of the Stokes number. For all Reynolds number cases, the correlation dimensions show the minimum value at $St_\eta \approx 1.0$ and increase with away from $St_\eta \approx 1.0$. These results nearly coincide with the result of previous researches [25][35][53], and suggest that the preferential concentration becomes most significant at $St_\eta \approx 1.0$. However, since these evaluations of nonuniformity have been derived by mathematical methods, they do not give the physical interpretations of the preferential concentration. Figure 2.28 shows the nonuniformity evaluated by number density profile around the coherent fine scale eddies defined as follows;

$$D_{num} = \int |N(r) - 1| dr. \tag{2.30}$$

D_{num} shows peak at $St_\eta \approx 1.0$ and decrease with away from $St_\eta \approx 1.0$ for all Reynolds number cases. This result is nearly consistent with the results shown in Figs. 2.26 and 2.27, and indicates that the physical interpretation of nonuniformity by preferential concentration is given based on the particle distribution around the coherent fine scale eddy.

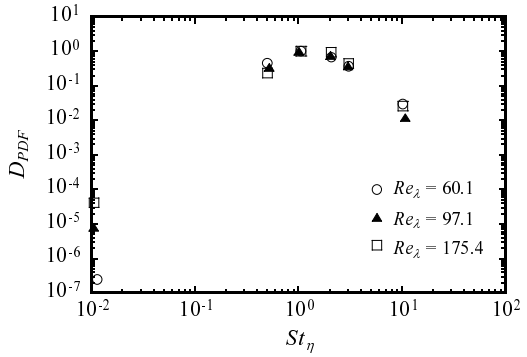

Figure 2.26: Nonuniformity of particle distribution based on PDF variance.

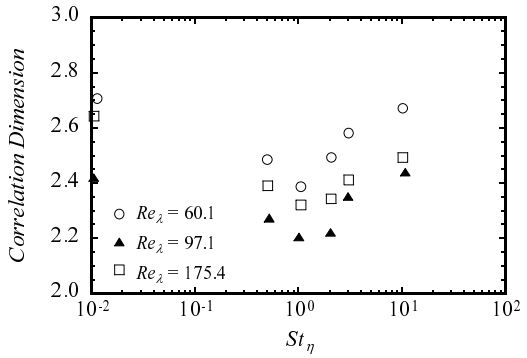

Figure 2.27: Nonuniformity of particle distribution based on correlation dimension.

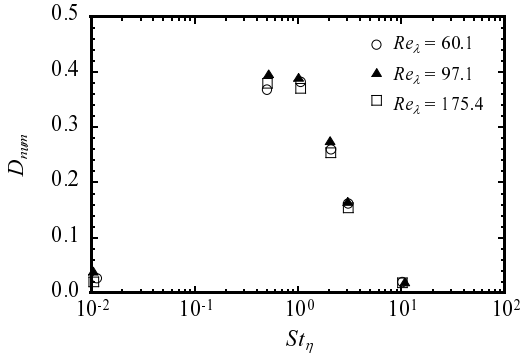

Figure 2.28: Nonuniformity of particle distribution based on number density around the coherent fine scale eddy.

Chapter 3

Droplet Dispersion and Vapor Mixing by the Coherent Fine Scale Structure in Turbulence

3.1 Preface

Almost spray combustors use the fuel which is liquid at normal temperature. In the combustors, liquid flues are atomized to very small droplet for fast evaporation and mixing. Then, they are sprayed into the combustor and disperse in it with evaporation. From previous chapter, it is clarified that particles which has particular Stokes number are located around the coherent fine scale eddy. The dispersion of droplet is considered as the same phenomena of that of particle. However, in the dispersion of droplet, it is necessary to take account of the change of droplet diameter and vapor mixing for evaporation.

Many studies about evaporative droplets have been conducted. Classical texts on droplets, including burning fuel droplets, tend to consider an isolated spherical droplet vaporizing in a stagnant environment [82][83]. In the simplified representation, the liquid has one chemical component, ambient gas conditions are subcritical, and evaporation occurs in a quasi-steady state. The classical result is that the square of the droplet diameter decreases linearly with time since heat diffusion and mass diffusion in the surrounding gas film are slow processes. This behavior

is described as the D^2 law as follows;

$$\frac{dD^2}{dt} = -K, \tag{3.1}$$

where K is the evaporation rate constant. On the other hand, a number of studies about flow field with many evaporative droplets have also been conducted, and some models for evaporative droplet are suggested. Miller et al. [59] evaluated eight Lagrangian droplet models. They included both equilibrium and non-equilibrium evaporation models and evaluated them through comparisons with a variety of single isolated droplet evaporation experiments.

In recent decades, there are many investigations on characteristics of droplet evaporation and fuel vapor mixing in turbulence by DNS. The group of Mashayek et al. has investigated the relationship between characteristics of droplet evaporation and their Stokes number by DNS of homogeneous isotropic turbulence with evaporating droplets [55][56][57][58]. The groups of Miller et al. and Bellan et al. have discussed about the droplet dispersion and evaporation in turbulence through DNS [60][68]. The effects of droplet species on characteristics of evaporation and vapor mixing has been studied by several researchers [66][69][70][71][78][79][81]. The effect of ambient gas conditions, such as in supercritical pressure, on characteristics of evaporation and vapor mixing has also been studied [62][72][73][76][77]. For large eddy simulation (LES), subgrid analysis has been studied [61][67][74][75][80]. Okong'o et al. have conducted LES with their subgrid model of evaporation and compared between the result of LES and DNS [76]. Furthermore, numerical simulations of reacting mixing layers with evaporating droplet have been studied by group of Miller et al. [63][64][65].

In this chapter, DNSs of homogeneous isotropic turbulence with evaporating droplets are conducted for several different Stokes numbers to clarify the relationships between droplet dispersion, vapor mixing and coherent fine scale structure in turbulence.

3.2 Numerical Method

3.2.1 Governing Equations

The governing equations of gas phase are continuity equation, compressible Navier-Stokes equations and conservation equations of energy and chemical species with the state equation of ideal gas as follows;

$$\frac{\partial \rho}{\partial t} + \frac{\partial \rho u_i}{\partial x_i} = S_{\mathrm{I}}, \tag{3.2}$$

$$\frac{\partial \rho u_i}{\partial t} + \frac{\partial \rho u_i u_j}{\partial x_j} = -\frac{\partial \tau_{ij}}{\partial x_j} + S_{\mathrm{II},i}, \tag{3.3}$$

$$\frac{\partial \rho E_t}{\partial t} + \frac{\partial}{\partial x_i}(\rho u_i E_t) = -\frac{\partial q_i}{\partial x_i} - \frac{\partial \tau_{ij} u_i}{\partial x_j} + S_{\mathrm{III}}, \tag{3.4}$$

$$\frac{\partial \rho Y_k}{\partial t} + \frac{\partial}{\partial x_i}(\rho u_i Y_k) = -\frac{\partial}{\partial x_i}(\rho Y_k V_{k,i}) + S_{\mathrm{IV},k}, \tag{3.5}$$

$$p = \rho R^0 T \sum_{k=1}^{I} \left(\frac{Y_k}{W_k} \right). \tag{3.6}$$

Here, Y_k, $V_{k,i}$, W_k and R^0 are mass fraction, diffusion velocity, molecular weight of species k and the universal gas constant, respectively. E_t denotes the total gas energy represented as follows [60];

$$E_t = e_t + 1/2 u_i u_i, \tag{3.7}$$

$$e_t = \sum_{k=1}^{N} h_k Y_k - \frac{p}{\rho} + h_V Y_V, \tag{3.8}$$

$$h_k = h_k^0 + \int_{T_0}^{T} c_{p,k} dT, \tag{3.9}$$

where e_t is internal energy, h_k and $c_{p,k}$ are enthalpy and specific heat at constant pressure of species k. Subscript V means vapor species. h_k^0 and h_V represent the reference enthalpy for the gas at $T = T_0$ and the reference enthalpy for the liquid. Here, this reference enthalpy for the liquid is equal to latent heat (L_V) [60]. τ_{ij} and q_i in Eqs. (3.3)-(3.4) are stress tensor and heat flux term. The detailed expression of these terms and the equations used in actual DNS are described in chapter 5.

The right hand side terms S_{I}, $S_{\mathrm{II},i}$, S_{III} and $S_{\mathrm{IV},k}$ describe the phase couplings of mass, momentum, energy and species as follows;

$$S_{\mathrm{I}} = -\sum_N \left\{ \frac{w_N}{\Delta V} \left[\frac{d}{dt} m_d \right]_N \right\}, \tag{3.10}$$

$$S_{\mathrm{II},i} = -\sum_N \left\{ \frac{w_N}{\Delta V} \left[\frac{d}{dt} m_d v_i \right]_N \right\}, \tag{3.11}$$

$$S_{\mathrm{III}} = -\sum_N \left\{ \frac{w_N}{\Delta V} \left[\frac{d}{dt} (m_d C_L T_d + \frac{1}{2} m_d v_i v_i) \right]_N \right\}, \tag{3.12}$$

$$S_{\mathrm{IV},k} = -\sum_N \left\{ \frac{w_N}{\Delta V} \left[\frac{d}{dt} m_d \right]_{N,k} \right\}. \tag{3.13}$$

Here, v and C_L mean velocity and heat capacity of droplet. Subscript d represents droplet. The summations are over all droplets residing within a local numerical discretization volume (ΔV). In this study, the summation is conducted with the geometrically weighted (w_N) contributions from all individual droplets residing within the discretization range $(i-1, i+1)$, $(j-1, j+1)$, $(k-1, k+1)$ centered around each numerical grid point with array indices (i, j, k). In practice, the contributions from each individual droplet are added to its eight nearest neighbor grid points using a geometrical weighting based on the distance between the droplet and each of the surrounding nodes.

3.2.2 Equations of Droplet Motion and Evaporation

As the same of particle cases, individual droplets are tracked in a Lagrangian framework under the assumption that the droplet volume is negligible. The equations for the droplet motion, temperature and mass are as follows [59];

$$\frac{dx_{d,i}}{dt} = v_i, \tag{3.14}$$

$$\frac{dv_i}{dt} = \frac{f_1}{\tau_d}(u_i - v_i), \tag{3.15}$$

$$\frac{dm_d}{dt} = -\pi D_d \cdot Sh \cdot \rho_g \Gamma_g \ln(1 + B_M), \tag{3.16}$$

$$\begin{aligned} m_d C_L \frac{dT_d}{dt} &= Q_d + \dot{m}_d L_V \\ &= \pi D_d \cdot Nu \cdot \lambda_g f_2 (T_g - T_d) + \dot{m}_d L_V, \end{aligned} \tag{3.17}$$

where subscript g represents gas phase, Q_d and L_V denote the heat flux and the latent heat of droplet evaporation. Γ_g and λ_g represent the diffusion coefficient and the thermal conductivity of gas. Nu and Sh are the Nusselt number and the Sherwood number defined below. The droplet response time τ_d is defined by as follows;

$$\tau_d = \frac{\rho_d D_d^2}{18 \mu_g}. \tag{3.18}$$

In this model, the internal droplet temperature and density are assumed to be uniform. The modified correlations, f_1 and f_2, are empirically correction for Stokes drag and the function of analytical evaporative heat transfer correction to the solid sphere Nusselt number which results from the quasi-steady gas-phase assumption, as described below;

$$f_1 = \frac{1 + 0.0545 Re_{sl} + 0.1 {Re_{sl}}^{1/2} (1 - 0.03 Re_{sl})}{1 + a|Re_b|^b}, \tag{3.19}$$

$$f_2 = \frac{\beta}{e^\beta - 1}, \tag{3.20}$$

$$a = 0.09 + 0.077 \text{exp}(-0.4 Re_{sl}), \tag{3.21}$$

$$b = 0.4 + 0.77 \text{exp}(-0.04 Re_{sl}), \tag{3.22}$$

where Re_{sl} and Re_b are the droplet Reynolds numbers based on the slip velocity U_{sl} and the blowing velocity U_b,

$$Re_{sl} = \frac{\rho_g U_{sl} D_d}{\mu_g}, \tag{3.23}$$

$$Re_b = \frac{\rho_g U_b D_d}{\mu_g}, \tag{3.24}$$

$$U_{sl} = |u_i - v_i| \quad \dot{m}_d = -\pi \rho_g D_d^2 U_b. \tag{3.25}$$

The mass transfer number B_M is calculated from the mass fraction of the fuel in the carrier gaseous phase Y_V and that at the surface of droplet $Y_{V,s}$.

$$B_M = \frac{Y_{V,s} - Y_V}{1 - Y_{V,s}}. \tag{3.26}$$

$Y_{V,s}$ is evaluated using the Clarsius-Clapeyron relation under the saturation pressure condition as,

$$Y_{V,s} = \frac{X_{neq,s}}{X_{neq,s} + (1 - X_{neq,s})\bar{W}/W_V}, \tag{3.27}$$

$$X_{eq,s} = \frac{P_{atm}}{P_g} \exp\left[\frac{L_V}{R^0/W_V}\left(\frac{1}{T_B} - \frac{1}{T_d}\right)\right], \tag{3.28}$$

where $X_{neq,s}$ is the mole fraction of fuel vapor at the droplet surface with non-equilibrium effect, P_{atm} is the atmospheric pressure, P_g is the pressure of the carrier gaseous phase at droplet and T_B is the boiling temperature of the liquid droplet. $\bar{W}$ and W_V are the averaged molecular weights of the carrier gaseous phase and molecular weight of the fuel vapor, respectively.

In this model, a non-equilibrium effect is considered using the Langmuir-Knudsen evaporation law. The non-dimensional evaporation parameter (β) is

$$\beta = -\left(\frac{3Pr_g\tau_d}{2}\right)\frac{\dot{m}_d}{m_d} = -\left(\frac{\rho_L Pr_g}{8\mu_g}\right)\frac{dD_d^2}{dt}. \tag{3.29}$$

The value of the Knudsen layer thickness L_K is computed by

$$L_K = \frac{{\mu_g}^T(2\pi T_d(R^0/W_V))^{1/2}}{Sc_g P_g}. \tag{3.30}$$

Finally, non-equilibrium effects are included in the droplet model using the Langmuir-Knudsen evaporation law as applied through the definition of the vapor fraction at the droplet surface,

$$X_{neq,s} = X_{eq,s} - \left(\frac{2L_K}{D_d}\right)\beta. \tag{3.31}$$

The Nusselt and Sherwood numbers are given based on the Ranz-Marshall correlation as follows;

$$Nu = 2.0 + 0.552{Re_{sl}}^{1/2}{Pr_g}^{1/3} \quad Sh = 2.0 + 0.552{Re_{sl}}^{1/2}{Sc_g}^{1/3}, \tag{3.32}$$

with

$$Pr_g = \mu_g c_{p,g}/\lambda_g \quad Sc_g = \mu_g/\rho_g\Gamma_g. \tag{3.33}$$

3.2.3 Numerical Procedure and Numerical Conditions

Spectral method is used to discretize the gas-phase governing equations and aliasing errors from nonlinear terms in the governing equations are fully removed by the 3/2 rule. Time advancement is conducted by a third-order Runge-Kutta scheme. The equations for droplets are solved with a second-order Adams-Bashforth scheme. The fluid velocity and physical quantity at droplet position is estimated by a fourth-order Lagrange interpolation.

Fully-developed homogeneous isotropic turbulence which was obtained from preliminary DNS is used for the initial velocity field. DNS are conducted for $Re_\lambda = 60.1$ with $128 \times 128 \times 128$ grid points, $Re_\lambda = 97.1$ with $256 \times 256 \times 256$ grid points. The statistics of the initial flow fields are shown in Table 3.1. The computational domain is selected to be 5mm^3. The initial positions of droplet are assumed to be random, and their initial velocities are supposed to be equal to the fluid velocity at their positions. Figure 3.1 shows isosurface of the second invariant of the velocity gradient tensor and droplets. The color of droplet is determined to be proportional to their diameter.

Gas and liquid phases are supposed to be composed of air and n-heptane (ref. Appendix A), respectively. The initial pressure and temperature of carrier gas are 1 atm and 400 K. The initial temperature of droplet is 300 K. The physical properties of droplet are shown in Table 3.2 [59]. In this chapter, all physical properties and the transport coefficients are constant with temperature. It is noted that the diffusion coefficient of n-heptane is equal to that of air, because if the diffusion coefficient of n-heptane is adapted, more resolved grid is needed for high Schmidt number. In this sense, the species are essentially not n-heptane, however, effects due to realistic air-hydrocarbon molecular weight ratios, heat capacity ratios and latent heat magnitude are retained.

Initial Stokes number and number of droplet are shown in Tables 3.3 and 3.4. The number of droplets is determined so that equivalent ratio becomes 0.5 at the time when all droplets evaporate. The mass loading ratio is 0.0324 for all cases.

Table 3.1: Statistics of the initial flow filed.

Re_λ	l [mm]	λ [mm]	η[mm]	u_{rms} [m/s]
60.1	0.793	0.239	0.0156	6.72
97.1	0.730	0.138	0.00722	18.6

Table 3.2: Physical properties of n-heptane droplet.

Density (ρ_L)	649.38 [kg/m^3]
Latent heat (L_V)	355753.1 [J/K]
Heat capacity (C_L)	2383.89 [J/kgK]
Boiling temperature (T_B)	371.6 [K]

Table 3.3: Numerical conditions for $Re_\lambda = 60.1$.

Case	τ_{d0} [s]	$St_{\eta 0}$	$St_{\lambda 0}$	St_{l0}	St_{c0}	D_{d0} [μm]	N_d
DL1	9.29*10^{-5}	10.1	2.61	0.787	1.51	7.69	23127
DL2	2.76*10^{-5}	3.00	0.776	0.234	0.449	4.19	142946
DL3	1.84*10^{-5}	2.00	0.519	0.156	0.300	3.43	261693
DL4	0.924*10^{-5}	1.00	0.260	0.0783	0.151	2.43	737141
DL5	0.467*10^{-5}	0.508	0.132	0.0396	0.0762	1.73	2048872

Table 3.4: Numerical conditions for $Re_\lambda = 97.1$.

Case	τ_{d0} [s]	$St_{\eta 0}$	$St_{\lambda 0}$	St_{l0}	St_{c0}	D_{d0} [μm]	N_d
DM1	1.98*10^{-5}	10.0	2.68	0.505	1.51	3.55	235128
DM2	0.593*10^{-5}	3.01	0.804	0.151	0.451	1.94	1434069
DM3	0.397*10^{-5}	2.01	0.538	0.101	0.302	1.59	2616960
DM4	0.201*10^{-5}	1.02	0.272	0.0512	0.153	1.13	7290431
DM5	0.0980*10^{-5}	0.500	0.133	0.0250	0.0745	0.79	20935682

(a) $Re_\lambda = 60.1$

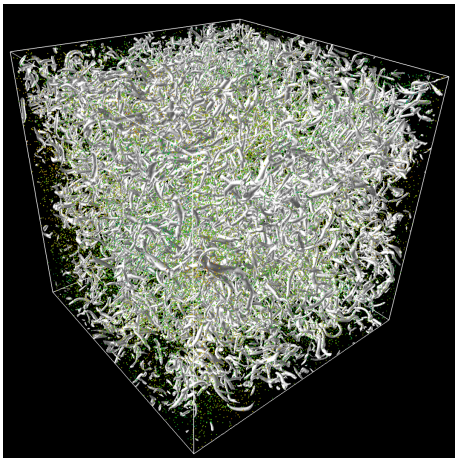

(b) $Re_\lambda = 97.1$

Figure 3.1: Isosurface of the second invariant of the velocity gradient tensor and droplets.

3.3 Characteristics of Droplet Evaporation and Motion

Figure 3.2 shows temporal developments of the droplet diameter for both Reynolds number cases. Here, $\langle D^2 \rangle$ represents the averaged value of the square of the droplet diameter, and is normalized by its initial value $\langle {D_0}^2 \rangle$. For each case, droplet diameter squared linearly decreases after short preheated period. Since vapor concentrations in flow field are low in these cases, evaporation rates follow the "d^2-law", which is observed in the single droplet evaporation. For the case of $St \approx 10$, the droplet diameter squared decreases slowly in the calculated time because of its large mass loadings. This tendency of droplet diameter is similar to the result of the previous research by Mashayek [56] for evaporating droplets in homogeneous isotropic turbulence.

Figure 3.3 shows developments of r.m.s. of velocity difference between the droplet and fluid at the droplet position. As the initial velocities of droplets were set equal to fluid velocities at the droplets positions, velocity difference increases with time in the initial period. After showing the peak, the velocity difference decreases slowly. In this period, droplet motions include no effect of the initial condition. In this chapter, analysis of DNS data are conducted at the time when the droplet diameter squared reaches to 20% of the initial droplet diameter squared except for $St \approx 10$ cases. At this time, droplet volume becomes less than 10 % by initial volume, and there are no droplet which has evaporated completely, yet. So the effects of change of diameter and vapor can be evaluated for all droplets. For the cases of $St \approx 10$, the results at $t^+ = 2.0$ for $Re_\lambda = 60.1$ and $t^+ = 1.2$ for $Re_\lambda = 97.1$ are analyzed because of low evaporation rate.

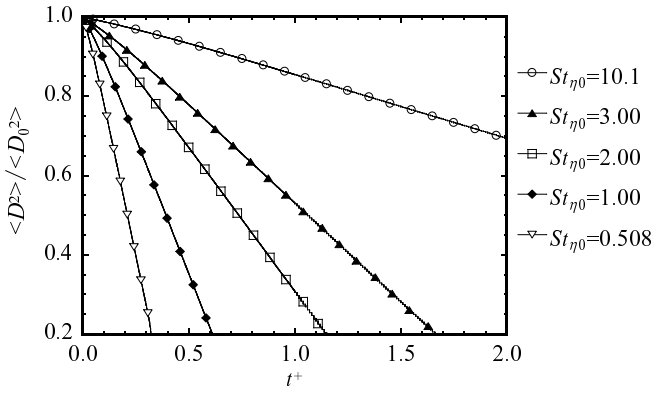

(a) $Re_\lambda = 60.1$

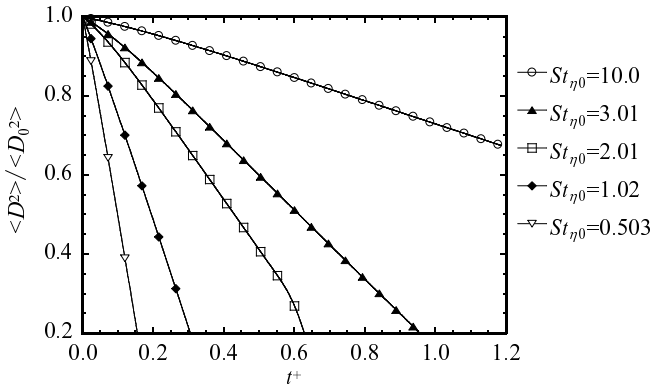

(b) $Re_\lambda = 97.1$

Figure 3.2: Developments of the normalized droplet diameter squared.

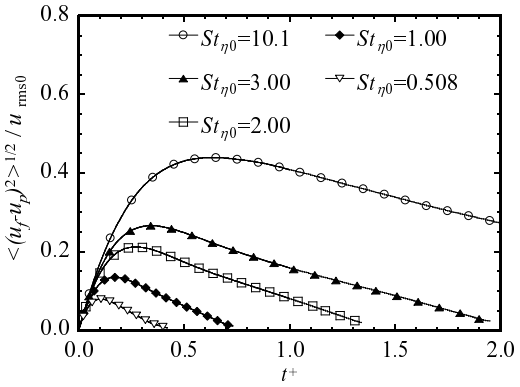

(a) $Re_\lambda = 60.1$

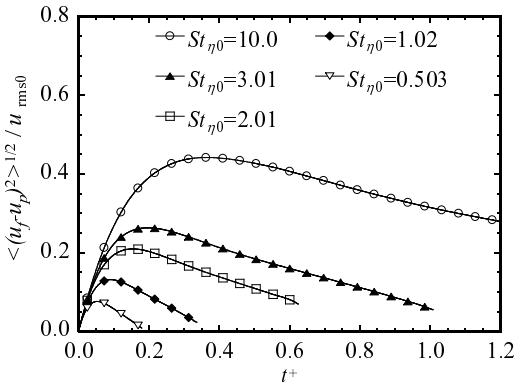

(b) $Re_\lambda = 97.1$

Figure 3.3: Developments of the velocity difference between the droplet and fluid.

3.4 Droplet Dispersion in Fine Scale Turbulence

3.4.1 Droplet Distributions and Turbulent Structure

The previous chapter and lots of studies [18][21] have been reported for particle dispersion in turbulence, and preferential concentration is observed in dispersion of particle with particular Stokes number. For evaporating droplets, since the diameter of droplet changes with time advancement, the phenomenon of preferential concentration might be different from that of particles.

Figures 3.4-3.5 show distributions of droplets and the second invariant of the velocity gradient tensor on a typical $x - y$ plane for each Reynolds number case. The droplet position is marked by a dot. In Fig. 3.5(d)(e), the number of droplet is downsized for easy understanding.

For the cases of $St_{\eta 0} \approx 10$ (especially in $Re_\lambda = 97.1$), droplet dispersions are nearly uniform in space. The droplets with $St_{\eta 0} \approx 10$ cannot follow the fluid motion and they are moving independent to the fluid flow due to their strong inertia. These characteristics result in nearly homogeneous distribution in space for both cases. However, for the other cases, droplet dispersion shows non-uniform distribution in space, and they tend to present around high second invariant regions.

Figure 3.6 shows droplet velocity vectors with the second invariant of the velocity gradient tensor on a typical $x - y$ plane for the cases of $St_{\eta 0} \approx 1.0$. For both cases, droplets tend to concentrate around the high second invariant regions. The rotating motions of droplets around these regions are observed clearly.

3.4.2 Statistical Characteristics of Droplet Dispersion

Figure 3.7 shows probability density functions (PDFs) of the second invariant of the velocity gradient tensor at the droplet position for both Reynolds number cases. For comparison, PDF of the second invariant of the whole flow field is plotted by a solid line for $St_{\eta 0} = 2.00$ ($Re_\lambda = 60.1$) and $St_{\eta 0} = 3.01$ ($Re_\lambda = 97.1$). For large Stokes number cases, probabilities of the second invariant at the

droplet positions nearly coincide with those of the whole flow field. If PDFs of second invariant of whole flow field for large Stokes number are plotted in Fig. 3.7, PDFs from the whole flow field and from droplet position well coincide. This result suggests that the spatial distribution of droplets has no correlation with the second invariant. For the cases of particular Stokes number, probabilities of droplets in large second invariant region decrease and those in negative second invariant region increase. This tendency is significant for the case of $St_{\eta 0} = 1 \sim 3$.

In previous chapter, it has been clarified that particles with Kolmogorov time scale tend to concentrate in low vorticity and high strain rate region. As the second invariant is defined by $Q = (W_{ij}W_{ij} - S_{ij}S_{ij})/2$, negative second invariant regions do not always correspond to low vorticity and high strain rate region. Figures 3.8-3.9 show PDFs of ${W_{ij}}^*{W_{ij}}^*$ and ${S_{ij}}^*{S_{ij}}^*$ at the droplet position for both Reynolds number cases. The probabilities of droplets with particular Stokes number are low in the high vorticity region. Whereas, probabilities for all investigated Stokes number show nearly same profile all range of the strain rate for $Re_\lambda = 60.1$ case. In the result of $Re_\lambda = 97.1$ case, the probabilities except for $St_{\eta 0} = 3.01$ case are high in the high strain rate region. This is because the plot from flow field is different. As the same of PDF of second invariant, if PDFs of strain rate of whole flow field for each case are plotted in Fig. 3.9, PDFs from the whole flow field and from droplet position well coincide. From these results, it implies that the balance of vorticity and strain rate is important to determine the preferential distribution of particle or droplet in turbulence.

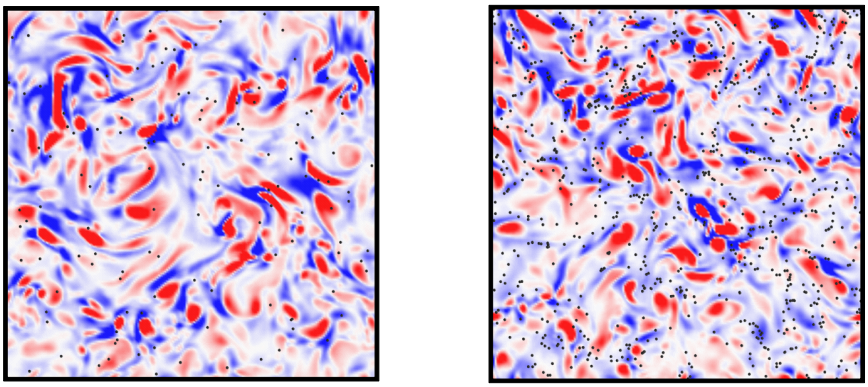

(a) $St_{\eta 0} = 10.1$ (b) $St_{\eta 0} = 3.00$

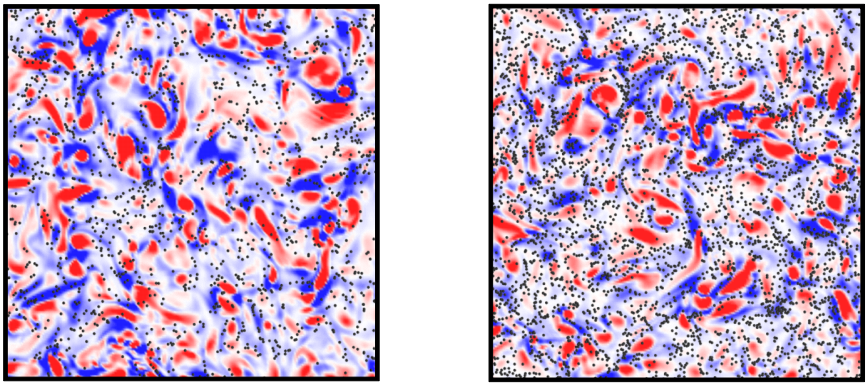

(c) $St_{\eta 0} = 2.00$ (d) $St_{\eta 0} = 1.00$

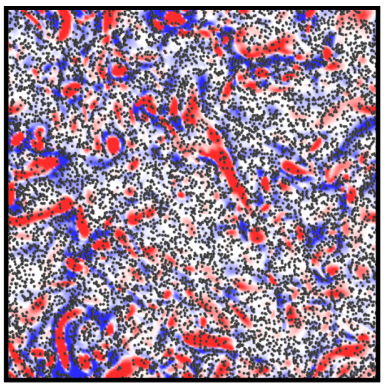

(e) $St_{\eta 0} = 0.508$

Figure 3.4: Distributions of droplets and the second invariant of the velocity gradient tensor on a typical cross-section for $Re_\lambda = 60.1$.

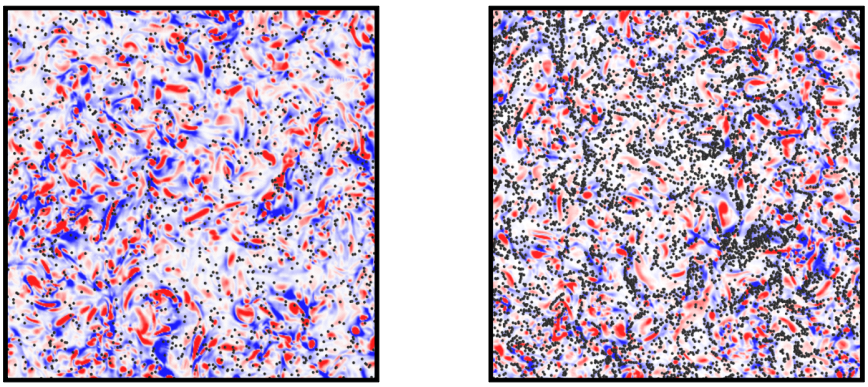

(a) $St_{\eta 0} = 10.0$

(b) $St_{\eta 0} = 3.01$

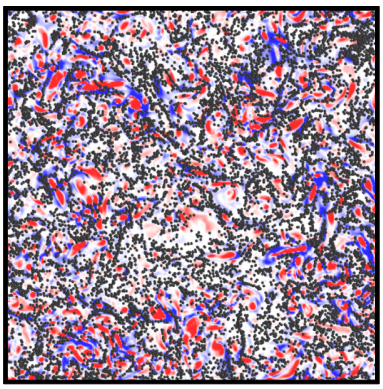

(c) $St_{\eta 0} = 2.01$

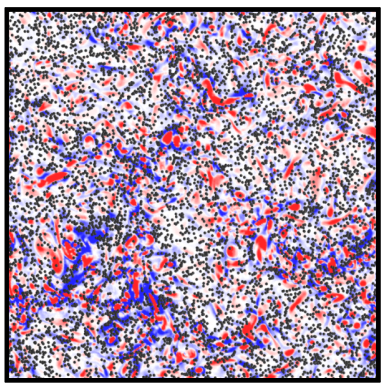

(d) $St_{\eta 0} = 1.02$

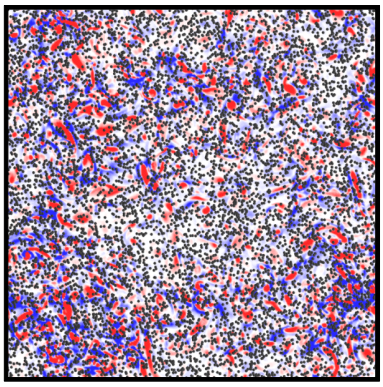

(e) $St_{\eta 0} = 0.503$

Figure 3.5: Distributions of droplets and the second invariant of the velocity gradient tensor on a typical cross-section for $Re_\lambda = 97.1$.

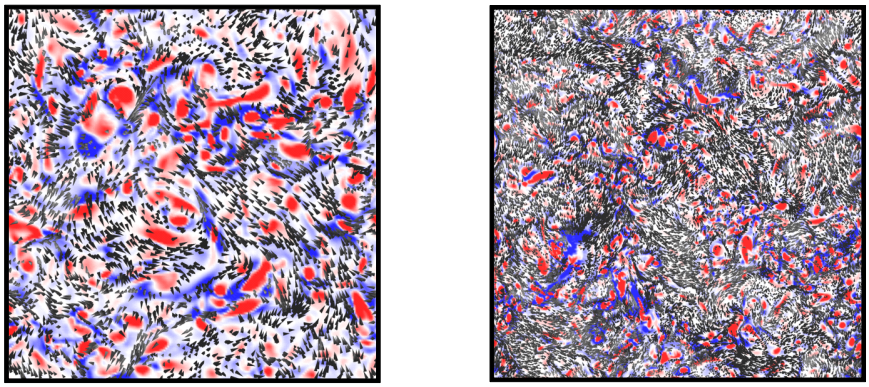

$St_{\eta 0} = 1.00$ $St_{\eta 0} = 1.02$

Figure 3.6: Droplet velocity vectors with the second invariant of the velocity gradient tensor on a typical cross-section for $Re_\lambda = 60.1$ (left) and $Re_\lambda = 97.1$ (right).

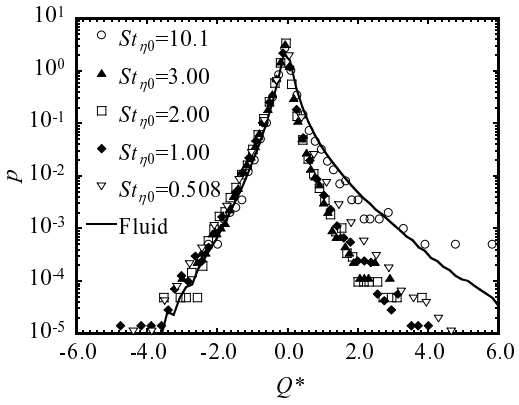

(a) $Re_\lambda = 60.1$

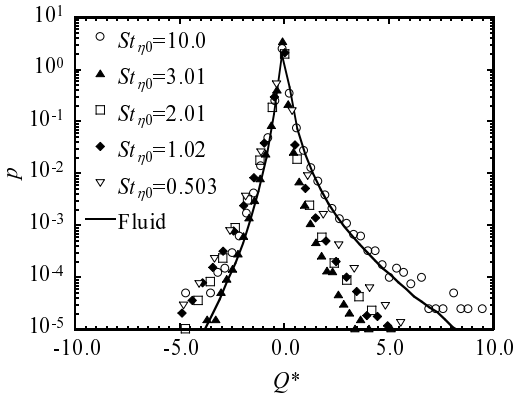

(b) $Re_\lambda = 97.1$

Figure 3.7: Probability density functions of the second invariant of velocity gradient tensor at the droplet position. Solid lines represent flow field.

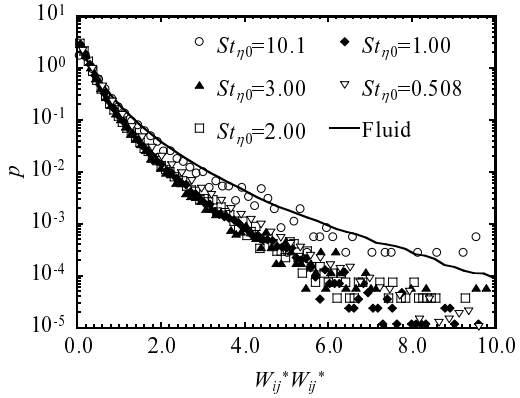

(a) $Re_\lambda = 60.1$

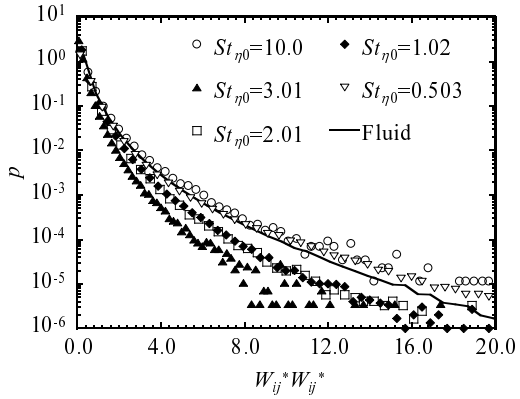

(b) $Re_\lambda = 97.1$

Figure 3.8: Probability density functions of $W_{ij}{}^* W_{ij}{}^*$ at the droplet position. Solid lines represent flow field.

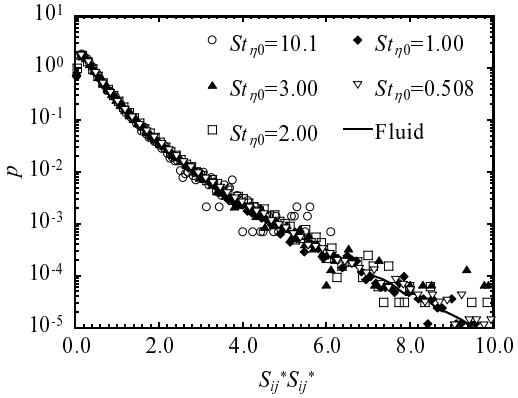

(a) $Re_\lambda = 60.1$

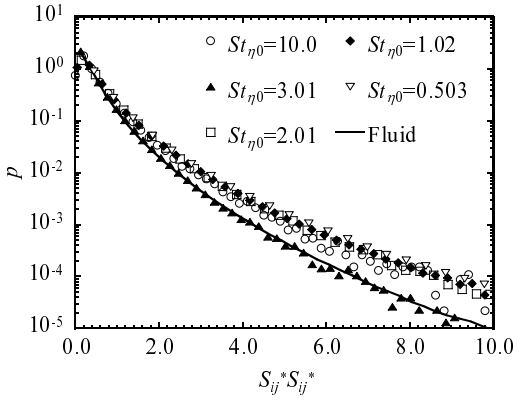

(b) $Re_\lambda = 97.1$

Figure 3.9: Probability density functions of ${S_{ij}}^* {S_{ij}}^*$ at the droplet position. Solid lines represent flow field.

3.5 Number Density of Droplet around the Coherent Fine Scale Eddies

Figure 3.10 shows number densities of droplet around the coherent fine scale eddies for both Reynolds number cases. The calculation method of number density of droplet around the coherent fine scale eddies is the same of that of previous chapter. Here, radial distance (r) and number densities (N) are normalized by radius of fine scale eddy (r_c) and mean number density in all domain (N_0), respectively.

In the case of $St_{\eta 0} = 10.1$ of $Re_\lambda = 60.1$, the profile is not smooth because of shortage of droplet number for this analysis. For $St_{\eta 0} = 10.0$ of $Re_\lambda = 97.1$, number densities are independent of distance from the center of fine scale eddies and nearly coincide with the mean number density, because droplets with large Stokes number cannot follow the fluid motion and their spatial distributions are nearly uniform as shown in Fig. 3.5(a). However, in other cases, number densities are low near the center of fine scale eddies, and increase with distance from the center and reach the maxima at about $r = 1.0r_c \sim 1.5r_c$. At the center of fine scale eddies, the number densities show the minimum value for $St_{\eta 0} = 1 \sim 3$, and tend to increase for smaller $St_{\eta 0}$ cases. It is noted that these profiles are different from that of particle case. This means the change of diameter by evaporation influences on the dispersion of droplet. In addition, the profiles of number densities of droplet are different between same initial Stokes number cases. This is because evaporation rate is varied in same initial Stokes numbers cases for initial droplet diameter, flow condition and so on. In the dispersion of evaporative droplet, evaporation rate K is also important parameter in addition to initial Stokes number.

3.6 Vapor Concentration in Small Scales

Figures 3.11-3.12 show distributions of fluctuation of vapor concentration on a typical $x - y$ plane for each Reynolds number case. Here, fluctuation means the

vapor concentration from the mean concentration in each case. For the case of $St_{\eta 0} = 0.503$ of $Re_\lambda = 97.1$, distribution of the vapor concentration is nearly uniform. For the case of $St_{\eta 0} \approx 10.0$, there are relatively large scale fluctuations. For other cases, small scale fluctuations are clearly observed, especially in the cases of $Re_\lambda = 97.1$.

Figure 3.13 shows energy spectra of vapor concentration for each Reynolds number case. These indicate that vapor distributions vary according to the droplets initial Stokes number, and it is especially significant in high wave number region.

Figure 3.14 shows distributions of droplets and the axes of the coherent fine scale eddies with vapor concentration on typical cross-sections for $St_{\eta 0} = 2.00$ and $Re_\lambda = 60.1$. Figure 3.15 shows vapor concentration around a typical axis of the coherent fine scale eddy. It is clearly observed that the vapor concentration is low near the axis of the coherent fine scale eddy and high around the axis. This means the coherent fine scale eddies significantly affect the forms of vapor distribution through droplet evaporation.

To investigate relationship between vapor mixing and coherent fine scale eddies, a phase-averaging analysis on the plane perpendicular to the axis of coherent fine scale eddies is conducted by the same method of previous chapter. Figure 3.16 shows phase-averaged distributions of the second invariant of the velocity gradient tensor, energy dissipation rate and velocity vectors on the plane perpendicular to the axis of coherent fine scale eddies for the case of $St_{\eta 0} = 2.00$ and $Re_\lambda = 60.1$. These results are almost same of that of the particle case in previous chapter.

Figures 3.17 and 3.18 show phase-averaged distributions of number density of droplet for each case. In these figures, number density is normalized by mean number density in all domains. For the cases of $St_{\eta 0} \approx 10$, the distributions are low at the center and high near the center. In other cases, number density shows a minimum value at the center of coherent fine scale structure. The number density increases with distance from the center and show the maxima on the major axis. This tendency is significant for the case of $St_\eta = 1.0 \sim 3.0$ and consistent with

the result shown in Fig. 3.10. Comparisons of these number density distributions with the results shown in Fig. 3.16 indicate that the number densities are low in the regions with strong solid body rotation, and high in the regions with high energy dissipation rate. The high density region is located at about 1.5 to 2.0 times of r_c on the major axis. It is noted that these distributions are different from the cases of particles. In particular, for large Stokes number cases, the distributions shows slight influence of coherent fine scale eddy on dispersion of this droplet.

Figures 3.19 and 3.20 show phase-averaged distributions of vapor concentration for both Reynolds number cases. For the case of $St_{\eta 0} \approx 10$, the distributions are nearly uniform. In other cases, however, vapor concentration shows a minimum value at the center of coherent fine scale structure. The vapor concentration increases with distance from the center and show the maxima on the major axis. This tendency is weakened for the case of $St_{\eta 0} \approx 0.5$. Comparing these vapor concentrations with the results shown in Fig. 3.16, the vapor concentrations are low in the regions with strong solid body rotation, and high in the regions with high energy dissipation rate. The high concentration region is located at about 1.5 to 2.0 times of r_c on the major axis. These results indicate that distribution of vapor concentration is closely related to the characteristics of coherent fine scale eddies.

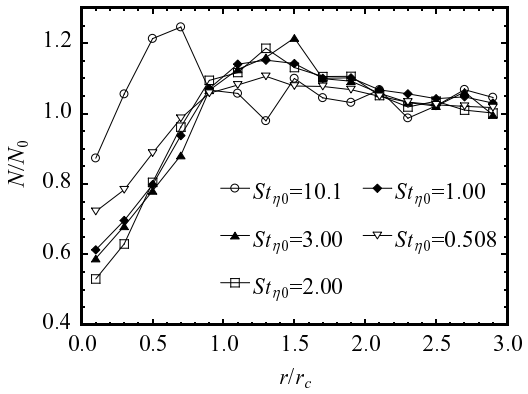

(a) $Re_\lambda = 60.1$

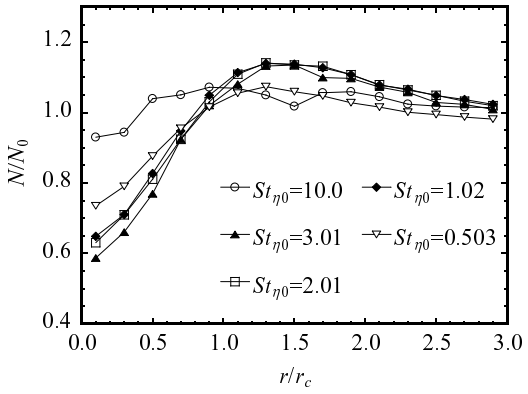

(b) $Re_\lambda = 97.1$

Figure 3.10: Number densities of droplet around coherent fine scale eddies.

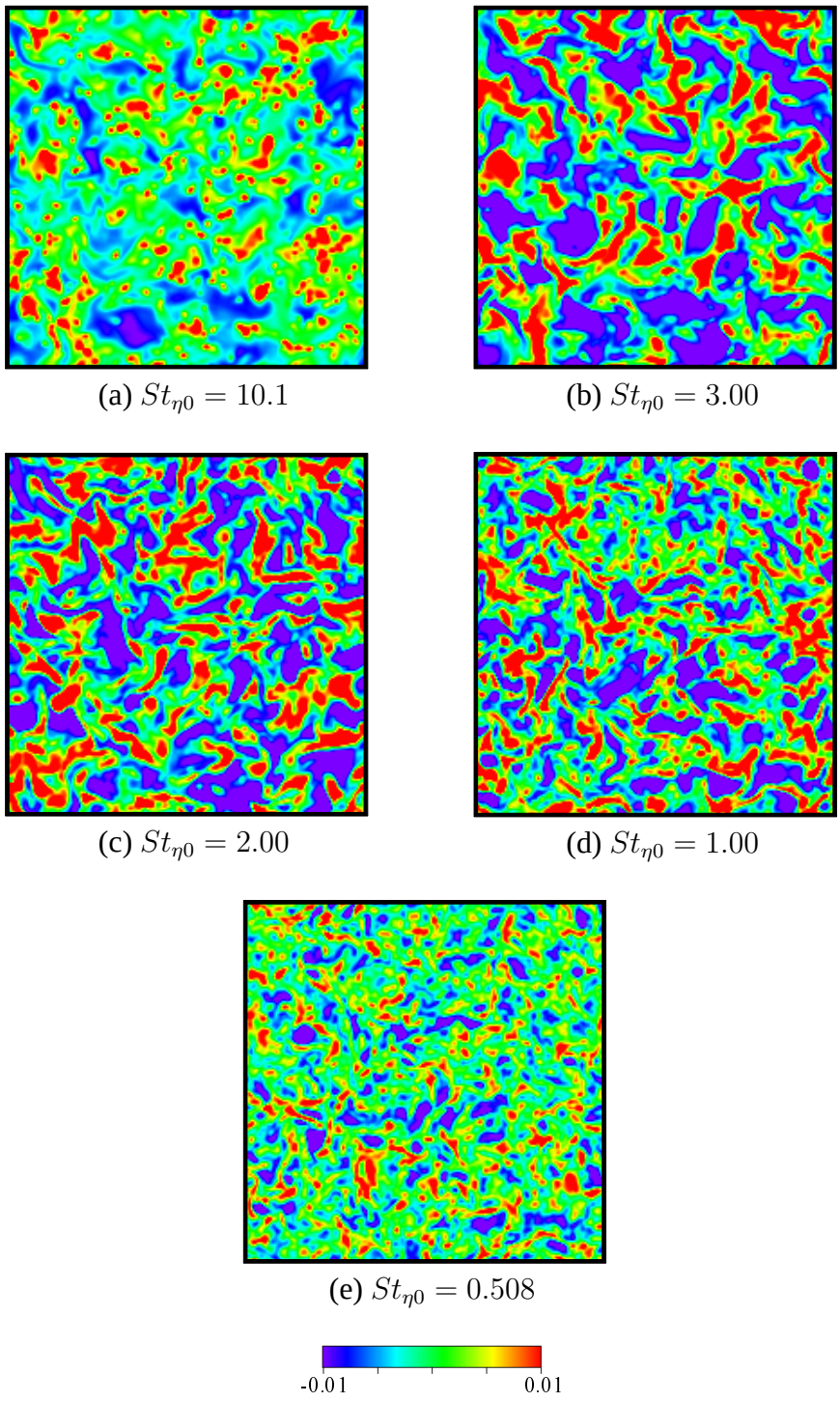

(a) $St_{\eta 0} = 10.1$ (b) $St_{\eta 0} = 3.00$

(c) $St_{\eta 0} = 2.00$ (d) $St_{\eta 0} = 1.00$

(e) $St_{\eta 0} = 0.508$

Figure 3.11: Distributions of fluctuation of vapor concentration on a typical $x - y$ plane for $Re_\lambda = 60.1$.

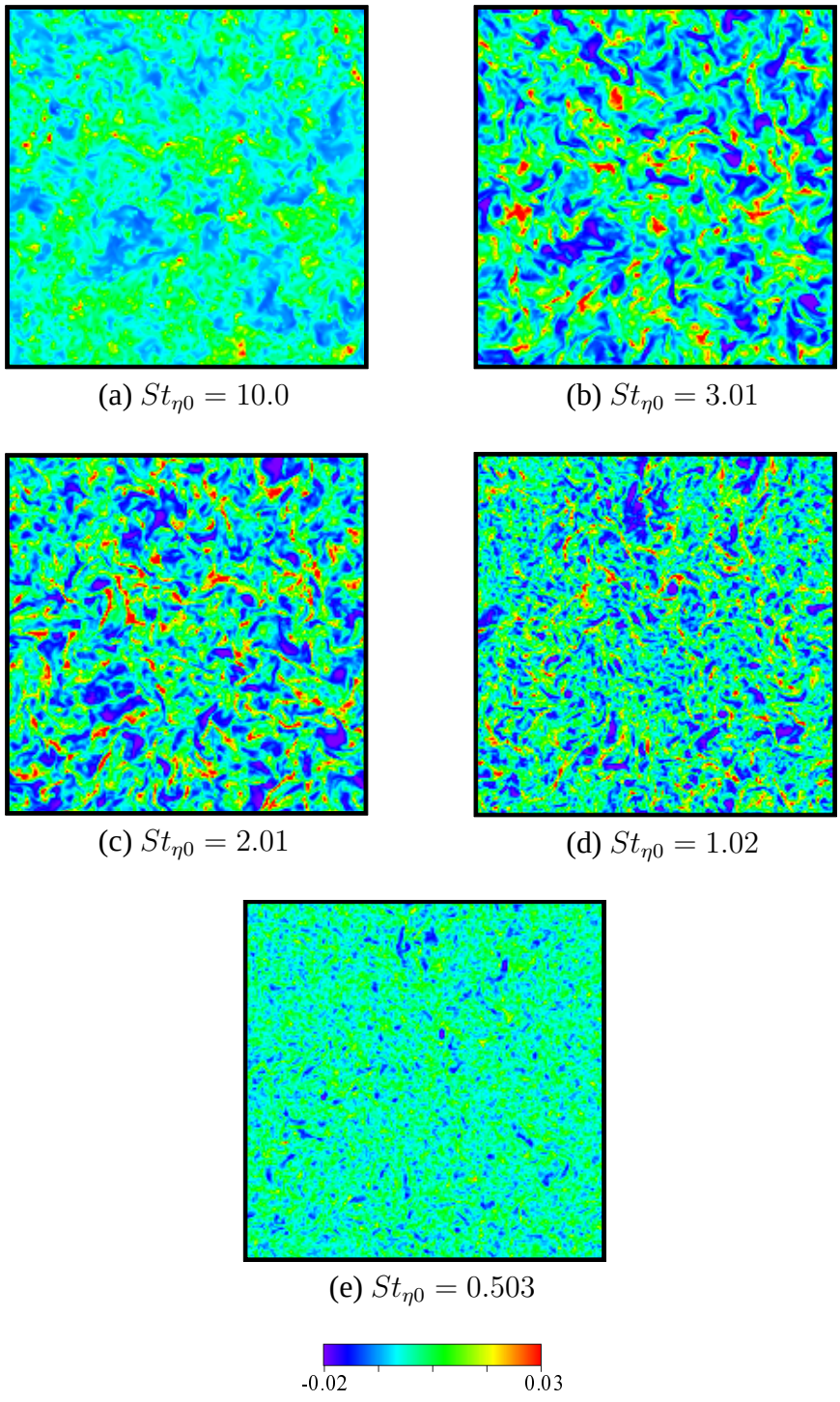

(a) $St_{\eta 0} = 10.0$

(b) $St_{\eta 0} = 3.01$

(c) $St_{\eta 0} = 2.01$

(d) $St_{\eta 0} = 1.02$

(e) $St_{\eta 0} = 0.503$

Figure 3.12: Distributions of fluctuation of vapor concentration on a typical $x - y$ plane for $Re_\lambda = 97.1$.

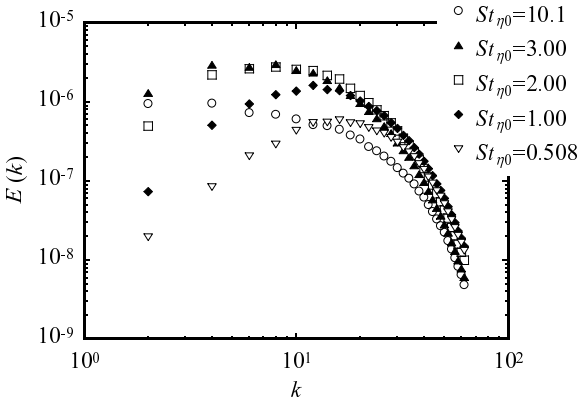

(a) $Re_\lambda = 60.1$

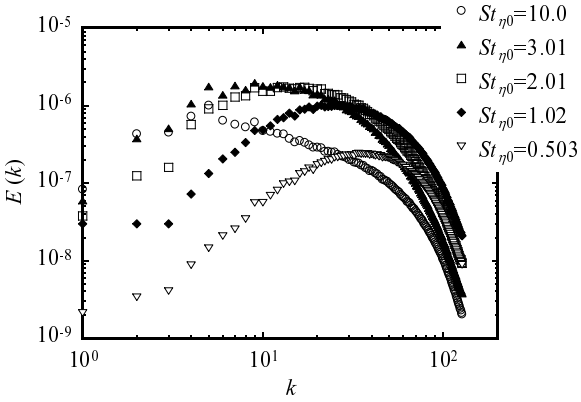

(b) $Re_\lambda = 97.1$

Figure 3.13: Energy spectra of vapor concentration.

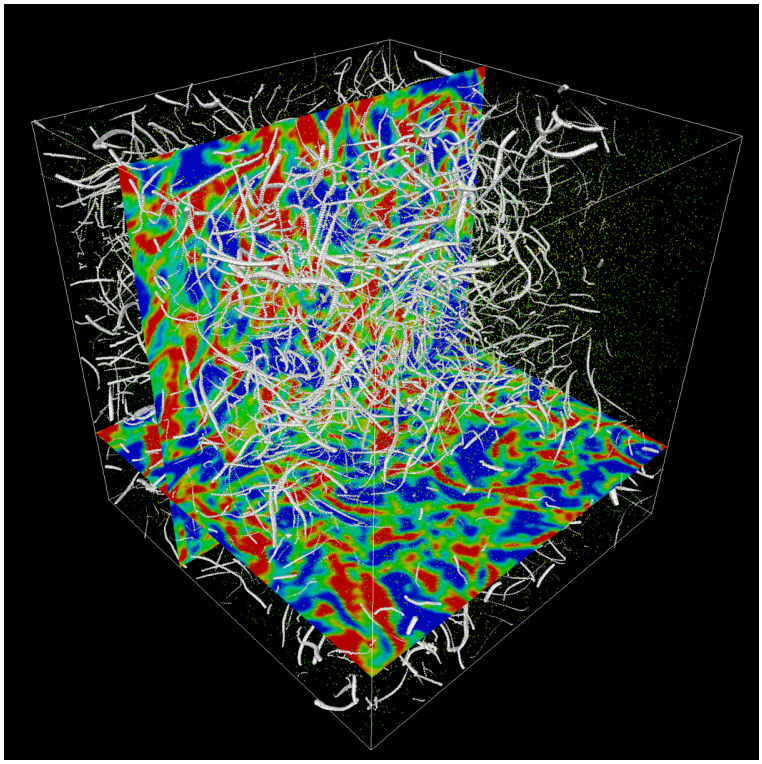

Figure 3.14: Distributions of droplets and the axis of coherent fine scale eddy with vapor concentration on typical cross-sections for $St_{\eta 0} = 2.00$ and $Re_\lambda = 60.1$.

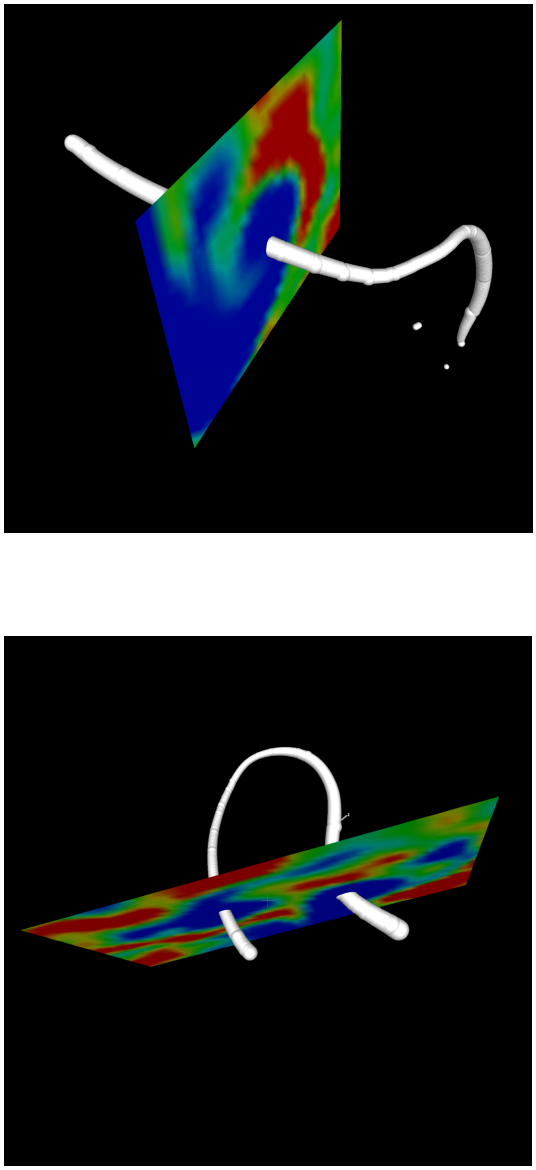

Figure 3.15: Vapor concentration around a typical axis of coherent fine scale eddy.

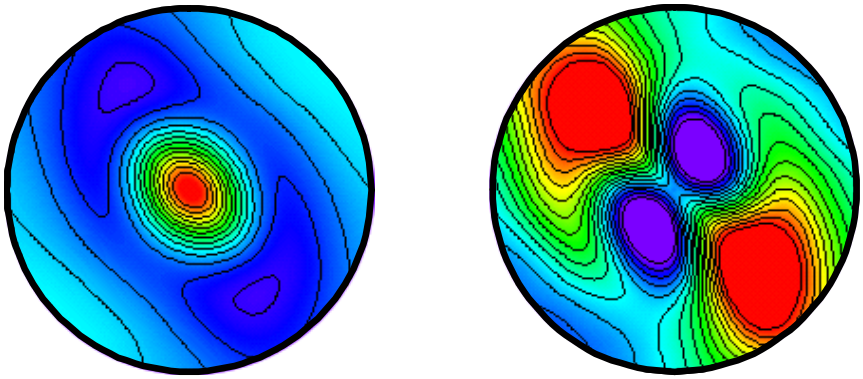

(a) Second invariant

(b) Energy dissipation rate

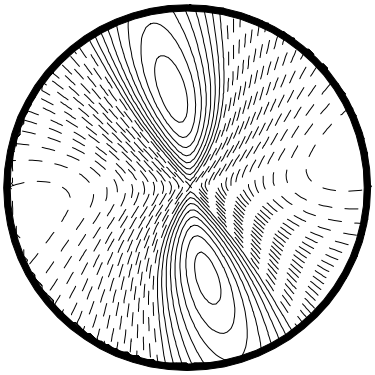

(c) Radial velocity

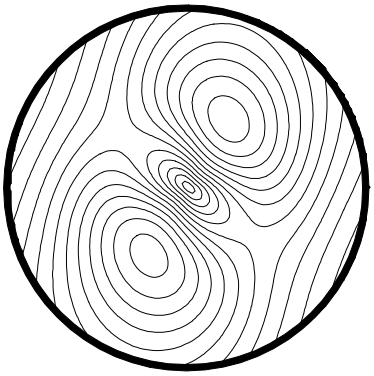

(d) Azimuthal velocity

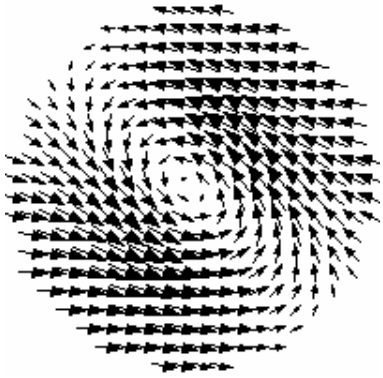

(e) Velocity vectors

Figure 3.16: Phase-averaged distributions on the plane perpendicular to the axis of the coherent fine scale eddies for $St_{\eta 0} = 2.00$ and $Re_\lambda = 60.1$.

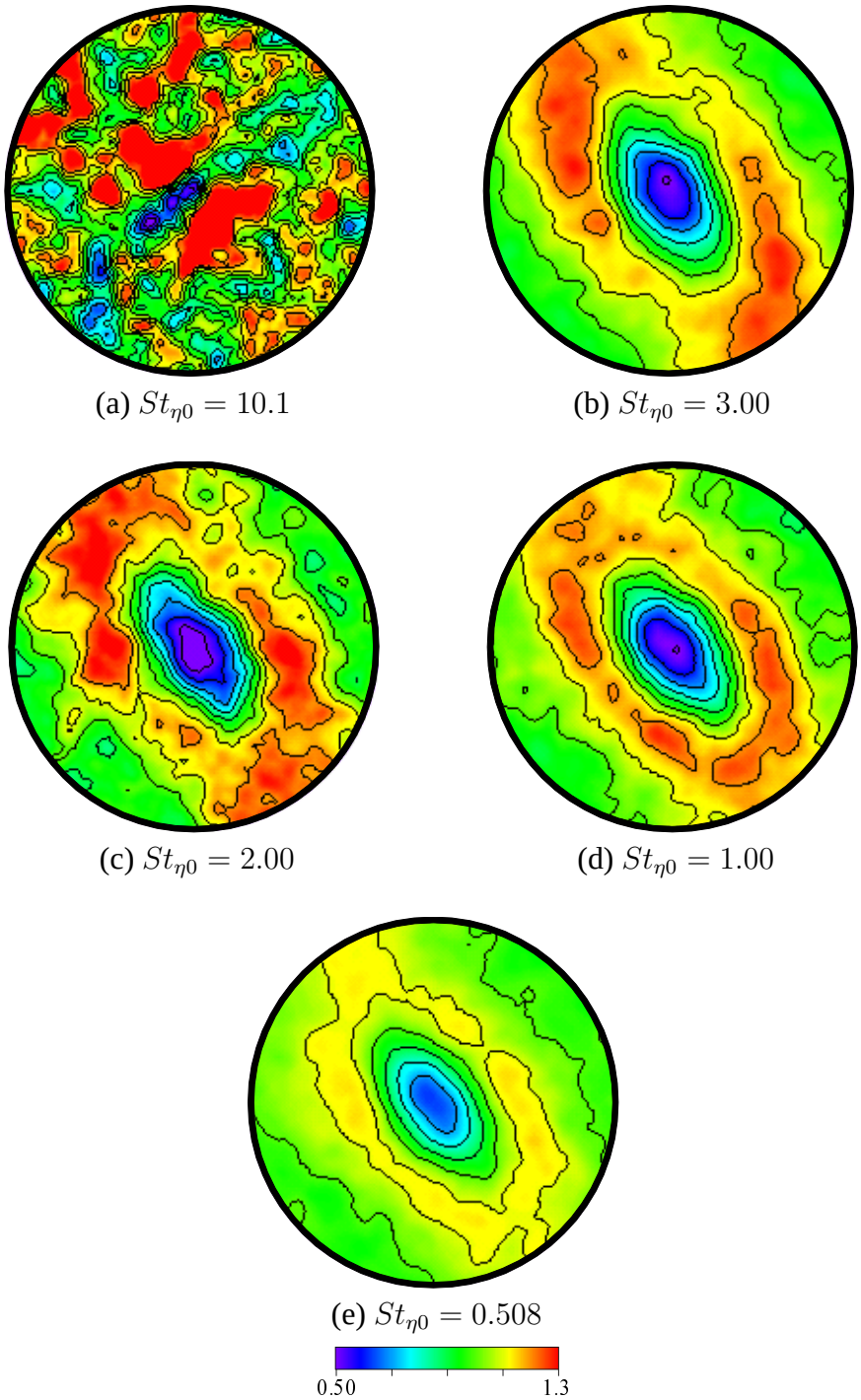

(a) $St_{\eta 0} = 10.1$ (b) $St_{\eta 0} = 3.00$

(c) $St_{\eta 0} = 2.00$ (d) $St_{\eta 0} = 1.00$

(e) $St_{\eta 0} = 0.508$

Figure 3.17: Phase-averaged distributions of number density of droplet on the plane perpendicular to the axis of the coherent fine scale eddy for $Re_\lambda = 60.1$.

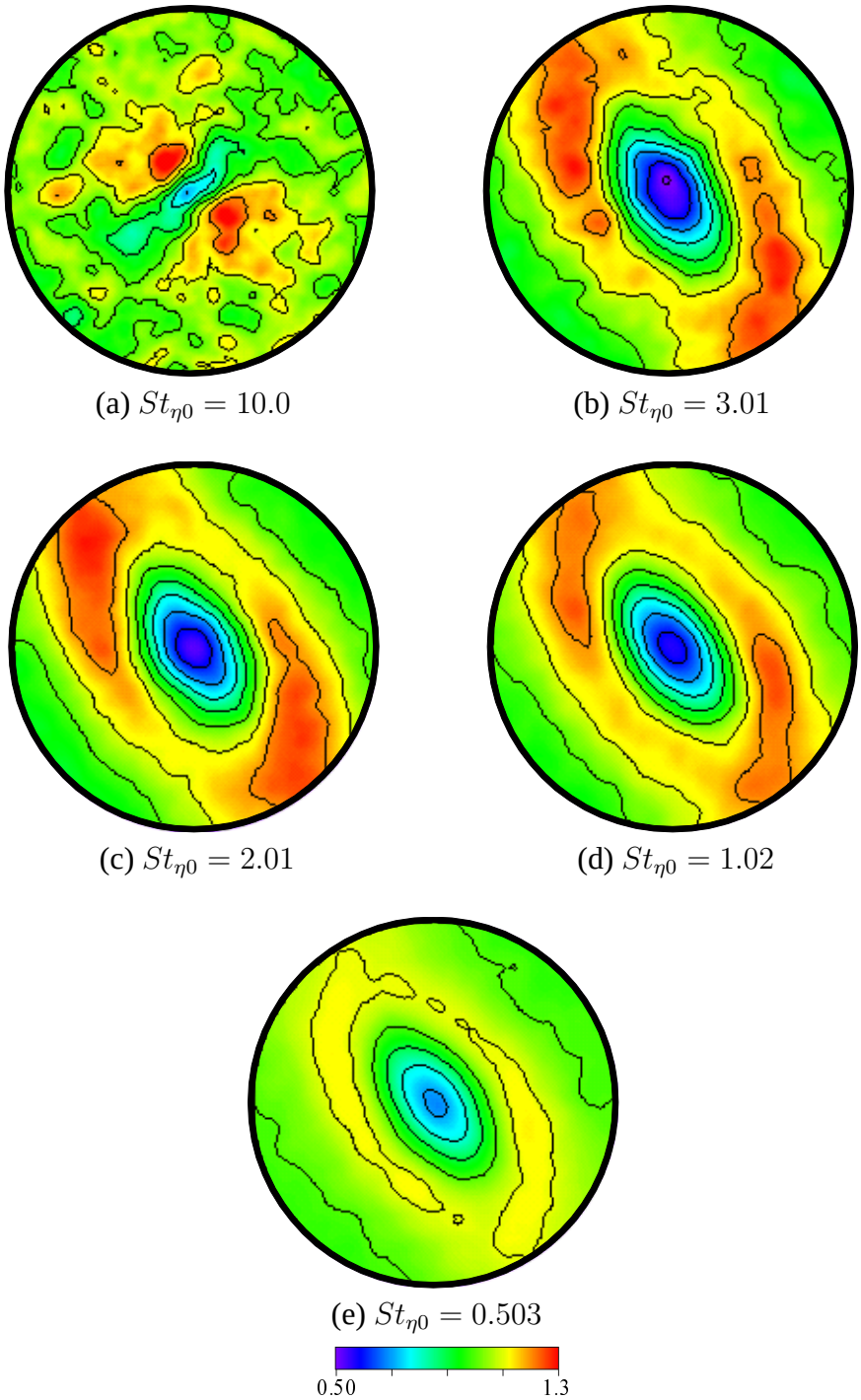

(a) $St_{\eta 0} = 10.0$ (b) $St_{\eta 0} = 3.01$

(c) $St_{\eta 0} = 2.01$ (d) $St_{\eta 0} = 1.02$

(e) $St_{\eta 0} = 0.503$

Figure 3.18: Phase-averaged distributions of number density of droplet on the plane perpendicular to the axis of the coherent fine scale eddy for $Re_\lambda = 97.1$.

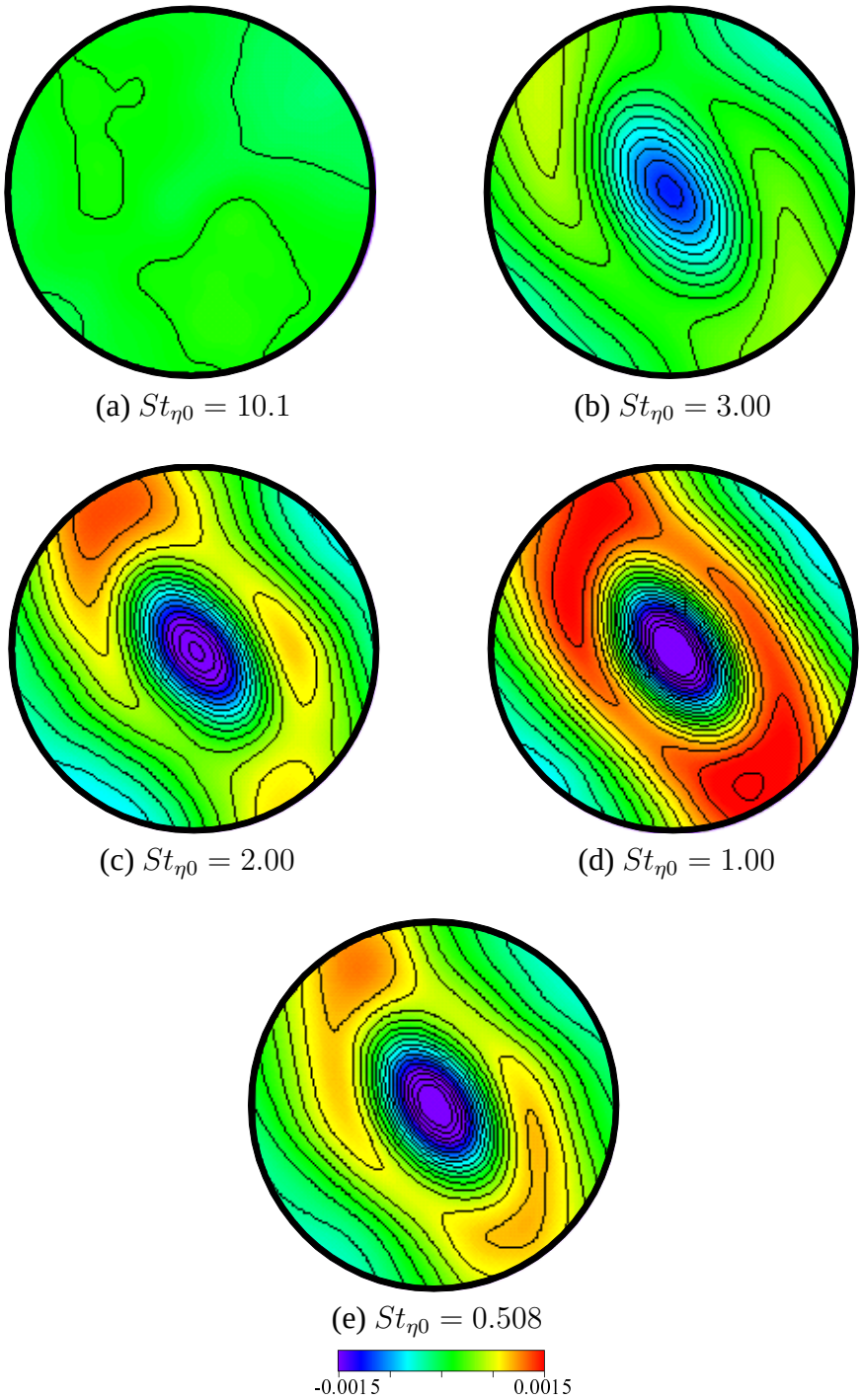

(a) $St_{\eta 0} = 10.1$ (b) $St_{\eta 0} = 3.00$

(c) $St_{\eta 0} = 2.00$ (d) $St_{\eta 0} = 1.00$

(e) $St_{\eta 0} = 0.508$

Figure 3.19: Phase-averaged distributions of fluctuation of vapor concentration on the plane perpendicular to the axis of the coherent fine scale eddies for $Re_\lambda = 60.1$.

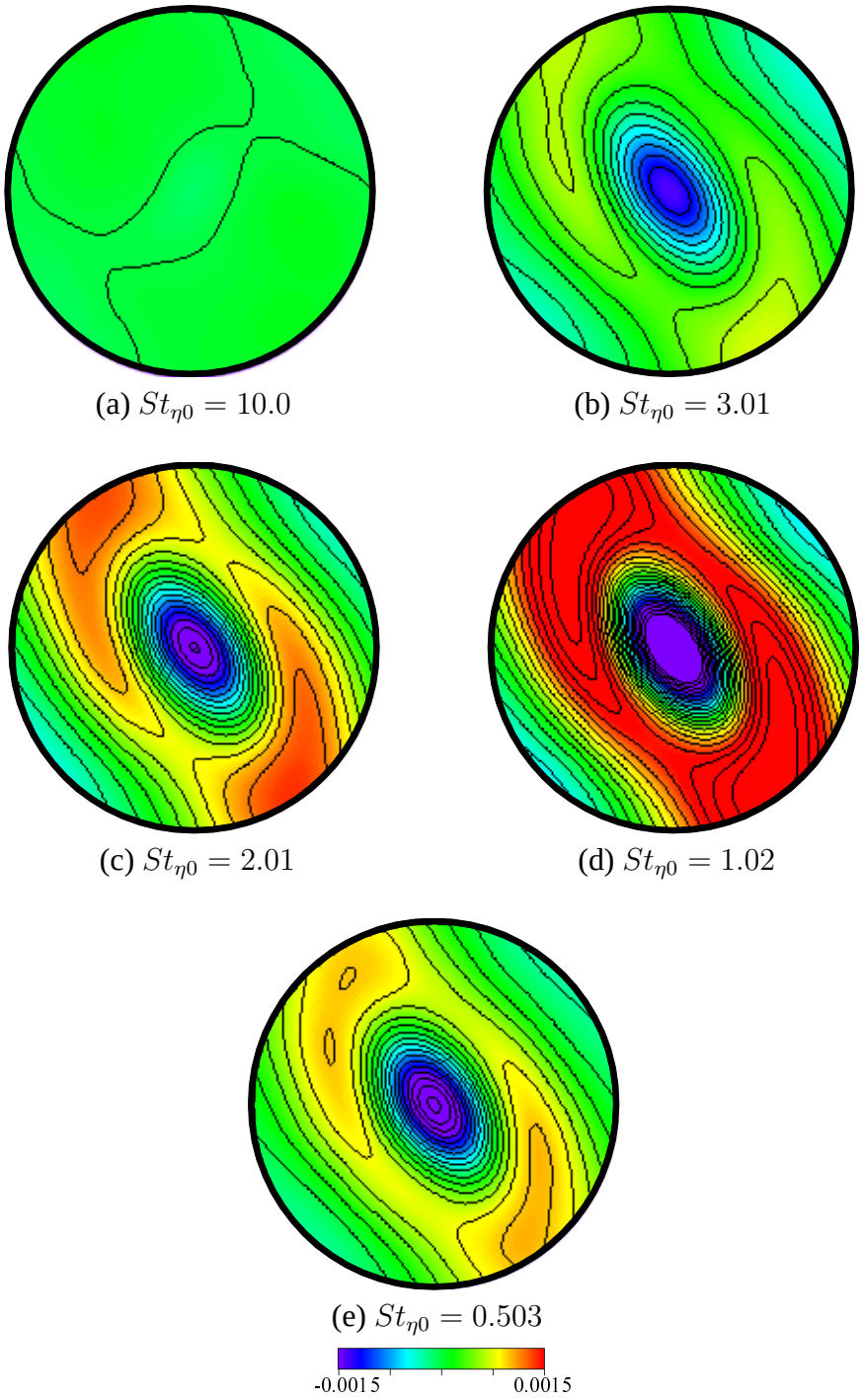

(a) $St_{\eta 0} = 10.0$ (b) $St_{\eta 0} = 3.01$

(c) $St_{\eta 0} = 2.01$ (d) $St_{\eta 0} = 1.02$

(e) $St_{\eta 0} = 0.503$

Figure 3.20: Phase-averaged distributions of fluctuation of vapor concentration on the plane perpendicular to the axis of the coherent fine scale eddies for $Re_\lambda = 97.1$.

Chapter 4

Ignition and Propagation of Turbulent n-Heptane/air Premixed Flames

4.1 Preface

In spray combustion, the fuel-air mixture is ignited by spark ignition or compression ignition or so on. These ignitions usually occur in turbulent flow. Therefore, it is necessary to investigate the ignition mechanism in turbulence. Especially, many investigation of the ignition mechanism in HCCI engine, which is not spray combustor, have been conducted, nowadays. In HCCI engine, the lean premixed fuel-air is automatically ignited by mixture compression. The HCCI engine has potential for higher efficiency compared with spark ignition engine, and lower emission compared with diesel engine. However, there are a lot of issues to realize HCCI engine practically. Narrow operating load range and engine noise are some examples of the problems. The most serious issue is the control of ignition. Many researchers have studied to overcome this issue experimentally, such as EGR, fuel reforming and so on [90][91][92], whereas the flame structures in the combustion chamber have not been clarified yet. Combustion modes in HCCI engine can be regarded as turbulent premixed flames because of premixed mixture and inhomogeneous flow field.

In our previous studies [93][94], we have conducted DNS of hydrogen/air turbulent premixed flames in three dimensional homogeneous isotropic turbulence with a detailed kinetic mechanism and have shown that the fine-scale structure in the unburnt side plays quite important roles on the local flame structure. Therefore, it is considered that the characteristics of turbulence are very important for ignition and propagation process of the mixture. To clarify mechanisms of ignition and propagation in turbulence, numerical approach is powerful because it is difficult to measure the local flame structure in turbulence experimentally.

In this chapter, DNS of ignition and propagation of n-heptane/air premixed flame in homogeneous isotropic turbulence are conducted to investigate effects of turbulence on the ignition and propagation process. For comparison, the results of hydrogen/air and methane/air premixed flames in homogeneous isotropic turbulence are also shown.

4.2 Numerical Method

4.2.1 Governing Equations

The governing equations are continuity equation, compressible Navier-Stokes equations and conservation equations of energy and chemical species including no coupling terms with dispersed phase as follows;

$$\frac{\partial \rho}{\partial t} + \frac{\partial \rho u_i}{\partial x_i} = 0, \tag{4.1}$$

$$\frac{\partial \rho u_i}{\partial t} + \frac{\partial \rho u_i u_j}{\partial x_j} = -\frac{\partial \tau_{ij}}{\partial x_j}, \tag{4.2}$$

$$\frac{\partial \rho E_t}{\partial t} + \frac{\partial}{\partial x_i}(\rho u_i E_t) = -\frac{\partial q_i}{\partial x_i} - \frac{\partial \tau_{ij} u_i}{\partial x_j}, \tag{4.3}$$

$$\frac{\partial \rho Y_k}{\partial t} + \frac{\partial}{\partial x_i}(\rho u_i Y_k) = -\frac{\partial}{\partial x_i}(\rho Y_k V_{k,i}) + \omega_k. \tag{4.4}$$

Stress tensor (τ_{ij}) and heat flux (q_i) in Eqs. (4.2)-(4.3) are represented as follows;

$$\tau_{ij} = \left[p + \left(\frac{2}{3}\mu - \kappa \right) \left(\frac{\partial u_i}{\partial x_i} \right) \right] \delta_{ij} - \mu \left[\frac{\partial u_i}{\partial x_j} + \frac{\partial u_j}{\partial x_i} \right], \tag{4.5}$$

where κ is the bulk viscosity.

$$q_i = -\lambda \frac{\partial T}{\partial x_i} + \rho \sum_{k=1}^{N} h_k Y_k V_{k,i} + R^0 T \sum_{k=1}^{N} \sum_{l=1}^{N} \left(\frac{X_k D_{T,k}}{W_k D_{kl}} \right) (V_{k,i} - V_{l,i}) + q_{R,i}. \tag{4.6}$$

Here, $D_{T,k}$ and D_{kl} are the thermal diffusion coefficient and the binary diffusion coefficient for species k and l. $q_{R,i}$ is a radiant heat transfer.

The mass diffusion velocity $V_{k,i}$ of kth species is determined as follows;

$$\begin{aligned} \frac{\partial X_k}{\partial x_i} =& \sum_{l=1}^{N} \left(\frac{X_k X_l}{D_{kl}} \right) (V_{k,i} - V_{l,i})) \\ &+ (Y_k - X_k) \frac{1}{p} \frac{\partial p}{\partial x_i} + \frac{\rho}{p} \sum_{l=1}^{N} Y_k Y_l (f_{k,i} - f_{l,i}) \\ &+ \sum_{l=1}^{N} \left[\left(\frac{X_k X_l}{\rho D_{kl}} \right) \left(\frac{D_{T,l}}{Y_l} - \frac{D_{T,k}}{Y_k} \right) \right] \frac{1}{T} \frac{\partial T}{\partial x_i}. \end{aligned} \tag{4.7}$$

In DNS of this study, conservation equation of energy is solved for ρT variable, based on following assumptions.

· No external forces

$$f_{k,i} = 0 \tag{4.8}$$

· Negligible the Sore effect

$$\sum_{l=1}^{N} \left[\left(\frac{X_k X_l}{\rho D_{kl}} \right) \left(\frac{D_{T,l}}{Y_l} - \frac{D_{T,k}}{Y_k} \right) \right] \frac{1}{T} \frac{\partial T}{\partial x_i} = 0 \tag{4.9}$$

· Negligible the Dufour effect

$$R^0 T \sum_{k=1}^{N} \sum_{l=1}^{N} \left(\frac{X_k D_{T,k}}{W_k D_{kl}} \right) (V_{k,i} - V_{l,i}) = 0 \tag{4.10}$$

· Negligible the diffusion of pressure gradient

$$(Y_k - X_k) \frac{1}{p} \frac{\partial p}{\partial x_i} = 0 \tag{4.11}$$

· Negligible the bulk viscosity

$$\kappa = 0 \tag{4.12}$$

· Negligible a radiant heat transfer

$$q_{R,i} = 0 \tag{4.13}$$

From these assumptions, the governing equations can be written as follows.

· The continuity equation:

$$\frac{\partial \rho}{\partial t} + \frac{\partial \rho u_i}{\partial x_i} = 0. \tag{4.14}$$

· The compressible Navier-Stokes equations:

$$\frac{\partial \rho u_i}{\partial t} + \frac{\partial \rho u_i u_j}{\partial x_j} = -\frac{\partial \tau_{ij}}{\partial x_j}. \tag{4.15}$$

· The energy conservation equation:.

$$\begin{aligned} &\frac{\partial \rho T}{\partial t} + \frac{\partial \rho u_i T}{\partial x_i} = \frac{1}{\bar{c_v}} \frac{\partial}{\partial x_i} \lambda \frac{\partial T}{\partial x_i} - \frac{1}{\bar{c_v}} \sum_{k=1}^{N} (\rho Y_k V_{k,i}) c_{p,k} \frac{\partial T}{\partial x_i} \\ &- \frac{T}{\bar{c_v}} \sum_{k=1}^{N} \left[R_k \frac{\partial}{\partial x_i} (\rho Y_k V_{k,i}) \right] - \frac{1}{\bar{c_v}} \tau_{ij} \frac{\partial u_i}{\partial x_j} - \frac{1}{\bar{c_v}} \sum_{k=1}^{N} h_k \omega_k + \frac{T}{\bar{c_v}} \sum_{k=1}^{N} R_k \omega_k. \end{aligned} \tag{4.16}$$

· The species conservation equations:

$$\frac{\partial Y_k}{\partial t} + u_i \frac{\partial Y_k}{\partial x_i} = -\frac{1}{\rho} \frac{\partial}{\partial x_i} (\rho Y_k V_{k,i}) + \frac{\omega_k}{\rho}. \tag{4.17}$$

The ideal-gas equation of state is

$$p = \rho R^0 T \sum_{k=1}^{N} \left(\frac{Y_k}{W_k} \right), R_k = \frac{R^0}{W_k}. \tag{4.18}$$

The diffusion velocity $V_{k,i}$ is represented with the use of diffusion velocity of species k in mixture (D_{mk}),

$$V_{k,i} = -\frac{1}{X_k} D_{mk} \frac{\partial X_k}{\partial x_i}. \tag{4.19}$$

The specific heat of the gas mixture at constant volume $\bar{c_v}$ is

$$\bar{c_v} = \sum_{k=1}^{N} c_{v,k} Y_k, \tag{4.20}$$

where $c_{v,k}$ means the specific heat at constant volume for species k.

4.2.2 Chemical Reaction

In general, chemical reactions can proceed in both the forward direction and the reverse direction. The general k set of chemical reactions including i species is denoted as follows;

$$\sum_{i=1}^{I} \nu'_{i,k} X_i \Longleftrightarrow \sum_{i=1}^{I} \nu''_{i,k} X_i, \tag{4.21}$$

where $\nu'_{i,k}$ is the stoichiometric coefficient for species i in elementary reaction k appearing as a reactant, $\nu''_{i,k}$ is the stoichiometric coefficient for species i in elementary reaction k appearing as a product. I means the number of elementary reactions in the reaction mechanism. Note that in this section, the means of subscripts are different from other sections. The production rate w_i of the ith species can be written as a summation of the rate-of-progress variables q_k for all reactions involving the kth species.

$$w_i = \sum_{k=1}^{K} (\nu''_{i,k} - \nu'_{i,k}) q_k. \tag{4.22}$$

The rate of progress variable q_i for the ith reaction is given by the difference of the forward and reverse rates as;

$$q_k = k_{f_k} \prod_{i=1}^{I} [X_i]^{\nu'_{i,k}} - k_{r_k} \prod_{i=1}^{I} [X_i]^{\nu''_{i,k}}. \tag{4.23}$$

The forward rate constants for the I reactions are generally assumed to have the following Arrhenius temperature dependence:

$$k_{f_k} = A_k T^{\beta_k} \exp\left(\frac{-E_k}{R^0 T}\right). \tag{4.24}$$

where the pre-exponential factor A_k, the temperature exponent β_k, and the activation energy E_k are specified for each elementary reactions. The reverse rate constants k_{r_k} are related to the forward rate constants through the equilibrium constants by

$$k_{r_k} = \frac{k_{f_k}}{K_{c_k}}. \tag{4.25}$$

Although K_{c_k} is given in concentration units, the equilibrium constants are more easily determined from the thermodynamic properties in pressure units; they are related by

$$K_{c_k} = K_{p_k} \left(\frac{P_{atm}}{RT} \right)^{\sum_{i=1}^{I} (\nu''_{i,k} - \nu'_{i,k})} . \tag{4.26}$$

The equilibrium constants K_{p_k} are obtained with the relationship

$$K_{p_k} = \exp \left(\frac{\Delta S_k}{R^0} - \frac{\Delta H_k}{R^0 T} \right) . \tag{4.27}$$

The changes of entropy S_i and enthalpy H_i for ith species, which occur in passing completely from reactants to products in the ith reaction, are represented as follows;

$$\frac{\Delta S_k}{R^0} = \sum_{i=1}^{I} (\nu''_{i,k} - \nu'_{i,k}) \frac{S_i}{R^0}, \tag{4.28}$$

$$\frac{\Delta H_k}{R^0 T} = \sum_{i=1}^{I} (\nu''_{i,k} - \nu'_{i,k}) \frac{H_i}{R^0 T}. \tag{4.29}$$

Three-body Reactions

In some reactions a "third body" is required for the reaction to proceed; this is often the case in dissociation or recombination reactions, such as

$$\mathrm{H} + \mathrm{O_2} + \mathrm{M} \Longleftrightarrow \mathrm{HO_2} + \mathrm{M}.$$

When a third body is needed, the concentration of the effective third body must appear in the expression for the rate-of-progress variable. Accordingly, the rate-of-progress variable is different from Eq. (4.23) by the first factor in the equation:

$$q_k = \left(\sum_{i=1}^{I} \alpha_{i,k} [X_i] \right) \left(k_{f_k} \prod_{i=1}^{I} [X_i]^{\nu'_{i,k}} - k_{r_k} \prod_{i=1} I [X_i]^{\nu''_{i,k}} \right) . \tag{4.30}$$

Here, $\alpha_{i,k}$ is contribution for kth elementary reaction as third-body of species i If all species in the mixture contribute equally as third bodies, then $\alpha_{i,k} = 1$ for all k, and the first factor is the total concentration of the mixture,

$$[M] = \sum_{i=1}^{I} [X_i]. \tag{4.31}$$

However, it is often the case that some species act more efficiently as third bodies than do others. In table A.2, the degree of contribution as third-body in reaction mechanism of this study is shown.

Fall-off Reaction

Under certain conditions, some reaction rate expressions depend on pressure as well as temperature. For example, the fall-off reaction has pressure dependence. As an example of a unimolecular/recombination fall-off reaction, consider methyl recombination. In the high-pressure limit, the appropriate description of the reaction is CH_3 + $CH_3 \Longleftrightarrow C_2H_6$. In the lowpressure limit, a third-body collision is required to provide the energy necessary for the reaction to proceed, i.e., the appropriate description is CH_3 + CH_3 + (M) $\Longleftrightarrow C_2H_6$ + (M). When such a reaction is at either limit, the (solely temperature-dependent) rate expressions are applicable. However, when the pressure and temperature are such that the reaction is between the limits, the rate expressions are more complicated. To denote a reaction that is in this "fall-off" region, the reaction is written with the (+M) enclosed in parentheses,

$$CH_3 + CH_3 + (M) \Longleftrightarrow C_2H_6 + (M).$$

There are several methods of representing the rate expressions in this fall-off region. The simplest one is due to Lindemann. Arrhenius rate parameters are required for both the high and low-pressure limiting cases, and the Lindemann form for the rate coefficient blends them to produce a pressure-dependent rate expression. In Arrhenius form, the parameters are given for the high-pressure limit (k_∞) and the low-pressure limit (k_0) as follows:

$$k_0 = A_0 T^{\beta_0} \exp\left(\frac{-E_0}{R_c T}\right), \tag{4.32}$$

$$k_\infty = A_\infty T^{\beta_\infty} \exp\left(\frac{-E_\infty}{R_c T}\right). \tag{4.33}$$

The rate constant at any pressure is then taken to be

$$k = k_\infty \left(\frac{P_r}{1 + P_r} \right) F, \tag{4.34}$$

where the reduced pressure P_r is given by,

$$P_r = \frac{k_0[M]}{k_\infty}, \tag{4.35}$$

where [M] is the concentration of the mixture, possibly including enhanced third-body efficiencies. If the F is unity, then this is the Lindemann form. The reaction mechanism used in DNS of this study adopts the Troe form. In the Troe form, F is given by

$$\log F = \left\{ 1 + \left[\frac{\log P_r + c}{n - d(\log P_r + c)} \right]^2 \right\}^{-1} \log F_{\text{cent}}. \tag{4.36}$$

The constants in Eq. (4.36) are

$$c = -0.4 - 0.67 \log F_{\text{cent}} \tag{4.37}$$

$$n = 0.75 - 1.27 \log F_{\text{cent}} \tag{4.38}$$

$$d = 0.14 \tag{4.39}$$

and

$$F_{\text{cent}} = (1 - \alpha) \exp\left(\frac{-T}{T^{***}} \right) + \alpha \exp\left(\frac{-T}{T^{*}} \right) + \exp\left(\frac{-T^{**}}{T} \right). \tag{4.40}$$

The four parameters α, T^*, T^{**} and T^{***} must be specified as input parameters.

4.2.3 Thermodynamic Properties

The temperature dependence of the viscosity, thermal conductivity, and diffusion coefficients are calculated using CHEMKIN-II packages [99][100] which are modified for vector/parallel computations. CHEMKIN presumes that the standard-state thermodynamic properties are thermally ”perfect”, in that they are only functions of temperature and are given in terms of polynomial fits to the molar heat

capacities at constant pressure:

$$\frac{C_{p,i}}{R^0} = \sum_{n=1}^{N} a_{n,i} T^{(n-1)}. \tag{4.41}$$

The superscript 0 refers to the standard-state 1 atmosphere. For perfect gases, however, the heat capacities are independent of pressure, and the standard-state values are the actual values. Other thermodynamic properties are given in terms of integrals of the molar heat capacities. First, the standardstate molar enthalpy is given by

$$H_i = \int_0^T C_{p,i} dT, \tag{4.42}$$

so that

$$\frac{H_i}{R^0 T} = \sum_{i=1}^{N} \frac{a_{n,i} T^{(n-1)}}{n} + \frac{a_{N+1,i}}{T}, \tag{4.43}$$

where the constant of integration $a_{N+1,i}$ is the standard heat of formation at 0 K. Normally, however, this constant is evaluated from knowledge of the standard heat of formation at 298 K, since the polynomial representations are usually not valid down to 0 K. Therefore, the enthalpy of each species is defined as follows;

$$H_i = \int_{298}^{T} C_{p,i} dT + H_i(298). \tag{4.44}$$

As the same way, the entropy of each species is given by integration of specific heat

$$S_i = \int_0^T \frac{C_{p,i}}{T} dT \tag{4.45}$$

so that

$$\frac{S_i}{R^0} = a_{1,i} \ln T + \sum_{n=2}^{N} \frac{a_{n,i} T^{(n-1)}}{n-1} + a_{N+2,i} \tag{4.46}$$

where the constant of integration $a_{N+2,i}$ is evaluated from knowledge of the standard-state entropy at 298 K. The above equations are stated for an arbitrary-order polynomial, but the CHEMKIN package is designed to work with thermodynamic data in the form used in the NASA chemical equilibrium code. In this study, N is 5 in calculation of coefficient.

In addition, $c_{p,i}$ and $\bar{c_v}$ are related to $C_{p,i}$ based on following equations.

$$c_{p,i} = C_{p,i}/W_i \tag{4.47}$$

$$C_{v,i} = C_{p,i} - R^0 \tag{4.48}$$

$$c_{v,i} = C_{v,i}/W_i \tag{4.49}$$

$$\bar{c_v} = \sum_{i=1}^{I} c_v Y_i \tag{4.50}$$

4.2.4 Transport Coefficients

The viscosity η_i, thermal conductivity λ_i and binary diffusion coefficient D_{ij} are calculated using fitting procedure as function of temperature.

$$\ln \eta_i = \sum_{n=1}^{N} a_{n,i} (\ln T)^{n-1} \tag{4.51}$$

$$\ln \lambda_i = \sum_{n=1}^{N} b_{n,i} (\ln T)^{n-1} \tag{4.52}$$

$$\ln D_{ij} = \sum_{n=1}^{N} c_{n,i} (\ln T)^{n-1} \tag{4.53}$$

Here, coefficient $a_{n,i}$, $b_{n,i}$ and $c_{n,i}$ are computed to $N = 4$ from TRANSPORT of CHEMKIN PACKAGE [100]. The Wilke formula for mixture viscosity is given by

$$\nu = \sum_{i=1}^{I} \frac{X_i \eta_i}{\sum_{j \neq i}^{I} X_j \Phi_{ij}} \tag{4.54}$$

where,

$$\Phi_{ij} = \frac{1}{\sqrt{8}} \left(1 + \frac{W_i}{W_j}\right)^{-\frac{1}{2}} \left\{1 + \left(\frac{\eta_i}{\eta_j}\right)^{\frac{1}{2}} \left(\frac{W_j}{W_i}\right)^{\frac{1}{4}}\right\}^2 . \tag{4.55}$$

For the mixture averaged thermal conductivity, a combination averaging formula is used as follows;

$$\lambda = \frac{1}{2} \left(\sum_{i=1}^{I} X_i \lambda_i + \frac{1}{\sum_{i=1}^{I} X_i / \lambda_i} \right) . \tag{4.56}$$

The mixture diffusion coefficient for species i is computed as;

$$D_{im} = \frac{\sum_{j \neq i}^{I} X_j W_j}{\bar{W} \sum_{j \neq i}^{I} X_j / D_{ij}}. \tag{4.57}$$

4.2.5 Numerical Procedure and Numerical Conditions

The governing equations are solved by using a fourth order central finite difference scheme. To damp any spurious high-wave number oscillations, a fourth order compact finite difference filter [96] is used. Navier-Stokes Characteristic Boundary Condition (NSCBC) [97][98] is assumed in all directions. Time integration is implemented by a third order Runge-Kutta scheme. For n-heptane/air cases, reaction source terms in species equations are implemented by an implicit method [101][102] (ref. Appendix B).

Figure 4.1 shows a schematic of the flow field used in this study. As an initial condition, high temperature region which is regarded as an ignition kernel is given at the center of computational domain, and the ignition starts from this kernel. Initial temperature distribution (T_{ini}) is given as Gaussian distribution;

$$T_{ini} = (T_{max} - T_{pre}) e^{-\frac{{r_c}^2}{2\sigma^2}} + T_{pre}, \tag{4.58}$$

$$\frac{{r_c}^2}{2\sigma^2} = \ln\left\{ \frac{T_{max} - T_{pre}}{T_{ig} - T_{pre}} \right\}, \tag{4.59}$$

where T_{max} is the maximum temperature of the ignition kernel, T_{pre} is preheat temperature, T_{ig} is auto-ignition temperature, and r_c is radius of the ignition kernel. A premixed mixture is assumed to be uniform for all cases. Numerical parameters of DNS conducted in the present study are listed in Table 4.1. Here, ID C7R-, HR- and CR- mean n-heptane/air mixture, hydrogen/air mixture and methane/air mixture. δ_F and δ_L are flame thickness defined by $\delta_F = \nu / S_L$ using kinematic viscosity (ν) in unburned mixture and by laminar flame thickness based on temperature gradient, respectively. L and N represent computational domain size and grid points in each direction. To investigate the Reynolds number effects on the ignition and propagation process, DNS are conducted with different Reynolds number.

For hydrogen/air and methane/air mixture cases, time is normalized by the flame time (τ_F), which is calculated based on laminar flame thickness and laminar flame velocity as follows;

$$\tau_F = \frac{\delta_L}{S_L}. \tag{4.60}$$

A reduced kinetic mechanism which includes 37 reactive species and 61 elementary reactions [134] is used for n-heptane/air mixture (ref. AppendixA). A detailed kinetic mechanism which includes 12 reactive species and 27 elementary reactions [103][104][105] is used for hydrogen/air mixture and GRI Mech. 2.11 (49 reactive species and 279 elementary reactions) [106] is used for methane/air mixture. In Fig. 4.2, each calculation condition is plotted in the turbulent combustion diagram by Peters [107]. Both n-heptane cases are classified in thin reaction zones. For comparison, laminar conditions are also calculated.

Table 4.1: Numerical Parameters of DNS.

ID	Re_λ	u'_{rms}/S_L	l/δ_F	l/δ_L	T_{max} [K]	T_{pre} [K]	r_c [mm]	L [mm]	N
C7R47	47.1	6.42	21.0	2.68	1600	700	1.0	10	513
C7R106	106.8	15.9	20.0	2.74	1600	700	1.0	10	513
HR47	47.1	0.77	174.3	3.04	1500	800	0.7	10	1025
HR66	66.4	1.93	88.2	1.54	1500	800	0.7	15	1537
HR71	71.9	1.93	78.0	1.36	1500	800	0.7	10	1025
HR106	106.8	1.92	166.7	2.91	1500	800	0.7	10	1025
CR47S	47.1	3.02	44.4	6.21	2200	950	2.0	10	1025
CR47W	47.1	1.51	88.9	12.43	2200	950	2.0	20	2049
CR71S	71.9	7.54	19.9	2.78	2200	950	2.0	10	1025
CR71W	71.9	3.77	39.7	5.55	2200	950	2.0	20	2049
CR106S	106.8	7.50	42.5	5.94	2200	950	2.0	10	1025
CR106W	106.8	3.75	84.9	11.88	2200	950	2.0	20	2049

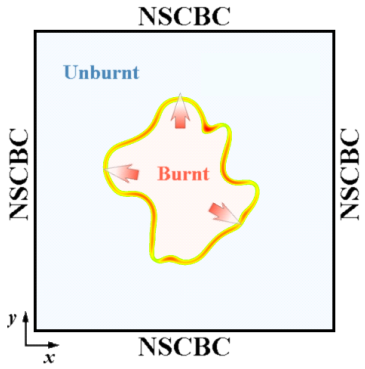

Figure 4.1: Geometry of the flow field.

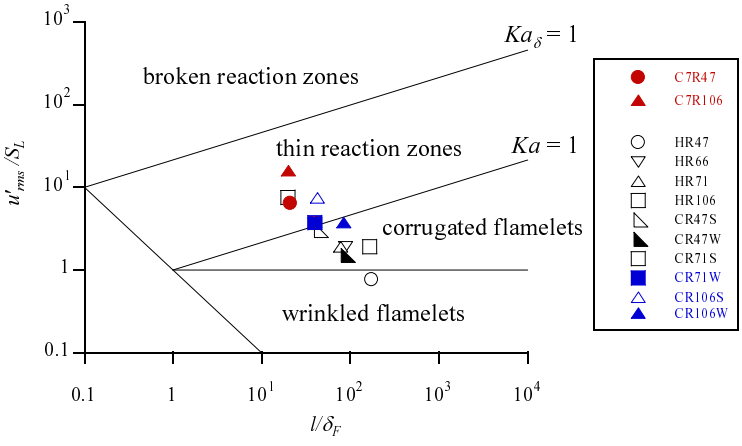

Figure 4.2: Numerical conditions of the present DNS on the combustion diagram by Peters.

4.3 Effects of Turbulence on Ignition

Figures 4.3 and 4.4 show temporal developments of temperature and vorticity distributions in induction phase before ignition for C7R47 and C7R106. Here, temperature is denoted by colors and vorticity distribution is shown by contour lines. The interval of contour lines of vorticity is 30000s-1 for C7R47 and 50000s-1 for C7R106. In C7R47 which is low Reynolds number case, high temperature region is slightly stretched by surrounding eddies. In contrast, high temperature region in C7R106, which is high Reynolds number and high turbulence intensity case, is distorted tremendously and stretched toward low temperature region by strong eddies.

For the ignition of hydrocarbon/air mixture, amount of H atom is very important. Figure 4.5 shows distributions of mole fraction of H atom with vorticity in the induction phase for C7R106. The mole fraction is normalized by the maximum value at each time. The distortion of high concentration region of H atom is similar to that of high temperature region. For low Reynolds number case, the distortion of H atom distribution by turbulence is not significant, however. for high turbulence intensity case, H atom distribution is strongly distorted by the eddy and H atoms which are transported into low temperature regions disappear. In these regions, productions of intermediate through H atom are suppressed.

Figure 4.6 shows temporal developments of the maximum temperature for each Reynolds number case. For comparison, temporal developments of the maximum temperature for hydrogen/air mixture and methane/air mixture are also shown. Here, HR71-i represents the result from different ignition point in same turbulent flows. In this study, ignition delay is assumed as period until getting to thermal runaway. Thermal runaway is defined as inflection point of temperature in rapid rise of the maximum temperature. The rise of temperature in C7R47 is similar to that of the laminar case, and the difference of ignition delay between C7R47 and laminar is small. In contrast, the ignition delay of C7R106 is larger than that of the laminar case. The reason is that, as shown in Fig. 4.4, the degree

of distortion of high temperature region is large for C7R106, and the high temperature region is distorted such that being separated by the surrounding eddies. This mechanism is interpreted as follows; maintenance of high energy region near the ignition point is difficult due to thermal loss which is caused by distortion (or turbulent diffusion) and cooling of main high temperature region by the eddies, and the resulting suppression of radical production requires much more time for the ignition. The ignition delay tends to increase with turbulence intensity. This tendency is similar to the results of hydrogen/air cases. For methane/air cases, decreases of the temperature in the induction phase are smaller than that for hydrogen/air cases, and the ignition delay tends to increase with turbulence intensity.

4.4 Effects of Local Turbulence Characteristics

Figure 4.7 shows distributions of temperature and vorticity in the induction phase and propagation process for HR71 with different ignition point. The interval of contour lines of vorticity is 120000s^{-1}. In each case, the ignition kernel is given at different points in the statistically same turbulent field. In induction phase, the high temperature region is stretched by eddies in a different way for each case. As shown in Fig. 4.6(b), the temporal developments of the maximum temperature show that the ignition delay is different even if the turbulent field is statistically same. Therefore, it is considered that the ignition delay significantly depends on local characteristics of turbulence. In propagation process, the ignition takes place from three points with different timing in HR71-1, while the ignition in HR71-2 takes place only from one point. These results imply that consideration of local characteristics of turbulence is important for estimation of the ignition delay.

Figure 4.8 shows relation between the ignition delay time (t') and mean strain rate ($\langle S_{ij}S_{ij}\rangle$) for hydrogen/air and methane/air cases. Mean strain rate represents an average of strain rate which is in the region of initial ignition kernel. The ignition delay tends to increase with increase of mean strain rate except for HR71-1 and HR106. In HR71-1 and HR106, the flames are ignited from several points

since the initial high temperature region is separated by eddies (Fig. 4.7(c)), and the ignition delay additionally increases compared to other cases. The ignition delay can be approximated as $t'/\tau_F \propto \langle S_{ij}S_{ij}\rangle^{0.57}$ for hydrogen/air cases and $t'/\tau_F \propto \langle S_{ij}S_{ij}\rangle^{0.16}$ for methane/air cases. Increasing rate of the ignition delay for hydrogen/air cases is larger than that for methane/air cases. This might be caused by the reason that total energy given at initial high temperature region is different. Since initial energy for methane/air cases is larger than that for hydrogen/air cases, the radical production required for ignition is enhanced and the ignition occurs earlier. This leads to decrease of total thermal loss caused by turbulent diffusion in the induction phase.

4.5 Effects of Turbulence on Propagation

Figures 4.9 and 4.10 show the temporal developments of distributions of heat release rate and vorticity in propagation process for C7R47 and C7R106. The heat release rate is normalized by the twice of maximum heat release rate (ΔH_L) of freely propagating laminar flame which includes no effect of flame geometry such as curvature and is approximated as one dimensional. The flame front is stretched and is disturbed its evolution by the strong eddies for both cases. The flame propagates along the edge of eddies. The high temperature region which is separated from the initial ignition kernel in the induction phase is ignited later than main kernel. This result suggests that multiple points ignition with timing difference may occur even for an initial ignition kernel in turbulence. Furthermore, the high heat release rate is observed at the flame fronts that are enclosed by the burnt gas or that are convex toward the burnt side. The high heat release rate of these flame fronts has also been reported by previous studies on statistically-planer turbulent premixed flame propagating in homogeneous turbulence [93].

Figure 4.11 shows distributions of heat release rate and vorticity in the flame propagation process for different fuel cases. The heat release rate are normalized by corresponding ΔH_L. For hydrocarbon case, the heat release rate shows the

significantly rapid rise just after the ignition and high in the whole flame elements compared to that of hydrogen and methane case. For methane case, the flame thickness is so thinner than other cases. For all cases, the high heat release rate is observed at the flame fronts that are enclosed by the burnt gas or that are convex toward the burnt side.

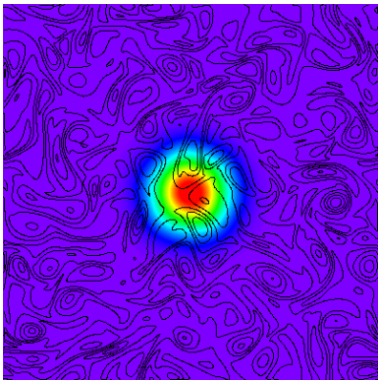

(a) $t = 0.0024$msec

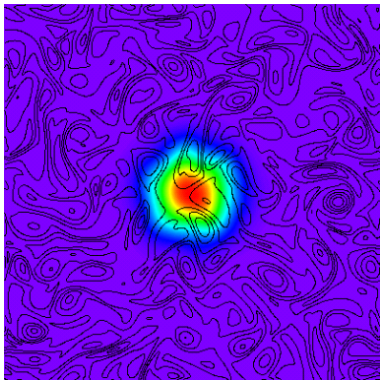

(b) $t = 0.0072$msec

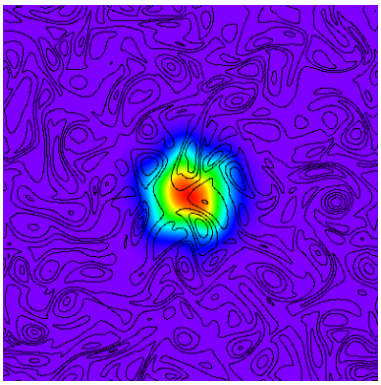

(c) $t = 0.012$msec

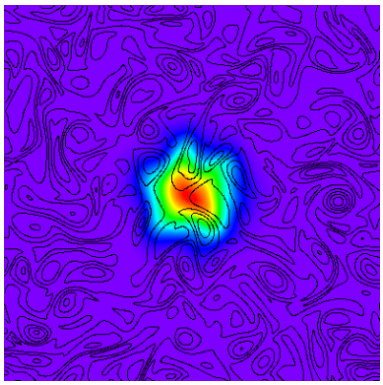

(d) $t = 0.0168$msec

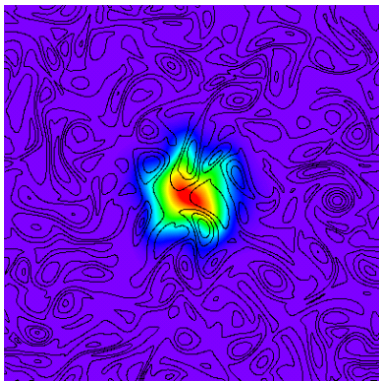

(e) $t = 0.0216$msec

Figure 4.3: Temporal developments of temperature and vorticity in induction phase for C7R47.

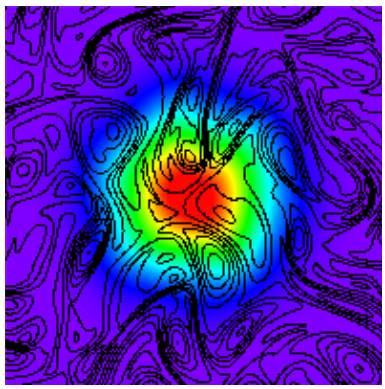

(a) $t = 0.0024$msec

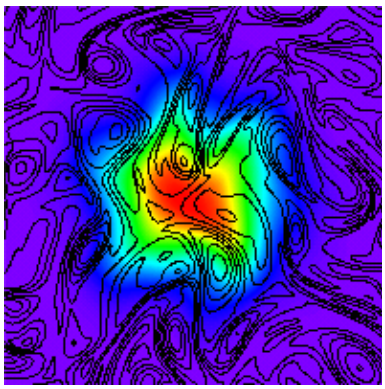

(b) $t = 0.0072$msec

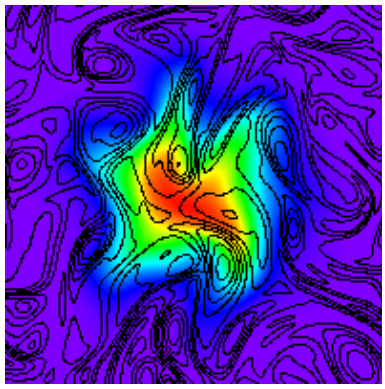

(c) $t = 0.012$msec

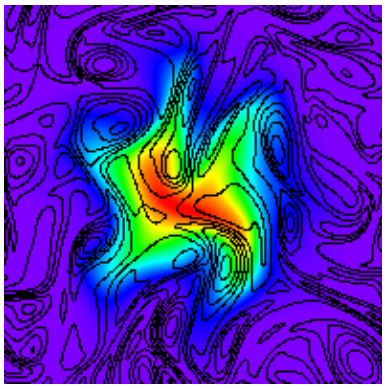

(d) $t = 0.0168$msec

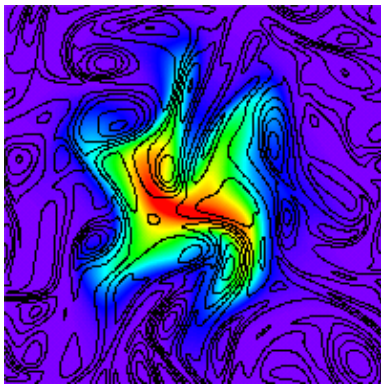

(e) $t = 0.0216$msec

Figure 4.4: Temporal developments of temperature and vorticity in induction phase for C7R106.

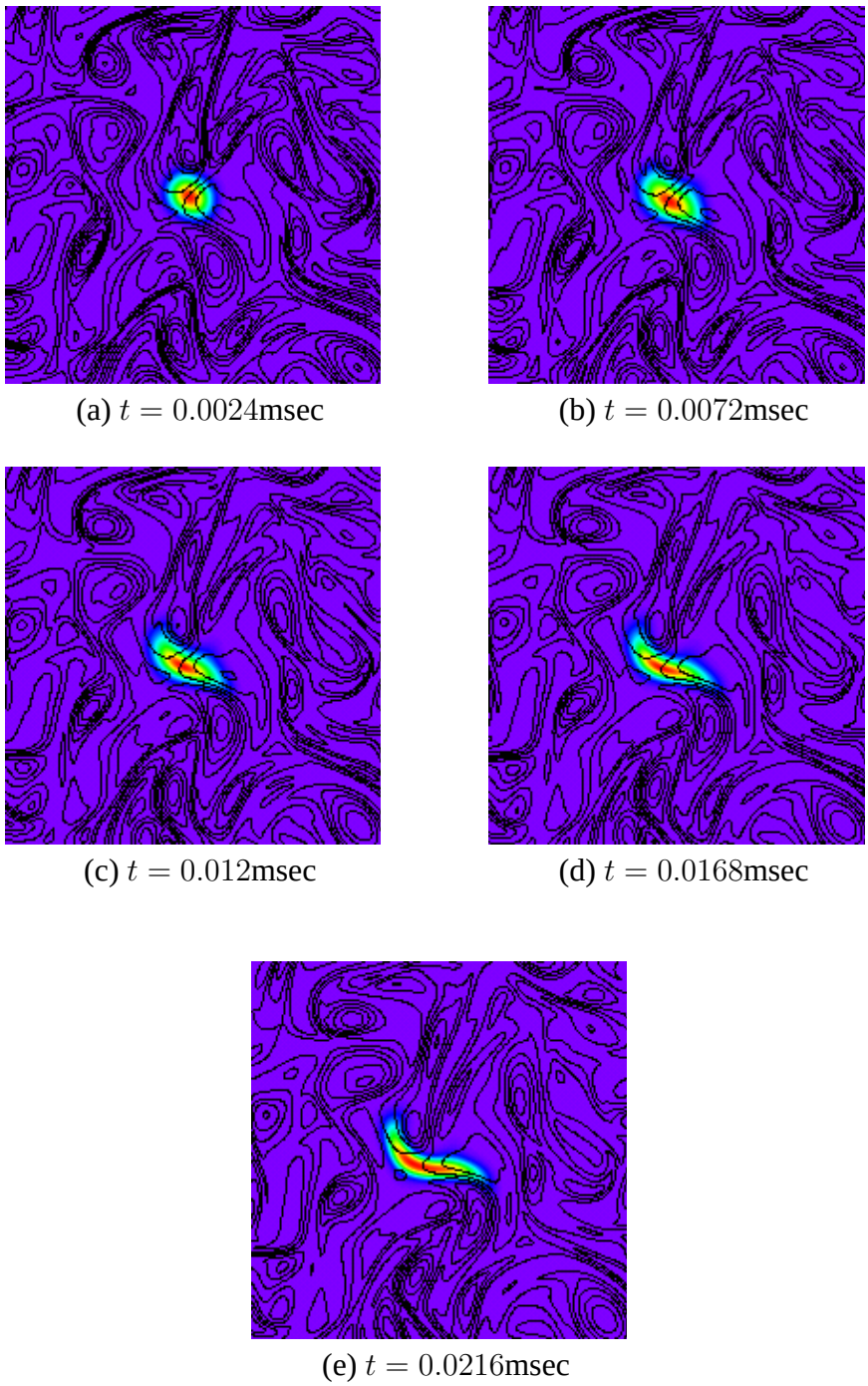

(a) $t = 0.0024$msec (b) $t = 0.0072$msec

(c) $t = 0.012$msec (d) $t = 0.0168$msec

(e) $t = 0.0216$msec

Figure 4.5: Temporal developments of mole fraction of H atom and vorticity in induction phase for C7R106.

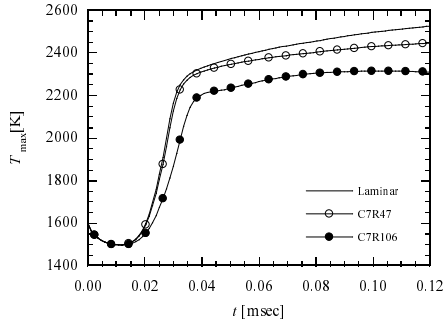

(a) C_7H_{16}

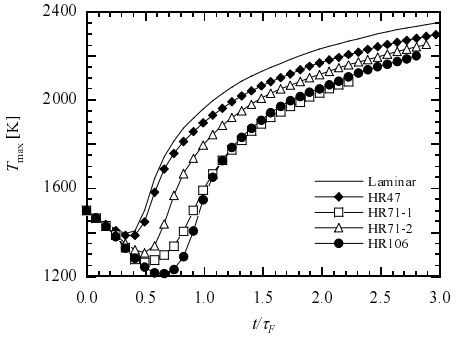

(b) H_2

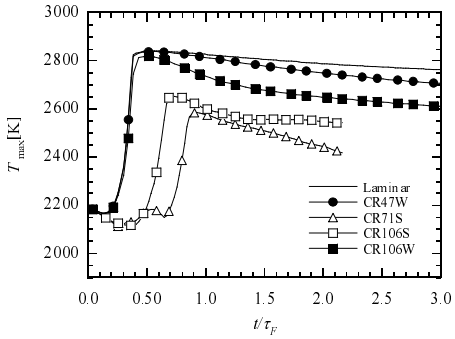

(c) CH_4

Figure 4.6: Temporal developments of maximum temperature for each fuel.

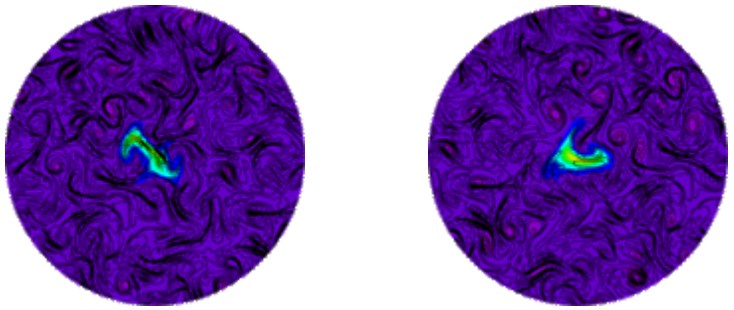

(a) HR71-1 (b) HR71-2

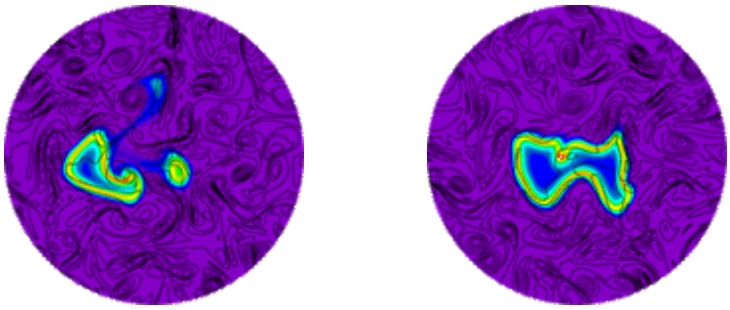

(c) HR71-1 (d) HR71-2

Figure 4.7: Distributions of temperature and vorticity in induction phase for HR71-1(a), HR71-2(b) ($t/\tau_F = 0.412$), in propagation process for HR71-1(c) and HR71-2(d) ($t/\tau_F = 1.40$).

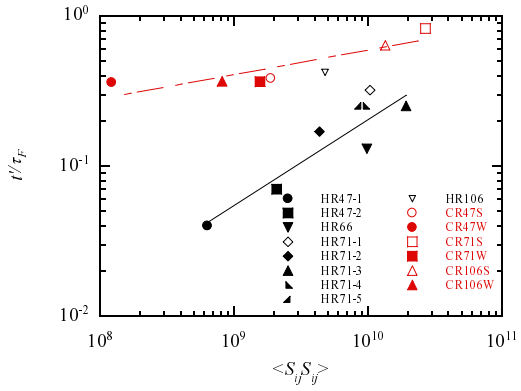

Figure 4.8: Relation between ignition delay and mean strain rate.

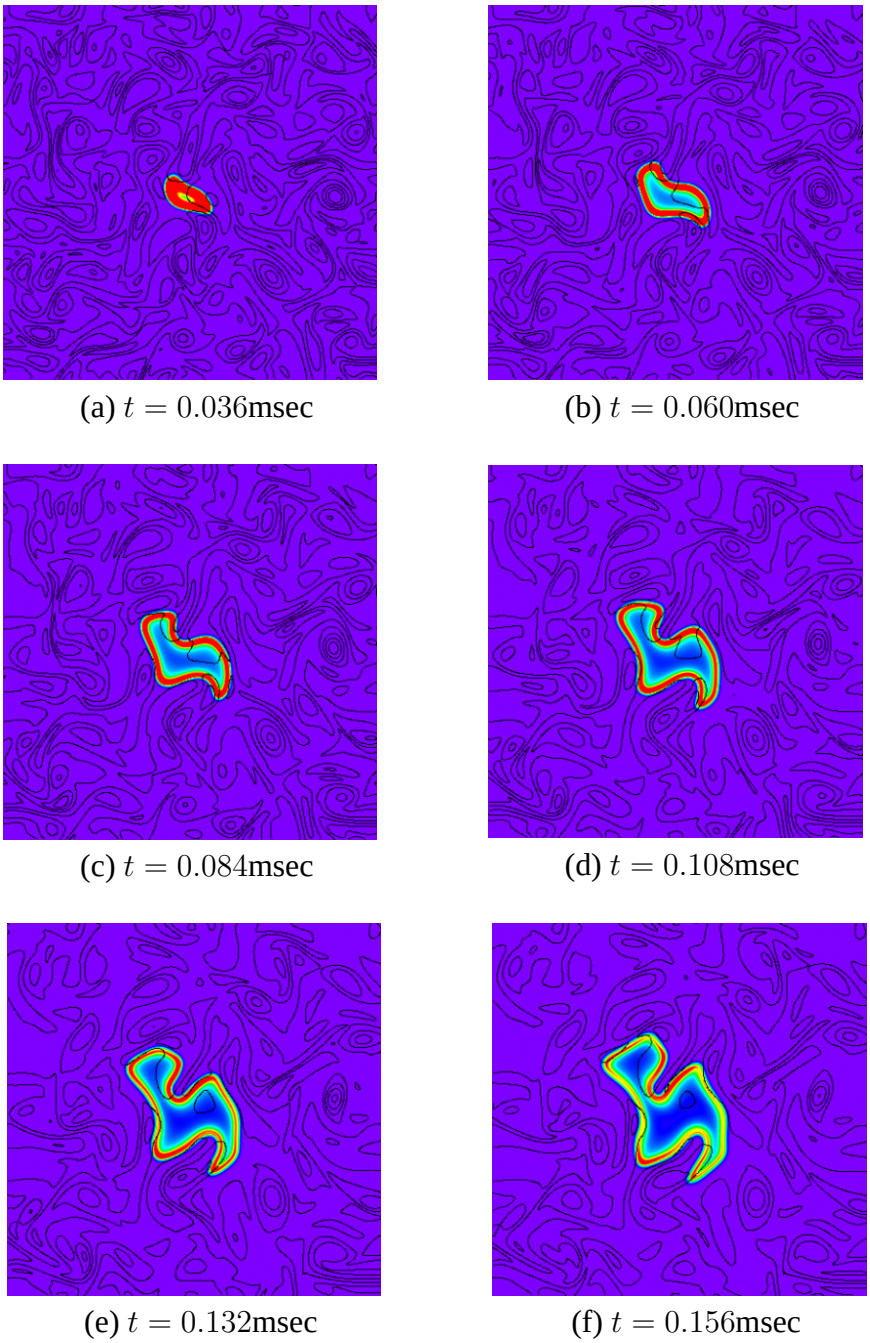

(a) $t = 0.036$msec (b) $t = 0.060$msec

(c) $t = 0.084$msec (d) $t = 0.108$msec

(e) $t = 0.132$msec (f) $t = 0.156$msec

Figure 4.9: Temporal developments of distributions of heat release rate and vorticity in propagation process for C7R47.

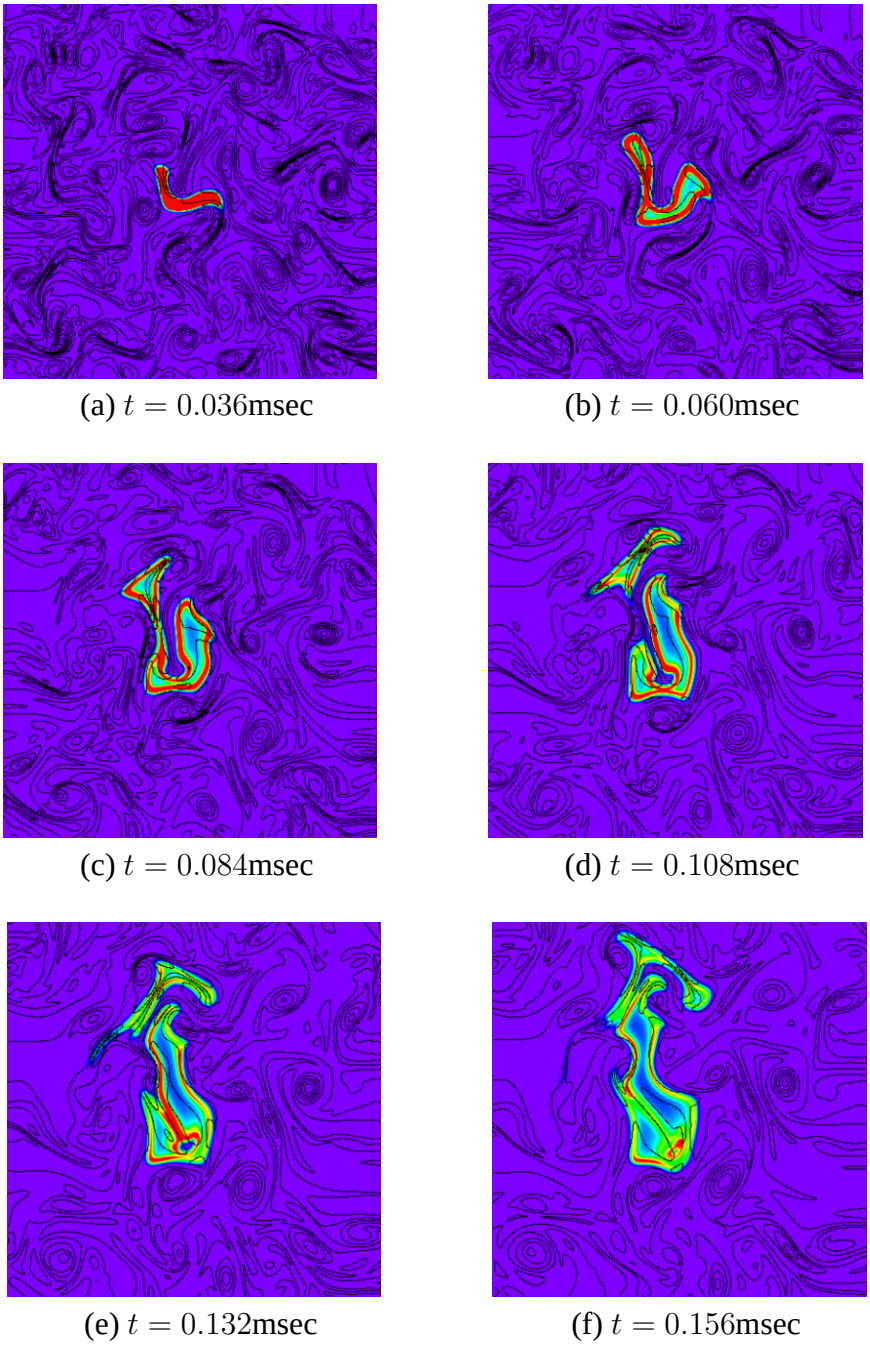

(a) $t = 0.036$msec (b) $t = 0.060$msec

(c) $t = 0.084$msec (d) $t = 0.108$msec

(e) $t = 0.132$msec (f) $t = 0.156$msec

Figure 4.10: Temporal developments of distributions of heat release rate and vorticity in propagation process for C7R106.

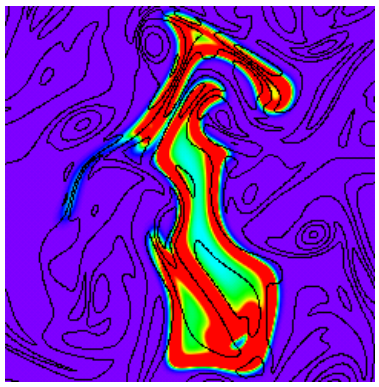

(a) C_7H_{16}

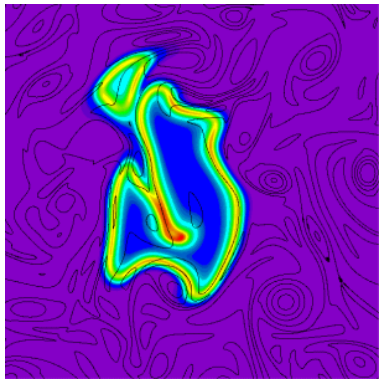

(b) H_2

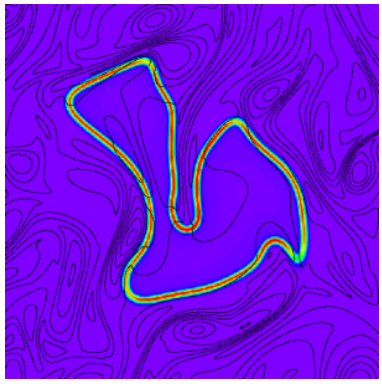

(c) CH_4

Figure 4.11: Distributions of heat release rate and vorticity in propagation process for each fuel.

Chapter 5

Ignition of n-Heptane Vapor in Turbulence

5.1 Preface

There are numerous studies about spray combustion [108][109][110][111], which are from basic ones to applications on actual machine, because it has been adopted to practical combustors for a long time. However, the design of industrial spray combustors has been conducted based on the empirical rule yet. As mentioned in chapter 1, this is because the phenomena in spray combustion are very complex, since it consists of several processes such as atomization, dispersion of the fuel droplets, their evaporation, vapor mixing and ignition. Besides they simultaneously proceed with interaction between each other. It is very difficult to measure each of the elemental process by experiments, so expectations for numerical simulations have been raised with developments of computational science and technology.

In numerical simulations of spray combustion of practical combustors including dispersion and evaporation of fuel droplets, Reynolds Averaged Navier-Stokes Simulation (RANS), which uses the averaged model represented by $k - \epsilon$ model, has been adopted for small computational cost. Although good agreement has been obtained for some averaged quantities with the use of these averaged models, there are essential limitations for simulation of unsteady phenomena, such as the

interaction between droplets and eddies. LES of spray combustion has also been conducted, and good results are achieved for not only averaged but also fluctuate quantities [112][113][114][115]. In LES, it is essentially impossible to clarify the relationship between spray combustion and turbulent structure in combustors, since LES cannot resolve fine scales in turbulence. To resolve the fine scale structures in turbulence and investigate the relationship between spray combustion and them, DNS, which does not use any turbulence model, is needed.

The group of Cant et al. conducted three-dimensional DNS of spark ignition in a homogeneous isotropic turbulent field with n-heptane evaporating droplets [116][117]. They investigated temporal development of structure of the ignition kernel for different sizes of droplets and the ignition kernel. They also conducted DNS of spark ignition in a mixing layer. The phenomena of ignition and flame propagation were analyzed with various sizes and volatility of the fuel droplets [118]. Wang and Rutland studied evaporation and ignition in a two-dimensional homogeneous isotropic turbulent field and a jet flow with n-heptane evaporating droplets by DNS [119][120]. The air temperature and the equivalent ratio were used for a parametric study of these DNS. Xia and Luo studied diluted combustion using DNS in a three-dimensional temporally developing reacting shear-layer with an oxidizer stream laden with evaporating droplets [123]. In their DNS, the initial Stokes number and the mass loading ratio were changed as parameters, and they showed that evaporating droplets enhance micro mixing and combustion under certain conditions. Luo et al. investigated n-heptane spray flames in a swirl combustor by three-dimensional DNS [121][122][124]. They analyzed the flame structure, the evaporation rate and the relationship between the mixture fraction and the scalar dissipation rate with the geometry, inflow condition and equivalent ratio as parameters. The group of Réveillon et al. performed two-dimensional DNS of spray jet flames and discussed the phenomena of spray combustion in terms of the topology of the droplet group combustion regimes and the partially premixed model [125][126][127][128][129]. Baba and Kurose conducted two-dimensional DNS of spray jet flames, and they investigated the combustion char-

acteristics to validate a steady-flamelet model and a flamelet/progress-variable approach [130]. They showed that their modified flamelet/progress-variable approach was superior to the other combustion models, particularly for the spray flames, by comparing the DNS results obtained with various combustion models.

In this chapter, to clarify the relationship between ignition in spray combustion and the coherent fine scale eddies, DNS of homogeneous isotropic turbulence with evaporating n-heptane droplets under high temperature condition has been conducted by using a reduced kinetic mechanism and considering dependence of the transport and thermal properties on temperature.

5.2 Numerical Method

5.2.1 Governing Equations

The equations of droplet motion and evaporation are the same as those of chapter 3. The governing equations of gas phase are the continuity equation, the compressible Navier-Stokes equations and the conservation equations of energy and chemical species including coupling terms with dispersed phase as follows;

$$\frac{\partial \rho}{\partial t} + \frac{\partial \rho u_i}{\partial x_i} = S_{\mathrm{I}}, \tag{5.1}$$

$$\frac{\partial \rho u_i}{\partial t} + \frac{\partial \rho u_i u_j}{\partial x_j} = -\frac{\partial \tau_{ij}}{\partial x_j} + S_{\mathrm{II},i}, \tag{5.2}$$

$$\frac{\partial \rho E_t}{\partial t} + \frac{\partial}{\partial x_i}(\rho u_i E_t) = -\frac{\partial q_i}{\partial x_i} - \frac{\partial \tau_{ij} u_i}{\partial x_j} + S_{\mathrm{III}}, \tag{5.3}$$

$$\frac{\partial \rho Y_k}{\partial t} + \frac{\partial}{\partial x_i}(\rho u_i Y_k) = -\frac{\partial}{\partial x_i}(\rho Y_k V_{k,i}) + \omega_k + S_{\mathrm{IV},k}. \tag{5.4}$$

These equations and phase coupling terms are the same as those of chapter 3 except for equations of chemical species. In the equations of chemical species, reaction rate term ω_k is added in this DNS.

From the same assumptions in chpater 4, the governing equations can be written as follows:

· The continuity equation:

$$\frac{\partial \rho}{\partial t} + \frac{\partial \rho u_i}{\partial x_i} = S_{\mathrm{I}}. \tag{5.5}$$

· The compressible Navier-Stokes equations:

$$\frac{\partial \rho u_i}{\partial t} + \frac{\partial \rho u_i u_j}{\partial x_j} = -\frac{\partial \tau_{ij}}{\partial x_j} + S_{\mathrm{II},i}. \tag{5.6}$$

· The energy conservation equation:

$$\begin{aligned}
&\frac{\partial \rho T}{\partial t} + \frac{\partial \rho u_i T}{\partial x_i} = \frac{1}{\bar{c_v}} \frac{\partial}{\partial x_i} \lambda \frac{\partial T}{\partial x_i} - \frac{1}{\bar{c_v}} \sum_{k=1}^{N} (\rho Y_k V_{k,i}) c_{p,k} \frac{\partial T}{\partial x_i} \\
&- \frac{T}{\bar{c_v}} \sum_{k=1}^{N} \left[R_k \frac{\partial}{\partial x_i} (\rho Y_k V_{k,i}) \right] - \frac{1}{\bar{c_v}} \tau_{ij} \frac{\partial u_i}{\partial x_j} - \frac{1}{\bar{c_v}} \sum_{k=1}^{N} h_k \omega_k + \frac{T}{\bar{c_v}} \sum_{k=1}^{N} R_k \omega_k \\
&+ \left(T + \frac{1}{2\bar{c_v}} u_i u_i \right) S_{\mathrm{I}} - \frac{1}{\bar{c_v}} h_V S_{\mathrm{IV},k} - \frac{1}{\bar{c_v}} u_i S_{\mathrm{II},i} + \frac{1}{\bar{c_v}} S_{\mathrm{III}} \\
&- \frac{1}{\bar{c_v}} \sum_{k=1}^{N} h_k S_{\mathrm{IV},k} + \frac{T}{\bar{c_v}} \sum_{k=1}^{N} R_k S_{\mathrm{IV},k} + \frac{1}{\bar{c_v}} h_V \frac{\partial}{\partial x_i} (\rho Y_V V_{V,i}) - \frac{1}{\bar{c_v}} h_V \omega_V.
\end{aligned} \tag{5.7}$$

· The species conservation equations:

$$\frac{\partial Y_k}{\partial t} + u_i \frac{\partial Y_k}{\partial x_i} = -\frac{1}{\rho} \frac{\partial}{\partial x_i} (\rho Y_k V_{k,i}) + \frac{1}{\rho} S_{\mathrm{IV},k} - \frac{Y_k}{\rho} S_{\mathrm{I}} + \frac{\omega_k}{\rho}. \tag{5.8}$$

The ideal-gas equation of state is

$$p = \rho R^0 T \sum_{k=1}^{N} \left(\frac{Y_k}{W_k} \right), R_k = \frac{R^0}{W_k}. \tag{5.9}$$

Diffusion velocity $V_{k,i}$ is represented by the diffusion velocity of species k in mixture (D_{mk}),

$$V_{k,i} = -\frac{1}{X_k} D_{mk} \frac{\partial X_k}{\partial x_i} \tag{5.10}$$

The specific heat of the gas mixture at constant volume $\bar{c_v}$ is

$$\bar{c_v} = \sum_{k=1}^{N} c_{v,k} Y_k, \tag{5.11}$$

where $c_{v,k}$ denotes the specific heat at constant volume for species k.

Numerical methods for chemical reaction and calculation methods for thermodynamic properties and transport coefficients are the same as those of chapter 4.

5.2.2 Numerical Procedure and Numerical Conditions

The spectral method is used to discretize the gas-phase governing equations and aliasing errors from nonlinear terms in the governing equations are fully removed by the 3/2 rule. Time advancement is conducted by a third-order Runge-Kutta scheme. Here, the reaction terms are handled implicitly, using a point implicit method (ref. Appendix B). The equations for droplets are solved with a second-order Adams-Bashforth scheme. The fluid velocity and the other physical quantities at the droplet position are estimated by a fourth-order Lagrange interpolation.

Fully-developed homogeneous isotropic turbulence which was obtained from preliminary DNS is used as the initial velocity field. DNS is conducted for $Re_\lambda = 60.1$ with $128 \times 128 \times 128$ grid points. The statistics of the initial flow fields are shown in Table 5.1. The computational domain is selected to be 5 mm^3. The initial positions of droplets are assumed to be random, and their initial velocities are supposed to be equal to the fluid velocity at their positions.

Gas and liquid phases are supposed to be composed of air and n-heptane, respectively. The ignition in n-heptane/air mixture is simulated using a reduced kinetic mechanism, which includes 61 elementary reactions and 37 reactive species [134](ref. Appendix A). The initial pressure and the temperature of carrier gas are 10 atm and 1500 K. The initial temperature of droplet is 300 K. The physical properties of the droplet are shown in Table 5.2 [59].

The initial Stokes number and the number of the droplets are shown in Table 5.3. In this chapter, the initial Stokes number is determined to be the most significant preferential concentration in droplet dispersion, based on the results in chapter 3. The number of droplets is determined so that the equivalent ratio

becomes $\phi = 0.5$ at the time when all droplets evaporate. The mass loading ratio is 0.0324.

Table 5.1: Statistics of the initial flow filed.

Re_λ	l [mm]	λ [mm]	η[mm]	u_{rms} [m/s]
60.1	0.793	0.239	0.0156	6.12

Table 5.2: Physical properties of n-heptane droplet.

Density (ρ_L)	649.38 [kg/m^3]
Latent heat (L_V)	219215.2 [J/K]
Heat capacity (C_L)	2383.89 [J/kgK]
Boiling temperature (T_B)	475.95 [K]

Table 5.3: Numerical conditions.

Case	τ_{d0} [s]	$St_{\eta 0}$	$St_{\lambda 0}$	St_{l0}	St_{c0}	D_{d0} [μm]	N_d
SL1	1.01*10^{-5}	1.00	0.259	0.0780	0.150	4.00	453477

Table 5.4: Species in reactions mechanism of this study.

No.	Species	No.	Species
1	C_7H_{16}	21	CH_3CO
2	C_7H_{15}	22	CH_3O
3	$C_7H_{15}O_2$	23	CH_3
4	$C_7H_{14}O_2H$	24	CH_2O
5	$C_7H_{14}O_2HO_2$	25	CO_2
6	C_7KET21	26	CO
7	C_6H_{12}	27	O_2
8	$C_5H_{11}CO$	28	OH
9	C_5H_{11}	29	O
10	C_4H_9	30	H_2O_2
11	C_3H_8	31	H_2O
12	C_3H_7	32	HO_2
13	C_3H_6	33	H_2
14	C_3H_5	34	HCO
15	C_3H_4	35	H
16	C_2H_6	36	CH_4
17	C_2H_5	37	N_2
18	C_2H_4		
19	C_2H_3		
20	CH_3CHO		

5.3 Temporal Developments in Ignition

5.3.1 Temporal Developments of Droplet Characteristics and Gas Phase

Figure 5.1 shows temporal development of the averaged value of the square of the droplet diameter $\langle D^2 \rangle$ normalized by its initial value $\langle {D_0}^2 \rangle$. The square of the droplet diameter linearly decreases, which follows the d^2-law, after the short preheat period. The value of $\langle D^2 \rangle / \langle {D_0}^2 \rangle$ is about 0.7 at $t^+ = 0.19 \sim 0.23$. Figure 5.2 shows development of r.m.s. of velocity difference between the droplet and the fluid at the droplet position. As the initial velocities of droplets were set equal to the fluid velocities at the droplets positions, velocity difference increases with time in the initial period. In the period of temperature increase (Fig. 5.2(a)), the velocity difference shows a peak and nearly constant. Here, slight increase of the velocity difference is observed at about $t^+ = 0.20$. Since such an increase was not observed in the previous results (Figs. 2.2 and 3.3), the effect of gas dilatation on droplets behavior causes this increase. Although the influence of the initial condition may remain from the result of r.m.s. of the velocity difference at $t^+ = 0.23$, the droplets already tend to localize around the coherent fine scale eddy (Figs. 5.19 and 5.20) at this time. This distribution is similar to that of the previous chapters which were analyzed at time when there was no influence of the initial condition. In addition, the number of the droplets is so large and their initial position is random. From these points, the time of analysis is considered to be adequate.

Figure 5.3 shows temporal developments of temperature and heat release rate. In the temperature development, the maximum temperature, the mean temperature and the minimum temperature are plotted. In the heat release rate development, the maximum heat release rate and the mean heat release rate are plotted, and these heat release rates are normalized by the maximum heat release rate in zero-dimensional n-heptane/air ignition whose initial pressure is 10 atm, initial temperature is 1500 K and equivalent ratio is 0.5. From the developments of the

mean and minimum temperature, it is observed that the gas temperature deceases until about $t^+ = 0.18$. This reason is the heat transfer from the flow filed to the droplets and the latent heat of evaporation. At about $t^+ = 0.18$, the maximum temperature rapidly increases from 1500 K to 2000 K. On the other hand, the mean and minimum temperature increase more modestly at later time than maximum temperature. This difference represents that ignition does not occur in all flow field uniformly, but occurs in various region locally. The maximum heat release rate increases at earlier time than that of temperature, it reaches 40 % of zero-dimensional ignition. As the same of temperature, the mean heat release rate increases very modestly. It indicates that the state of ignition is significantly different at each local point.

Figures 5.4 and 5.5 show temporal developments of mass fraction of major species. In each species, maximum and mean values are plotted. The mass fraction of C_7H_{16} increases with time advancement due to the evaporation of fuel droplet, it reaches about 0.036 in maximum one. From the development of the mean mass fraction of C_7H_{16}, it decreases from $t^+ = 0.14$ after showing a peak. This means that the reaction of C_7H_{16} becomes beyond the evaporation in the gas field, and the mass fraction decreases to zero from this time. At $t^+ = 0.23$, the mass fraction of C_7H_{16} becomes about zero, so all C_7H_{16} generated by the fuel droplet evaporation are consumed through reaction. From the development of the maximum mass fraction of CO_2, the mass fraction rapidly increases at about $t^+ = 0.18$, but the increase of the mean mass fraction is slight. Whereas, the mass fraction of intermediate OH begins to increase at about $t^+ = 0.14$. The increase rate is quite small compared to that of CO_2. The maximum OH mass fraction rapidly increases from $t^+ = 0.20$. The increase rate is larger than that of CO_2. From Fig. 5.5, the mass fraction of H and O begins to increase at $t^+ = 0.10$, it means that the reaction of C_7H_{16} also begins at this time. The increase of mass fraction of CO begins a bit later than these of H and O, since the production of CO occurs at the advanced stage of the oxidization reaction of C_7H_{16}.

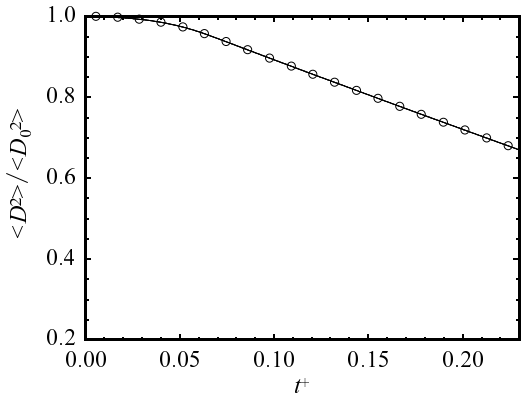

Figure 5.1: Temporal developments of the normalized droplet diameter squared.

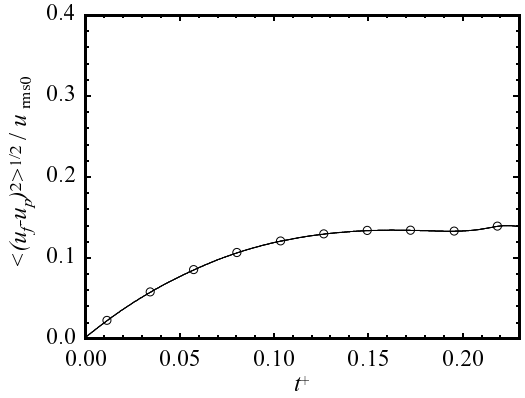

Figure 5.2: Temporal developments of the velocity difference between the droplet and the fluid.

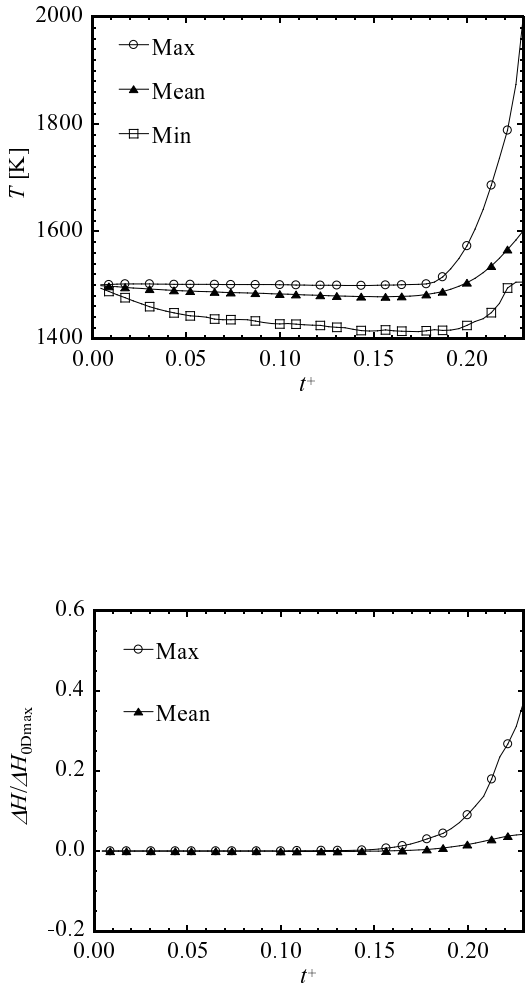

Figure 5.3: Temporal developments of temperature and heat release.

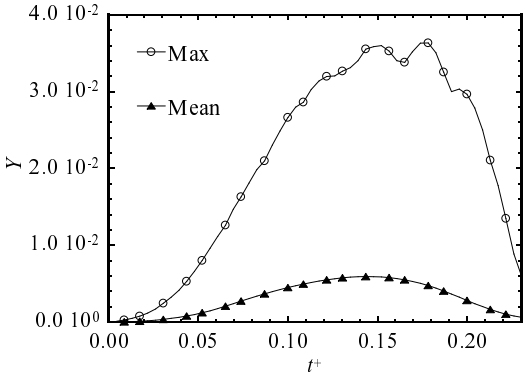

C_7H_{16}

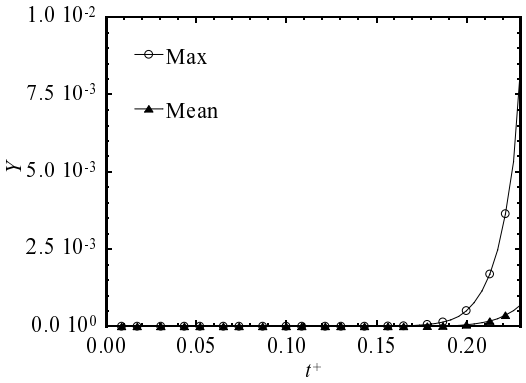

CO_2

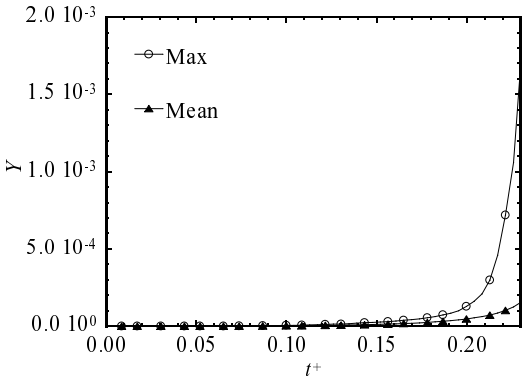

OH

Figure 5.4: Temporal developments of mass fraction of major species.

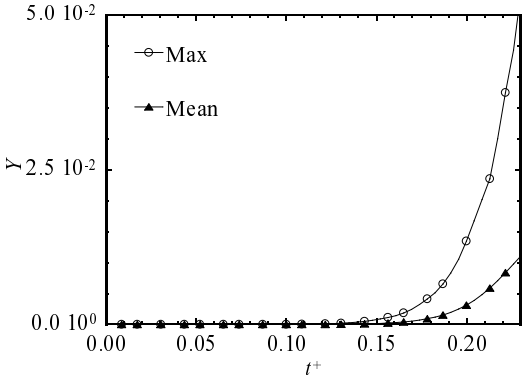

CO

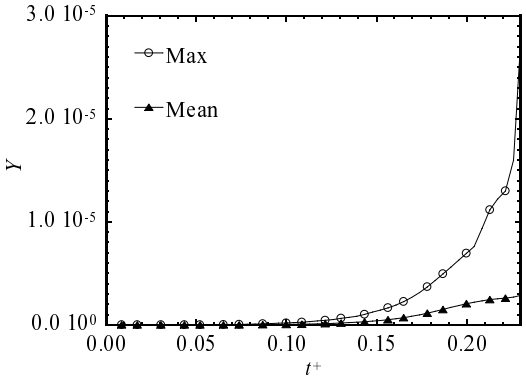

H

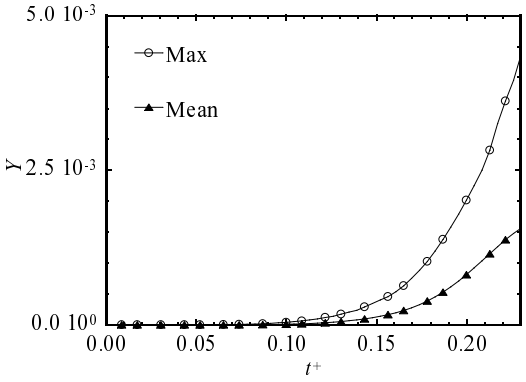

O

Figure 5.5: Temporal developments of mass fraction of major species.

5.3.2 Temporal Developments of Distributions on a Typical Cross-section

Figures 5.6-5.14 show the temporal developments of distributions of temperature, heat release rate and major species on a typical cross-section.

From the temperature distribution at $t^+ = 0.174$, there are many low temperature regions, which is caused by heat transfer and the latent heat by evaporation before temperature increases by reaction. The increase of temperature begins at $t^+ = 0.192 \sim t^+ = 0.209$, and the region where temperature increases is like streaky at $t^+ = 0.209$. The rate of temperature increase at the region where reaction had begun at $t^+ = 0.209$ is higher than other regions. It is considered that these regions become primary ignition points.

Temporal developments of heat release distribution show that heat release rate begins to increase at $t^+ = 0.14 \sim t^+ = 0.15$, and increased region is like fine streaky same as temperature distribution. These local fine streaky regions are expanded to all flow field, then the high heat release rate regions are observed in most parts of flow field at $t^+ = 0.226$. From Figs. 5.8 and 5.9, C_7H_{16} concentration increases through the fuel droplet evaporation. The distribution shows the small scale fluctuation in whole flow field caused by preferential concentration of droplet dispersion, as mentioned in chapter 3. The concentration of C_7H_{16} reaches peak at $t^+ = 0.14$, then it decreases for reaction of C_7H_{16} in ignition. Although reaction and evaporation is occurring simultaneously, almost C_7H_{16} has disappeared at $t^+ = 0.226$, because time scale of reaction is shorter than that of production by evaporation. Here, it is noted that all primary ignition do not occur at regions where C_7H_{16} concentration is high, compared to the distributions between Fig. 5.7 and Fig. 5.9. From Figs. 5.10 and 5.11, the distributions of products, CO_2, and reactant, O_2, are contradictory for increase and decrease of species. Figures 5.12-5.14 shows temporal developments of distributions of mass fraction of intermediate species. Although the regions where species concentration becomes high are nearly same, the rates of increase are different from each species. Since H

species is produced at initial stage in decomposition reaction of C_7H_{16}, its concentration begins to increase at $t^+ = 0.174$. On the other hand, the concentrations of OH and CO significantly increase at $t^+ = 0.209 \sim t^+ = 0.226$.

5.3.3 Statistical Characteristics in Ignition

Figures 5.15-5.18 show PDFs of heat release rate, temperature and major species at $t^+ = 0.192 \sim t^+ = 0.226$. Circle and solid line represent PDFs of these values at droplet position and from whole flow field.

The probabilities of heat release rate at droplet position are slightly larger than that of whole flow field. This tendency becomes more significant with time. In particular, high heat release rate is observed at droplet position at $t^+ = 0.226$. Since the range of PDF of heat release rate is extended at $t^+ = 0.226$, the ignition level is obviously different in various regions. From the PDF of temperature, low temperature is observed at droplet position at $t^+ = 0.192$ compared to that of whole flow field, because of heat transfer to droplet and the latent heat by evaporation. At $t^+ = 0.209$, PDF at droplet position nearly coincide with that of whole flow field. As is the case with heat release rate, temperature at droplet position is higher than that of whole flow field at $t^+ = 0.226$, and the range of PDF becomes extended.

Temporal development of the probabilities of C_7H_{16} shows the concentration decreases with time for decomposition reaction, and the difference between PDF at droplet position and that of whole flow field becomes smaller. From the PDF of mass fraction of O_2, the low concentration region spreads with time, especially at droplet position. The maximum concentration is nearly constant for these times. For the probabilities of CO_2, OH, CO and H, these species are generated over reaction, and the tendency of temporal development of PDFs are similar to that of heat release rate.

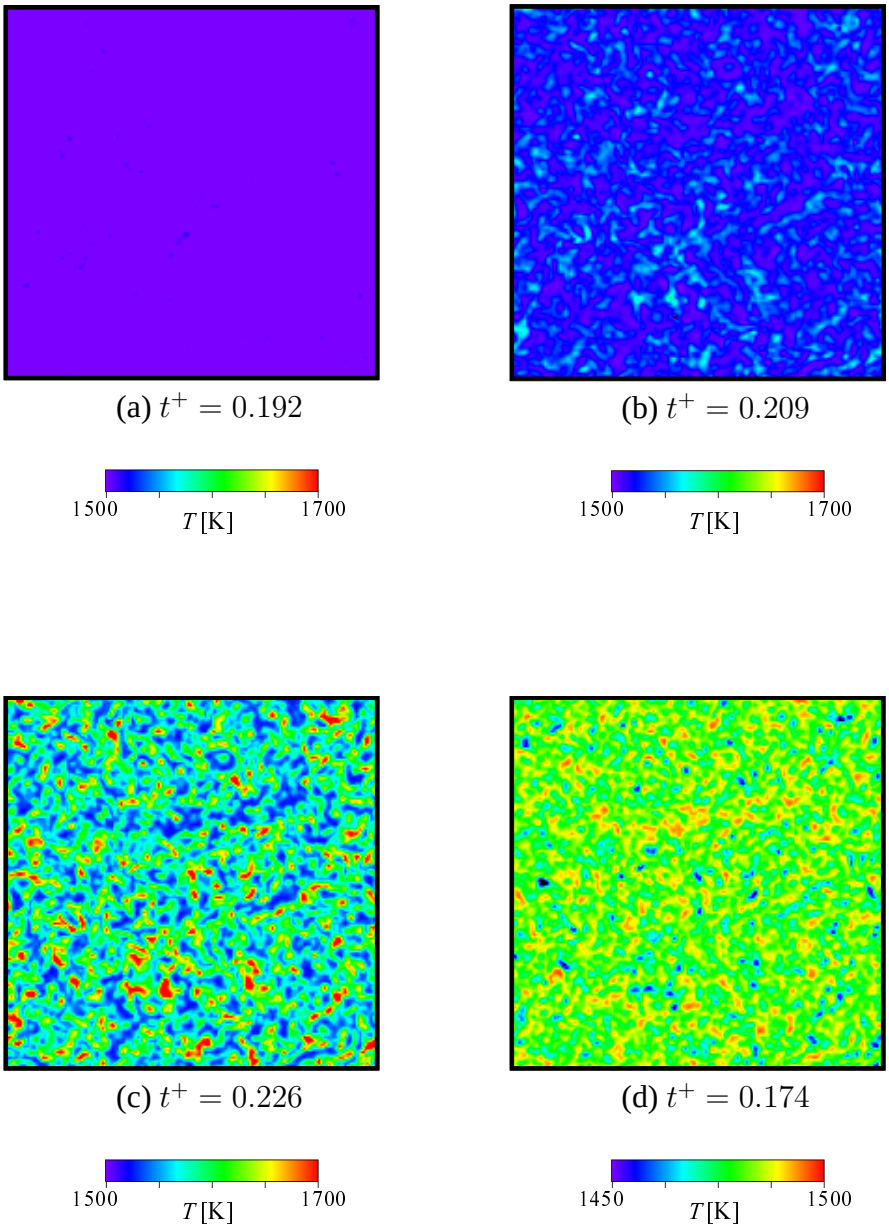

(a) $t^+ = 0.192$ (b) $t^+ = 0.209$

(c) $t^+ = 0.226$ (d) $t^+ = 0.174$

Figure 5.6: Temporal developments of distributions of temperature.

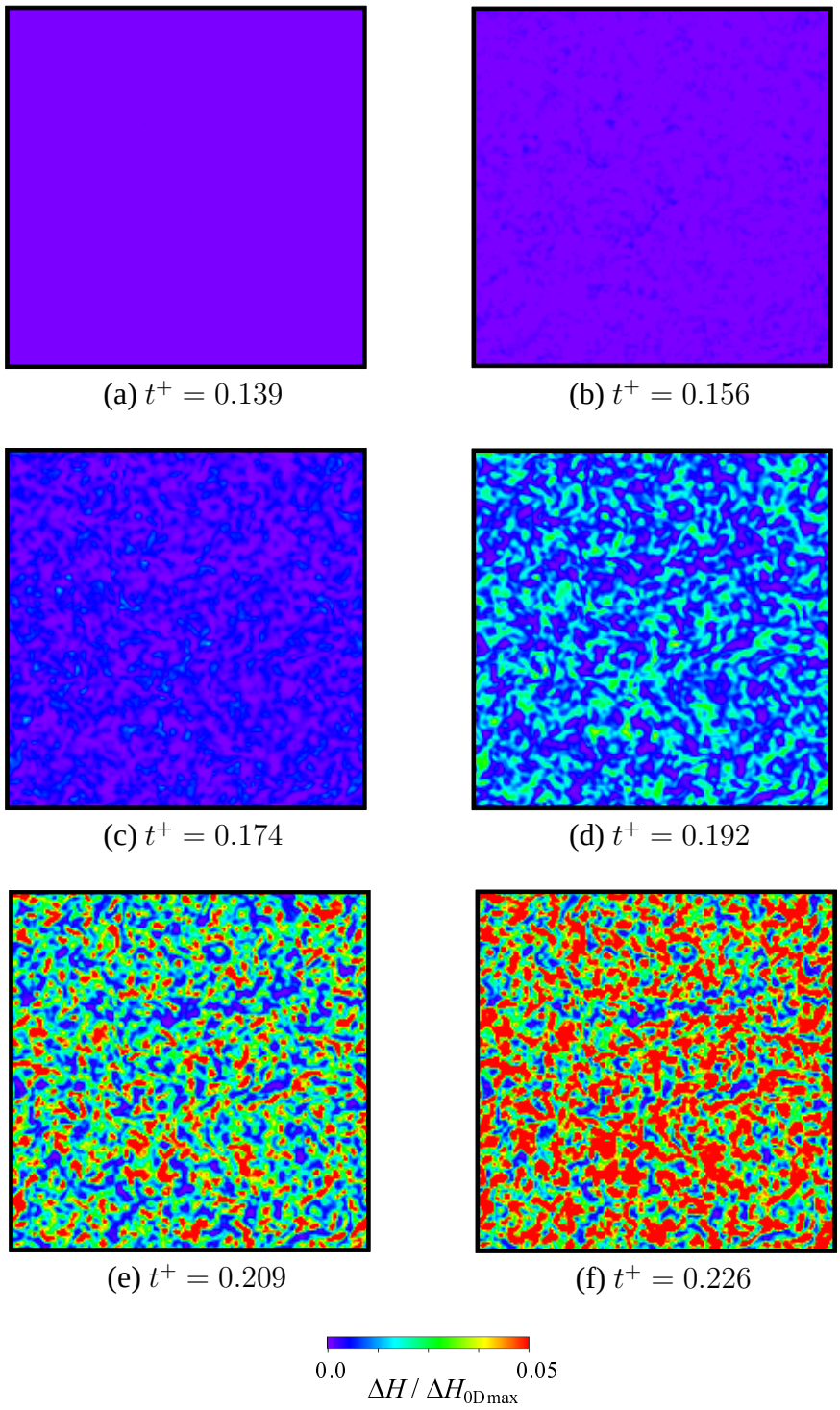

(a) $t^+ = 0.139$ (b) $t^+ = 0.156$

(c) $t^+ = 0.174$ (d) $t^+ = 0.192$

(e) $t^+ = 0.209$ (f) $t^+ = 0.226$

Figure 5.7: Temporal developments of distributions of heat release rate.

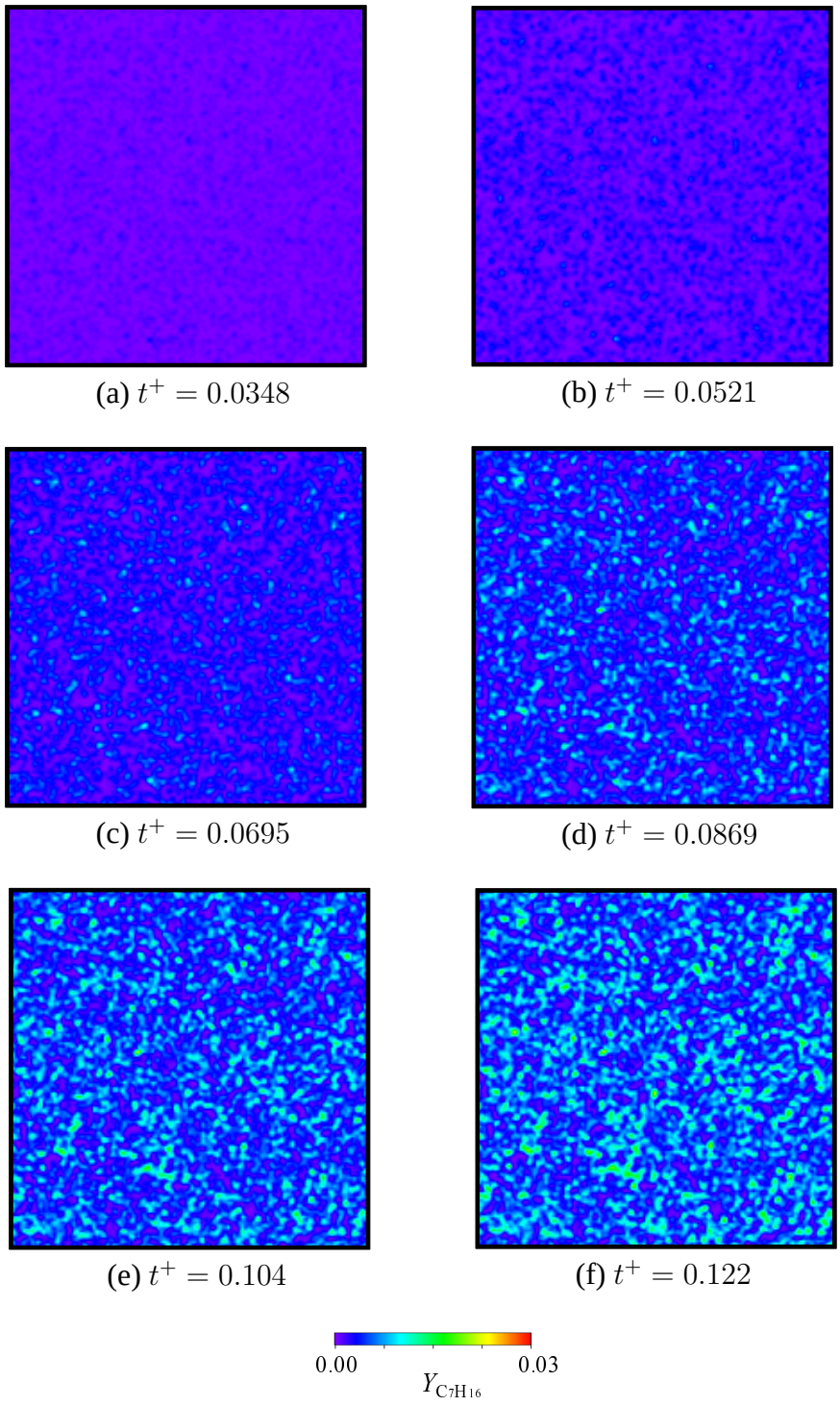

(a) $t^+ = 0.0348$ (b) $t^+ = 0.0521$

(c) $t^+ = 0.0695$ (d) $t^+ = 0.0869$

(e) $t^+ = 0.104$ (f) $t^+ = 0.122$

Figure 5.8: Temporal developments of distributions of mass fraction of C_7H_{16}.

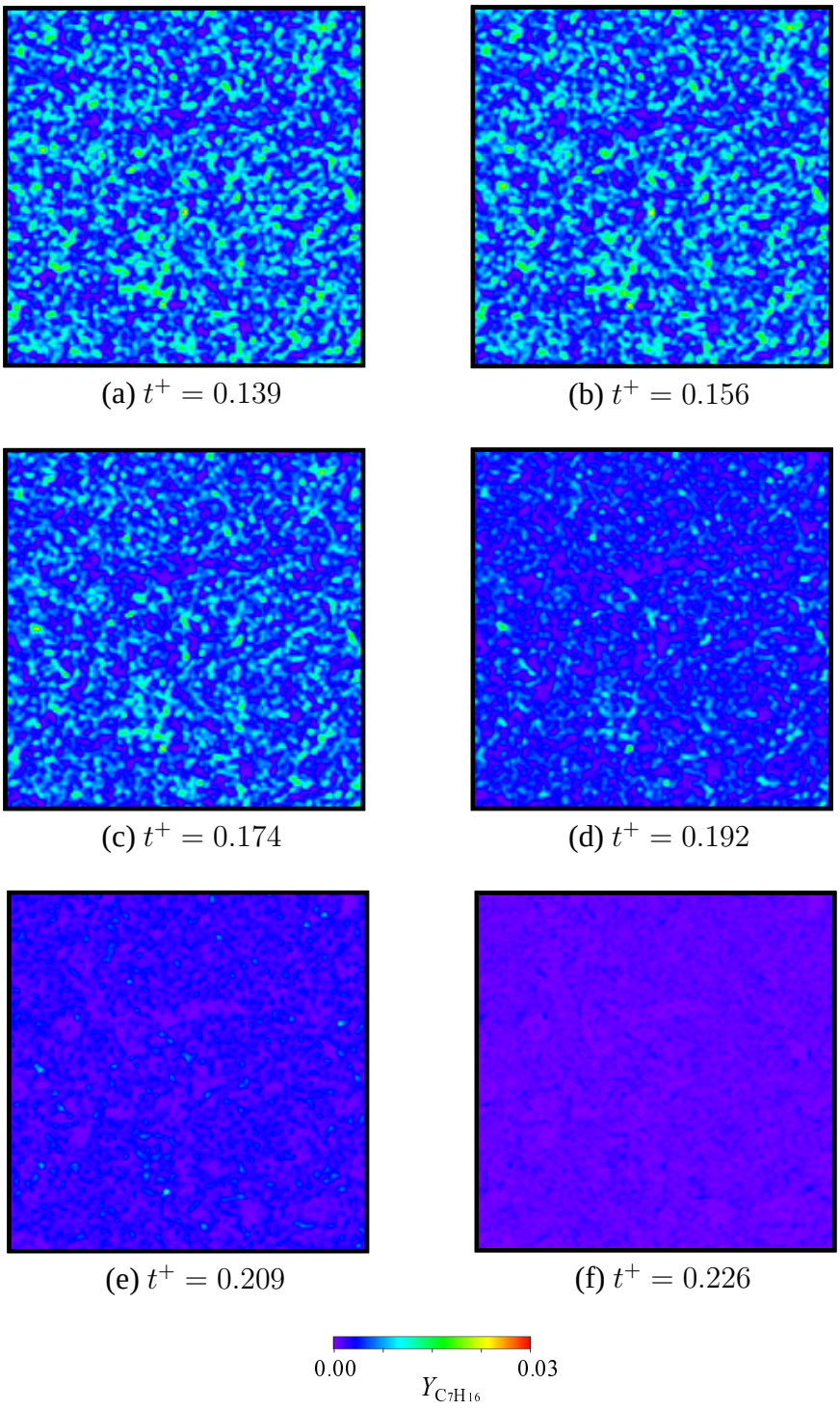

(a) $t^+ = 0.139$ (b) $t^+ = 0.156$

(c) $t^+ = 0.174$ (d) $t^+ = 0.192$

(e) $t^+ = 0.209$ (f) $t^+ = 0.226$

Figure 5.9: Temporal developments of distributions of mass fraction of C_7H_{16}.

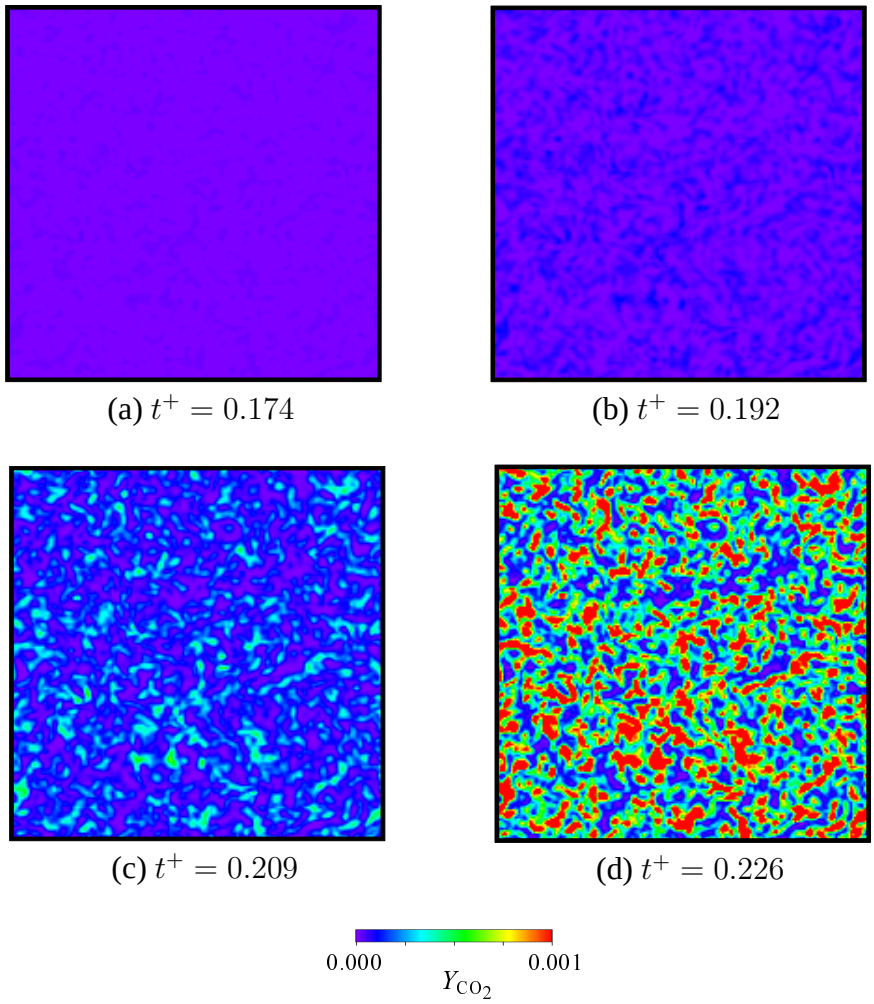

(a) $t^+ = 0.174$ (b) $t^+ = 0.192$

(c) $t^+ = 0.209$ (d) $t^+ = 0.226$

Figure 5.10: Temporal developments of distributions of mass fraction of CO_2.

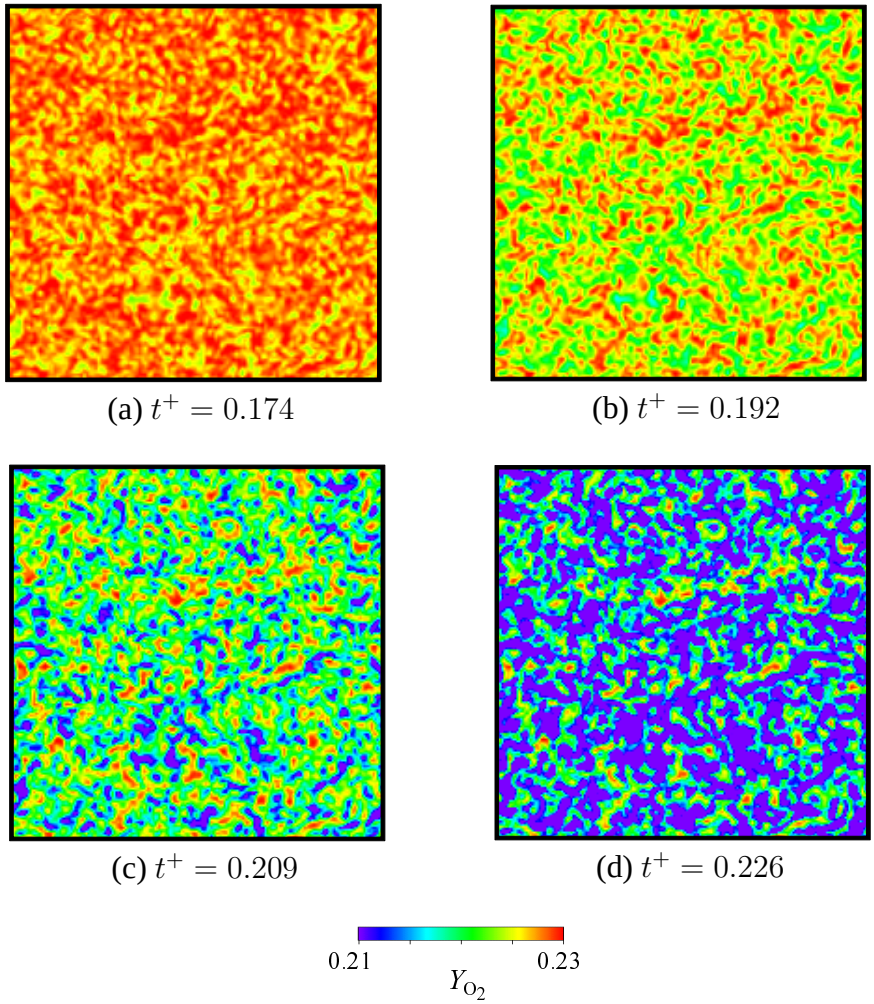

(a) $t^+ = 0.174$ (b) $t^+ = 0.192$

(c) $t^+ = 0.209$ (d) $t^+ = 0.226$

Figure 5.11: Temporal developments of distributions of mass fraction of O_2.

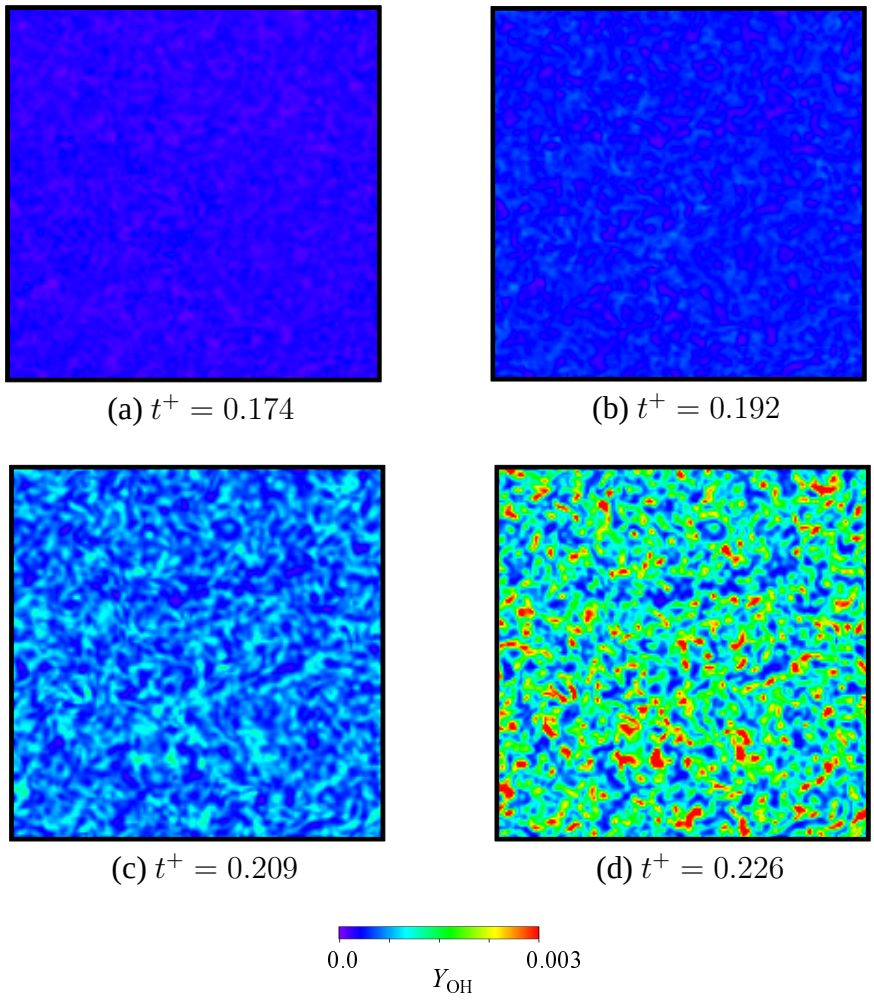

(a) $t^+ = 0.174$ (b) $t^+ = 0.192$

(c) $t^+ = 0.209$ (d) $t^+ = 0.226$

Figure 5.12: Temporal developments of distributions of mass fraction of OH.

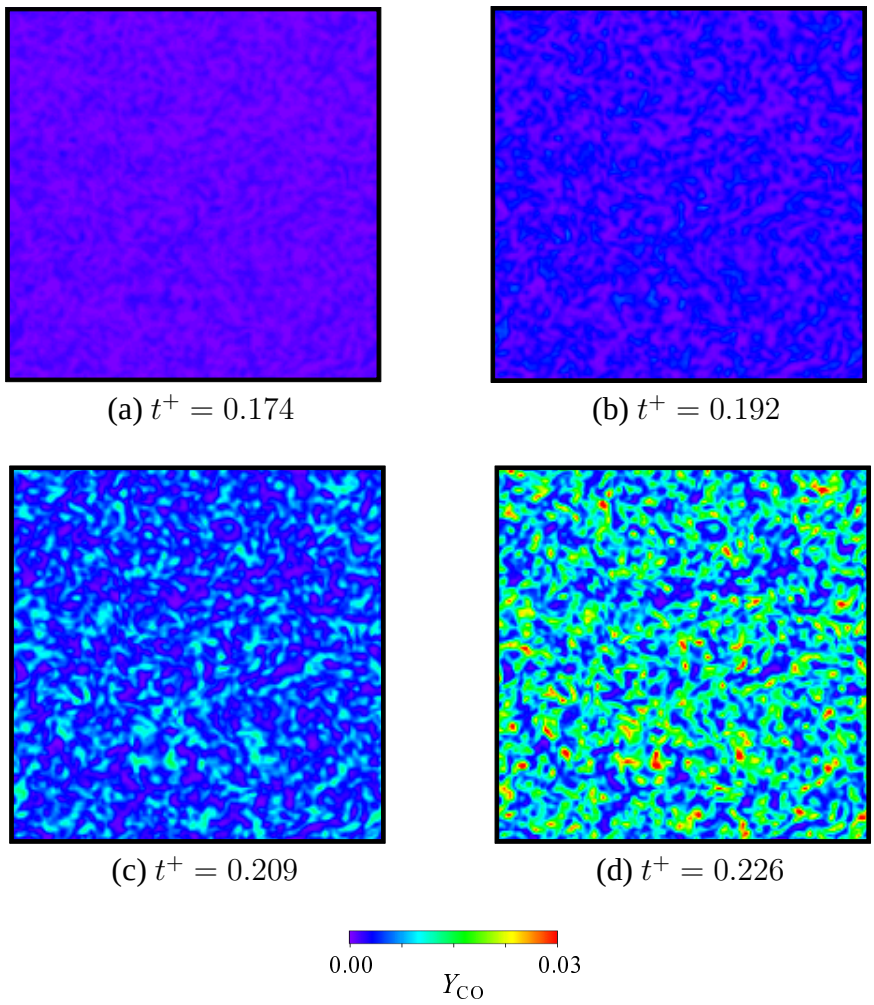

(a) $t^+ = 0.174$ (b) $t^+ = 0.192$

(c) $t^+ = 0.209$ (d) $t^+ = 0.226$

Figure 5.13: Temporal developments of distributions of mass fraction of CO.

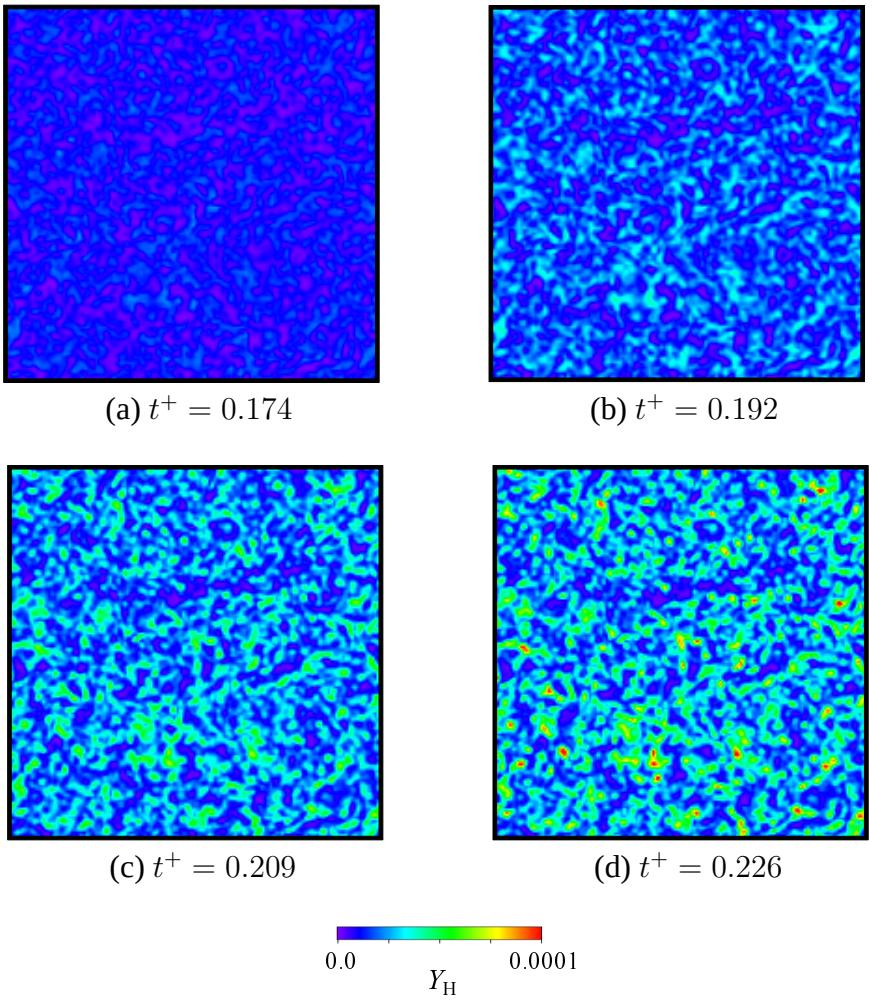

(a) $t^+ = 0.174$ (b) $t^+ = 0.192$

(c) $t^+ = 0.209$ (d) $t^+ = 0.226$

Figure 5.14: Temporal developments of distributions of mass fraction of H.

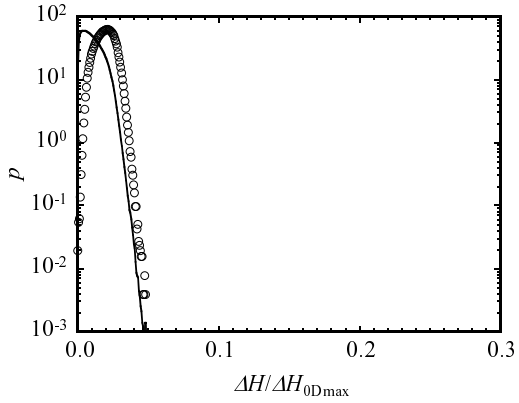

(a) $t^+ = 0.192$

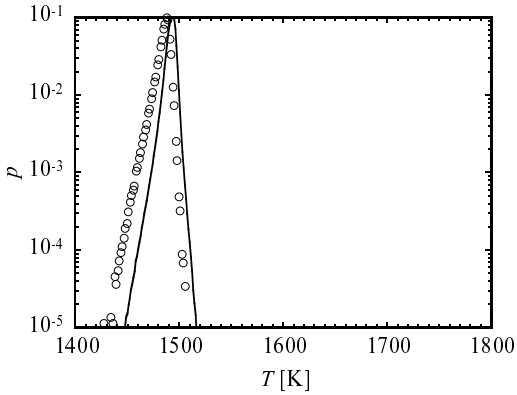

(a) $t^+ = 0.192$

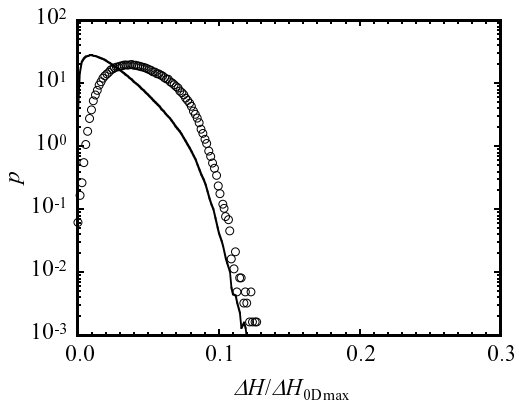

(b) $t^+ = 0.209$

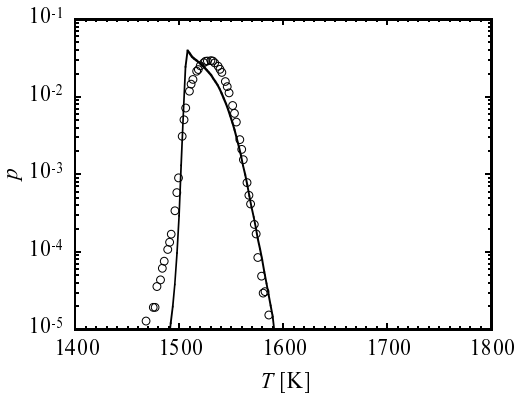

(b) $t^+ = 0.209$

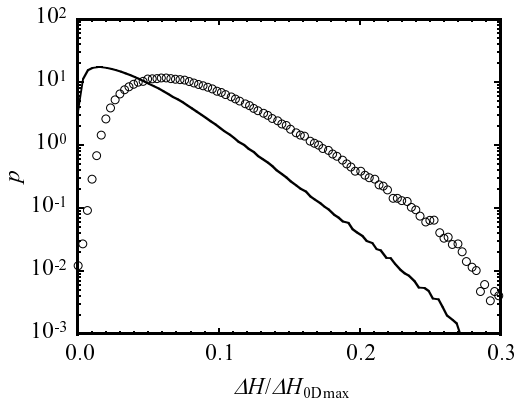

(c) $t^+ = 0.226$

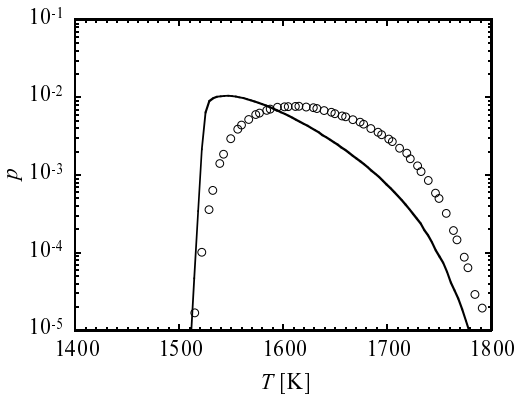

(c) $t^+ = 0.226$

Figure 5.15: PDF of heat release rate (left) and temperature (right) at droplet position. Solid lines represent PDF of whole flow field.

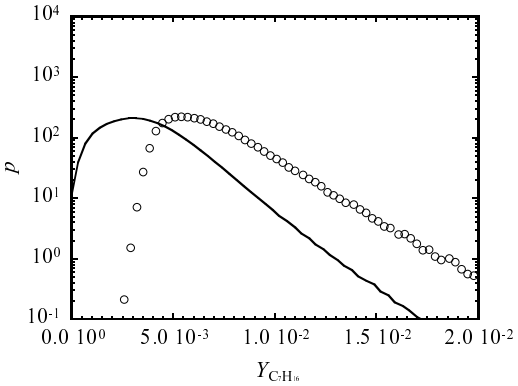

(a) $t^+ = 0.192$

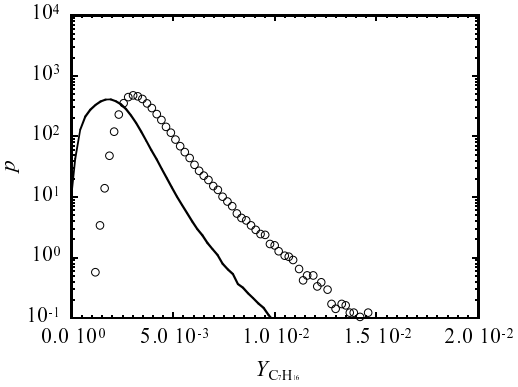

(b) $t^+ = 0.209$

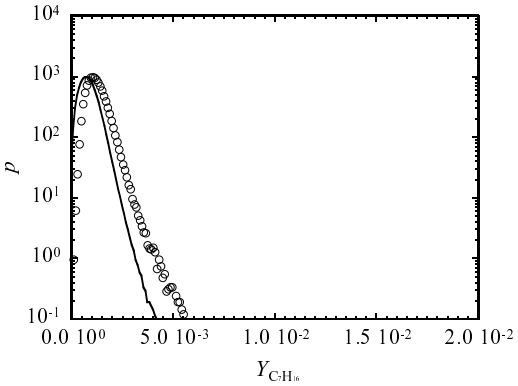

(c) $t^+ = 0.226$

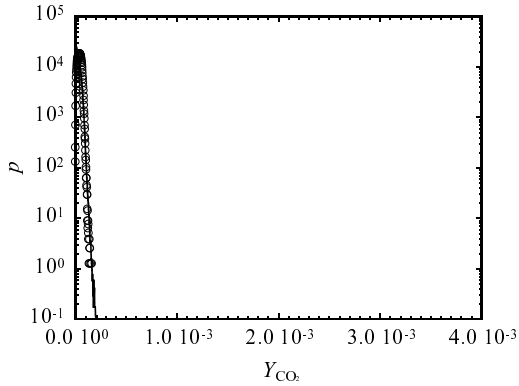

(a) $t^+ = 0.192$

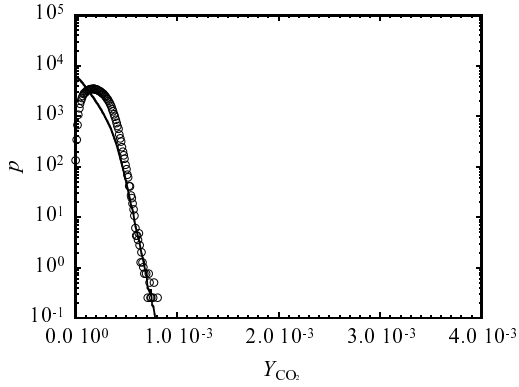

(b) $t^+ = 0.209$

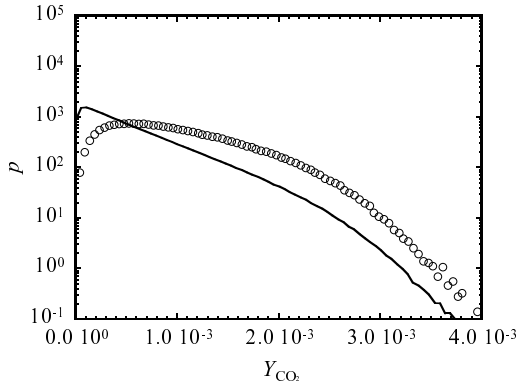

(c) $t^+ = 0.226$

Figure 5.16: PDF of mass fraction of C_7H_{16} (left) and CO_2 (right) at droplet position. Solid lines represent PDF of whole flow field.

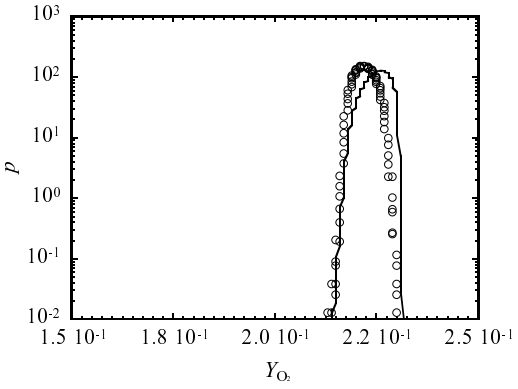

(a) $t^+ = 0.192$

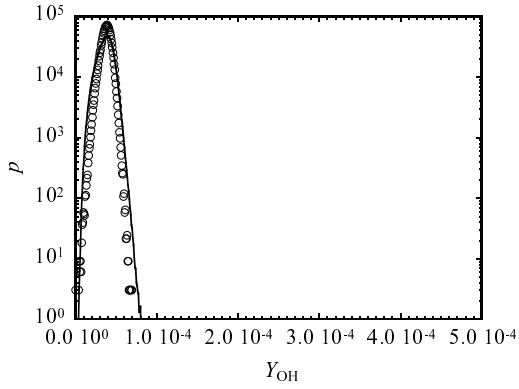

(a) $t^+ = 0.192$

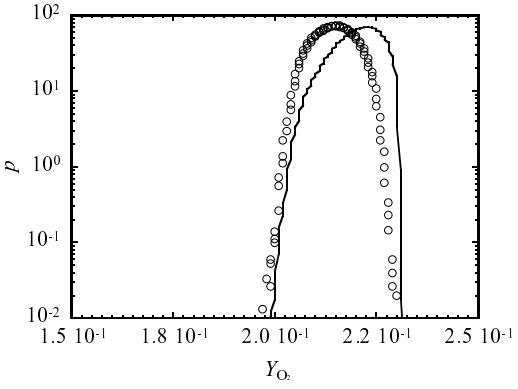

(b) $t^+ = 0.209$

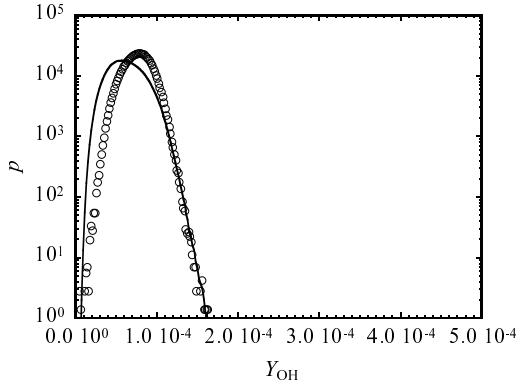

(b) $t^+ = 0.209$

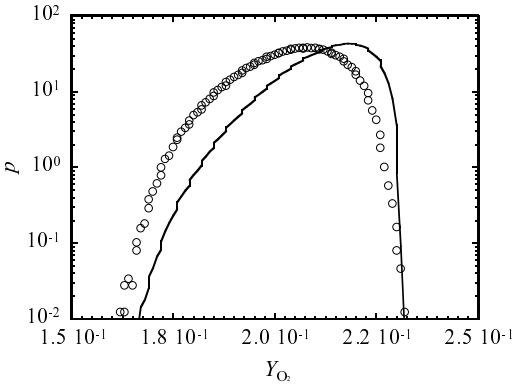

(c) $t^+ = 0.226$

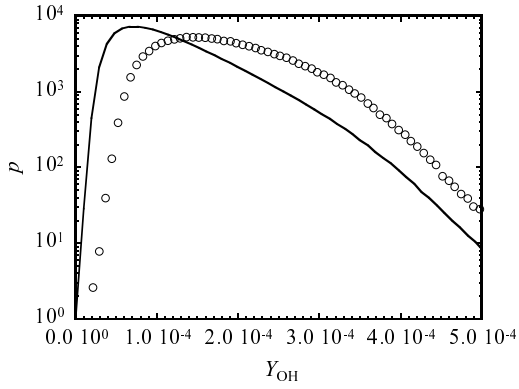

(c) $t^+ = 0.226$

Figure 5.17: PDF of mass fraction of O_2 (left) and OH (right) at droplet position. Solid lines represent PDF of whole flow field.

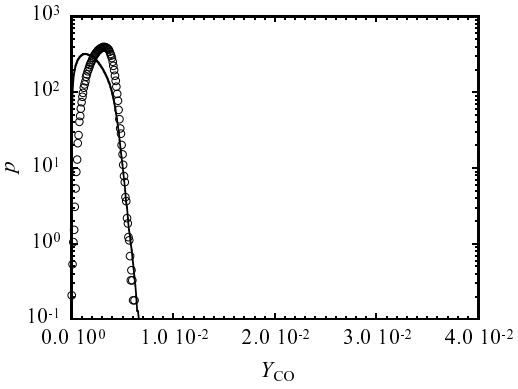

(a) $t^+ = 0.192$

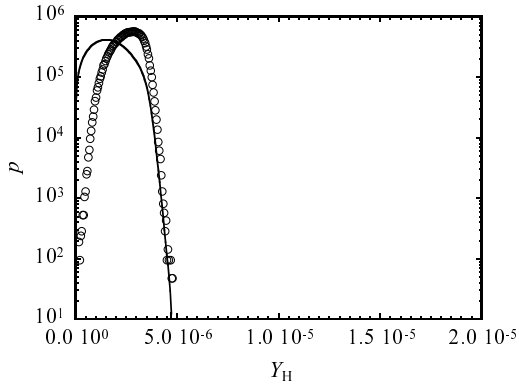

(a) $t^+ = 0.192$

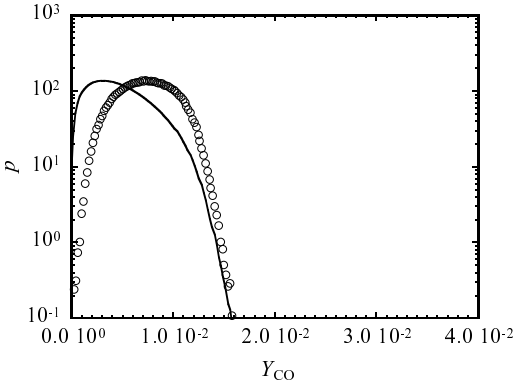

(b) $t^+ = 0.209$

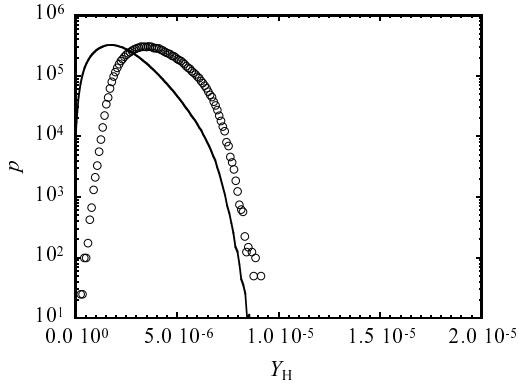

(b) $t^+ = 0.209$

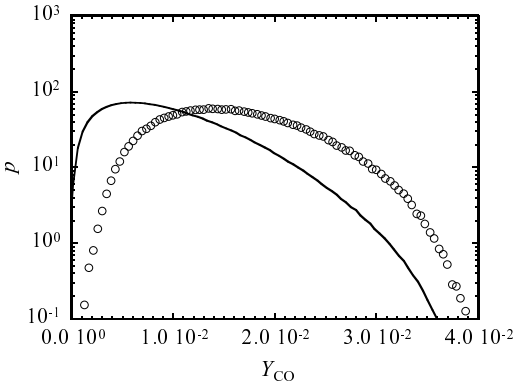

(c) $t^+ = 0.226$

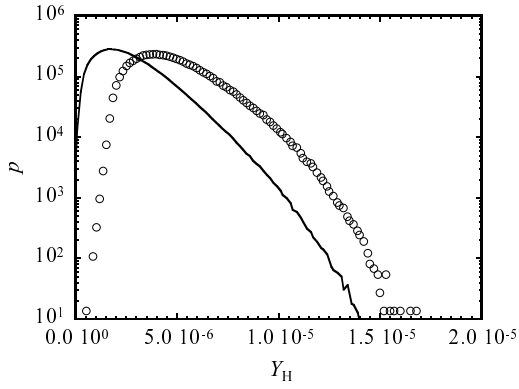

(c) $t^+ = 0.226$

Figure 5.18: PDF of mass fraction of CO (left) and H (right) at droplet position. Solid lines represent PDF of whole flow field.

5.4 Vapor Concentration and Ignition in Fine Scale

5.4.1 Temporal Developments of Ignition in Fine Scale

Figure 5.19 shows number density of droplet around the coherent fine scale eddies at $t^+ = 0.226$. Here, radial distance (r) and number density (N) are normalized by radius of fine scale eddy (r_c) and mean number density in all domain (N_0), respectively. Number density is low near the center of fine scale eddies, and increase with distance from the center and reaches the maxima at about $r = 1.5r_c$. Although the computational time may not be enough for the statistical analysis, the profile of number density is similar to that of previous chapters. Figure 5.20 shows temporal developments of phase-averaged distributions of number density of droplet on the plane perpendicular to the axis of the coherent fine scale eddy. In these figures, number density is normalized by mean number density in all domains. The method of phase-averaging is the same in previous chapters. The number density shows a minimum value at the center of the coherent fine scale structure. The number density increases with distance from the center and is high around the major axis. These tendencies are similar to the previous ones. It is noted that shape of distribution near the center of the coherent fine scale structure changes with time. The details of this change are discussed in more depth later.

In this analysis, the Kolmogorov scale and Kolmogorov velocity is used of mean value of whole flow field at each time. The change of physical property and dilatation influence the local structure of flow field. Although the Kolmogorov scale and Kolmogorov velocity should be determined at local position, these influences are considered to be small comparatively in the analysis times, which are early period of ignition.

Figure 5.21 shows isosurfaces of temperature and the distribution of axis of the coherent fine scale eddy with droplets at $t^+ = 0.226$. Figure 5.22 shows temperature distribution and isosurfaces of temperature around a typical axis of the coherent fine scale eddy. It is clearly observed that the high temperature regions are localized around the axis of the coherent fine scale eddy. In addition, many

small ignition cores are observed.

Figures 5.23-5.26 show temporal developments of phase-averaged distributions of heat release rate, temperature and major species on the plane perpendicular to the axis of the coherent fine scale eddies. In these figures, the values of distributions represent the fluctuation from the value at center of each fine scale eddy.

The distributions of heat release rate show that it becomes high at the region where the distance is about $2.0r_c$ from the center on the major axis. In addition, the heat release rate becomes high on the upper and under side of the center in these figures. The heat release rate increases with time in these regions. From the distributions of temperature at $t^+ = 0.192$, the temperature is the highest at the center of eddy, and lower around the center. The droplets are localized around the center (Fig. 5.20), heat transfer to the droplets and the latent heat of evaporation makes the temperature lower. At $t^+ = 0.209$, the temperature increases around the center in accordance with the increase of heat release rate. Especially, at the region on the upper and under side of the center, this tendency is significant.

The distribution of C_7H_{16} concentration at $t^+ = 0.192$ is similar to Fig. 3.19(d). The C_7H_{16} concentration shows a minimum value at the center of the coherent fine scale structure, and increases with distance from the center and show the maxima on the major axis. The mass fraction decreases with time for reaction, and has nearly consumed on the plane of the coherent fine scale eddies at $t^+ = 0.226$. On the other hands, CO_2 is generated with time. The high concentration region coincides with the high temperature region at $t^+ = 0.226$. From the distributions of O_2 concentration, the concentration is the highest at the center of eddy, and lower around the center because of reaction with C_7H_{16} at high C_7H_{16} concentration region. In the region, O_2 has consumed and the concentration becomes lower with time.

Temporal developments of distributions of OH, CO and H concentration show similar pattern to that of heat release rate. Here, the timing of increase is different for each species. The H concentration already increases around the center of eddy

at $t^+ = 0.192$. Subsequently, the CO concentration increases around the center of eddy at $t^+ = 0.209$. In this time, the fluctuation is small on the plane for OH concentration and the concentration rapidly increases at $t^+ = 0.226$.

For each distribution, the shape near the center has changed with time. At $t^+ = 0.192$, the shape of distribution near the center is like elliptical, then it is deformed to like gourd-shaped at $t^+ = 0.209 \sim t^+ = 0.226$. From the distribution of temperature, there are high temperature regions upper and under side of the center of the eddy. The eddy is compressed by dilatation of fluid at these regions, and the shape of center of the eddy has changed. Figure 5.27 shows temporal developments of phase-averaged distributions of the second invariant of the velocity gradient tensor on the plane perpendicular to the axis of the coherent fine scale eddies. At $t^+ = 0.192$, the shape of distribution near the center is clear elliptical, and nearly coincides with that in previous chapter (Fig. 2.23(a)). With time advancement, the ellipse changes to shape which is compressed from upper and under.

5.4.2 Influence on the Coherent Fine Scale Eddy by Ignition

Figures 5.28 and 5.29 show individual distributions of the second invariant of the velocity gradient tensor, azimuthal velocity and temperature on the plane perpendicular to the axis of the coherent fine scale eddies at $t^+ = 0.226$. From the distribution of the second invariant and temperature, it is clearly observed that temperature does not increase at the regions where the second invariant is negative. This is because the reaction is prevented by high energy dissipation rate in these regions as shown in chapter 4.

In chapter 2, it is shown that particles with particular Stokes number are localized around the coherent fine scale eddies, especially at the high energy dissipation rate region on the plane perpendicular to the axis of the coherent fine scale eddies. Additionally, in chapter 3, it is also shown that droplets with particular initial Stokes number are localized around the coherent fine scale eddies and va-

por concentration is high at the high energy dissipation rate region on the plane perpendicular to the axis of the coherent fine scale eddies. These tendencies are observed in this case. However, the reaction does not promote at these regions for the high energy dissipation rate. As a result, the high temperature regions, in which reaction advances, are at upper and under side of the center of the eddy, where vapor concentration is high and energy dissipation rate is low. Therefore, the coherent fine scale eddies are compressed by the dilatation of gas fluid at these high temperature regions.

The dispersion of particles and droplets with particular Stokes number are influenced by the coherent fine scale eddies, and they are localized around these eddies. The ignition has occurred at these regions where the vapor concentration becomes high through evaporation of localized droplets, then the high temperature regions have been formed around the coherent fine scale eddy. Accordingly, the gas fluid compresses the coherent fine scale eddy by the dilatation. In this way, spray combustion in fine scale structure proceeds with interaction between the coherent fine scale eddies and droplet dispersion, vapor mixing, ignition.

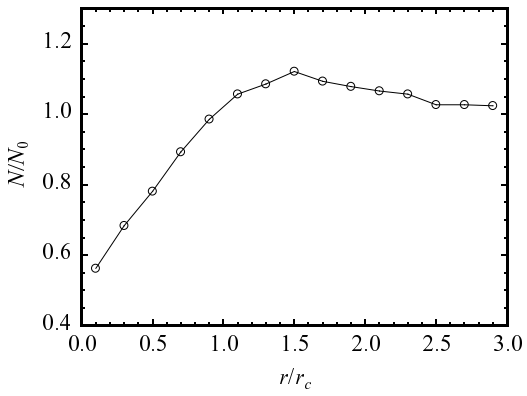

Figure 5.19: Number densities of droplet around the coherent fine scale eddies.

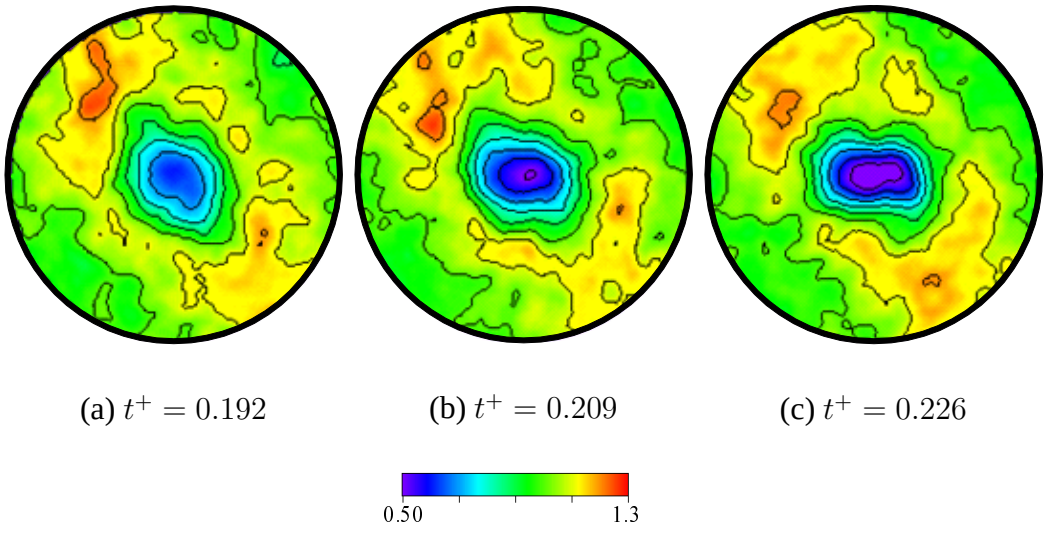

(a) $t^+ = 0.192$ (b) $t^+ = 0.209$ (c) $t^+ = 0.226$

Figure 5.20: Temporal developments of phase-averaged distributions of number density of droplet on the plane perpendicular to the axis of the coherent fine scale eddy.

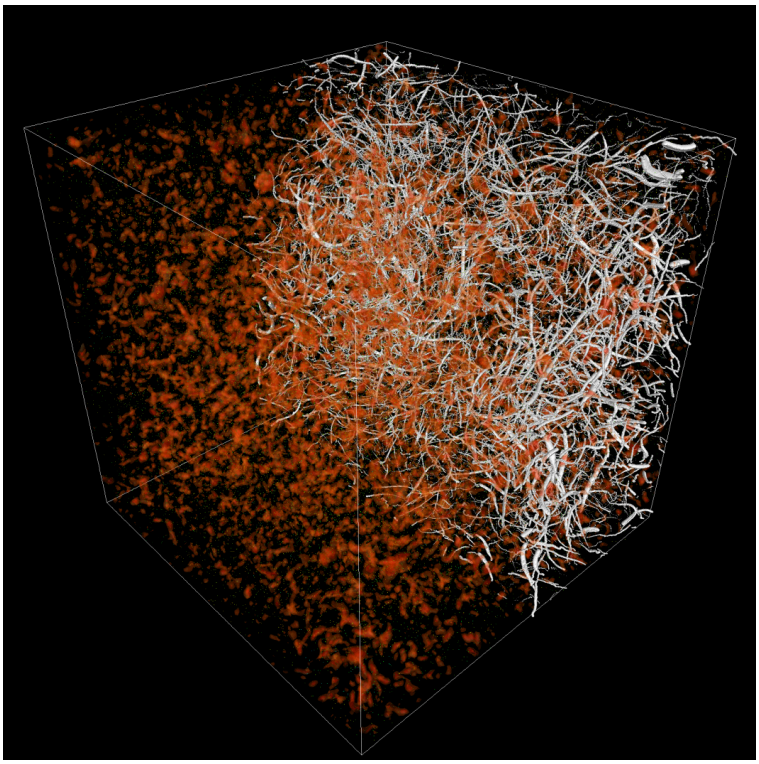

Figure 5.21: Distributions of the axis of the coherent fine scale eddy and isosurface of temperature with droplets at $t^+ = 0.226$.

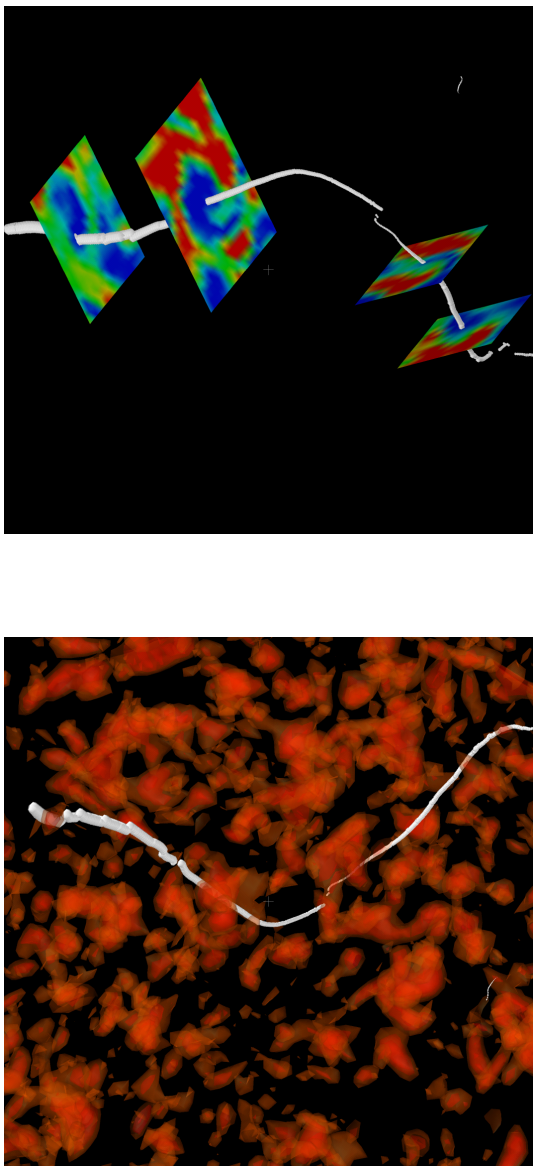

Figure 5.22: Distribution and isosurface of temperature around an axis of the coherent fine scale eddy

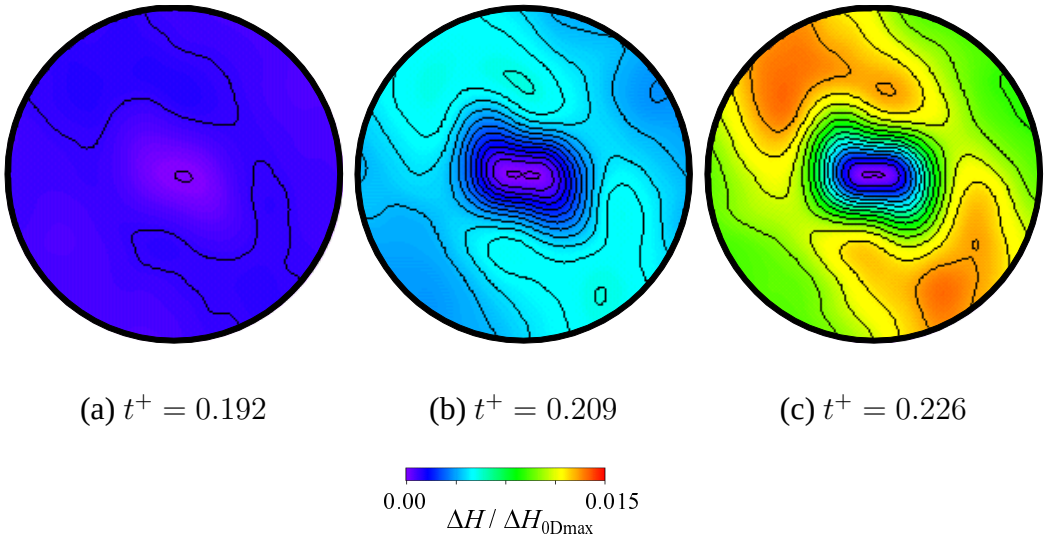

(a) $t^+ = 0.192$ (b) $t^+ = 0.209$ (c) $t^+ = 0.226$

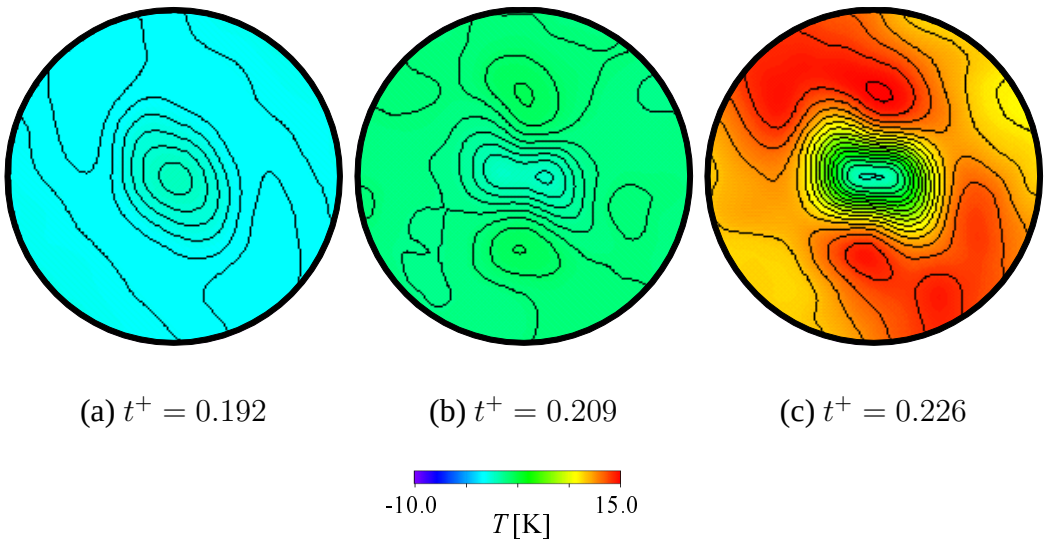

(a) $t^+ = 0.192$ (b) $t^+ = 0.209$ (c) $t^+ = 0.226$

Figure 5.23: Temporal developments of phase-averaged distributions of heat release rate (upper) and temperature (under) on the plane perpendicular to the axis of the coherent fine scale eddies.

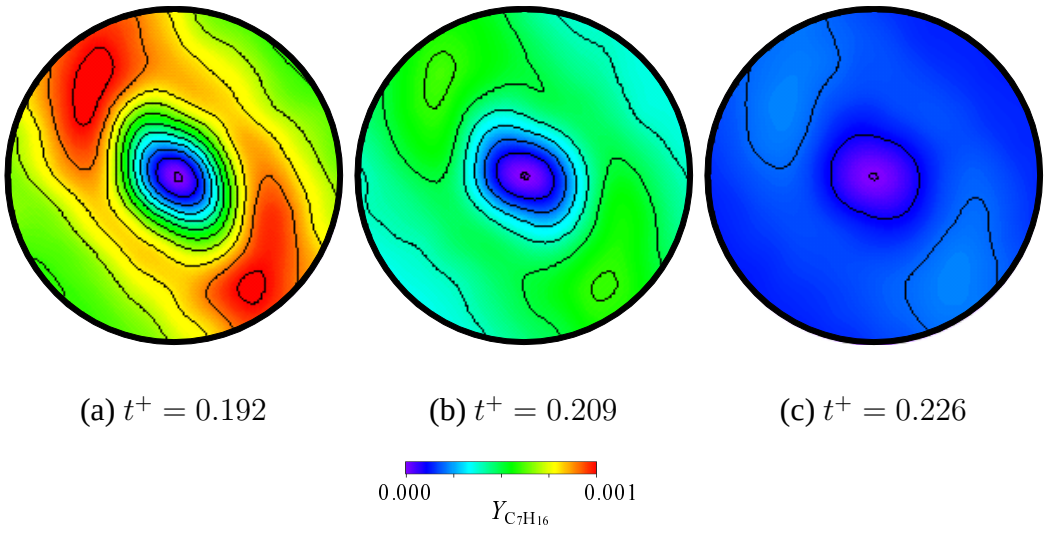

(a) $t^+ = 0.192$ (b) $t^+ = 0.209$ (c) $t^+ = 0.226$

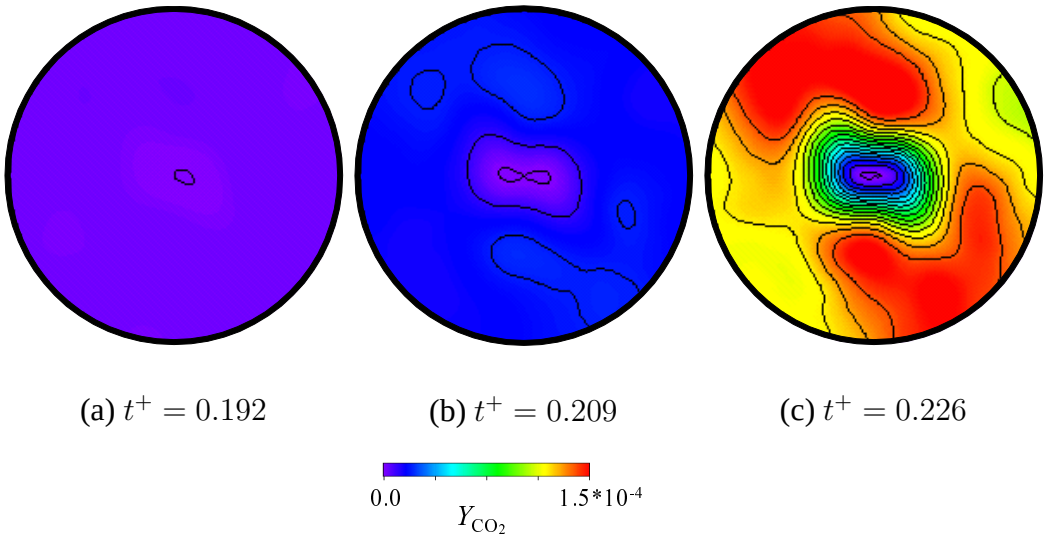

(a) $t^+ = 0.192$ (b) $t^+ = 0.209$ (c) $t^+ = 0.226$

Figure 5.24: Temporal developments of phase-averaged distributions of mass fraction of C_7H_{16} (upper) and CO_2 (under) on the plane perpendicular to the axis of the coherent fine scale eddies.

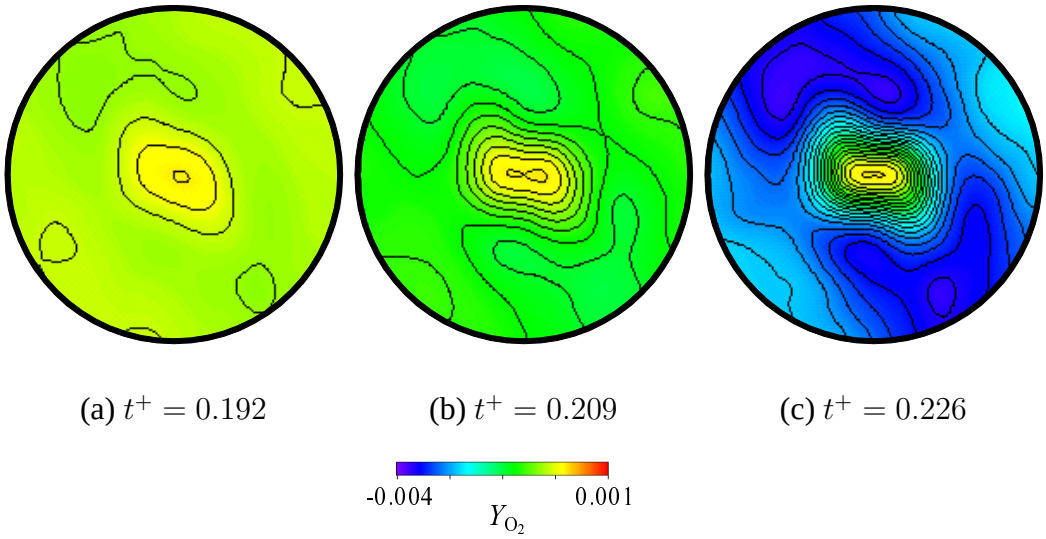

Figure 5.25: Temporal developments of phase-averaged distributions of mass fraction of O_2 (upper) and OH (under) on the plane perpendicular to the axis of the coherent fine scale eddies.

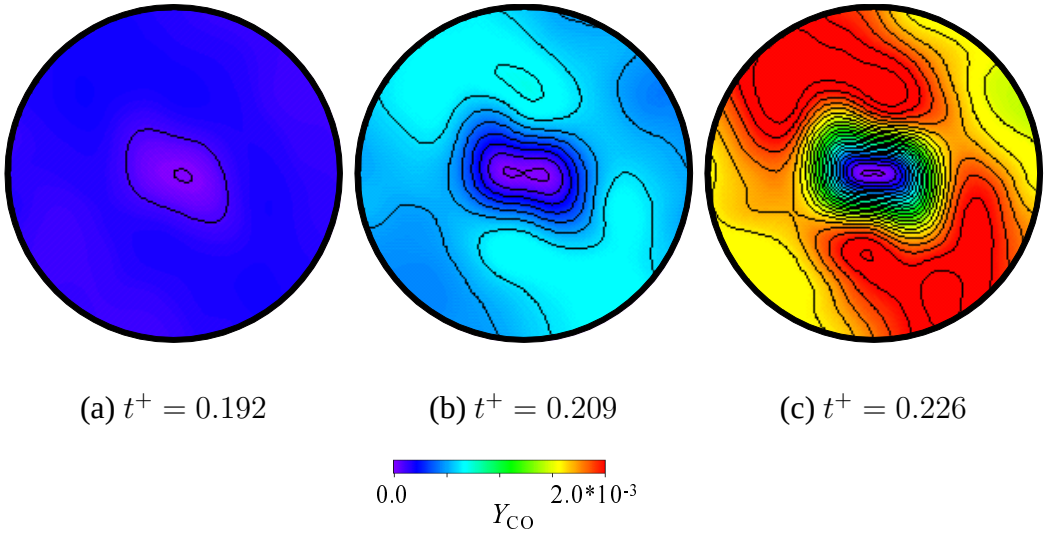

(a) $t^+ = 0.192$ (b) $t^+ = 0.209$ (c) $t^+ = 0.226$

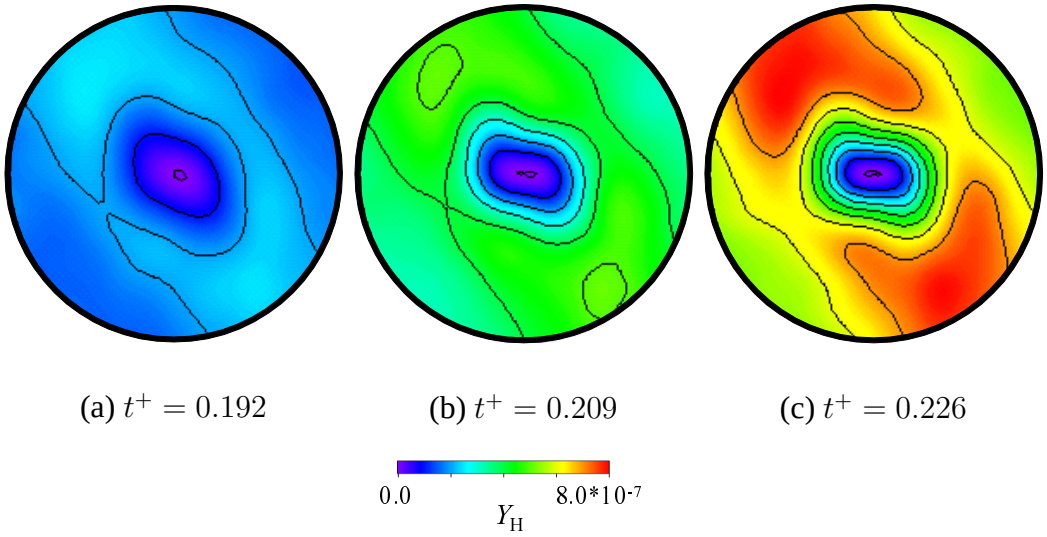

(a) $t^+ = 0.192$ (b) $t^+ = 0.209$ (c) $t^+ = 0.226$

Figure 5.26: Temporal developments of phase-averaged distributions of mass fraction of CO (upper) and H (under) on the plane perpendicular to the axis of the coherent fine scale eddies.

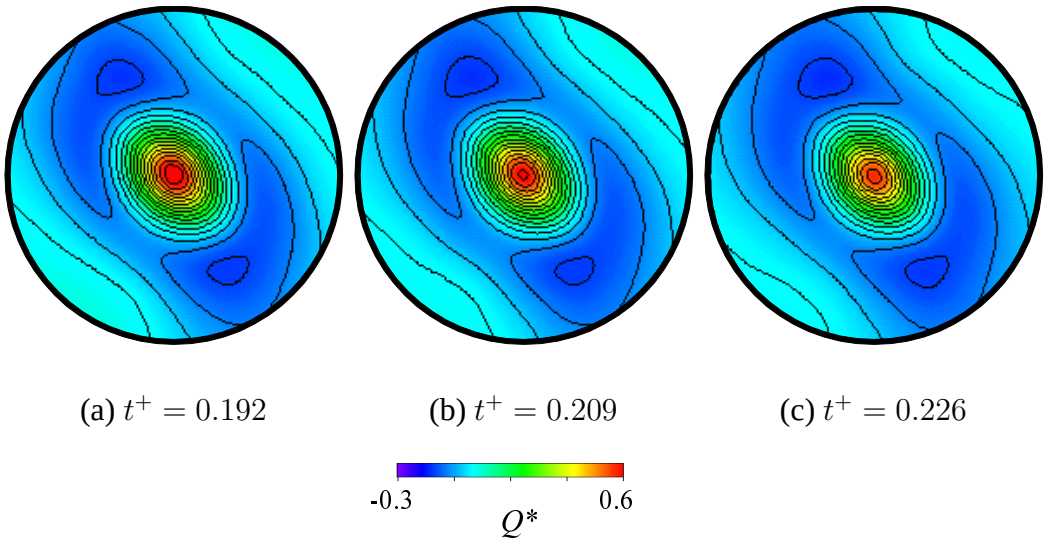

(a) $t^+ = 0.192$ (b) $t^+ = 0.209$ (c) $t^+ = 0.226$

Figure 5.27: Temporal developments of phase-averaged distributions of the second invariant of the velocity gradient tensor on the plane perpendicular to the axis of the coherent fine scale eddies.

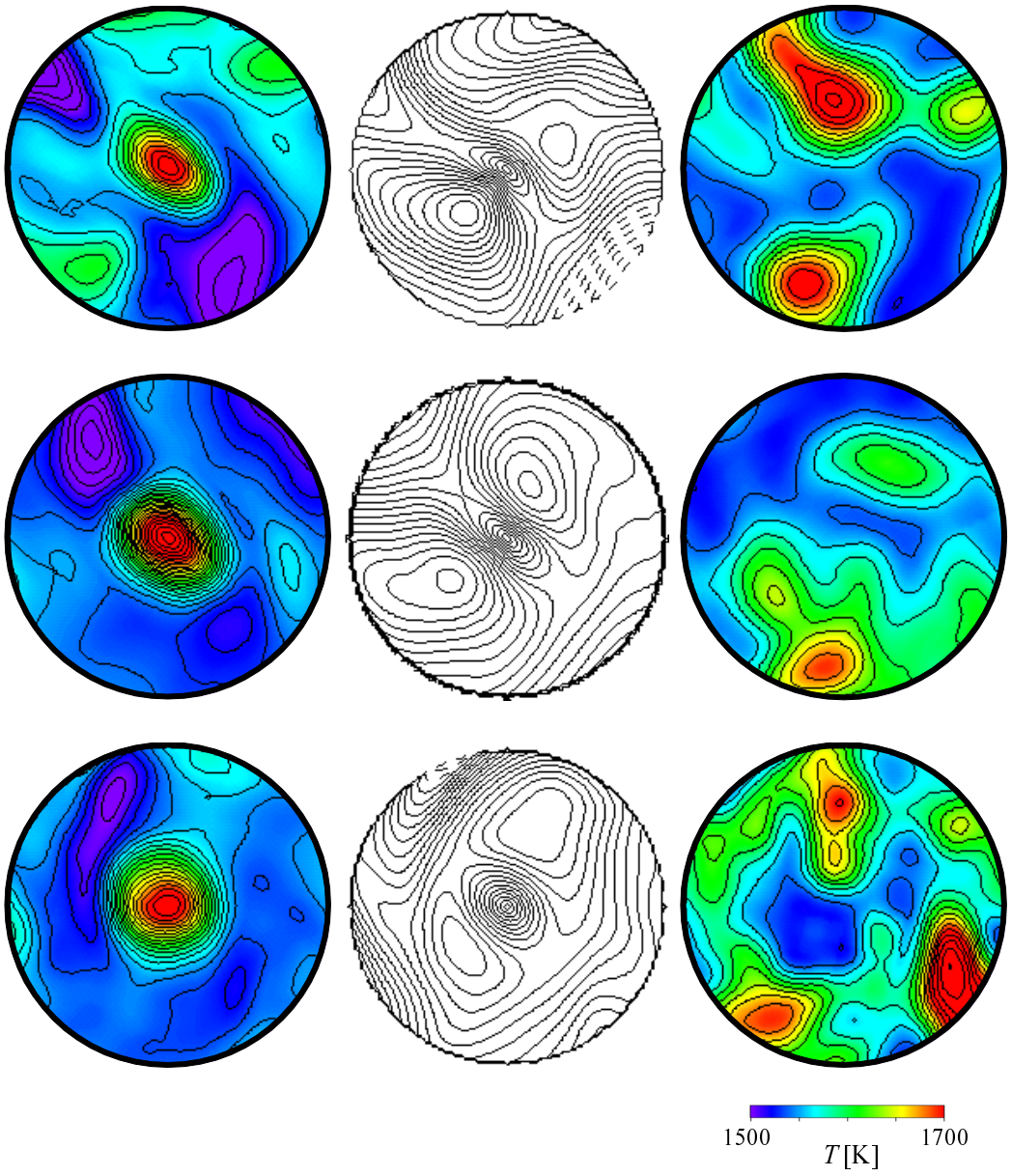

Figure 5.28: Individual distributions of the second invariant of the velocity gradient tensor (left), azimuthal velocity (center) and temperature (right) on the plane perpendicular to the axis of the coherent fine scale eddies at $t^+ = 0.226$.

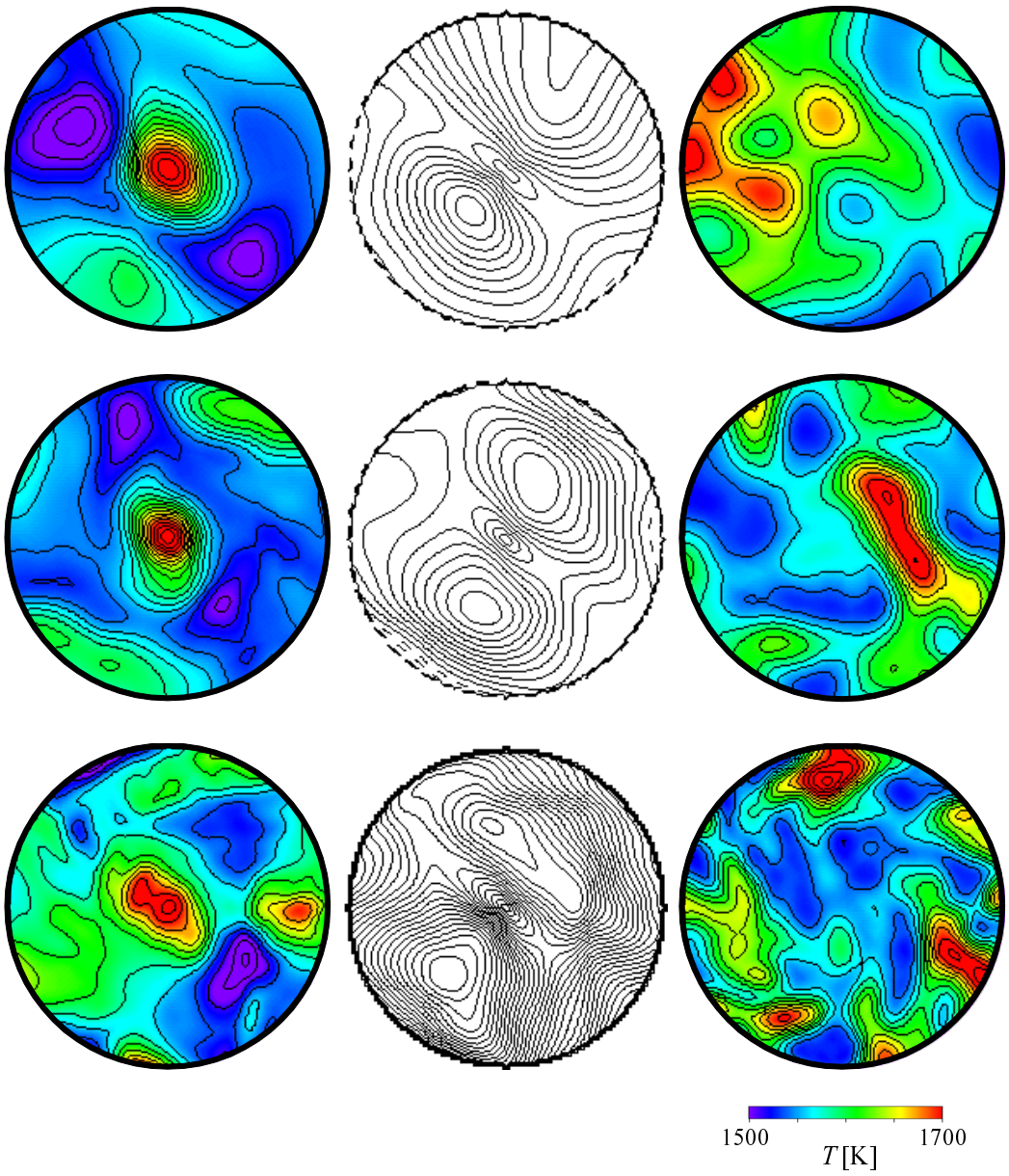

Figure 5.29: Individual distributions of the second invariant of the velocity gradient tensor (left), azimuthal velocity (center) and temperature (right) on the plane perpendicular to the axis of the coherent fine scale eddies at $t^+ = 0.226$.

Chapter 6

Conclusions

In this study, direct numerical simulations have been performed to investigate the relationships between the coherent fine scale structure regarded as universal structure in turbulence and each process in spray combustion. The results obtained in each chapter are summarized in the present chapter as follows.

In chapter 2, to clarify the relationship between particle dispersion and the coherent fine scale eddies, DNSs of homogeneous isotropic turbulence with particles which have different Stokes number have been conducted. The following conclusions are obtained.

(1) Particles with the Stokes number which is close to the influential Stokes number are localized around the coherent fine scale eddies. The number densities of these particles show the maxima at about 1.0 to 2.0 times of the radius of the coherent fine scale eddies.

(2) The theoretical expectation of the influential Stokes number is presented based on the Burgers' vortex model for the coherent fine scale eddy in turbulence, and coincides with DNS results.

(3) On the plane perpendicular to the rotating axis of the coherent fine scale eddy, number densities of particles with the Stokes number which is close

to the influential Stokes number are low at the center of the fine scale eddy, and high in the regions with high energy dissipation rate of the turbulent kinetic energy around the fine scale eddy. This location is at about 1.5 to 2.0 times of the eddy radius on the major axis of the fine scale eddy.

In chapter 3, to clarify the relationship between droplet dispersion, vapor mixing and the coherent fine scale eddies, DNSs of homogeneous isotropic turbulence with evaporating n-heptane droplets which have different initial Stokes number are conducted. The following conclusions are obtained.

(1) Droplets with the initial Stokes number which is close to the influential Stokes number are localized around the coherent fine scale eddies. The number densities of these droplets show the maxima at about 1.0 to 1.5 times of the radius of the coherent fine scale eddies.

(2) Distribution of vapor concentration on the plane perpendicular to the rotating axis of the coherent fine scale eddies is closely related to the elliptic feature of the fine scale eddies. For a particular initial Stokes number, the vapor concentration is high in the regions with high energy dissipation rate of the turbulent kinetic energy around the fine scale eddy. This location is at about 1.5 to 2.0 times of the eddy radius on the major axis of the fine scale eddy.

(3) The profiles of number density of droplets are different for the same initial Stokes number in different Reynolds number cases. This implies that in dispersion of evaporative droplets, evaporation rate K is also an important parameter in addition to the initial Stokes number of droplets.

In chapter 4, to clarify the effects of turbulence on the ignition and propagation process, DNSs of ignition and propagation of n-heptane/air premixed flame in two-dimensional homogeneous isotropic turbulence are conducted, including a reduced kinetic reaction of n-heptane/air mixture with temperature dependence of the transport and thermal properties. The following conclusions are obtained.

(1) In the induction phase, the high temperature region is stretched and its evolution is disturbed by surrounding eddies. This impediment leads to a significant ignition delay compared with the laminar case.

(2) Ignition delay increases with the increase of mean strain rate in the initial high temperature region. The ignition of the mixture delays significantly if the high temperature region is separated by eddies in the induction phase.

(3) In the propagation process, the flame fronts that are enclosed by the burnt side shows high heat release rate, and the flame propagation behaviors depend on the fuel species.

In chapter 5, to clarify the relationship between ignition in spray combustion and the coherent fine scale eddies, DNS of homogeneous isotropic turbulence with evaporating n-heptane droplets under a high temperature condition are conducted, including a reduced kinetic reaction of n-heptane/air mixture with temperature dependence of the transport and thermal properties. The following conclusions are obtained.

(1) With time advancement, many high temperature regions as the ignition core have appeared due to the reaction in n-heptane/air mixture which was formed through evaporation of the fuel droplet. The scales of these regions are small and localized around the coherent fine scale eddies.

(2) Distribution of vapor concentration on the plane perpendicular to the rotating axis of the coherent fine scale eddies is high in the regions with high energy dissipation rate of the turbulent kinetic energy around the coherent fine scale eddy. This location is at about 1.5 to 2.0 times of the eddy radius on the major axis of the coherent fine scale eddy.

(3) On the plane perpendicular to the rotating axis of the coherent fine scale eddies, the reaction does not promote in high energy dissipation rate regions. The high temperature regions are formed at about 1.5 times of the radius of the coherent fine scale eddies on the axis which is obtained by rotating the major axis to $-\pi/4$. In these regions, vapor concentration is relatively high and the energy dissipation rate is low.

(4) The coherent fine scale eddies are compressed due to the dilatation of the gas fluid in high temperature regions.

References

[1] BP Energy Outlook 2030

[2] Oak Ridge National Laboratory

[3] Kang, S.-J., ”Study on Coherent Fine Scale Eddies and Large-Scale Structures in Turbulent Channel Flows”, *Doctor thesis*, Tokyo Institute of Technology (2005).

[4] Townsend, A. A., ”On the Fine-scale Structure of Turbulence”, *Proc. R. Soc., London*, Vol. A208 (1951), pp. 534-542.

[5] Corrsin, S., ”Turbulent Dissipation Fluctuations”, *Phys. Fluid*, Vol. 10 (1962), pp. 1301-1302.

[6] Tennekes, H., ”Simple Model for the Small-scale Structure of Turbulence”, *Phys. Fluid*, Vol. 11 (1968), pp. 669-761.

[7] Lundgren, T. S., ”Strained Spiral Vortex Model for Turbulent Fine Structure”, *Phys. Fluid*, Vol. 25 (1982), pp. 2193-2203.

[8] Pullin, D. I. and Saffiman, P. G., ”On the Lundgren-Townsend Model of Turbulent Fine Scales”, *Phys. Fluid*, Vol. A5 (1993), pp. 126-145.

[9] Jiménez, J., Wray, A. A., Saffman, P. G. and Rogallo, R. S., ”The Structure of Intense Vorticity in Isotropic Turbulence”, *J. Fluid Mech.*, Vol. 255 (1993), pp. 65-90.

[10] Tanahashi, M., Miyauchi, T. and Ikeda, J., ”Identification of Coherent Fine Scale Structure in Turbulence”, *Fluid Mech. and Its Applications IUTAM Symposium on Simulation and Identification of Organized Structures in Flow*, Vol. 52 (1999), pp. 131-140, Kluwer Academic Publishers.

[11] Tanahashi, M., Iwase, S., Uddin, Md. A. and Miyauchi, T., ”Three-dimensional Features of Coherent Fine Scale Eddies in Turbulence”, *Proceedings of 1st Int. Symp. Turbulence and Shear Flow Phenomena*, (1999), pp. 79-84.

[12] Tanahashi, M., Iwase, S. and Miyauchi, T., ”Appearance and Alignment with Strain Rate of Coherent Fine Scale Eddies in Turbulent Mixing Layer”, *J. Turbulence*, Vol. 2 (2001), 6.

[13] Tanahashi, M., Kang, S.-J., Miyamoto, T., Shiokawa, S. and Miyauchi, T., ”Scaling Law of Fine Scale Eddies in Turbulent Channel Flows up to Re_τ=800”, *Int. J. Heat and Fluid Flow*, Vol. 25 (2004), pp. 331-340.

[14] Tanahashi, M., Fujibayashi, K. and Miyauchi, T., ”Fine Scale Eddy Cluster and Energy Cascade in Homogeneous Isotropic Turbulence”, *IUTAM Bookseries IUTAM Symposium on Computational Physics and New Perspectives in Turbulence*,Vol. 4 (2008), pp. 67-72, Springer.

[15] Del Álamo, J. C., Jiménez, J., Zandonade, P. and Moser, R. D., ”Self-similar Vortex Clusters in the Turbulent Logarithmic Region”, *J. Fluid Mech.*, Vol. 561 (2006), pp. 329-358.

[16] Wang, Y., Tanahashi, M. and Miyauchi, T., ”Coherent Fine Scale Eddies in Turbulence Transition of Spatially-developing Mixing Layer”, *Int. J. Heat and Fluid Flow*, Vol. 28 (2007), pp. 1280-1290.

[17] He, W., Tanahashi, M. and Miyauchi, T., ”Direct Numerical Simulation of Turbulent Taylor-Couette Flow with High-Reynolds Number”, *Proceedings of 11th European Turbulence Conference*, (2007), pp. 215-218.

[18] Squires, K. D. and Eaton, J. K., ”Particle Response and Turbulence Modification in Isotropic Turbulence”, *Phys. Fluid*, Vol. A2 (1990), pp. 1191-1203.

[19] Squires, K. D. and Eaton, J. K., ”Preferential Concentration of Particles by Turbulence”, *Phys. Fluid*, Vol. A3 (1991), pp. 1169-1178.

[20] Wang, L. P. and Maxey, M. R., ”Settling Velocity and Concentration Distribution of Heavy Particles in Homogeneous Isotropic Turbulence”, *J. Fluid Mech.*, Vol. 256 (1993), pp. 27-68.

[21] Wang, Q. and Squires, K. D., ”Large Eddy Simulation of Particle-laden Turbulent Channel Flow”, *Phys. Fluid*, Vol. 8 (1996), pp. 1207-1223.

[22] Ling, W., Chung, J. N., Troutt, T. R. and Crowe, C. T., ”Direct Numerical Simulation of a Three-dimensional Temporal Mixing Layer with Particle Dispersion”, *J. Fluid Mech.*, Vol. 358 (1998), pp. 61-85.

[23] Goto, S. and Vassilicos, J. C., ”Self-similar Clustering of Inertial Particles and Zero-acceleration Points in Fully Developed Two-dimensional Turbulence”, *Phys. Fluid*, Vol. 18 (2006), 115103.

[24] Chen, L., Goto, S. and Vassilicos, J. C., ”Turbulent Clustering of Stagnation Points and Inertial Particles”, *J. Fluid Mech.*, Vol. 553 (2006), pp. 143-154.

[25] Fessler, J. R., Kulick, J. D. and Eaton, J. K., ”Preferential Concentration of Heavy Particles in a Turbulent Channel Flow”, *Phys. Fluid*, Vol. 6 (1994), pp. 3742-3749.

[26] Wood, A. M., Hwang, W. and Eaton, J. K., ”Preferential Concentration of Particles in Homogeneous and Isotropic Turbulence”, *Int. J. Multiphase Flow*, Vol. 31 (2005), pp. 1220-1230.

[27] Aliseda, A., Cartellier, A., Hainaux, F. and Lasheras, J.C., ”Effect of Preferential Concentration on the Settling Velocity of Heavy Particles in Homogeneous Isotropic Turbulence”, *J. Fluid Mech.*, Vol. 468 (2002), pp. 77-105.

[28] Yoshimoto, H. and Goto, S., ”Self-similar Clustering of Inertial Particles in Homogeneous Turbulence”,, *J. Fluid Mech.*, Vol. 577 (2007), pp. 275-286.

[29] Marcu, B. and Meiburg, E., ”The Effects of Streamwise Braid Vortices on the Particle Dispersion in a Plane Mixing Layers. . Equilibrium Points and Their Stability”, *Phys. Fluids*, Vol. 8 (1996), pp. 715-733.

[30] Marcu, B., Meiburg, E. and Raju, N.,”The Effects of Streamwise Braid Vortices on the Particle Dispersion in a Plane Mixing Layers. . Nonlinear Particle Dynamics”, *Phys. Fluids*, Vol. 8 (1996), pp. 734-753.

[31] Marcu, B. and Meiburg, E., ”Three-dimensional Features of Particle Dispersion in a Nominally Plane Mixing Layer”, *Phys. Fluids*, Vol. 8 (1996), pp. 2266-2274.

[32] Bec, J., Biferale, L., Cencini, M., Lanotte, A., Musacchino, S. and Toshi, F., ”Heavy Particle Concentration in Turbulence at Dissipative and Inertial Scales”, *Phys. Rev. Lett.*, Vol. 98 (2007), 084502.

[33] Maxey, M. R. and Riley, J. J., ”Equation of Motion for a Small Rigid Sphere in a Nonuniform Flow”, *Phys. Fluids*, Vol. 26 (1983), pp. 883-889.

[34] Elghobashi, S., ”On Predicting Particle-laden Turbulent Flows”, *Applied Scientific Research*, Vol. 52 (1994), pp. 309-329.

[35] Tang, L., Wen, F., Yang, Y., Crowe, C. T., Chung, J. N. and Troutt, T. R., ”Self-organizing Particle Dispersion Mechanism in a Plane Wake”, *Phys. Fluids*, Vol. A 4 (1992), pp. 2244-2251.

[36] Marcu, B., Meiburg, E. and Newton, P. K., ”Dynamics of Heavy Particles in a Burgers Vortex”, *Phys. Fluids*, Vol. 7 (1995), pp. 400-410.

[37] Tanahashi, M., Tanimura, S. and Miyauchi, T., ”Particle Dispersion and Coherent Fine Scale Eddies in Homogeneous Isotropic Turbulence”, *Proceedings of 4th JSME-KSME Thermal Eng. Conf.*, No. 2 (2000), pp. 443-448.

[38] Miyauchi, T., Tanahashi, M., Takata, N. and Iwase, S., ”Scalar Dissipation Rate and Coherent Fine Scale Eddies in Turbulence”, *Proceedings of Int. Symp. on Dynamics and Statistics of Coherent Structures in Turbulence*, (2002), pp. 249-258.

[39] Kang, S.-J., Tanahashi, M. and Miyauchi, T., ”Elliptic Feature of Coherent Fine Scale Eddies in Turbulent Channel Flows”, *J. Mechanical Science and Technology*, Vol. 20 (2006), pp. 262-270.

[40] Moffatt, H. K., Kida, S. and Ohkitani, K., ”Stretched Vortices - the Sinews of Turbulence; Large-Reynolds-number Asymptotics”, *J. Fluid Mech.*, Vol. 259 (1994), pp. 241-264.

[41] Soria, J., Sondergaard, R., Cantwell, B. J., Chong, M. S. and Perry, A. E., ”A Study of the Fine-scale Motions of Incompressible Time-developing Mixing Layers”, *Phys. Fluids*, Vol. 6 (1994), pp. 871-884.

[42] Siggia, E. D., ”Numerical Study of Small Scale Intermittency in Three Dimensional Turbulence”, *J. Fluid Mech.*, Vol. 107 (1981), pp. 375-406.

[43] Kerr, R. M. V., ”Higher-order Derivative Correlations and the Alignment of Small-scale Structures in Isotropic Numerical Turbulence”, *J. Fluid Mech.*, Vol. 153 (1985), pp. 31-58.

[44] She, Z.-S., Jackson, E. and Orszag, S. A., ”Intermittent Vortex Structures in Homogeneous Isotropic Turbulence”, *Nature*, Vol. 344 (1990), pp. 226-228.

[45] Ruetsch, G. R. and Maxey, M. R. ”Small-scale Features of Vorticity and Passive Scalar Fields in Homogeneous Isotropic Turbulence”, *Phys. Fluids*, Vol. A3 (1991), pp. 1587-1597.

[46] Ruetsch, G. R. and Maxey, M. R., ”The Evolution of Small-scale Structures in Homogeneous Isotropic Turbulence”, *Phys. Fluids*, Vol. A4 (1992), pp. 2747-2760.

[47] Vincent, A. and Meneguzzi, M., ”The Spatial Structure and Statistical Properties of Homogeneous Turbulence”, *J. Fluid Mech.*, Vol. 225 (1991), pp. 1-20.

[48] Vincent, A. and Meneguzzi, M., ”The Dynamics of Vorticity Tubes in Homogeneous Turbulence”, *J. Fluid Mech.*, Vol. 258 (1994), pp. 245-254.

[49] Hunt, J. C. R., Wray, A. A. and Moin, P., ”Eddies, Stream and Convergence Zones in Turbulent Flows”, *CTR Report*, CTR-S88 (1988), 193.

[50] Chong, M. S., Perry, A. E. and Cantwell, B. J., ”A General Classification of Three-dimensional Flow Field”, *Phys. Fluids*, Vol. A2 (1990), pp. 765-777.

[51] Blackburn, H. M., Mansour, N. N. and Cantwell, B. J., ”Topology of Fine-scale Motions in Turbulent Channel Flow”, *J. Fluid Mech.*, Vol. 310 (1996), pp. 269-292.

[52] Grassberger, P. and Procaccia, I., ”Measuring the Strangeness of Strange Attractors”, *Physica D*, Vol. 9 (1983), pp. 189-208.

[53] Hogan, R. C. and Cuzzi, J. N., ”Stokes and Reynolds Number Dependence of Preferential Particle Concentration in Simulated Three-dimensional Turbulence”, *Phys. Fluids*, Vol. 13 (2001), pp. 2938-2945.

[54] Sirignano, W. A., ”Fluid Dynamics and Transport of Droplets and Sprays”, (1999), Cambridge University Press.

[55] Mashayek, F., Jaberi, F. A. and Miller, R. S., ”Dispersion and Polydispersity of Droplets in Stationary Isotropic Turbulence”, *Int. J. Multiphase Flow*, Vol. 23 (1997), pp. 337-355.

[56] Mashayek, F., ”Direct Numerical Simulation of Evaporating Droplet Dispersion in Forced Low Mach Number Turbulence”, *Int. J. Heat Mass Transfer*, Vol. 41 (1998), pp. 2601-2617.

[57] Mashayek, F., ”Droplet-turbulence Interactions in Low-Much-number Homogeneous Shear Two-phase Flows”, *J. Fluid Mech.*, Vol. 367 (1998), pp. 163-203.

[58] Gao, Z. and Mashayek, F., ”Stochastic Modeling of Evaporating Droplets Polydispered in Turbulent Flows”, *Int. J. Heat Mass Transfe*, Vol. 47 (2004), pp. 4339-4348.

[59] Miller, R. S., Harstad, K. and Bellan, J., ”Evaluation of Equilibrium and Non-equilibrium Evaporation Models for Many-droplet Gas-liquid Flow Simulations”, *Int. J. Multiphase Flow*, Vol. 24 (1998), pp. 1025-1055.

[60] Miller, R. S. and Bellan, J., ”Direct Numerical Simulation of a Confined Three-dimensional Gas Mixing Layer with One Evaporating Hydrocarbon-droplet-laden Stream”, *J. Fluid Mech.*, Vol. 384 (1999), pp. 293-338.

[61] Miller, R. S. and Bellan, J., ”Direct Numerical Simulation and Subgrid Analysis of a Transitional Droplet Laden Mixing Layer”, *Phys. Fluids*, Vol. 12 (2000), pp. 650-671.

[62] Miller, R. S., ”Long Time Mass Fraction Statistics in Stationary Compressible Isotropic Turbulence at Super Critical Pressure”, *Phys. Fluids*, Vol. 12 (2000), pp. 2020-2032.

[63] Miller, R. S., ”Effects of Nonreacting Solid Particle and Liquid Droplet Loading on an Exothermic Reacting Mixing Layer”, *Phys. Fluids*, Vol. 13 (2001), pp. 3303-3320.

[64] Khatumria, V. C. and Miller, R. S., ”Numerical Simulation of a Fuel Droplet Laden Exothermic Reacting Mixing Layer”, *Int. J. Multiphase Flow*, Vol. 29 (2003), pp. 771-794.

[65] Lou, H. and Miller, R. S., ”On Ternary Species Mixing and Combustion in Isotropic Turbulence at High Pressure”, *Phys. Fluids,* Vol. 16 (2004), pp. 1423-1438.

[66] Varanasi, K. K., Clack, H. K. and Miller, R. S., ”On Preferential Diffusion of Binary Component Liquid Droplets Evaporating in a Two-phase Mixing Layer”, *Int. J. Multiphase Flow*, Vol. 30 (2004), pp. 1235-1257.

[67] Okong’o, N. and Bellan, J., ”A Priori Subgrid Analysis of Temporal Mixing Layers with Evaporating Droplets”, *Phys. Fluids*, Vol. 12 (2000), pp. 1573-1591.

[68] Abdel-Hameed, H. and Bellan, J., ”Direct Numerical Simulations of Two-phase Laminar Jet Flows with Different Cross-section Injection Geometries”, *Phys. Fluids*, Vol. 14 (2002), pp. 3655-3674.

[69] Harstad, K. and Bellan, J., ”Modeling Evaporation of Jet A, JP-7, and RP-1 Drops at 1 to 15 bars.”, *Combustion and Flame*, Vol. 137 (2004), pp. 163-1772.

[70] Harstad, K. and Bellan, J., ”Modeling of Multicomponent Homogeneous Nucleation Using Continuous Thermodynamics”, *Combustion and Flame*, Vol. 139 (2004), pp. 252-262.

[71] Harstad, K. and Bellan, J., ”Mixing Rules for Multicomponent Mixture Mass Diffusion Coefficients and Thermal Diffusion Factors”, *J. Chem. Phys.*, Vol. 120 (2004), pp. 5664-5673.

[72] Okong’o, N. and Bellan, J., ”Perturbation and Initial Reynolds Number Effects on Transition Attainment of Supercritical, Binary, Temporal Mixing Layers”, *Comput. Fluids*, Vol. 33 (2004), pp. 1023-1046.

[73] Okong’o, N. and Bellan, J., ”Turbulence and Fluid-front Area Production in Binary-species, Supercritical, Transitional Mixing Layers”, *Phys. Fluids*, Vol. 16 (2004), pp. 1467-1492.

[74] Okong'o, N. and Bellan, J., "Consistent Large-eddy Simulation of a Temporal Mixing Layer Laden with Evaporating Drops. Part1. Direct Numerical Simulation, Formulation and a Priori Analysis", *J. Fluid Mech.*, Vol. 499 (2004), pp. 1-47.

[75] Okong'o, N. Leboissetier, A. and Bellan, J., "Detailed Characteristics of Drop-laden Mixing Layers: Large Eddy Simulation Predictions Compared to Direct Numerical Simulation", *Phys. Fluids*, Vol. 20 (2008), 103305.

[76] Taskinoglu, E. S. and Bellan, J., "A Posteriori Study Using a DNS Database Describing Fluid Disintegration and Binary-species Mixing Under Supercritical Pressure: Heptane and Nitrogen", *J. Fluid Mech.*, Vol. 645 (2010), pp. 211-254.

[77] Okong'o, N. and Bellan, J., "Small-scale Dissipation in Binary-species, Thermodynamically Supercritical, Transitional Mixing Layers", *Comput. Fluids*, Vol. 39 (2010), pp. 1112-1124.

[78] Clercq, P. C. and Bellan, J., "Direct Numerical Simulation of a Transitional Temporal Mixing Layer Laden with Multicomponent-fuel Evaporating Drops Using Continuous Thermodynamics", *Phys. Fluids*, Vol. 16 (2008), pp. 1884-1907.

[79] Clercq, P. C. and Bellan, J., "Direct Numerical Simulation of Gaseous Mixing Layers Laden with Multicomponent-liquid Drops: Liquid-specific Effects", *J. Fluid Mech.*, Vol. 533 (2005), pp. 57-94.

[80] Leboissetier, A., Okong'o, N. and Bellan, J., "Consistent Large-eddy Simulation of a Temporal Mixing Layer Laden with Evaporating Drops. Part2. A Posteriori Modeling.", *J. Fluid Mech.*, Vol. 523 (2005), pp. 37-78.

[81] Clercq, P. C. and Bellan, J., "Modeling of Multicomponent-fuel Drop-laden Mixing Layers Having a Multitude of Species", *Proc. Combust. Inst.*, Vol. 30 (2005), pp. 2011-2019.

[82] Spalding, D. B., ”The Combustion of Liquid Fuels”, *Proc. Combust. Inst.*, Vol. 4 (1953), pp. 847-864.

[83] Ranz, W. E. and Marshall, W. R., ”Evaporation from Drops Part ”, *Chem. Eng. Prog.*, Vol. 49 (1952), pp. 173-180.

[84] Downing, C. G., ”The Evaporation of Drops of Pure Liquids at Elevated Temperatures: Rates of Evaporation and Wet-bulb Temperatures”, *A. I. Ch. E. Journal*, Vol. 12 (1966), pp. 760-766.

[85] Wong, S. C. and Lin, A. C., ”Internal Temperature Distributions of Droplets Vaporizing in High-temperature Convective Flows”, *J. Fluid Mech.*, Vol. 237 (1992), pp. 671-687.

[86] Orain, M., Mercier, X. and Grisch, F., ”PLIF Imaging of Fuel-vapor Spatial Distribution Around a Monodisperse Stream of Acetone Droplets: Comparison with Modeling”, *Combust. Sci. and Tech.*, Vol. 177 (2005), pp. 249-278.

[87] Starner, S. H., Gounder, J. and Masri, A. R., ”Effects of Turbulence and Carrier Fluid on Simple, Turbulent Spray Jet Flames”, *Combust. Flame*, Vol. 143 (2005), pp. 420-432.

[88] Castanet, G., Levouche, M. and Lemoine, F., ”Heat and Mass Transfer of Combusting Monodisperse Droplets in a Linear Stream”, *Int. J. Heat Mass Transfer*, Vol. 48 (2005), pp. 3261-3275.

[89] Boivin, M., Simonin, O. and Squires, K. D., ”Direct Numerical Simulation of Turbulence Modulation by Particles in Isotropic Turbulence”, *J. Fluid Mech.*, Vol. 375 (1998), pp. 235-263.

[90] Kaimai, T., Tsunemoto, H. and Ishitani, H., ”Effects of a Hybrid Fuel System with Diesel and Premixed DME/Methane Charge on Exhaust Emissions in a Small DI Diesel Engine”, *SAE Technical Paper*, Vol. 1999-01-1509, pp. 1-7.

[91] Stanglmaier, R. H., Ryan III, T. W. and Souder, J. S., ”HCCI Operation of a Dual-Fuel Natural Gas Engine for Improved Fuel Efficiency and Ultra-Low NOx Emission at Low to Moderate Engine Loads”, *SAE Technical Paper*, Vol. 2001-01-1897, pp. 1-7.

[92] Law, D., Allen, J. and Chen, R., ”On the Mechanism of Controlled Auto Ignition”, *SAE Technical Paper*, Vol. 2002-01-0421, pp. 1-9.

[93] Tanahashi, M., Fujimura, M. and Miyauchi, T., ”Coherent Fine Scale Eddies in Turbulent Premixed Flames”, *Proc. Combust. Inst*, Vol. 28 (2000), pp. 529-535.

[94] Tanahashi, M., Nada, Y., Ito, Y. and Miyauchi, T., ”Local Flame Structure in the Well-Stirred Reactor Regime”, *Proc. Combust. Inst*, Vol. 29 (2002), pp. 2041-2049.

[95] Miyauchi, T., Tanahashi, M., Sasaki, K. and Ozeki, T., ”Transport Phenomena in Combustion” Chen, C. H. ed., Taylor and Francis, pp. 1095-1105.

[96] Lele, S. K., ”Compact Finite Difference Schemes with Spectral-like Resolution”, *J. Compt. Phys.*, Vol. 103 (1992), pp. 16-42.

[97] Poinsot, T. J. and Lele, S. K., ”Boundary Conditions for Direct Simulations of Compressible Viscous Flows”, *J. Comput. Phys.*, Vol. 101 (1992), pp. 104-129.

[98] Baum, M., Poinsot, T. and Thévenin, D., ”Accurate Boundary Conditions for Multicomponent Reactive Flows”, *J. Comput. Phys.*, Vol. 116, (1994), pp. 247-261.

[99] Kee, R. J., Rupley, F. M. and Miller, J. A., ”Chemkin-II: a Fortran Chemical Kinetics Package for the Analysis of Gas Phase Chemical Kinetics”, *Sandia Report*, SAND89-8009B, (1989).

[100] Kee, R. J., Dixon-Lewis, G., Warnatz, J., Coltrin, M. E. and Miller, J. A., "A Fortran Computer Code Package for the Evaluation of Gas-Phase Multicomponent Transport Properties", *Sandia Report*, SAND86-8246, (1986).

[101] Byrne, G. D. and Hindmarsh, A. C., "A Polyalgorithm for the Numerical Solution of Ordinary Differential Equations", *ACM Transactions on Mathematmal Software*, Vol. 1 (1975), pp. 71-96.

[102] Brown, P. N., Byrne, G. D. and Hindmarsh, A. C., "VODE, A Variable-coefficient ODE Solver", *SIAM Journal on Scientific and Statistical Computing*, Vol. 10 (1989), pp. 1038-1051.

[103] Miller, J. A. and Bowman, C. T., "Mechanism and Modeling of Nitrogen Chemistry in Combustion", *Prog. Energy Combust. Sci.*, Vol. 15 (1989), pp. 287-338.

[104] Smooke, M. D. and Giovangigli, V., "Formulation of the Premixed and Nonpremixed Test Problems, Reduced Kinetic Mechanisms and Asymptotic Approximations for Methane-air Flames", *Springer-Verlag*, pp. 1-28, (1991).

[105] Kee, R. J., Rupley, F. M., Meeks, E. and Miller, J. A., "Chemkin-III: A Fortran Chemical Kinetics Package the Analysis of Gas-phase Chemical and Plasma Kinetics, *Sandia Report*, SAND96-8216, (1996).

[106] Bowman, C. T., Hanson, R. K., Davidson, D. F., Gardliner, Jr., W. C., Lissianski, V., Smith, G. P., Golden, D. M., Frenklach, M. and Goldenberg, M., (http://www.me.berkeley.edu/gri_mech/).

[107] Peters, N., "The Turbulent Burning Velocity for Large-Scale and Small-Scale Turbulence", *J. Fluid Mech.*, Vol. 384 (1999), pp. 107-132.

[108] Low, C. K., "Recent Advances in Droplet Vaporization and Combustion", *Prog. Energy Combust. Sci.*, Vol. 8 (1982), pp. 171-201.

[109] Sirignano, W. A., ”Fuel Droplet Vaporization and Spray Combustion Theory”, *Prog. Energy Combust. Sci.*, Vol. 9 (1983), pp. 291-322.

[110] Faeth, G. M., ”Evaporation and Combustion of Sprays”, *Prog. Energy Combust. Sci.*, Vol. 9 (1983), pp. 1-76

[111] Sirignano, W. A., ”Fluid Dynamics of Sprays -1992 Freeman Scholar Lecture”, *J. Fluid Eng.*, Vol. 115 (1993), pp. 345-378.

[112] Xia, J., Luo, K. H. and Kumar, S., ”Large-eddy Simulation of Interactions between a Reacting Jet and Evaporating Droplets,” *Flow, Turbul. Combust.*, Vol. 80 (2008), pp. 133-153.

[113] Galpin, J., Naudin, A., Vervisch, L., Angelberger, C., Colin, O. and Domingo, P., ”Large-eddy Simulation of a Fuel-lean Premixed Turbulent Swirl-burner”, *Combust. Flame*, Vol. 155 (2008), pp. 247-266.

[114] Moin, P. and Apte, S., ”Large-eddy simulation of Realistic Gas Turbine Combustors”, *AIAA J.*, Vol. 44(4) (2006), pp. 698-708.

[115] Patela, N., Kirtasa, M., Sankarana, V. and Menon, S., ”Simulation of Spray Combustion in a Lean-direct Injection Combustor”, *Proc. Combust. Inst.*, Vol. 31 (2007), pp. 2327-2334.

[116] Neophytou, A., Mastorakos, E. and Cant, R. S., ”The Internal Structure of Igniting Turbulent Sprays as Revealed by Complex Chemistry DNS”, *Combust. Flame*, in Press (2011).

[117] Neophytou, A., Mastorakos, E. and Cant, R. S., ”Complex Chemistry Simulations of Spark Ignition in Turbulent Sprays”, *Proc. Combust. Inst.*, Vol. 33 (2011), pp. 2135-2142.

[118] Neophytou, A., Mastorakos, E. and Cant, R. S., ”DNS of Spark Ignition and Edge Flame Propagation in Turbulent Droplet-laden Mixing Layers”, *Combust. Flame*, Vol. 157 (2010), pp. 1071-1086.

[119] Wang, Y. and Rutland, C. J., ”Effects of Temperature and Equivalence Ration on the Ignition of n-Heptane Fuel Spray in Turbulent Flow”, *Proc. Combust. Inst.*, Vol. 30 (2005), pp. 893-900.

[120] Wang, Y. and Rutland, C. J., ”Direct Numerical Simulation of Ignition in Turbulent n-Heptane Liquid-fuel Spray Jets”, *Combust. Flame*, Vol. 149 (2007), pp. 353-365.

[121] Luo, K., Desjardins, O. and Pitsch, H., ”DNS of Droplet Evaporation and Combustion in a Swirling Combustor”, *CTR Annual Research Briefs*, (2008), pp. 1-13.

[122] Luo, K., Pitsch, H. and Pai, M. G., ”Direct Numerical Simulation of Three-dimensional Swirling n-Heptane Spray Flames”, *CTR Annual Research Briefs*, (2009), pp. 171-183.

[123] Xia, J. and Luo, K. H., ”Direct Numerical Simulation of Diluted Combustion by Evaporating Droplets”, *Proc. Combust. Inst.*, Vol. 32 (2009), pp. 2267-2274.

[124] Luo, K., Pitsch, H. Pai, M. G. and Desjardins, O., ”Direct Numerical Simulation and Analysis of Three-dimensional n-Heptane spray Flames in a Model Swirl Combustor”, *Proc. Combust. Inst.*, Vol. 33 (2011), pp. 2143-2152.

[125] Domingo, P., Vervisch, L. and Réveillon, J., ”DNS Analysis of Partially Premixed Combustion in Spray and Gaseous Turbulent Flame-bases Stabilized in Hot Air”, *Combust. Flame*, Vol. 140 (2005), pp. 172-195.

[126] Réveillon, J. and Vervisch, L., ”Analysis of Weakly Turbulent Dilute-spray Flames and Spray Combustion Regimes”, *J. Fluid Mech.*, Vol. 537 (2005), pp. 317-347.

[127] Réveillon, J. and Vervisch, L., ”Accounting for Spray Vaporization in Turbulent Combustion Modeling”, *CTR Proc. Summer Program*,(1998), pp. 25-38.

[128] Réveillon, J. and Vervisch, L., ”Spray Vaporization in Nonpremixed Turbulent Combustion Modeling: A Single Droplet Model”, *Combust. Flame*, Vol. 121 (2000), pp. 75-90.

[129] Réveillon, J., Massot, M. and Pera, C., ”Analysis and Modeling of the Dispersion of Vaporizing Polydispersed Sprays in Turbulent Flows”, *CTR Proc. Summer Program*, Vol. 121 (2002), pp. 393-404.

[130] Baba, Y. and Kurose, R., ”Analysis and Flamelet Modeling for Spray Combustion”, *J. Fluid Mech.*, Vol. 612 (2008), pp. 45-79.

[131] Curran, H. J., Gaffuri, P., Pitz, W. J. and Westbrook, C. K., ”A Comprehensive Modeling Study of n-Heptane Oxidation”, *Combust. Flame*, Vol. 114 (1998), pp. 149-177.

[132] Seiser, R., Pitsch, H., Seshadri, K., Pitz, W. J. and Curran, H. J., ”Extinction and Autoignition of n-Heptane in Counterflow Configuration”, *Proc. Combust. Inst.*, Vol. 28 (2000), pp. 2029-2037.

[133] Liu, S., Hewson, J. C., Chen, J. H. and Pitsch, H., ”Effects of Strain Rate on High-pressure Nonpremixed n-Heptane Autoignition in Counterflow”, *Combust. Flame*, Vol. 137 (2004), pp. 320-339.

[134] Maroteaux, F. and Noel, L., ”Development of a Reduced n-Heptane Oxidation Mechanism for HCCI Combustion Modeling”, *Combust. Flame*, Vol. 146 (2006), pp. 246-267.

[135] Patel, A,, Kong, S.-C. and Reitz, R. D., ”Development and Validation of a Reduced Reaction Mechanism for HCCI Engine Simulations”, *SAE Paper*, 2004-01-0558 (2004).

[136] Bikas, G. and Peters, N., ”Kinetic Modeling of n-Decane Combustion and Autoignition”, *Combust. Flame*, Vol. 126 (2001), pp. 1456-1475.

[137] Lutz, A. E., Kee, R. J. and Miller, J. A., ”SENKIN: A Fortran Program for Predicting Homogeneous Gas Phase Chemical Kinetics with Sensitivity Analysis”, *Sandia Report*, SAND87-8248, (1992).

[138] Kee, R. J., Grcar, J. F., Smooke, M. D. and Miller, J. A., ”PREMIX: A Fortran Program for Modeling Steady One-Dimensional Premixed Flames”, *Sandia Report*, SAND85-8240, (1985).

[139] Chevalier, C., Louessard, P., Muller, U. C. and Warnatz, J., ”A Detailed Low-temperature Reaction Mechanism of n-Heptane Auto-ignition”, *Int. Symp. COMODIA 90*, (1990), pp. 93-97.

[140] Golovitchev, V. I., http://www.tfd.chalmers.se/ valeri/

[141] Ciezki, H. K. and Adomeit, G., ”Shock-tube Investigation of Self-ignition of n-Heptane-air Mixtures under Engine Relevant Conditions”, *Combust. Flame*, Vol. 93 (1993), pp. 421-433.

[142] Chen, J. H., Hawkes, E. R., Sankaran, R., Mason, S. D. and Im, H. G., ”Direct Numerical Simulation of Ignition Front Propagation in a Constant Volume with Temperature Inhomogeneities; . Fundamental Analysis and Diagnostics”, *Combust. Flame*, Vol. 145 (2006), pp. 128-144.

[143] Chakraborty, N., Hawkes, E. R., Chen, J. H. and Cant, R. S., ”The Effects of Strain Rate and Curvature on Surface Density Function Transport in Turbulent Premixed Methane-air and Hydrogen-air Flames: A Comparative Study”, *Combust. Flame*, Vol. 154 (2008), pp. 259-280.

[144] Nada, Y., Tanahashi, M. and Miyauchi, T., ”Effect of Turbulence Characteristics on Local Flame Structure of H_2-Air Premixed Flames”, *J. Turbulence*, Vol. 5 (2004), 16.

[145] Tsuboi, N., Eto, K. and Hayashi, A. K., ”Detailed Structure of Spinning Detonation in a Circular Tube”, *Combust. Flame,* Vol. 149 (2007), pp. 144-161.

[146] Daimon, Y. and Matsuo, A., ”Unsteady Features on One-dimensional Hydrogen-air Detonations”, *Phys. Fluids*, Vol. 19 (2007), 116101.

[147] Mehl, M., Curran, H. J., Pitz, W. J. and Westbrook, C. K., ”Chemical Kinetic Modeling of Component Mixtures Relevant to Gasoline”, *European Combustion Meeting*, LLNL-CONF-410968 (2009).

[148] Westbrook, C. K., Pitz, W. J., Herbint, O., Curran, H. J. and Silke, E. J., ”A Comprehensive Detailed Chemical Kinetic Reaction Mechanism for Combustion of n-Alkane Hydrocarbons from n-Octane to n-Hexadecane”, *Combust. Flame*, Vol. 156 (2009), pp. 181-199.

[149] Pepiot-Desjardins, P. and Pitsch, H., ”An Automatic Chemical Lumping Method for the Reduction of Large Chemical Kinetic Mechanisms”, *Combust. Theory Mod,*, Vol. 12 (2008), pp. 1089-1108.

[150] Niemeyer, K. E., Sung, C. J. and Raju, M. P., ”Skeletal Mechanism Generation for Surrogate Fuels Using Directed Relation Graph with Error Propagation and Sensitivity Analysis”, *Combust. Flame,* Vol. 157 (2010), pp. 1760-1770.

[151] Zeppieri, S. P., Klotz, S. D. and Dryer, F. L., ”Modeling Concepts for Larger Carbon Number Alkanes: A Partially Reduced Skeletal Mechanism for n-Decane Oxidation and Pyrolysis”, *Proc. Combust. Inst.*, Vol. 28 (2000), pp. 1587-1595.

[152] Zhao, Z., Li, J., Dryer, F. L. and Zeppieri, S. P., ”Burning Velocities and a High-temperature Skeletal Kinetic Model for n-Decane”, *Combust. Sci. Tech.*, Vol. 177 (2005), pp. 89-106.

[153] Lu, T., Law, C. K., Yoo, C. S. and Chen, J. H., ”Dynamic Stiffness Removal for Direct Numerical Simulations”, *Combust. Flame*, Vol. 156 (2009), pp. 1542-1551.

[154] 笠木伸英, 河村洋, 長野靖尚, 宮内敏雄 編, ”乱流工学ハンドブック”, 朝倉書店, (2009)

[155] 山本義隆, ”磁力と重力の発見 1（古代・中世）”, みすず書房, (2003)

[156] 山本義隆, ”磁力と重力の発見 2（ルネサンス）”, みすず書房, (2003)

[157] 山本義隆, ”磁力と重力の発見 3（近代の始まり）”, みすず書房, (2003)

[158] 山本義隆, ”熱学思想の史的展開 1”, 筑摩書房, (2008)

[159] 山本義隆, ”熱学思想の史的展開 2”, 筑摩書房, (2008)

[160] 山本義隆, ”熱学思想の史的展開 3”, 筑摩書房, (2008)

[161] 熊谷清一郎, ”火”, 岩波書店, (1979)

[162] 新岡崇, 河野通方, 佐藤順一 編, ”燃焼現象の基礎”, オーム社出版局, (2001)

Appendix A

Examination of Chemical Reaction Model of n-Heptane/Air Mixture

A.1 Preface

Normally, fuels of spray combustion are Gasoline or light oil etc., which are liquid at normal temperature. Their combustion mechanisms are so complex, because these fuels are blend materials. Therefore, simple mechanisms for only one component in these fuels, such as one-step or a few step reaction models, are often used in numerical simulations. In the case of numerical simulation of ignition or flame propagation, reaction model influences the results of these simulations. In addition, for the calculation cost, it is necessary to select the appropriate reaction model.

The object of this chapter is to examine the chemical reaction models of n-heptane/air combustion.

A.2 Numerical Method

In this chapter, zero-dimensional analyses of auto-ignition and one-dimensional analyses of freely propagating are conducted for five chemical reaction models by SENKIN [137] and PREMIX [138] of CHEMKIN.

Table A.1 shows chemical reaction models used in these analyses. Model-1 is

Table A.1: Chemical reaction models.

Model ID	Number of species	Number of reactions	Reference
Model-1	550	2450	Curren et al. [131]
Model-2	159	770	Seiser et al. [132]
Model-3	43	185	Liu et al. [133]
Model-4	37	61	Maroteaux and Noel [134]
Model-5	29	52	Patel et al. [135]

detailed chemical reaction model for n-heptan/air mixture and model-2 is reduced model derived from model-1. Model-3 is derived from Chevalier's model [139] and used for DNS of spray combustion. Model-4 and Model-5 are derived from Golovitchev's model [140] for simulation of HCCI engine.

In zero-dimensional analyses, constant volume and adiabatic system are assumed. Initial pressure ,temperature and equivalent ratio are changed as parameter. In one-dimensional analyses, pressure is 1 atm and preheat temperature is 1000 K with stoichiometric ratio.

A.3 Comparison of Ignition Delay Time

Figure A.1 shows ignition delay time for each case. Here, ignition delay time is defined as the time which the temperature increases 400 K from initial temperature. For comparison, experimental results by Ciezki et al. [141] are also shown. From Fig. A.1, all models indicate similar tendency for ignition delay time to initial temperature. These does not depend on initial pressure and equivalent ratio. The tendency of ignition delay time to initial temperature is different between high temperature region and low temperature region. This phenomenon is caused by n-heptane/air reaction mechanism, which has two bifurcation mechanisms, and is called as negative temperature coefficient regime. Especially, ignition delay time decreases dramatically in high temperature region because of rapid generation of OH radical.

Change of ignition delay time by equivalence ratio is slight, on the other hand, increase of initial pressure makes ignition delay time decrease clearly. Compared 5 models results, ignition delay time are relatively agreement with each other except for Model-5. In Model-5, the ignition delay time become 2-3 times of other models at high temperature region.

Figure A.2 shows temporal developments of temperature and mass fraction of major species for each case. From the temporal developments of temperature, ignition delay times nearly coincide in all cases except for Model-5. In Model-5, the ignition delay time is about 6 msec larger than other cases. From the temporal developments of mass fractions, O_2 are rapidly consumed at ignition term. C_7H_{16} moderately decreases at same term, because C_7H_{16} decomposes to lower hydrocarbons at a stage prior to ignition. The mass fraction of OH shows sharp peak at ignition except for Model-4. The profile of mass fraction of H_2O_2 of Model-5 is extremely different with other models, and the mass fraction at peak is very high.

A.4 Comparison of One-dimensional Flame Propagation

Figure A.3 shows spatial distributions of temperature and mole fraction of major species for Model-2 to Model-5. Initial condition are $\phi = 1.0$, T_0 =1000 K and P_0=13.5 bar. Laminar flame thicknesses in Model-4 and Model-5 are about two or three times than Model-2 and Model-3. The distributions of mass fractions of C_7H_{16}, O_2 and CO_2 are nearly coincide with each model. On the other hand, distributions of OH and H_2O_2, which are intermediates, are different for each model. In Model-4, increase of OH at flame sheet is moderate. In Model-5, the concentration of H_2O_2 at flame zone is very high, and this is consistent with the result of zero-dimensional analyses.

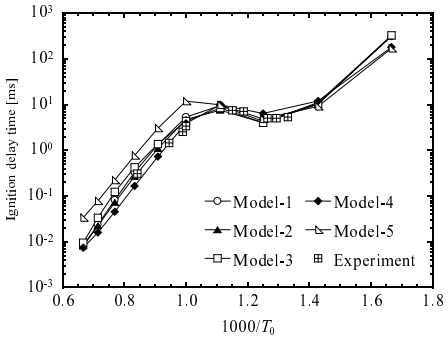

(a) $\phi = 0.5$, P_0=13.5 bar

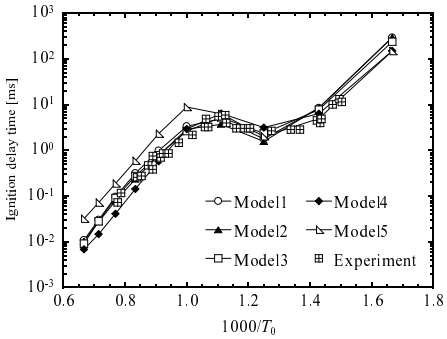

(b) $\phi = 1.0$, P_0=13.5 bar

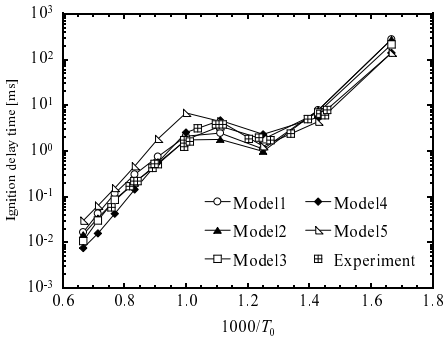

(d) $\phi = 2.0$, P_0=13.5 bar

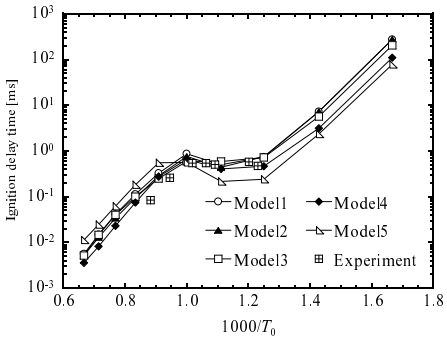

(d) $\phi = 1.0$, P_0=42.0 bar

Figure A.1: Ignition delay time.

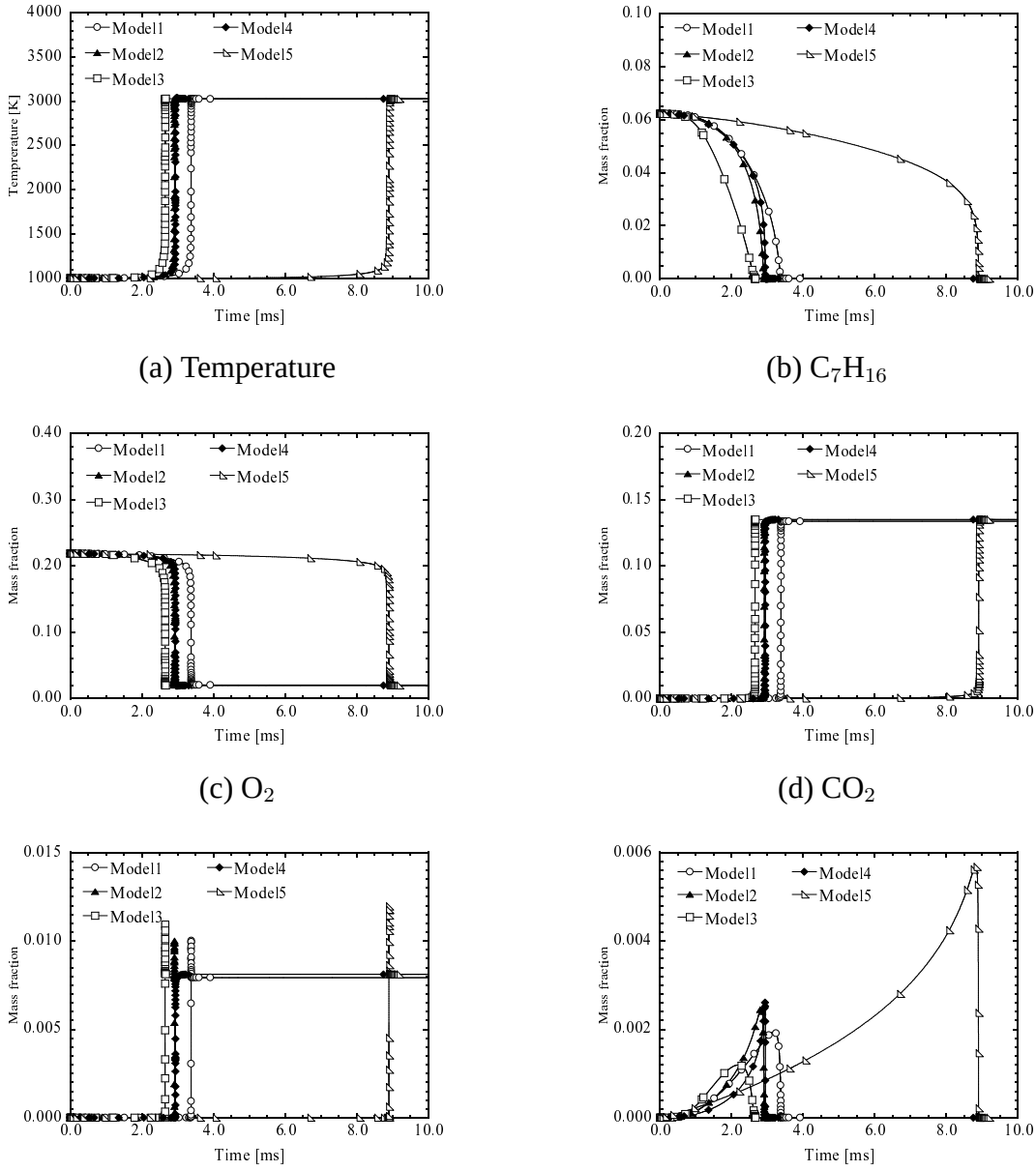

(a) Temperature

(b) C_7H_{16}

(c) O_2

(d) CO_2

(e) OH

(f) H_2O_2

Figure A.2: Temporal developments of temperature and mass fraction of major species for $\phi = 1.0$, T_0 =1000 K and P_0=13.5 bar .

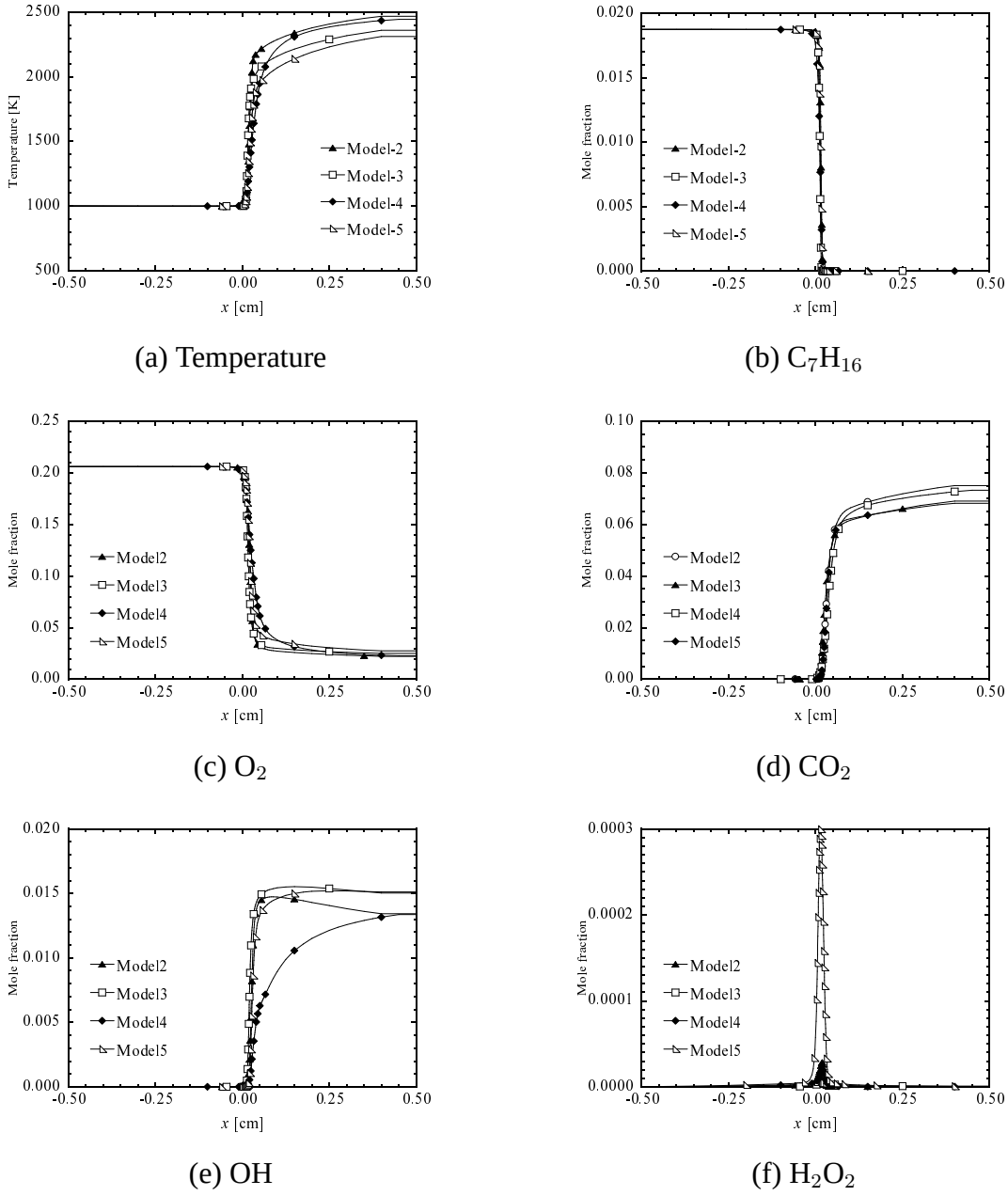

(a) Temperature

(b) C_7H_{16}

(c) O_2

(d) CO_2

(e) OH

(f) H_2O_2

Figure A.3: Spatial distributions of temperature and mole fraction of major species $\phi = 1.0$, T_0 =1000 K and P_0=13.5 bar .

Table A.2: 61 reactions and 37 species mechanism for n-heptane ignition.

No.	Reaction	A	b	E (cal)
1	$C_7H_{16} + O_2 = C_7H_{15-1} + HO_2$	2.500E+13	0.0	48810
2	$C_7H_{16} + O_2 = C_7H_{15-2} + HO_2$	2.800E+14	0.0	47180
3	$C_7H_{16} + H = C_7H_{15-1} + H_2$	5.600E+07	2.0	7667
4	$C_7H_{16} + H = C_7H_{15-2} + H_2$	4.380E+07	2.0	4750
5	$C_7H_{16} + OH = C_7H_{15-1} + H_2O$	8.600E+09	1.1	1815
6	$C_7H_{16} + OH = C_7H_{15-2} + H_2O$	4.800E+09	1.3	690.5
7	$C_7H_{16} + HO_2 = C_7H_{15-1} + H_2O_2$	8.000E+12	0.0	19300
8	$C_7H_{16} + HO_2 = C_7H_{15-2} + H_2O_2$	1.000E+13	0.0	16950
9	$C_7H_{16} + CH_3 = C_7H_{15-1} + CH_4$	1.300E+12	0.0	11600
10	$C_7H_{16} + CH_3 = C_7H_{15-2} + CH_4$	8.000E+11	0.0	9500
11	$C_7H_{16} = C_7H_{15-1} + H$	3.972E+19	-0.95	103200
12	$C_7H_{16} = C_7H_{15-2} + H$	1.248E+21	-1.34	100700
13	$C_7H_{16} = C_4H_9 + C_3H_7$	2.000E+16	0.0	80710
14	$C_7H_{15-1} + O_2 = C_7H_{15}O_2$	2.000E+12	0.0	0
15	$C_7H_{15-2} + O_2 = C_7H_{15}O_2$	2.000E+12	0.0	11600
16	$C_7H_{15}O_2 = C_7H_{14}O_2H$	6.000E+11	0.0	20380
17	$C_7H_{14}O_2H + O_2 = C_7H_{14}O_2HO_2$	2.340E+11	0.0	0
18	$C_7H_{14}O_2HO_2 = C_7KET21 + OH$	2.965E+13	0.0	26700
19	$C_7KET21 = C_5H_{11}CO + CH_2O + OH$	1.000E+16	0.0	42400
20	$C_5H_{11}CO = C_5H_{11} + CO$	1.000E+11	0.0	9600
21	$C_5H_{11} = C_2H_5 + C_3H_6$	3.200E+13	0.0	28300
22	$C_7H_{15-1} = C_2H_4 + C_5H_{11}$	2.500E+13	0.0	28810
23	$C_7H_{15-2} = CH_3 + C_6H_{12}$	3.000E+13	0.0	29800
24	$C_6H_{12} = C_3H_7 + C_3H_5$	1.000E+16	0.0	68000
25	$C_7H_{15-2} = C_4H_9 + C_3H_6$	1.200E+13	0.0	29600
26	$C_7H_{15-1} = C_7H_{15-2}$	2.000E+11	0.0	18100
27	$C_4H_9 = C_2H_5 + C_2H_4$	2.500E+13	0.0	28810
28	$C_3H_7 = C_2H_4 + CH_3$	9.600E+13	0.0	30950
29	$C_3H_6 = C_2H_3 + CH_3$	6.150E+15	0.0	85500
30	$C_3H_5 + OH = CH_3CHO + CH_3$	3.500E+11	0.0	85500
31	$C_3H_5 + O_2 = C_3H_4 + HO_2$	6.000E+11	0.0	10000
32	$C_3H_4 + OH = C_2H_3 + CH_2O$	1.000E+12	0.0	0
33	$C_3CO + M = CH_3 + CO + M$ All species in the mixture contribute contribute equally as third body	1.800E+16	0.0	14400
34	$CH_3CHO + OH = CH_3CO + H_2O$	1.000E+13	0.0	0
35	$CH_3O + CO = CH_3 + CO_2$	1.570E+14	0.0	11800

No.	Reaction	A	b	E (cal)
36	CH_3O (+M) = CH_2O + H (+M)			
	Low	2.344E+25	-2.7	30600
	High	2.000E+13	0.0	27420
37	CH_3 + HO_2 = CH_3O + OH	4.300E+13	0.0	0
38	CH_3 + O_2 = CH_2O + OH	4.800E+10	0.0	9000
39	CO + O + M = CO_2 + M	6.170E+14	0.0	3000
	All species in the mixture contribute contribute equally as third body			
40	CO + OH = CO_2 + H	3.510E+07	1.3	-758
41	HO_2 + CO = CO_2 + OH	5.800E+13	0.0	22930
42	H_2 + O_2 = OH + OH	1.700E+13	0.0	47780
43	O + OH = O_2 + H	4.000E+14	-0.5	0
44	H + O_2 + M = HO_2 + M	2.800E+18	-0.86	0
	Enhanced third body efficiencies O_2 = 0, H_2O = 0, CO =0.75, CO_2 = 1.5, C_2H_6 = 1.5, N_2 =0,			
45	H + O_2 + N_2 = HO_2 + N_2	2.600E+19	-1.24	0
46	OH + HO_2 = H_2O + O_2	7.500E+12	0.0	0
47	H + HO_2 = OH + OH	1.700E+14	0.0	875
48	HO_2 + HO_2 = H_2O_2 + O_2	2.000E+12	0.0	0
49	OH + OH (+M) = H_2O_2 (+M)			
	High	7.600E+13	-0.37	0
	Low	4.800E+18	-0.9	-1700
	Troe parameters: 1, 1.0E-15, 1500, 1.0E+15			
	Enhanced third body efficiencies H_2 = 2, H_2O =6, CO =1.5, CO_2 = 2, C_2H_6 = 3, N_2 =0.7, CH_2 = 4			
50	H_2O_2 +OH = H_2O + HO_2	1.000E+13	0.0	1800
51	H_2O_2 +H = H_2O + OH	1.000E+13	0.0	3590
52	CH_2O + OH = HCO + H_2O	2.430E+10	1.18	-447
53	CH_2O + HO_2 = HCO + H_2O_2	3.000E+12	0.0	8000
54	HCO + O_2 = HO_2 + CO	3.300E+12	-0.4	0
55	CH_4 + O = CH_3 + H_2O_2	1.020E+09	1.5	8604
56	CH_4 + HO_2 = CH_3 + H_2O_2	1.000E+13	0.0	18700
57	C_2H_4 + OH = CH_2O + CH_3	6.000E+13	0.0	960
58	C_2H_5 + O_2 = C_2H_4 + HO_2	2.000E+10	0.0	-2200
59	C_2H_3 + HO_2 = CH_2O + HCO	4.000E+12	0.0	-250

No.	Reaction	A	b	E (cal)
60	C_3H_8 (+M) = C_2H_5+CH_3 (+M)			
	High	9.900E+22	-1.6	84429
	Low	2.237E+27	-2.88	67448
	Troe parameters: 1, 1.0E-15, 1500, 1.0E+15			
	Enhanced third body efficiencies			
	H_2 = 2, H_2O =6, CO =1.5,			
	CO_2 = 2, C_2H_6 = 3, N_2 =0.7,			
	CH_2 = 4			
61	H + C_3H_7 (+M) = C_3H_8 (+M)			
	High	3.613E+13	0.0	0.0
	Low	4.42E+61	-13.545	11357
	Troe parameters: 0.315, 369, 3258, 6667			
	Enhanced third body efficiencies			
	H_2 = 2, H_2O =6, CO =1.5,			
	CO_2 = 2, C_2H_6 = 3, N_2 =0.7,			
	CH_2 = 4			

(A: frequency factor, b: pre-exponential temperature exponent, E: activation energy)

Appendix B

Adoption of a Point-implicit Time Integration Method to DNS of Turbulent Combustion

B.1 Preface

In the combustion DNS, an explicit method has been generally used for the time integration scheme [142][143][144], and because of chemical reaction term, their time increment have to be nanosecond order for hydrogen/air and methane/air premixed flame. On the other hand, a point-implicit method in which only chemical reaction term is integrated implicitly and other terms are integrated by explicit method has been used in the simulation of supersonic flow field with chemical reaction [145][146]. When an implicit method is adopted to the time integration, the convergence calculation increases the amount of computation, whereas the time increment can be increased. Therefore, total computation time can be reduced because the stiffness of chemical reaction is prevented by an implicit method. However, the influence on DNS results by using the point-implicit method has not been cleared yet.

The objective of this chapter is to clarify the influence of a point-implicit time integration method on DNS results of combustion by comparing the DNS results for explicit time integration method with that for point-implicit one. Fur-

thermore, adoption of point-implicit time integration method to DNS of high hydrocarbon/air combustions, such as n-heptane/air, iso-octane/air and n-decane/air mixture, is also studied to examine the stiffness of chemical reaction mechanism for these fuels.

B.2 Numerical Method

B.2.1 Governing Equations and Numerical Scheme

Here, the conservation equations of mass, momentum, energy and chemical species are used for the governing equation for all numerical simulations including two -dimensional DNS. Details of the governing equations can be found in chapter 4. A detailed kinetic mechanism which includes 12 reactive species and 27 elementary reactions is used to represent hydrogen/air reaction, and GRI2.11 [106] which includes 49 reactive species and 279 elementary reactions is used to represent methane/air reaction. For high hydrocarbon/air reactions, reduced kinetic mechanisms are used. The details of these mechanisms are shown in section B3.5. Temperature dependence of the viscosity, thermal conductivity and diffusion coefficients are taken into account by linking CHEMKIN packages [99][100] with modifications for vector/parallel computations.

B.2.2 Point-implicit Scheme

In an explicit time integration method, the low storage third-order Runge-Kutta scheme is used for time integration for all terms in governing equations. In a point-implicit time integration method, time splitting method is adopted to time integration of the chemical species conservation equation. The species conservation equations are written as follows;

$$\frac{\partial Y_i}{\partial t} + \boldsymbol{u} \cdot \bigtriangledown Y_i = -\frac{1}{\rho} \bigtriangledown \cdot (\rho Y_i V_i) + \frac{\omega_i}{\rho} \, . \tag{B.1}$$

Where, ρ and $\boldsymbol{u}$ represent density and velocity vector. Y_i, $\boldsymbol{V_i}$ and ω_i represent mass fraction, diffusion velocity and source term for species i. By introducing

intermediate time step, Eq. (B.1) is split into two equations;

$$\frac{Y_i^* - Y_i^n}{dt} = -\boldsymbol{u} \cdot \bigtriangledown Y_i - \frac{1}{\rho} \bigtriangledown \cdot (\rho Y_i V_i) \,, \tag{B.2}$$

$$\frac{Y_i^{n+1} - Y_i^*}{dt} = \frac{\omega_i}{\rho} \,. \tag{B.3}$$

Where superscript n represents time step, and $*$ means intermediate step. First, time integration of convective term and diffusion term are conducted by the low storage third-order Runge-Kutta scheme (Eq. (B.2)). Next, chemical reaction source term is integrated by implicit method (Eq. (B.3)). In this study, VODE solver which is developed in Lawrence Livermore National Laboratory is used for implicit time integration. The details of VODE solver is referenced in the previous researches [101][102].

B.2.3 Test Problems

Here, three fundamental combustion fields are selected to investigate availability of the point-implicit scheme to DNS of turbulent combustion. The first problem is auto-ignition of various fuels . In this test, effects of the point-implicit scheme on simulated combustion process are discussed in a view point of chemical stiffness because this problem does not include convection of the fluid. In section B.3.1, auto-ignition of hydrogen/air and methane/air mixture is analysed for different time increment. If the explicit scheme was used, a typical time increment is 3 ns for both fuels. The initial temperature is set to 1500 K and the equivalence ratio is 1.0 for all cases. The availability limit of the point-implicit scheme is shown by changing the time increment from 3 ns to 3 ms. The obtained results are compared with those of the explicit scheme with Δt =3 ns and well-known SENKIN [137] of CHEMKIN. In section B.3.5, to show the importance of the implicit scheme in DNS of high hydrocarbon fuels, the increment is varied both for the explicit and implicit scheme.

Second test problem is freely propagating laminar premixed flames. In this test, convection effects including CFL number limit are shown for hydrogen/air

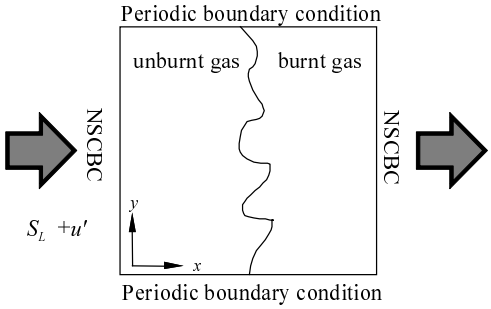

Figure B.1: Computational object of two-dimensional DNS.

and methane/air flames. The preheat temperature is 900 K, and equivalence ration is 1.0 for all cases. The distribution which was calculated by PREMIX [138] of CHEMKIN is used as an initial distribution. The computational domain is set to 1cm for all cases. The governing equations are discretized by the fourth order central finite difference scheme. To show the grid number requirement for the point-implicit scheme, grid number is changed under the condition of $\Delta t = 3$ ns. After showing the minimum grid number, the time increment is varied.

The final test problem is two-dimensional turbulent premixed flame propagating in homogeneous turbulence. Figure B.1 shows a schematic of the flow field used in two-dimensional DNS. In the two-dimensional DNS, the governing equations are discretized by the fourth-order central difference scheme in the flame propagation direction and the boundary condition in this direction is the Navier-Stokes characteristic boundary condition (NSCBC) [97][98]. The Fourier spectral method is used in the cross direction and the boundary condition in this direction are periodic. The preheat temperature is 700 K and equivalence ratio is 1.0. Computational domain is 1.074cm in flame propagation direction and 0.537cm in cross direction. Grid point and time increment are 1281×512 and 1.5 ns for explicit method and 385×192 and 15 ns for point-implicit method.

B.3 Results and Discussion

B.3.1 Zero-dimensional Analysis of Ignition

In this section, zero-dimensional analyses of auto-ignition are conducted for hydrogen/air and methane/air mixture by using DNS code of turbulent combustion.

Figure B.2 shows the temporal developments of temperature in zero-dimensional hydrogen/air and methane/air ignition obtained by explicit time integration method and point-implicit time integration method. Here, "E" represents result of explicit method and "I" represents that of point-implicit method. The width of time increment is also shown with each method. For comparison, the results by SENKIN of CHEMKIN are also plotted. For hydrogen case, the temporal developments of temperature by explicit method with $\Delta t = 3$ ns is in good agreement with that by point-implicit method with Δt =3 ns and 30 ns and that by SENKIN. Density, heat release rate and mass fraction of all chemical species are also in good agreement (not shown here). In the case of $\Delta t = 300$ ns, the temporal development of temperature differs from the explicit one after 0.02 ms, and there is about 100 K differences at 0.1 ms. In the case of $\Delta t = 3$ ms, the temporal development of temperature is different from other cases after ignition. For methane case, the temporal developments of temperature for point-implicit method with $\Delta t = 3$ ns and 30ns are in good agreement with that by explicit method and SENKIN. In the case of $\Delta t = 300$ ns, the profile near the ignition is slightly different from the cases of $\Delta t = 3$ ns and 30 ns. In the case of $\Delta t = 3$ ms, the temperature after the ignition is clearly different from other cases but the time of temperature rapid increase is almost same. When explicit method is adopted, the maximum width of time increment is less than 10 ns for both fuels because of their stiffness. From above results, the time increment can be increased to ≈ 30 ns by using point-implicit method

B.3.2 One-dimensional Analysis of Flame Propagation

In this section, one-dimensional analysis of freely propagating hydrogen/air and methane/air premixed flames are conducted to show the effectiveness of the point implicit scheme by using DNS code. In the DNS code, pressure term is directly solved without any simplifications. In general, one-dimensional analysis of a laminar premixed flame such as PREMIX of CHMEKIN is conducted under the assumption of constant pressure through the flame.

If the explicit scheme is used for all terms in the governing equations, grid requirement are increased because sharp peaks in chemical reaction rates of several species causes numerical instabilities. There is a possibility that the usage of the implicit scheme for chemical reaction terms reduces number of numerical grid. Figure B.3 shows distributions of temperature, density, heat release rate and H_2O_2 mole fraction of one-dimensional laminar methane/air premixed flame obtained by the point-implicit scheme with a constant time increment ($\Delta t = 3$ ns) and varying grid number. For comparison, the result obtained by fully explicit scheme, which is calculated with the same time increment and 1025 grid points, is presented.

Distributions of temperature, density and heat release rate obtained by the point-implicit scheme well coincide with those by the explicit scheme even for the minimum grid number in this analysis ($N_x = 257$). The distribution of H_2O_2 mole fraction, however, shows small oscillation near the flame front for $N_x = 257$. Similar analyses have been done for the hydrogen/air laminar flame and the minimum grid number requirement is also shown for the point-implicit scheme.

The maximum time increment for the point-implicit scheme was clarified both for hydrogen/air and methane/air laminar premixed flames with the minimum grid number shown in above. Figure B.4 shows flame structure of methane/air premixed flame for various time increment and $N_x = 385$. Up to $\Delta t = 30$ ns, the flame structure except for H_2O_2 mole fraction agrees with that by explicit scheme. Similar to grid requirement test in Fig. B.3, small oscillation of H_2O_2 distribution

is observed near the flame front.

These results suggest that the usage of a point-implicit scheme reduces both grid and computational time requirements simultaneously. It should be noted that the maximum time increment is determined by CFL limit for the point-implicit scheme.

B.3.3 Two-dimensional DNS of Turbulent Premixed Flame Propagation

Figure B.5 shows the distributions of heat release rate and temperature of hydrogen/air turbulent premixed flame propagation for explicit time integration method and point-implicit time integration method.

In Fig. B.5, distributions of heat release rate and temperature for point-implicit case coincide with these for explicit method. To investigate these distributions in more detail, distributions of temperature, density, heat release rate and fluid velocity in flame propagation direction at $y = 0$ are shown in Fig. B.6. All distributions for point-implicit method case are in good agreement with those for explicit method. Therefore, point-implicit method can be adopted to DNS of turbulent combustion. Figure B.7 and B.8 show the same results for methane/air turbulent premixed flame propagation. The preheat temperature is 700 K and equivalence ratio is 1.0. Computational domain is 1.05cm in flame propagation direction and 0.525cm in cross direction. Grid point and time increment are 1281×512 and $\Delta t = 1.5$ ns for explicit method and 768×192 and $\Delta t = 13$ ns for point-implicit method. The distributions for point-implicit method are in good agreement with those of explicit method same as hydrogen/air case. Therefore point-implicit method also can be adopted to DNS of methane/air turbulent premixed flame.

B.3.4 Comparison of Computational Time in Two-dimensional DNS of Turbulent Premixed Flame Propagation

To evaluate the computational load of DNS with explicit method and point-implicit method, the computational time of two-dimensional DNS of hydrogen/air and methane/air turbulent premixed flame propagation is obtained for both methods. Numerical conditions such as number of grid point, time increment and turbulent property are same for each fuel case. These simulations are conducted by TSUBAME Grid Cluster in Tokyo Institute of Technology, with AMD Opteron 880. The computational time for point-implicit method is about 1.26 times that for explicit method in hydrogen/air flame, and about 1.96 times in methane/air flame. The maximum size of time increment is 3 ns in our previous two- or three-dimensional DNS with explicit time integration, and smaller size of time increment is needed to use fuel species with stronger stiffness, such as n-heptane as follows. On the other hand, from above results, time increment of over 10 ns can be used for point-implicit method, and hence it is possible to reduce the whole computational time.

B.3.5 High Hydrocarbon/air Combustion

DNS results of high hydrocarbon/air combustion are shown in the section. In the actual engines, gasoline or light oil are generally used for fuels, so it needs to conduct the DNS of turbulent combustion with these fuels to clarify the combustion phenomena in actual engines. The detailed chemical reaction mechanisms of such fuels are too complex to adopt to the DNS, because they are composed of high hydrocarbon species. The detailed chemical reaction mechanism of n-heptane combustion, for example, includes more than 500 chemical species and 2000 elementary reactions [131], and that of iso-octane combustion includes more than 800 chemical species and 3700 elementary reactions [147]. A detailed mechanism for n-alkane hydrocarbons from n-octane to n-hexadecane was suggested by Westbrook et al[148]. This mechanism includes more than 2000 chemical

species and 8000 elementary reactions. For these detailed mechanisms, many reduced mechanisms of high hydrocarbon combustions have been suggested for n-heptane [132][133][135], iso-octane [149][150] and n-decane [151][136][152] combustions. In this study, the models which includes 37 chemical species and 61 elementary reactions [134], 109 chemical species and 491 elementary reactions [149] and 67 chemical species and 600 elementary reactions [136] are used for n-heptane/air, iso-octane/air and n-decane/air combustion, respectively.

Figure B.9 shows the temporal developments of temperature of zero-dimensional n-heptane/ air ignition for explicit time integration method and point-implicit time integration method. For comparison, the results by SENKIN are also plotted. The initial temperature is 1500 K and the equivalence ratio is 1.0 for all cases. In Fig. B.9(a), even if time increment is very small such as 0.05 ns or 0.025 ns, the temperature development shows nonphysical behavior. Although the temperature developments for the case of Δt =0.00625 ns is in good agreement with that for SENKIN, it is not realistic to use such a small time increment for two- or three-dimensional DNS. In Fig. B.9(b), the temperature development for point-implicit method with $\Delta t = 3$ ns, 30 ns are in good agreement with that for SENKIN and explicit method with $\Delta t = 0.00625$ns. From these results, if explicit time integration is adopted to DNS, it needs to use extremely small time increment for n-heptane/air combustion compared with hydrogen/air or methane/air combustion, because the stiffness of chemical reaction is very strong. Such a computational stiffness is observed for other reaction mechanisms, for example, by Liu et al. [133] and Patel et al. [135].

For these stiffness, Lu et al. [153] suggested the method of stiffness removal in chemical reaction of n-heptane/air combustion. They conducted the removal of chemical species which are causes of stiffness, and examined the result of non-stiffness reaction mechanisms. From these operations, explicit time integration could be adopted for DNS of n-heptane/air combustion with non-stiffness chemical reaction. However, it needs a lot of costs to conduct these operations for various chemical reaction mechanisms, such as n-heptane/air, iso-octane/air, n-

decane/air and so on. In addition, it is considered that all chemical reaction mechanisms cannot be adopted by their method. The point-implicit method can be used to high hydrocarbon/air combustion without such operations.

Figure B.10 shows the temporal developments of temperature of zero-dimensional ignition with point-implicit time integration method for iso-octane/air and n-decane/air combustion. Temperature developments for point-implicit method with $\Delta t = 3$ ns, 30 ns are in good agreement with that for SENKIN. For explicit time integration, the time increment needs to be picoseconds order same as the case of n-heptane/air.

From these results, the computational time of DNS of high hydrocarbon combustion with explicit time integration will be very large even if the fastest super computer is used. On the other hand, in the point-implicit method, the time increment can be same order as hydrogen/air and methane/air combustion, so DNS of high hydrocarbon/air combustion becomes possible. The point-implicit method is very useful for DNS which considers fuel including reactions with strong stiffness, and the computational time can be dramatically reduced.

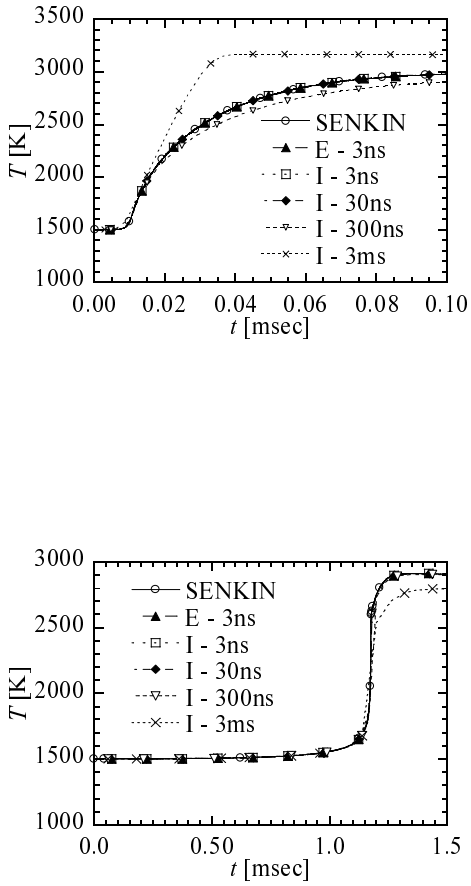

Figure B.2: Temporal developments of temperature in zero-dimensional hydrogen/air (upper) and methane/air ignition (lower).

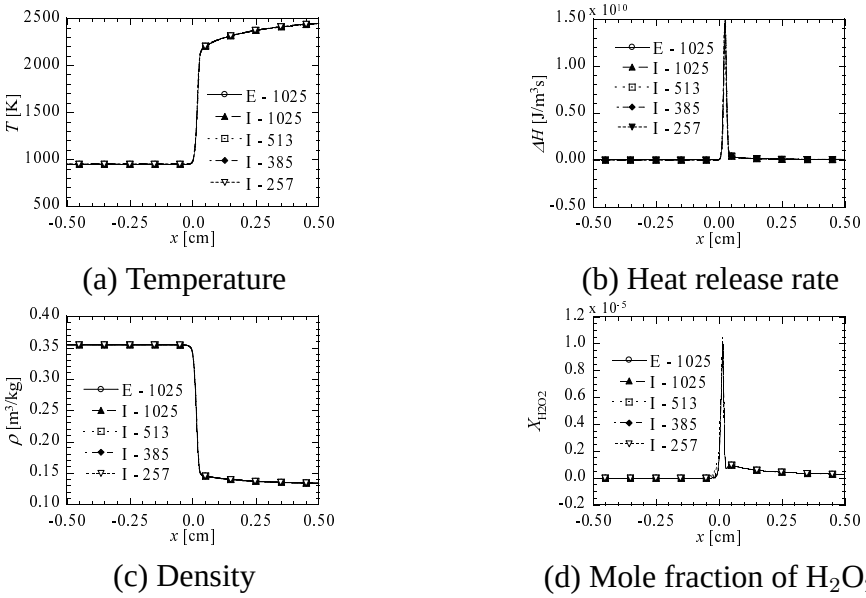

(a) Temperature (b) Heat release rate

(c) Density (d) Mole fraction of H_2O_2

Figure B.3: Spatial distributions of temperature, heat release rate, density and mole fraction of H_2O_2 of methane/air premixed flame for different grid point cases.

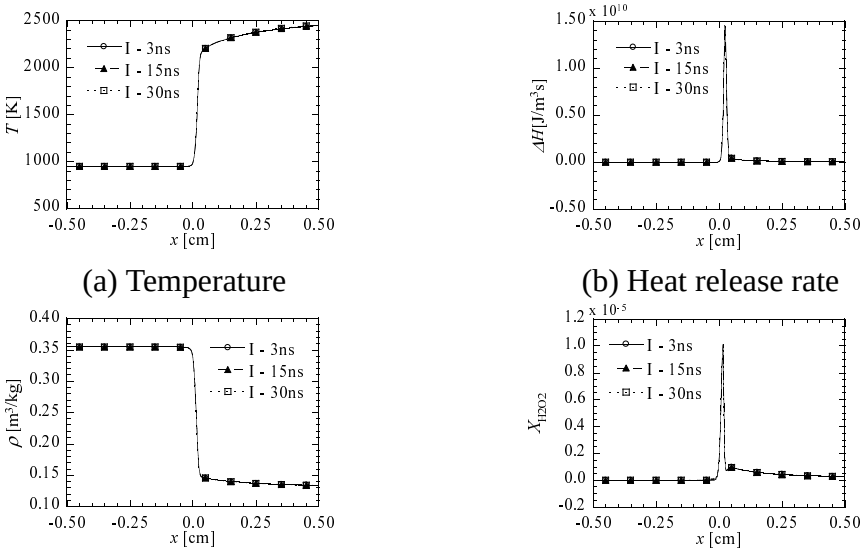

(a) Temperature (b) Heat release rate

(c) Density (d) Mole fraction of H_2O_2

Figure B.4: Spatial distributions of temperature, heat release rate, density and mole fraction of H_2O_2 of methane/air premixed flame for different time increment cases.

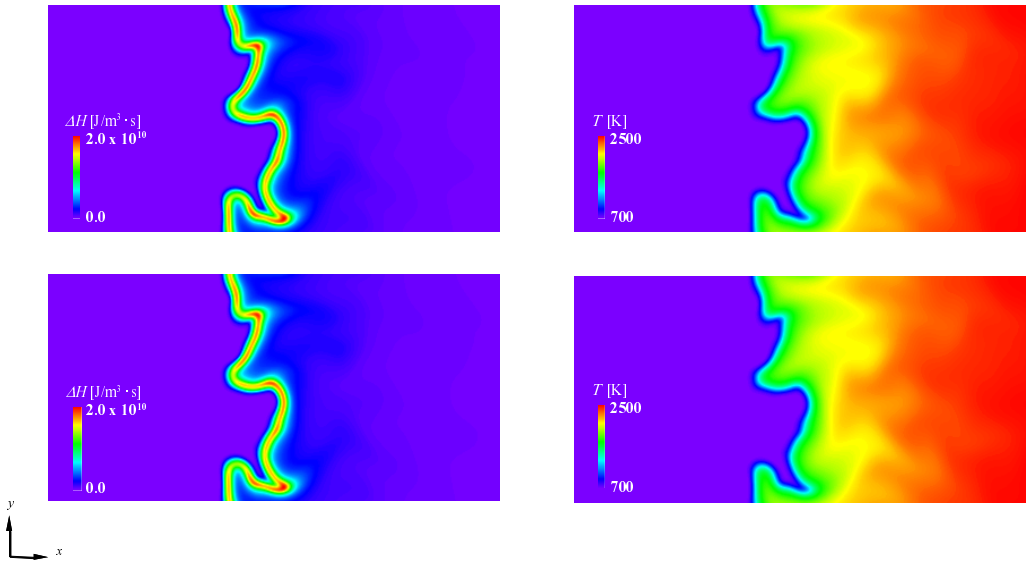

Figure B.5: Distributions of heat release rate (left) and temperature (right) for explicit method (upper) and point-implicit method (lower).

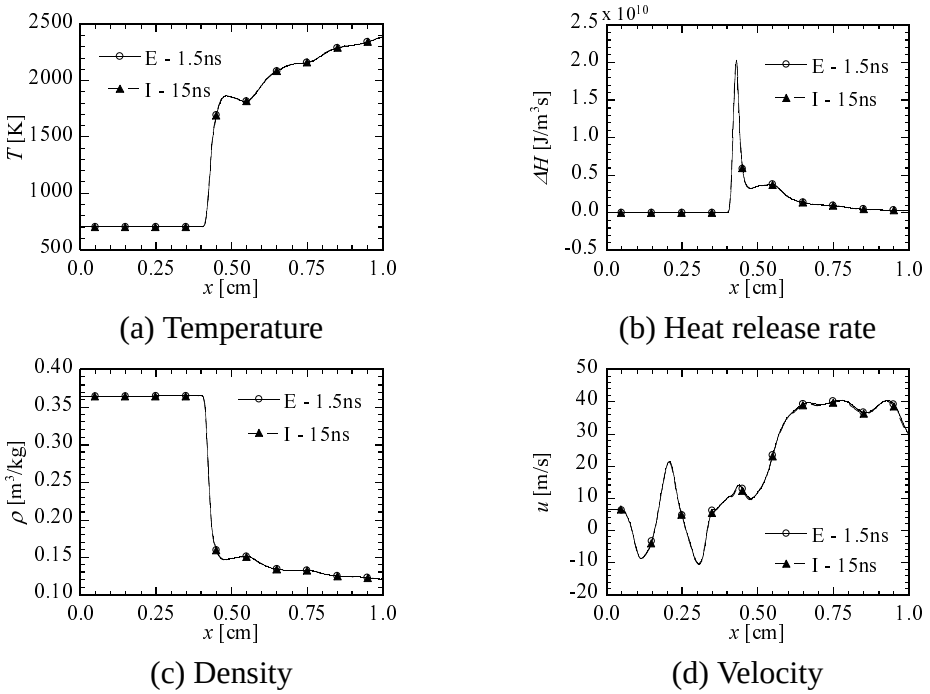

(a) Temperature

(b) Heat release rate

(c) Density

(d) Velocity

Figure B.6: Spatial distributions of temperature, heat release rate, density and velocity in x direction at $y = 0$.

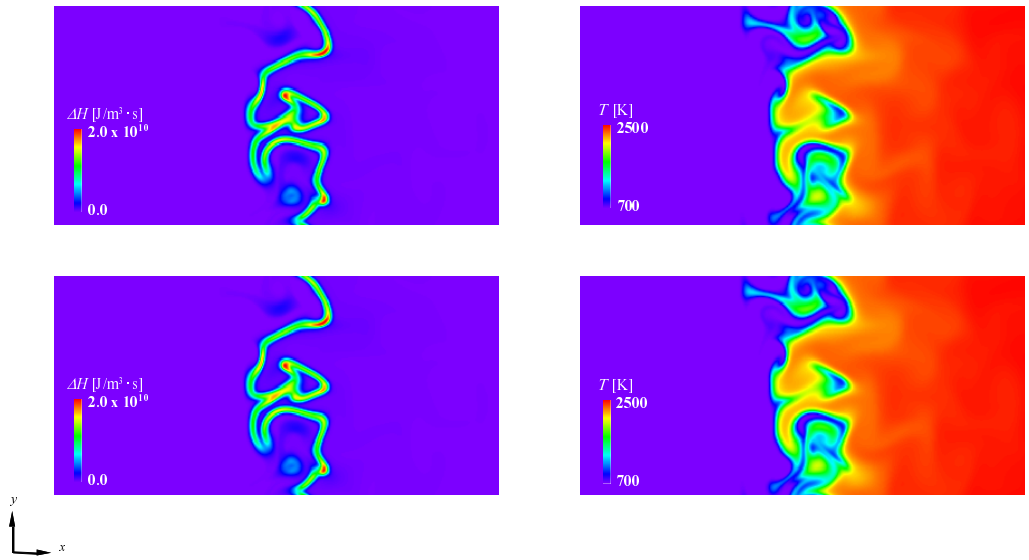

Figure B.7: Distributions of heat release rate (left) and temperature (right) for explicit method (upper) and point-implicit method (lower).

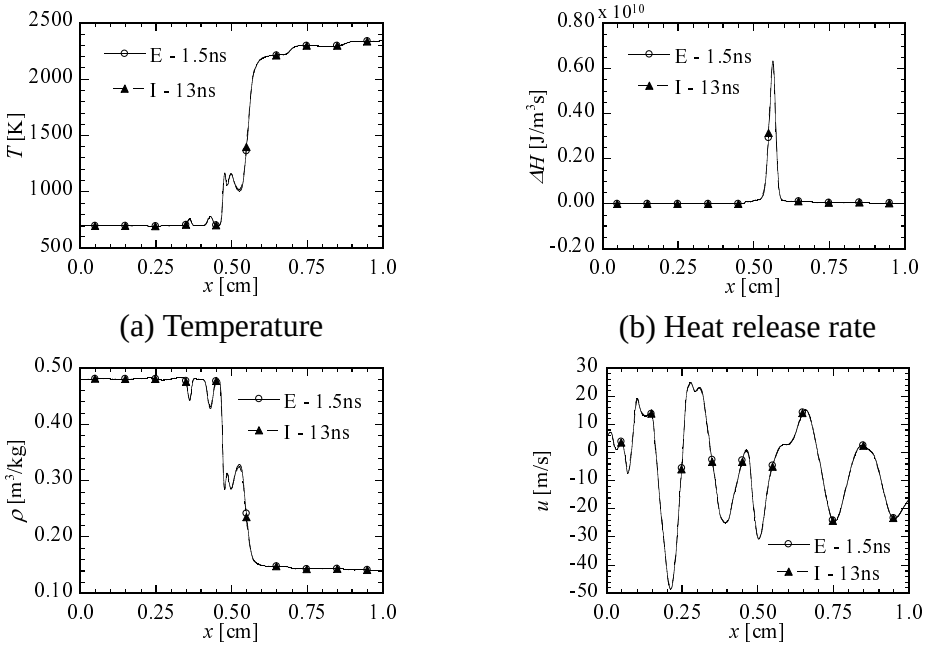

(a) Temperature (b) Heat release rate

(c) Density (d) Velocity

Figure B.8: Spatial distributions of temperature, heat release rate, density and velocity in x direction at $y = 0$.

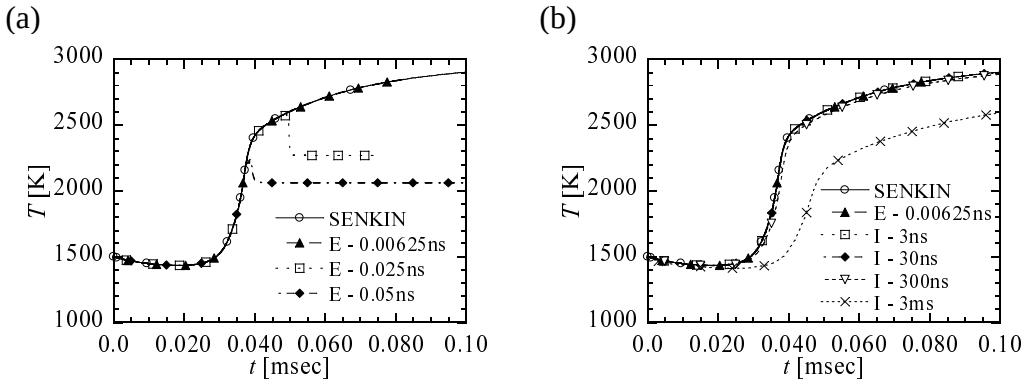

Figure B.9: Temporal developments of temperature in zero-dimensional ignition for n-heptane/air by explicit method (left) and by point-implicit method (right).

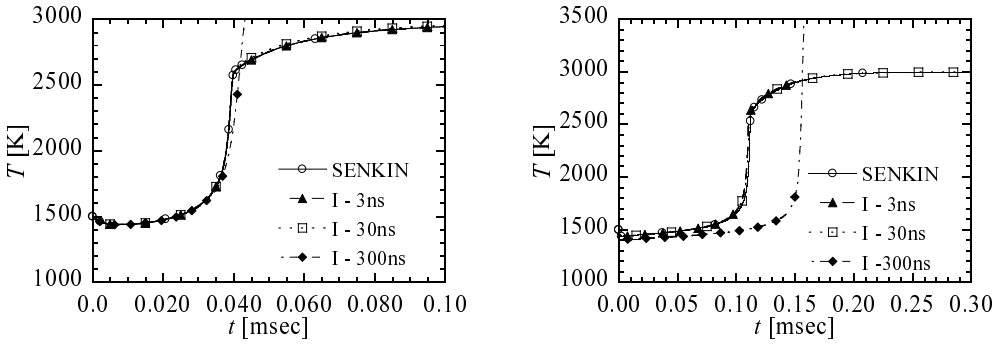

Figure B.10: Temporal developments of temperature in zero-dimensional iso-octane/air (left) and n-decane/air (right) ignition.

Acknowledgments

First and foremost, I would like to express my deeply sincere thanks to Professor Toshio Miyauchi, for his warm encouragements and thoughtful advices.

I am heartily thankful to Associate Professor Mamoru Tanahashi, for his wonderful supports.

I would like to thank Assistant Professors Naoya Fukushima, Youngsam Shim, Masayasu Shimura and Post Doctoral Itaru Yoshikawa. This thesis would not have been possible without their encouragement and supports. Especially, I received enormous supports from Masayasu Shimura. I want to particularly thank him.

I must also acknowledge Assistant Professors Takehiko Seo at Yamaguchi University, Lecturer Yuzuru Nada at Tokushima University, Associate Professor Gyung-Min Choi at Pusan University and Dr. Xinliang Li. They have given many useful advices to me. I wish to thank Shinobu Tokuda for many helpful discussions in seminar.

A very special thanks goes to the members of Miyauchi and Tanahashi Laboratory and graduated people.

My special gratitude to Dr. Shin-Jeong Kang and Yiefei Wang for sharing the

laboratory room with me for a long time. Thanks for your daily help and humor.

My deepest appreciation goes to Syuji Kato, Satoshi Kikuta, Kazuaki Hirasawa, Kunihiro Fukue, Syohei Inoue, Eisuke Hinode, Kuniharu Fujibayashi, Syohei Taka, Nobuhiro Shiwaku, Kiyoshi Terakado, Takeharu Fujisawa, Wenqi He, Hiroki Okada, Tetsu Hirayama, Shingo Matsuura, Hwa-Yeong Yu, Eriko Yamaki, Koichi Obana, Taisuke Kubota, Yasuhiro Tominaga, Takuya Yamaguchi, Takashi Ueda, Shoichi Tanaka, Akihiko Tsunemi, Tomoaki Fushimi, Yuki Minamoto, Satoshi Suzuki, Yushi Tsuzuki, Hiroaki Fukumoto, Komei Yamawaki, Yoshihiro Horiko. Especially, I want to thank Eisuke Hinode, Nobuhiro Shiwaku, Wenqi He, Shingo Matsuura, Akihiko Tsunemi and Makito Katayama. I am much indebted to them to accomplish this thesis.

I am deeply grateful to all secretaries of Miyauchi and Tanahashi Laboratory.

Special thanks also to Lecturer Nedunche Swaminathan at University of Cambridge and Associate Professor Yongmann M. Chung at University of Warwick. I have greatly benefited from the discussion with them. I would particularly like to thank to Markus Kindler, Alireza Mahdavifar, Claudio Lettieri and Rouzbeh Riazi. From talks with them, I have learned much knowledge about overseas.

I gratefully acknowledge Professor Akiko Matsuo and all of the group members of Matsuo Laboratory at Keio University. Especially, I would like to thank to Associate Professor Kazuaki Inaba, Dr. Yu Daimon, Dr. Hiroaki Miura and Hayato Morishita for their heartfelt supports. Many thanks go in particular to Hayato Sakamoto, Yasutomo Sasaki, Shigeru Sato, Takuya Shiraishi, Yohei Ando, Katsuya Nakajima, Noriyoshi Arai, Yuichi Katakura, Wataru Kobashi and Kazuya Watanabe for sharing the wonderful time with me.

I received generous support from everyone of my friends. I would like to express my special gratitude to Hideo Miki and Keiichiro Inaura. They made enormous contribution to me.

Finally, I would like to express my deeply sincere thanks to my mother Fumiko Sato, my brother Yuzuru Sato, my sister Tomomi Shimamura, my brother-in-law Hideharu Shimamura, my sister-in-law Kumiko Sato, my niece Yu Shimamura, my nephew Takumi Shimamura and my little niece Kanoko Sato. All supports of my family were invaluable.

The most important acknowledgement goes to ”My Fine Eddy”, Miki Uzumaki, for her support and patience. I would like to dedicate this thesis to you.